Cranfield University

Ricardo Nuno Gonçalves Correia

Development of a Pore Pressure Sensor Employing Fibre Bragg Gratings

School of Engineering
Engineering Photonics Group

PhD Thesis

Cranfield University

School of Engineering
Engineering Photonics Group

PhD Thesis
2008

Ricardo Nuno Gonçalves Correia

Development of a Pore Pressure Sensor Employing Fibre Bragg Gratings

Supervisor: Dr. Stephen W. James
Professor Ralph P. Tatam

December 2008

Abstract

Monitoring pore pressure is important to understand and predict the mechanical behaviour of soil, helping engineers to assess the stability of slopes and built infrastructures. The instrumentation used to monitor pore pressure should provide dense or extended spatial monitoring of the pore pressure and facilitate multiplexing with other sensors to form a multi-parameter monitoring system. The aim of this research was to develop a Fibre Bragg Grating (FBG) pore pressure sensor for soil applications, satisfying the typical measurement requirement of 1 kPa resolution over a 300 kPa measurement range with the potential for multiplexing. The technique used to develop the sensor consisted of transducing pressure into a transverse load applied to the central section of an FBG. This loading configuration induces a narrow spectral drop-out in the reflection spectrum of the FBG that tracks across its bandwidth in response to the applied load. The effect of this loading configuration on the reflection spectrum of a bare FBG was modelled with the aim of optimising the sensor range and resolution. An improvement of the sensor sensitivity to transverse load was obtained using a novel packaging technique that consisted of embedding the central section of the FBG within an epoxy cube. The deformation of the epoxy cube in response to transverse load resulted in the application of an axial strain to the embedded section of the FBG, which improved the load sensitivity. Moreover, this technique provided an efficient protection of the fibre against mechanical damage. A sensor housing was designed to allow the amplification/reduction of the load resulting from the pressure applied to a diaphragm. A pressure resolution of 0.2 kPa over a 100 kPa measurement range was obtained using a 6 mm long FBG with a 2 mm long section embedded in a epoxy cube which satisfies the sensor requisites.

Acknowledgements

Firstly, I would like to thank Dr. Stephen W. James for his excellent supervision and support throughout these three years. I am also very grateful to Professor Ralph P. Tatam and Dr. Edmon Chehura for their guidance and support.

I would also like to thank Steve Staines for his help producing the required mechanical parts and for his brilliant ideas.

My thanks must also go to Dr. Li Jin for his help in the final phase of the project and to all the members of the Engineering Photonics Group for creating such an enjoyable working environment.

Above all, I would like to thank to my parents for their love and support that proudly made me who I am, my brother, and a very special thank you to my future wife Catarina Henriques for her support and motivation throughout these 12 years.

Contents

List of Figures

List of Tables

Chapter 1

Introduction

Soils are unconsolidated layers that cover the earth's surface. It is on this structure that human infrastructures are built and therefore a good understanding of the mechanics of the soil systems to assess their stability is required. A soil system consists of particles of different sizes and shapes, usually rock fragments or clay particles, with water and gas occupying the voids between them (Atkinson, 2007). In a saturated soil where no water movement exists, equilibrium between the stresses in the solid and liquid phases exists. The stress result of internal forces acting on the contact points of the particles is called effective stress and the stress within the liquid phase (water) is called pore pressure. The combination of these two stresses represents the total stress at a point.

When a saturated soil is subject to external forces resulting for example from building an infrastructure, the state of equilibrium is altered and changes to the effective stresses and the pore water pressures occur. This increase of pore water pressure dissipates with time and is dependent on the drainage conditions and permeability of the soil. The pore pressure increases immediately after the application of a load and the pressurised water tends to flow towards the free drained areas (Aysen, 2005). This happens particularly in clay soils. With time, the excess pore pressure reduces and the volume of the clay layer decreases to balance the volume of expelled water. When the pore pressure returns to its initial value, the applied load is fully supported by the soil particles. This phenomenon is known as consolidation and is of extreme importance for the stability of infrastructures.

The stability of slopes is highly dependent on the pore water pressure. Many of the failures occurring in slopes occur after periods of heavy or prolonged rain or after changes in the groundwater conditions where pore pressure increase leads to a reduction in the effective stress and strength of the soil and consequent occurrence of landslide.

Monitoring of pore pressure is of extreme importance to understand and predict the mechanical behaviour of the soil when subject to external perturbations (Strout and Tjelta, 2005). Measuring the pore pressure, engineers can have a good knowledge of the effective stress of the soil predicting what is going to be the volume change after consolidation and avoid damage or collapse of buildings due to underestimated calculations of the effective soil stress. Moreover, monitoring pore pressure, it is possible for scientists to predict the behaviour of a slope when subject to changes of pore pressure, predicting the triggering of a landslide and giving alerts for civil evacuation from risky zones helping save human lives (Picarelli *et al.*, 2005; Simoni *et al.*, 2004).

Pore pressure can be monitored using instrumentation capable of continuous measurement of pore pressure at different locations within the soil. These devices are called piezometers and they are commercially available using a wide variety of technology to transduce the measurand of interest (water pressure) into a readable recordable value. The typical measurement requirements of a piezometer are a resolution of at least 1 kPa over a range of 300 kPa. A description of the working principle of such devices is presented in Chapter 2. There are two main types of piezometers, electrical and fibre optic based. The main problems with the commercially available electrical devices are: 1) they lack the capability of being multiplexed in an array of sensors sensitive to the same or different measurands requiring therefore, several demodulation systems to measure a range of soil parameters and; 2) their dimensions may not be compatible with the requirements of the application.

Fibre Optic Sensors (FOS) have several advantages over their conventional electrical counterparts in that they are compact in size, robust, chemically inert, non-conductive and are immune to electromagnetic interference. Moreover, they do not make use of electrical signals and are therefore safe to be used at risky explosive sites. Two types of fibre optic pore pressure sensors are commercially available, a Fabry-Perot interferometer fibre optic sensor and a Fibre Bragg Grating (FBG) fibre optic sensor (Gavea sensors catalogue, 2008; FOS&S catalogue, 2008 and Roctest catalogue, 2008). The FBG based pore pressure sensor is preferred to the Fabry-Perot interferometer as it offers the ability to deploy an array of uniquely identifiable sensors within a single

optical fibre, capable of monitoring the same or different soil characteristics such as salinity, humidity, temperature, etc., offering dense or extended spatial coverage of the parameters to measure. As the output signal from these devices is wavelength encoded, (*i.e.* their response to the measured parameter has specific wavelength over a specific wavelength range defined for each sensor) they are self-referencing, rendering the information independent of fluctuating light levels and with a system immune to source power and connector loss problems that is a limitation of many other optical sensors (Othonos and Kalli, 1999).

1.1 Introduction to fibre optic sensing technology

FOS have been the subject of intensive research and development for applications over a vast number of fields from medicine, to engineering and defence (Binu *et al.*, 2008; Wang *et al.*, 2001 and Nellen *et al.*, 2003). They offer a wide number of advantages compared to traditional electrical and mechanical sensors as presented above. FOSs are divided in two main categories (intrinsic and extrinsic) depending on how the fibre optic sensing system measures the measurand of interest. In an intrinsic sensor, the measurand interacts directly with the optical fibre modifying some of its properties which results in a modification of the characteristics of the transmitted or reflected light. The properties of the light that can be modified are the intensity, phase, frequency, wavelength, polarisation, or modal distribution. In an extrinsic sensor, the interaction between light and the measurand takes place externally to the optical fibre, with the modulated light being returned to the same or another optical fibre to be delivered to the detectors and demodulation unit (Higuera, 2002). Depending on the modulation of the light travelling on the optical fibre, FOS can be further divided into four main categories (intensity modulated, phase modulated, spectrum modulated and time and frequency-modulated sensors) depending on the property of the light signal that is modulated. In this thesis, a spectrum modulated FOS based on FBG technology was investigated.

1.1.1 Fibre Bragg grating sensing principles

An FBG is an Ultra Violet (UV) radiation induced periodic modulation of the refractive index of the core of an optical fibre (Kashyap, 1999) formed by the illumination of the core of the optical fibre to the interference pattern formed between two coherent beams of UV light. This results on a photo-induced modulation of the refractive index of the core with a period smaller than 1 μm. The refractive index modulation of the FBG is shown in Figure 1-1 and represented by Equation (1-1) (Othonos and Kalli 1999).

$$n(x,y,z) = \vec{n}(x,y,z) + \delta n(x,y,z).\cos\left(\frac{2.\pi}{\Lambda} z\right) \quad \textbf{(1-1)}$$

where $\vec{n}(x,y,z)$ is the average refractive index of the core, $\delta n(x,y,z)$ is the modulation of the refractive index, and Λ is the grating period.

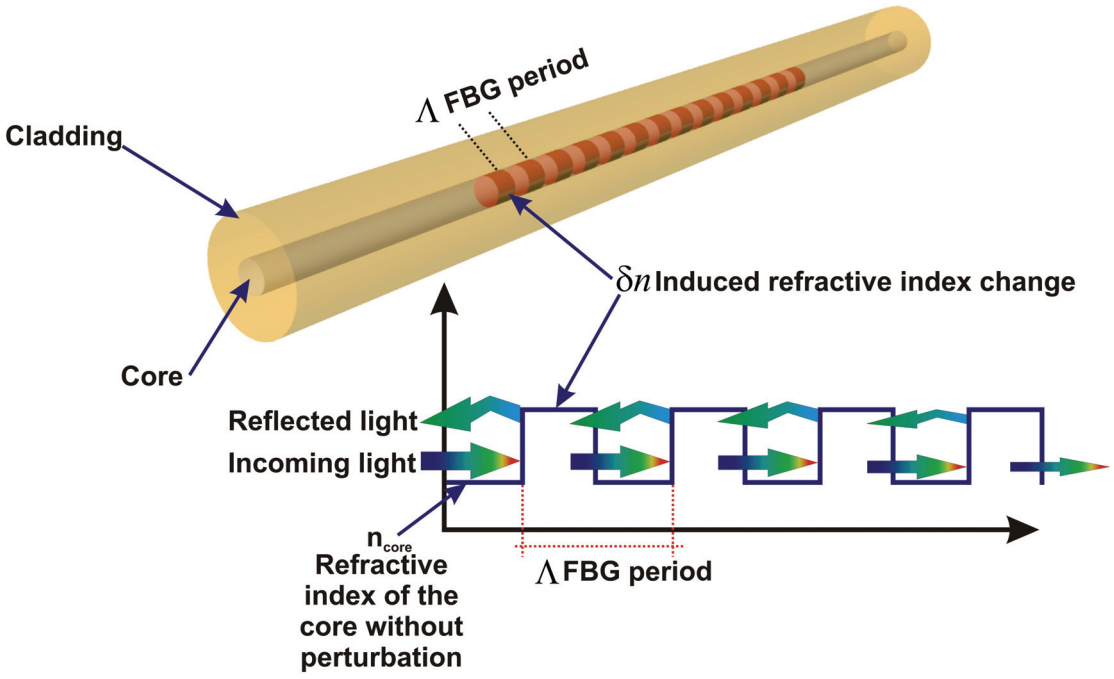

Figure 1-1: Refractive index change of a Fibre Bragg Grating (adapted from Zhao, 2001)

When an FBG is illuminated by a broadband optical source, a narrow-band spectral component corresponding to the Bragg resonance wavelength of the grating, λ_B, is reflected while all other wavelengths outside the narrow reflection band will be transmitted. The Bragg wavelength, λ_B, is given by (Rao, 1997):

$$\lambda_B = 2.n_{eff}.\Lambda \tag{1-2}$$

where n_{eff} is the effective refractive index of the optical fibre and Λ is the grating period.

A reflection spectrum of a 6 mm long FBG with a central wavelength 1547 nm and a grating period of 0.535 μm simulated using the transfer matrix method (Kashyap, 1999) is presented in Figure 1-2. In Chapter 3, a detailed description of the theoretical basis of FBGs, and methods for modelling their operation is presented.

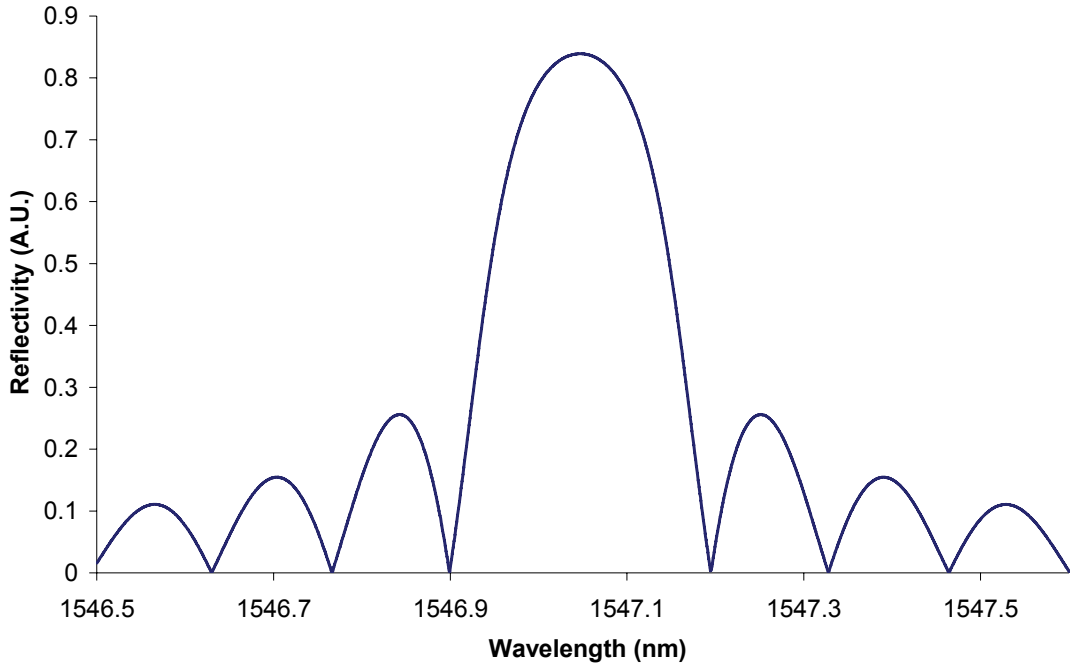

Figure 1-2: Simulated reflection spectrum of a 6 mm long FBG with central wavelength 1547 nm and a grating period of 0.535 μm using the transfer matrix method (Kashyap, 1999).

FBG sensing technology is based on the principle that if the period of the FBG or the refractive index of the fibre is changed, a change of the reflected Bragg wavelength λ_B will occur (Kashyap, 1999). An FBG is inherently sensitive to physical parameters such as temperature and isotropic pressure. If the temperature changes, a change in the Bragg wavelength λ_B occurs due to: 1) a change of the period Λ of the FBG affected by thermal expansion of the fibre and; 2) a change of the refractive index of the fibre n_{eff} due to a thermo-optic effect. The temperature response of an FBG is given by (Othonos and Kalli, 1999):

$$\Delta\lambda_B = \lambda_B.(\alpha_\Lambda + \alpha_n).\Delta T \tag{1-3}$$

where $\alpha_\Lambda = \left(\frac{1}{\Lambda}\right)\left(\frac{d\Lambda}{dT}\right) = 0.55\times10^{-6}\ ^\circ C^{-1}$ is the thermal expansion coefficient of a silica optical fibre and $\alpha_n = \left(\frac{1}{n_{eff}}\right)\left(\frac{dn_{eff}}{dT}\right) = 8.6\times10^{-6}\ ^\circ C^{-1}$ is the thermo-optic coefficient of a germanio-doped silica core fibre, ΔT is the temperature change and $\Delta\lambda_B$ the Bragg wavelength shift (Othonos and Kalli, 1999). The temperature sensitivity predicted from Equation (1-3) at a Bragg wavelength of 1550 nm is 13.7 pm/ºC (Othonos and Kalli, 1999).

Change of isotropic pressure acting on the FBG also changes the Bragg wavelength λ_B of the FBG. This happens due to a change of the period Λ of the FBG resulting from contraction of the FBG length and a change of the refractive index of the fibre due to a change of the FBG diameter. When an FBG is subject to a pressure ΔP, a fractional change $\Delta\lambda_B/\lambda_B$ is induced in the Bragg wavelength λ_B given by (Othonos, A. and Kalli, K., 1999):

$$\frac{\Delta\lambda_B}{\lambda_B} = \frac{\Delta\left(n_{eff}\Lambda\right)}{n_{eff}\Lambda} = \left[\frac{1}{\Lambda}\frac{d\Lambda}{dP} + \frac{1}{n_{eff}}\frac{dn}{dP}\right].\Delta P \tag{1-4}$$

For a Single Mode (SM) optical fibre, the fractional change in the diameter of the fibre is insignificant compared to the change in physical length and refractive index of the fibre, which are given by Equations (1-5) and (1-6) respectively (Hocker, 1979):

$$\frac{\Delta L}{L} = \frac{(1-2\nu)P}{E} \tag{1-5}$$

$$\frac{\Delta n_{eff}}{n_{eff}} = \frac{n_{eff}^{\ 2}}{2E}(1-2\nu)(2p_{12}+2p_{11}) \tag{1-6}$$

where E is the Youngs modulus of the fibre, ν is the Poisson ratio of the fibre and p_{11} and p_{12} are the strain optic tensor components. Over the sensing region, the fractional change of the period of the FBG is equal to the fractional change of the physical length $\frac{\Delta L}{L} = \frac{\Delta n_{eff}}{n_{eff}}$ and the wavelength pressure sensitivity of the FBG can be presented as (Othonos, A. and Kalli, K., 1999):

$$\Delta\lambda_B = \lambda_B\left[-\frac{(1-2\nu)}{E} + \frac{n_{eff}^{\ 2}}{2E}(1-2\nu)(2p_{12}+p_{11})\right]\Delta P \tag{1-7}$$

In 1993, Xu *et al.* experimentally measured $\frac{\Delta\lambda_B}{\Delta P}$ to be equal to -3.04x10^{-3} nm/MPa over a pressure range of 70 MPa for an FBG with central wavelength 1553 nm. This pressure sensitivity corresponds to a pressure resolution of 328.9 kPa (using a 1 pm resolution demodulation system to interrogate the sensor). This sensitivity of a bare FBG to isotropic pressure is very low and therefore techniques to amplify the response by transducing the pressure change into axial strain which acts on the FBG or to a non-isotropic transverse load acting on the FBG have been investigated.

A strain applied to an FBG affects its response through the expansion or compression of the grating region which changes the FBG period. A strain induced modification of the refractive index (strain-optic effect) also contributes to a change of the response of the FBG spectrum to strain. The strain response of the Bragg wavelength is given by (Othonos, A. and Kalli, K., 1999):

$$\Delta\lambda_B = \lambda_B.\left(1-\frac{n_{eff}^2}{2}\left(P_{12}-\nu\left(P_{11}-P_{12}\right)\right)\right).\Delta\varepsilon \tag{1-8}$$

where ν is Poisson's ratio and P_{11} and P_{12} are the strain-optic tensor components, $\Delta\lambda_B$ is the change in Bragg wavelength and $\Delta\varepsilon$ is the applied longitudinal strain. For a typical germanosilicate optical fibre with $P_{11} = 0.113$, $P_{12} = 0.252$, $\nu = 0.16$ and $n_{eff} = 1.482$ (Othonos, A. and Kalli, K., 1999) the strain sensitivity predicted from Equation (1-8) at a Bragg wavelength of 1550 nm is 1.2 pm/με.

A non-isotropic transverse load applied to an FBG changes the refractive index of the fibre (photo elastic phenomenon), inducing birefringence. Birefringence can be defined as the condition where two indices of refraction exist in the optical fibre. When a transverse load is applied to an FBG written in SM fibre, a refractive index change of the fibre along the axis which is being loaded occurs. This change of the refractive index leads to the reflection wavelength of the FBG along the loaded axis of a Bragg wavelength being different from the one reflected due to the light present in the other axis. As a result, the Bragg peak broadens with the increasing load until the two Bragg peaks split apart as the load is continuously increased (Figure 1-3).

The change in Bragg wavelength for light propagating in the x and y axis respectively is given by (Gafsi and El-Sherif, 2000):

$$\Delta\lambda_x = -\lambda_x \frac{n_{eff}^2}{2}\left(P_{11}\varepsilon_x + P_{12}\varepsilon_y\right) \quad \textbf{(1-9)}$$

$$\Delta\lambda_y = -\lambda_y \frac{n_{eff}^2}{2}\left(P_{11}\varepsilon_x + P_{12}\varepsilon_y\right) \quad \textbf{(1-10)}$$

where the strain along the *z* direction is assumed to be zero (case of plane strain, $\varepsilon_z = 0$), ε_x and ε_y are the strains along the *x* and *y* axis of the fibre.

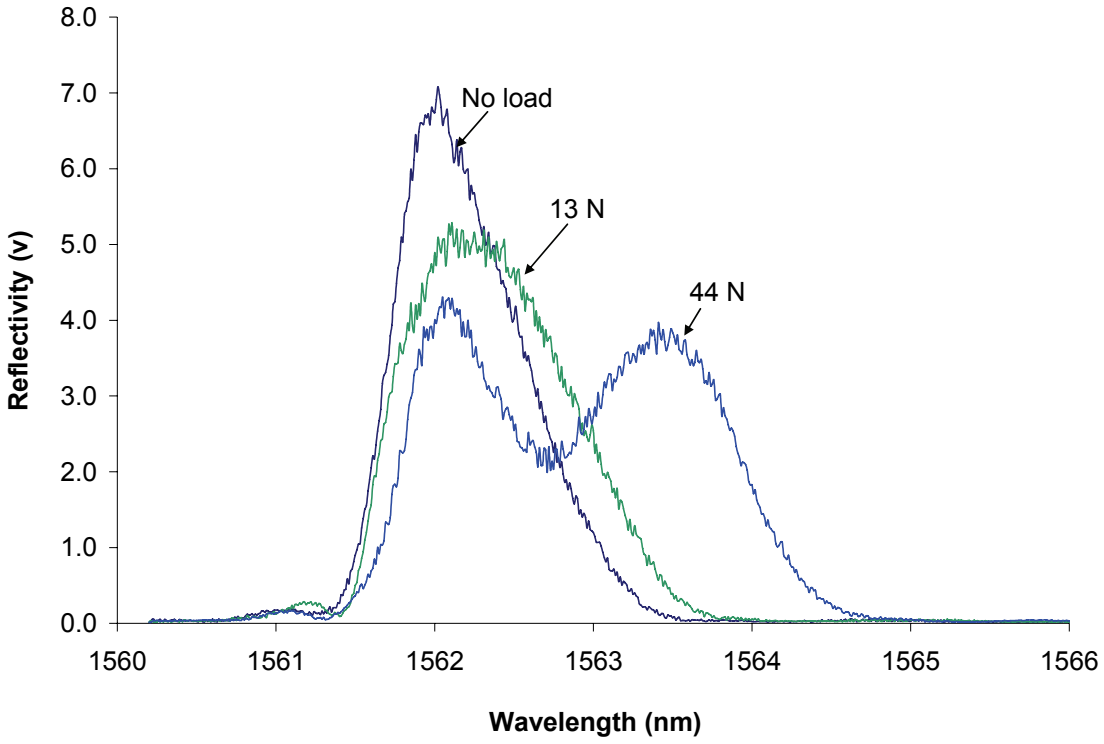

Figure 1-3: Experimental obtained reflection spectrum of a 2 mm SM FBG with central wavelength 1562 nm subject to transverse load all across its length (Blue: no load; Green: 13 N; Blue: 44 N).

A disadvantage of this technique is the difficulty in tracking the Bragg wavelength response for small loads as the two peaks are not yet separated. The transverse load of an FBG written in high birefringence Polarisation Maintaining (PM) fibre is more efficient. PM optical fibre is fabricated with anisotropic refractive index distribution in the core of the optical fibre, resulting in different refractive index over the eigenaxes of the fibre (Figure 1-4a). Therefore, the reflection spectrum of an FBG fabricated in PM fibre consists of two narrowly spaced Bragg peaks (Figure 1-4b). When the fibre is undisturbed, the peaks are already separated and therefore, the lack of resolution for small loads is removed.

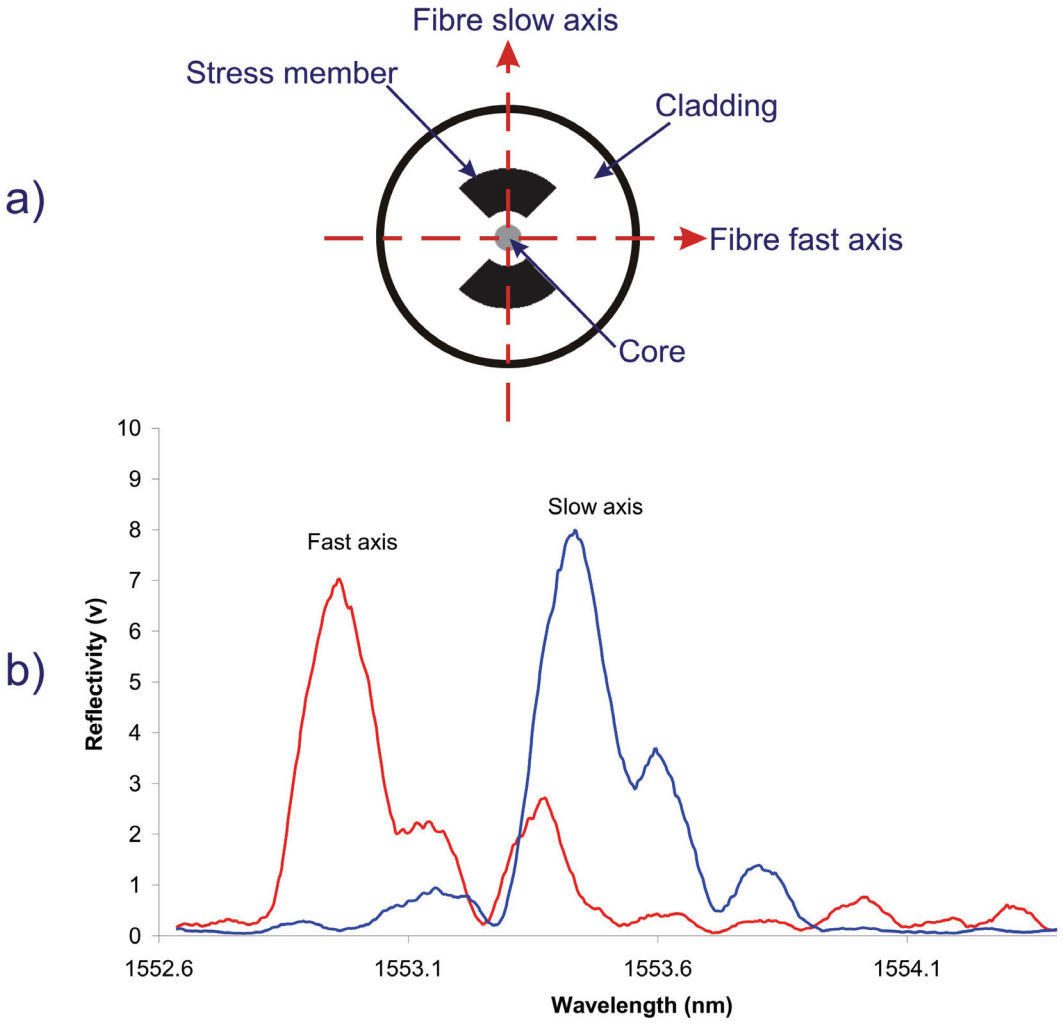

Figure 1-4: a) A schematic diagram of the cross-section of a bow-tie PM fibre; b) Experimental obtained reflection spectrum of the two eigenaxis of a 6 mm FBG written in bow-tie HiBi fibre with nominal central wavelength of 1553.5 nm.

Another technique that overcomes the lack of resolution for small loads applied transversely to an FBG is to localise the load over a small section in the centre of the FBG. When an FBG with uniform period is subject to a localised transverse applied load along a short central section of its length, a change of the original FBG refractive index profile occurs. On both sides of the loaded region the FBG remains unperturbed, with the grating period and effective refractive index unchanged, while over the loaded section a new FBG is formed due to the local change of the effective refractive index (Figure 1-5) (Matos *et al.*, 2001; Torres and Valente, 2002; Michaille *et al.*, 2003). This creates a phase relationship between the two gratings and, as result, a spectral drop-out

appears within the bandwidth of the original FBG spectrum (Figure 1-6), tracking across the FBG spectrum bandwidth in response to increasing load.

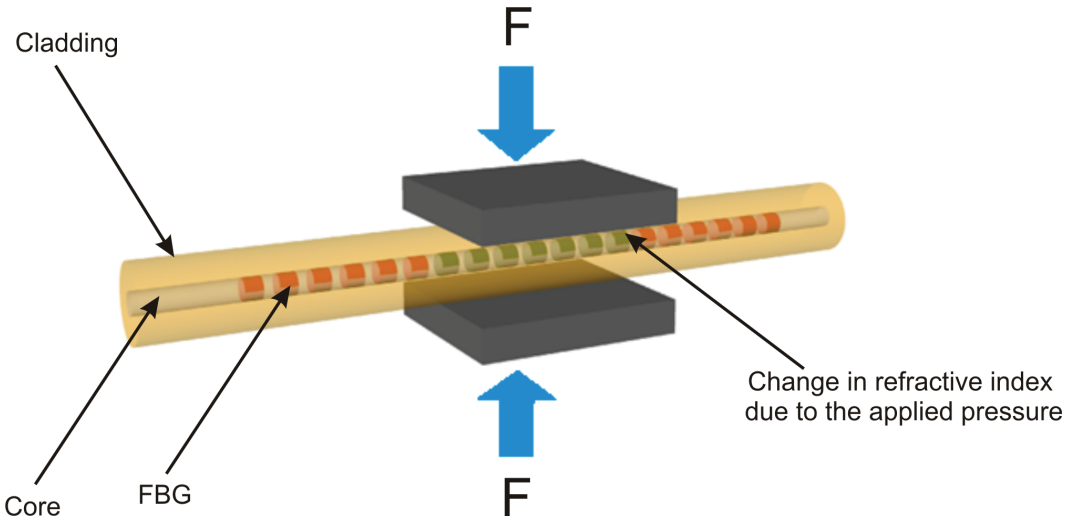

Figure 1-5: Schematic representation of a central section of an FBG with uniform period subject to transverse load with different colours representing different effective refractive index change (in orange the original effective refractive index of the FBG and in green the new local effective refractive index).

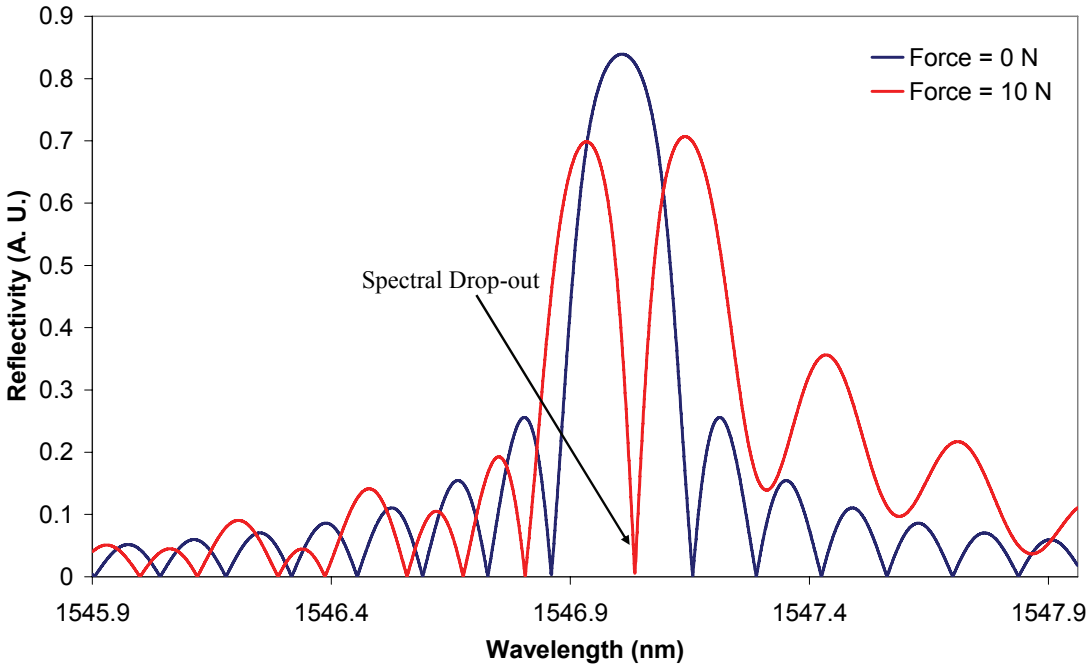

Figure 1-6: Theoretical simulated reflection spectrum of a 6 mm long FBG subject to a transverse load along 1 mm of its centre using the Transfer Matrix Method described in Section 3.3.1.

The development of a highly sensitive pressure sensor requires: 1) transducing of the pressure into axial strain acting on the fibre or; 2) to transverse load the FBG. A review of techniques aimed at enhancing the sensitivity of FBGs to pressure is presented in Chapter 2. No pore pressure sensors have been developed applying a local transverse load as opposed to using axial strain (Section 2.5.2). This work will contribute with new insights using transverse load and assessing the measurement range and sensitivity that can be obtained with this new technique.

1.2 Aim and objectives

The aim of this research study was to develop a fibre optic pore pressure sensor, based on FBG sensor technology, capable of measuring pore water pressure within the soil satisfying the required resolution of 1 kPa over a range of 300 kPa.

The objectives to achieve the above-mentioned aim were as follows:

1. To study the effect of applying a local transverse load into an FBG and the potential use of this technique to develop a pore pressure sensor optimising the range and resolution of the sensor to satisfy typical measurement requirements of 1 kPa resolution over a range of 300 kPa.

2. To develop a practical implementation of the optimised system capable of measuring pore pressure within soil.

1.3 Outline methodology

The first objective was achieved through:

Methodology 1:

- Development of a model of the spectral response of a FBG subjected to a transverse load based on the transfer matrix and Rouard's method modelling techniques. The model was used to analyse the effects of the location where the load is applied in the FBG, the length over which is applied and the influence of the FBG length on the spectral response of the FBG to the applied load.

Methodology 2:

- Design of experimental instrumentation, data acquisition and control software for the analysis of the spectral response of an FBG when subject to a transverse load across a small section of its length.
- Experimental analysis of the effect of applying a transverse load into a small section of an FBG written in SM optical fibre and highly birefringence optical fibre according to the optimized, simulated results obtained from methodology 1.
- Experimental analysis of the effect of applying a transverse load into an epoxy cube that embeds a small section of an FBG written in SM optical fibre and highly birefringence optical fibre according to the optimized, simulated results obtained from methodology 1.
- Optimization of the range and resolution through analyses of experimental designs to better transfer the load to the FBG.

In order to meet the second objective, the approach was carried out:

Methodology 3:

- Design and construction of a fibre optic pore pressure transducer using the optimized, experimental results obtained from methodology 2.
- Optimisation of the transducer performance
- Experimental test, calibration and characterisation of the developed pore pressure transducer.

1.4 Thesis Outline

Chapter 2: A review of pressure sensing technology including, an overview of the principles of operation of conventional and FBG pressure sensors is presented. Moreover, an overview of the working principles of commercially available conventional pore water pressure sensors and fibre optic pore pressure sensors are presented.

Chapter 3: This chapter presents the theoretical study of the effect of the application of a transverse load along a short sub-section of an FBG. The theory used to simulate the spectral behaviour of an FBG is outlined. Two techniques were used, the Transfer Matrix Method and Rouard's method. The effect of loading the FBG at different positions along its length, over different lengths and with a fixed ratio of loaded to unloaded lengths, but with different total FBG lengths is presented with the aim of finding the most suitable technique for the development of a pressure sensor.

A packaging technique that was experimentally investigated in Chapter 5 is also presented. The packing consisted of embedding the central section of the FBG within and epoxy cube. The deformation of the epoxy cube in response of a transverse load results in the application of an axial strain across the central section of the FBG. The effect of loading the epoxy cube localised at different positions along the FBG and over different lengths was studied.

Chapter 4: An experimental study of the effect of transversely loading an FBG along a sub-section located at its centre is presented. The experimental instrumentation used in this study is presented and the spectral characteristics of partially transverse loaded FBGs recorded in SM fibre are experimentally investigated. Two different loading techniques are reported; the loading of a sub-section located at the centre of the FBG (Section 4.3.1), and the loading of a sub-section that is half of the length of the FBG (Section 4.3.3). A technique that allows the independent and simultaneous measurement of temperature and pressure is presented in Section 4.3.2.

Section 4.4.1 shows the effect of partial transverse loading of FBGs written in PM optical fibre.

Chapter 5: Techniques for enhancing sensitivity of FBGs to pressure are presented. Previously reported sensitivity enhancing techniques are reviewed and the technique chosen for this study is presented in Section 5.2. This involves embedding a subsection of the FBG within an epoxy resin block. Section 5.3.1 presents the technique used to embed the FBG within the epoxy block and Section 5.3.2 presents the experimental results when the sensor was subject to transverse load and axial compression (Section 5.3.3). A study of the effect of transverse load an embedded subsection of an FBG written in PM fibre was undertaken and the experimental results obtained are presented in section 5.3.4.

In Section 5.4, methods for generating a spectral drop-out within the Bragg spectrum for zero load was investigated and the response of the structure to transverse load characterised.

Chapter 6: In this chapter, the design, construction and calibration of a fibre optic pore water pressure transducer are presented. Section 6.2 describes the developed sensor and Section 6.3.1 presents the results of an initial performance evaluation of the pressure sensor housing, pressurised with air.

The long term stability and repeatability of measurements made with the pressure sensor were assessed. The experimental arrangement used to calibrate the water pressure sensor is presented in Section 6.4.1 and the experimental results in Section 6.4.2

Chapter 7: The conclusions drawn from the study presented in this thesis and recommendations for future work aiming at improve the sensitivity, and performance of the developed sensor is presented.

References

Atkinson, J.:2007. The mechanics of soils and foundations. 2nd Edition, Taylor & Francis (Great Britain)

Aysen, A.:2005. Soil mechanics: basic concepts and engineering applications. Taylor & Francis (Great Britain)

Binu, S., Pillaia, V. P., Pradeepkumar, V., Padhyb, B. B., Joseph, C. S. and Chandrasekaran, N.: 2008 Fibre optic glucose sensor. *Materials Science and Engineering: C*. **29** (183-186)

FOS&S catalogue, 2008: Available at: http://www.fos-s.be/products/be-en/181/detail/item/417/navigationcats/230/ (Accessed 7th April 2008)

Gafsi, R. and El-Sherif, M. A.:2000. Analysis of induced-birefringence effects on fiber Bragg gratings. *Optical Fiber Technology*. **6** (299-323)

Gavea sensors catalogue, 2008: Available at: http://www.gaveasensors.com/eng/produtos_sensores_poropressao.html (Accessed 7th April 2008)

Higuera, J. M. L.:2002. Introduction to fibre optic sensing technology *In*: Higuera, J. M. L. (ed.) *Handbook of optical fibre sensing technology*. Great Britain, Wiley: 1-22

Hocker, G. B.:1979. Fibre-optic sensing of pressure and temperature. *Applied optics*. **18** (1445-1448)

Kashyap, R.:1999. Fiber Bragg Gratings. Academic Press (London)

Matos, C. J. S, Torres, P., Valente, L. C. G., Margulis, W., and Stubbe, R.:2001. Fiber Bragg Grating (FBG) Characterization and Shaping by Local Pressure. *Journal of Lightwave Technology*. **19** (1206-1211)

Michaille, L., Mccall, M. W., Lai, Y. C., and Williams, J. A. R.:2003. Analysis of single and multiple, non-permanent, tunable, birefringent spectral holes in a fibre-Bragg grating stop-band produced via uniaxial pressure. *Optics Communications*. **222** (1-8)

Nellen, Ph. M., Mauron, P., Frank, A., Sennhauser, U., Bohnert, K., Pequignot, P., Bodor, P. and Brandle, H.:2003. Reliability of fiber Bragg grating based sensors for downhole applications. *Sensors and actuators A*. **103** (364-376)

Othonos, A. and Kalli, K.:1999. Fiber Bragg Gratings: Fundaments and Applications in Telecommunications and Sensing. Artech House

Picarelli, L., Oboni, F., Evans, S. G., Mostyn, G. and Fell, R.:2005 Hazard characterisation and quantification. In Landslide Risk Management. Proceedings of the International Conference on Landslide Risk Management, Vancouver, Canada, 31 May-3 June 2005

Rao, Y. J.:1997. In-fibre Bragg grating sensors. *Measurement Science and Technology* **8** (355-375)

Roctest catalogue: 2008. Available at: http://www.roctest.com/index.php?module=CMS&id=72 (Accessed 4th April 2008)

Simoni, A., Berti, M., Generali, M., Elmi, C. and Ghirotti, M.:2004 Preliminary result from pore pressure monitoring on an unstable clay slope *Engineering Geology* **73** (117–128)

Strout, J. M. and Tjelta, T. I:2005. In situ pore pressures: What is their significance and how can they be reliably measured? *Marine and Petroleum Geology*. **22** (275-285)

Torres, P. and Valente, L. C. G.:2002. Spectral response of locally pressed fiber Bragg grating. *Optics Communications*. (285-291)

Wang, G., Pran, K., Sagvolden, G., Havsgard, G. B., Jensen, A. E., Johnson, G. A. and Vohra, S. T.:2001 Ship hull structure monitoring using fibre optic sensors. *Smart materials and structures*. **10** (472-478)

Xu, M. G., Reekie, L., Chow, Y. T and Dakin, J. P.:1993. Optical in-fibre grating high pressure sensor. *Electronics letters*. **29** (398-399)

Zhao, J.: 2001. An Object-oriented Simulation Program for Fibre Bragg Gratings. (unpublished PhD thesis), Rand Afrikaans University, Johannesburg

Chapter 2

Review of pressure sensing technology

2.1 Introduction

In this chapter a review of pressure sensing technology is presented. An overview of the principles of operation of conventional pressure sensors is presented in Section 2.2 and this is extended in Section 2.5.1 to review the working principles of commercially available conventional pore water pressure sensors.

An overview of the principles of operation of FOS is presented in Section 2.3 and in Section 2.4 fibre Bragg grating pressure sensors are reviewed focusing on their application as pressure sensors. Commercially available fibre optic pore pressure sensors are presented in Section 2.5.2.

2.2 Conventional pressure sensing technology

Pressure is an important parameter in many industrial processes like nuclear power, manufacturing, energy, and other everyday applications. The oldest recorded pressure transducer is the mercury column manometer, a barometer invented in 1643 by Evangelista Torricelli (Carr, 1993). Since then, numerous devices have used a wide range of technologies.

Pressure transducers operate by transducing the pressure applied to a sensing element into a mechanical displacement with amplitude proportional to the sensed pressure. There are three main types of pressure sensing elements: the diaphragm, the bellows and the bourdon tube (Figure 2-1).

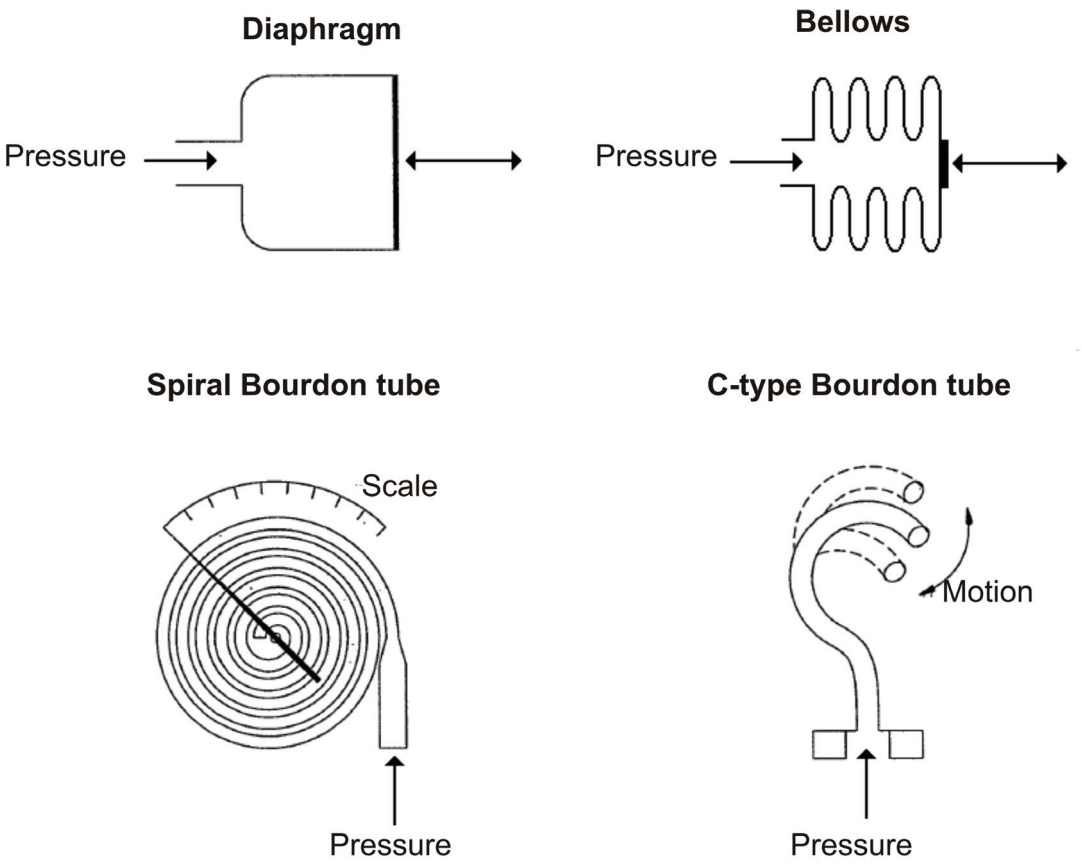

Figure 2-1: Three typical types of pressure sensing elements that convert the measured pressure into a mechanical displacement (Hashemian *et al.*, 1995).

The diaphragm sensing element consists of a circular plate fixed around the edges to a fixed surface. When a pressure is exerted in one side of the diaphragm, a mechanical displacement of the membrane is obtained.

The bellows sensing element consists of multi thin walled tubes that form deep convolutions and is sealed at one end. When pressure is applied to the bellows an attached rod suffers a mechanical displacement. The concept of this sensing element is similar to the diaphragm one but a more sizeable area is obtained.

The Bourdon tube is a curved or twisted tube with an elliptical cross section sealed at one end. The principle of operation of a Bourdon tube is that a closed end, coiled tube with a non circular cross section straightens out when pressure is applied, resulting in a accurate and repeatable mechanical displacement.

After transducing the pressure into a mechanical displacement, a conversion of the mechanical displacement into a read-out of the equivalent pressure value is required. Two types of conversions are possible for an accurate and reliable reading of the measured pressure. A direct read-out of the mechanical displacement though the movement of a pointer or by the converting the mechanical displacement into an electrical signal. This conversion is normally done by displacement sensors that rely on changing an electrical parameter, such as resistance or capacitance, or a magnetic characteristic such as inductance or reluctance. Figure 2-2 shows six types of displacement sensors that convert mechanical displacement into an electrical signal.

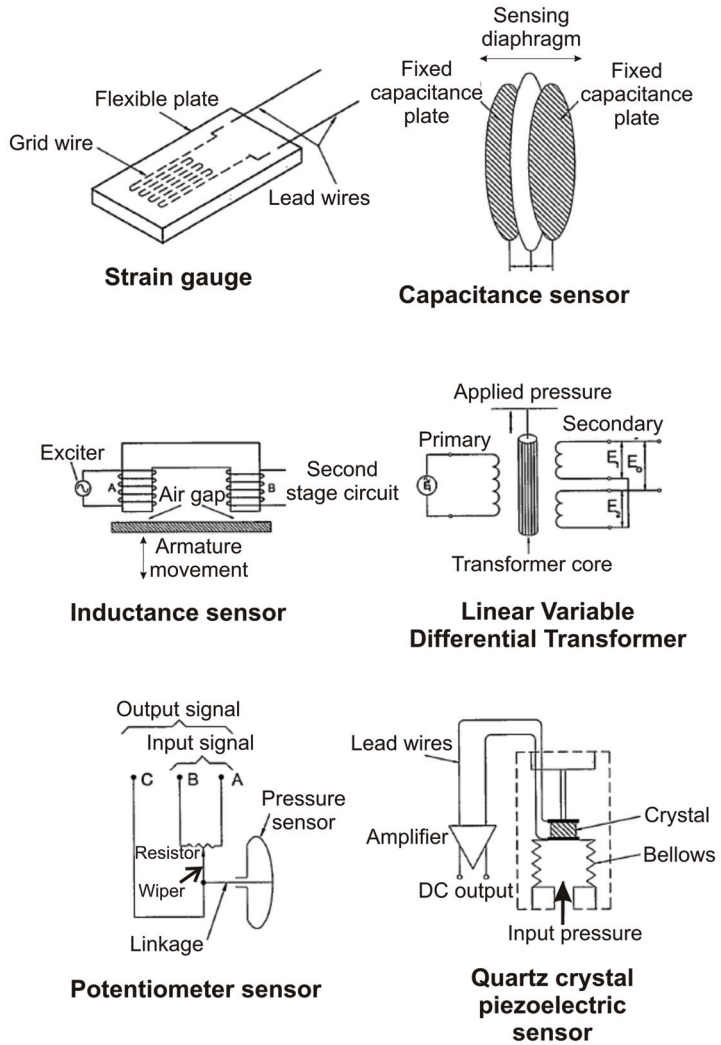

Figure 2-2: Six types of displacement sensors that convert mechanical displacement into an electrical signal (Hashemian *et al.*, 1995).

The strain gauge (Figure 2-2a) is a device that changes its resistance as a function of an applied stress. To maximize the measurement resolution, the small wires of the strain gauge are bonded into a flat or corrugated metal diaphragm, covering the maximum area as possible. When a stress is afterwards induced in the metal diaphragm the strain gauge resistance changes and a Wheatstone bridge is then used to measure the equivalent output voltage.

The displacement sensor presented in Figure 2-2b is a capacitance sensor that consists of two fixed metal plates separated by a metal diaphragm that moves according to the applied pressure. The capacitance (C1 and C2) depend on the distances between the movable diaphragm and the fixed plates. A Wheatstone similar to the one used with the strain gauge is then used to convert the pressure into a voltage.

Figure 2-2c show an inductance displacement sensor. The armature movement changes the permeance of the magnetic flux path around the fixed magnet. This magnetic flux is induced by the exciter coil (A) that is located on the left side of the magnet. The voltage observed on the right side of the magnet is dependent of distance of the armature from the magnet. The change in the size of the air gap results in a change in the electrical output induced in the sensing coil (B) on the right side of the magnet. Some inductance sensors use only one coil while other may change the relative positions of the two coils according to the amount of mechanical displacement.

In Figure 2-2d, a differential transformer is presented. The basic operation of a differential transformer is similar to that of an inductance sensor. The most common type is the linear variable differential transformer. When an alternating current electrical signal is applied to the primary coil it induces electrical signals in the two secondary coils (E1 and E2) with a phase difference dependent on the relative position of the transformer core which conveys the mechanical displacement. When the transformer core is in the centre of the two secondary coils, E1 and E2 are out of phase by 180 degrees and, therefore, cancel each other out. As the core moves from the centre, the relative phases change and a voltage (E0), which is proportional to the mechanical displacement, is induced.

The cheapest and simplest displacement sensor is the potentiometer (Figure 2-2e). The sensor is a simple form of a potentiometer sensor in which a slide wire resistor moves according to the sensed pressure. The difference between the output voltage and the input voltage is directly dependent on the position of the wiper. This is due to the change in resistance observed between the output terminals (A and C) as the wiper moves.

The last sensor presented in Figure 2-2f is the piezoelectric sensor. These sensors rely on the generation of an electrical signal due to strain applied to a crystalline structure like Quartz, tourmaline, Rochelle salt and titanate. Quartz is the most common material used in piezoelectric pressure transducers due to its high elasticity modulus, low hysteresis, linearity and high natural frequency (Sharifian, 2003). The induced voltage from the crystal is very small and must be amplified as shown in Figure 2-2f. This induced voltage is also direction sensitive, producing opposite voltage polarities for both tension and compression.

2.3 Fibre optic pressure technology

As mentioned in Section 1.1, FOS can be divided into four main categories (intensity modulated, phase modulated, spectrum modulated and time and frequency-modulated sensors) depending on the property of the light signal that is modulated.

2.3.1 Intensity modulated pressure sensors

Intensity modulated pressure sensors are simple devices where the light emitted from an optical source is carried along a fibre and its intensity is modified at the transducer. The modified light is then returned to an optical detector. The light intensity detected is a function of the measured variable. Intensity modulated sensors can be classified as using one or three general modulation mechanisms: transmission, reflection, and microbending (Figure 2-3).

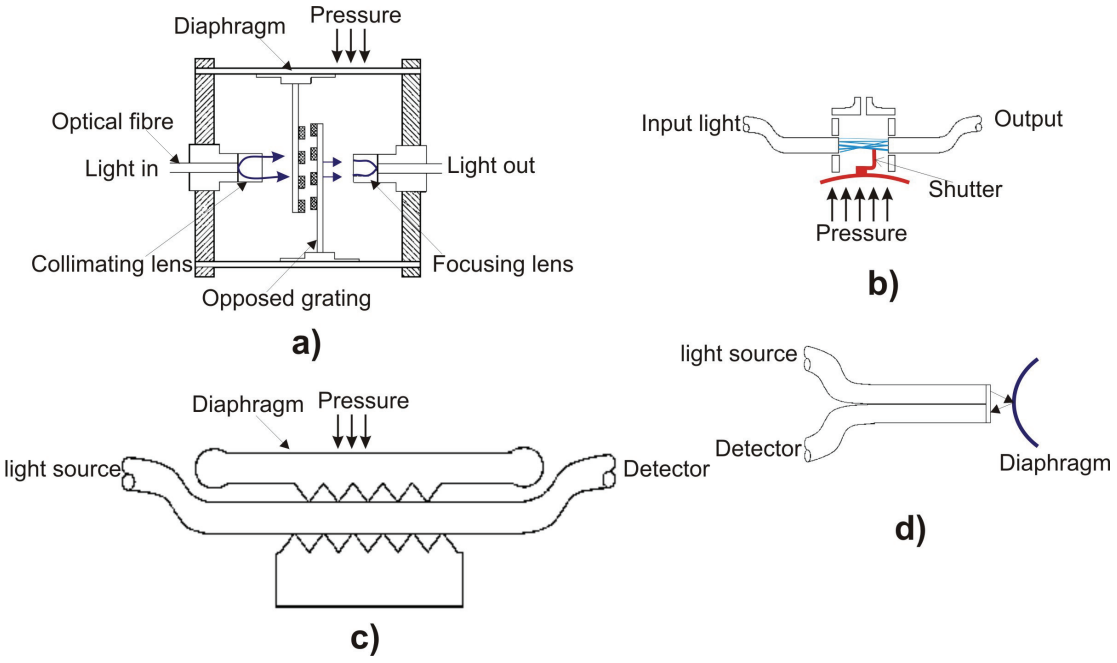

Figure 2-3: Four types of intensity modulated pressure sensors. a, b: Transmission intensity sensor; c: microbending pressure sensor and d: reflective intensity sensor (Hashemian et *al.*, 1995).

2.3.2 Interferometer pressure sensors

Phase modulated pressure sensors uses interferometric techniques such as Fabry-Perot interferometer to sense the measured variable. This is a high-resolution optical spectrometer that works on the principle of constructive interference. It consists of two partially transmitting mirrors that form a reflective cavity. When light enters the Fabry-Perot cavity, multiple reflections are experienced between the mirrors so that the light can produce multiple interferences. Fabry-Perot Interferometers can be divided in two categories, intrinsic Fibre Fabry-Perot Interferometers (FFPI) and Extrinsic fibre Fabry-Perot Interferometers (EFPI) (Yu and Yin, 2002). In extrinsic sensors, the light exits the fibre is modulated externally before being re-launched into either the same or a different fibre. This forms an interferometric cavity outside the fibre, with the fibre acting as a medium to transmit light into and out of the Fabry-Perot cavity. In intrinsic sensors, the light is modulated within the fiber. The Fabry-Perot cavity is usually formed by a section of fibre with its two end faces cleaved or coated with reflective coatings. Figure 2-4 shows an EFPI and FFPI pressure sensor.

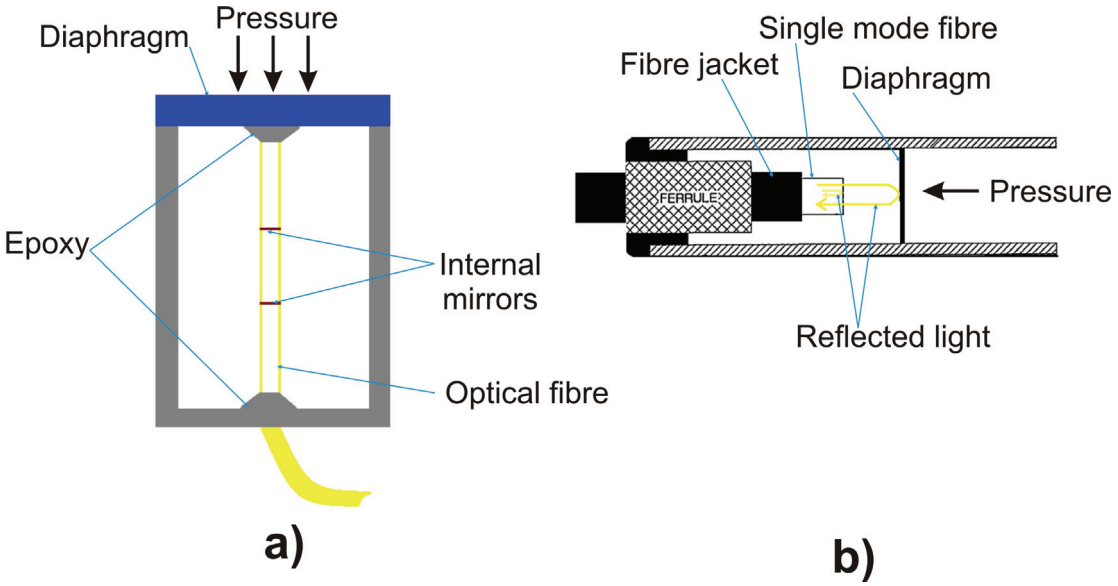

Figure 2-4: Interferometric pressure sensor. a) Intrinsic fibre Fabry-Perot pressure sensor (Yin et *al.*, 2008); b) extrinsic fibre Fabry-Perot pressure sensor (Hashemian et *al.*, 1995).

In the following section a review of spectrum modulated pressure sensors, more precisely FBG pressure sensing technology is revised.

2.4 Review of fibre Bragg grating pressure sensors

The sensing principles of FBGs were presented in Section 1.1. The pressure measurement capability of a bare FBG was first experimentally demonstrated in 1993 by Xu *et al.* A pressure sensitivity of -3.04×10^{-3} nm/MPa, equivalent to a pressure resolution of 328.9 kPa, was achieved when monitoring hydrostatic pressure over a measurement range of 70 MPa with an FBG of central wavelength 1553.3 nm written in standard SM optical fibre. This demonstrated that FBGs written in bare fibre are capable of measuring hydrostatic pressure. Although this simple technique allowed the development of very small pressure sensors, it is limited by the low intrinsic pressure sensitivity exhibited by FBGs. A number of approaches for enhancing the pressure sensitivity of FBGs have been reported.

Transducing the pressure into an axial load can increase the pressure sensitivity, as the sensitivity to axial load is considerably larger than that due to hydrostatic loading. In 1996, Xu *et al.* reported a pressure sensor based upon an FBG housed in a glass bubble.

The pressure experienced by the glass bubble was transduced into axial strain acting on the FBG, increasing the pressure sensitivity by a factor of 8.

A gain in hydrostatic pressure sensitivity of more than an order of magnitude was demonstrated in 1999 by Hill and Cranch. The entire length of an FBG with central wavelength 1543 nm written in SM optical fibre was embedded in a hard polymer with Young's modulus E = 1 GPa and placed in a water filled pressure vessel. A pressure sensitivity of -6.52×10^{-2} nm/MPa was achieved.

In 2001, the sensitivity was further increased by 3 orders of magnitude by Zhang *et al.* by embedding an FBG in a polymer filled metal jacket with a small aperture at the end, such that the pressure applied in the longitudinal axial direction of the fibre imposed an axial compression of the polymer and fibre (Figure 2-5). The polymer used was silicon rubber that has a Young's modulus of 190 MPa.

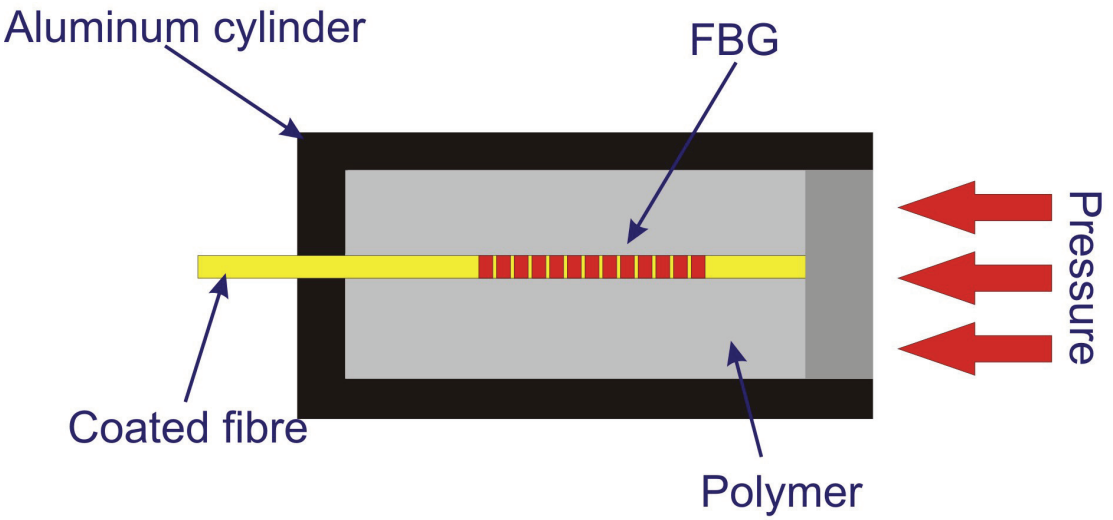

Figure 2-5: Schematic diagram of the polymer filled metal jacket FBG pressure sensor (Zhang et *al.*, 2001).

Later, in 2004, Sheng *et al.* presented a similar scheme based on the transverse compression of a Silicon rubber polymer with Young's modulus E = 180 MPa. In this work, the pressure acting through a hole on the side of the sensor element induced a transverse compression of the compliant polymer, applying an axial extension load to the FBG (Figure 2-6).

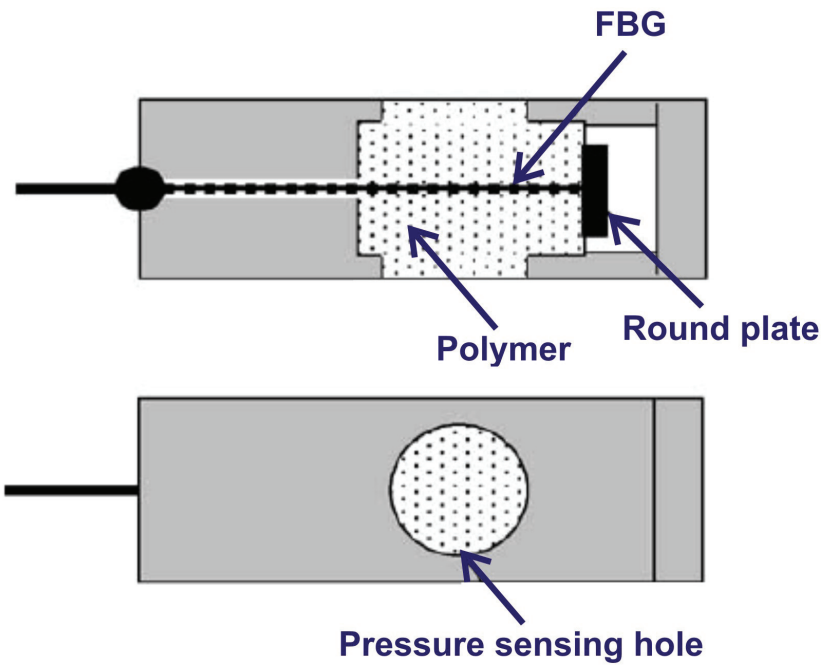

Figure 2-6: Schematic diagram of a lateral pressure sensor using a FBG (Sheng *et al.*, 2004).

One end of the FBG is fixed at the end of the sensor housing while the other end is glued to a round plate attached to the polymer surface. The stress result of the pressure acting on the side holes of the sensor is applied over the area of the round plate resulting on the axial stretching of the fibre. This technique allowed a further order of magnitude improvement in sensitivity, 33.88 nm/MPa achieved when monitoring pressure over a measurement range of 0.2 MPa.

A number of other mechanical enhancement schemes were proposed, including a piston based system (Yamate *et al.*, 2002). In this system, pressure acting on the piston induces a load that is applied transversely to an FBG (Figure 2-7).

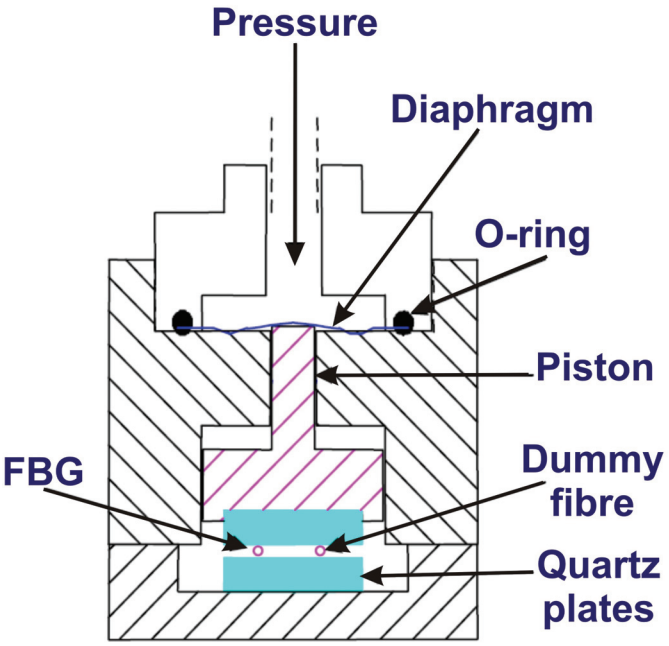

Figure 2-7: Schematic of transversely loaded Bragg grating pressure transducer (Yamate *et al.*, 2002)

A T-shaped triangular cantilever fibre sensor structure mounted on bellows based sensing element (Maier *et al.*, 2003), a piston-like diaphragm with a hard core in the centre (Zhang *et al.*, 2007) and a differential FBG design mounted on a circular plate (Ho *et al.*, 2008) are other mechanical enhancement schemes proposed.

In Chapter 1 it was shown that the wavelength shift of an FBG due to an applied axial strain is equal to $\Delta\lambda_B = \lambda_B \cdot \left(1 - \frac{n_{eff}^2}{2}\left(P_{12} - \nu\left(P_{11} - P_{12}\right)\right)\right).\Delta\varepsilon$. This means that for the same applied pressure, identical FBGs written at 1300 nm and 1500 nm demonstrate different wavelength changes. In this review the pressure sensitivity of each sensor is presented in terms of wavelength change per applied pressure and, when possible, normalised to the initial Bragg wavelength of the FBG sensor. The value of the pressure resolution assumes that a demodulation system with a wavelength resolution of 1 pm is used to interrogate the sensor.

Table 2-1 presents a summary of different pressure sensors with details of the FBG Bragg wavelength, the pressure measurement range, pressure sensitivity, normalised pressure sensitivity, and pressure resolution.

Table 2-1: Pressure sensitivity of FBG based pressure sensors

FBG pressure sensor configuration	FBG Bragg wavelength (nm)	Pressure measurement range (MPa)	Pressure sensitivity (nm/MPa)	Normalised pressure sensitivity $\frac{\Delta\lambda}{\lambda} = X \ \ MPa^{-1}$	Pressure resolution (kPA)	Reference
FBG attached to a piston-like diaphragm with a hard core in its centre	1527	[0 – 0.2]	9.53	2.2x10-3	0.11	Zhang *et al.*, 2007
Differential FBG pressure sensor attached to a thin circular plate	~ 1550	[0 – 0.25]	6.25	4.0x10-3	0.16	Ho *et al.*, 2008
FBG embedded in polymer and shielded in a metal tube – pressure transduced into axial compression of the polymer/FBG	1547.0	[0 – 0.44]	-5.28	-3.41x10-3	0.19	Zhang *et al.*, 2001

FBG pressure sensor configuration	FBG Bragg wavelength (nm)	Pressure measurement range (MPa)	Pressure sensitivity (nm/MPa)	Normalised pressure sensitivity $\frac{\Delta\lambda}{\lambda} = X \ MPa^{-1}$	Pressure resolution (kPA)	Reference
FBG embedded in a polymer half filled metal tube with a round plate attached to the FBG and polymer – pressure transduced into axial strain of the polymer/FBG through side hole	1539.82	[0 – 0.2]	33.88	2.2x10-2	2.95x10-2	Sheng et a., 2004
T-shaped triangular cantilever fibre sensor structure mounted on bellow based sensing element	~ 1550	[0 – 0.15] [0 – 0.08]	20 70	~ 1.29x10-2 ~ 4.52x10-2	5.0x10-2 1.43x10-2	Maier *et al.*, 2003
Hydrostatic pressure measured on an FBG coated with two different polymers	1540.2	[0 – 9.5]	-8.07x10-2	-5.24x10-5	12.39	Liu *et al.*, 2000
Hydrostatic pressure measured on a hard polymer coated FBG	1543	[0 – 3.45]	-6.52x10-2	-4.23x10-5	15.34	Hill and Cranch, 1999

FBG pressure sensor configuration	FBG Bragg wavelength (nm)	Pressure measurement range (MPa)	Pressure sensitivity (nm/MPa)	Normalised pressure sensitivity $\frac{\Delta\lambda}{\lambda} = X \ MPa^{-1}$	Pressure resolution (kPA)	Reference
Transversely loaded FBG with mechanically sensitivity enhancing using a piston sensing element	~ 1550	[13.79 – 34.47]	4.79x10-2	~ 3.09x10-5	20.89	Yamate *et al.*, 2002
FBG housed on a glass bubble – pressure transduced into axial strain	1310.92	[0 – 14]	-27.79x10-3	-2.12x10-5	35.98	Xu *et al.*, 1996
FBG mechanically clamped between two concentric steel tubes – transduces pressure into axial strain	~ 1550	[0 – 100]	2. 24x10-2	~ 1.45x10-5	44.64	Nellen *et al.*, 2003
Hydrostatic pressure measured on a high birefringence optical fibre	1556.82	[0 – 10]	2.0x10-2	1.28x10-5	50	Chen *et al.*, 2003
Hydrostatic pressure measured on a bare SM fibre	1553.3	[0 – 70]	-3.04x10-3	-1.98x10-6	328.9	Xu *et al.*, 1993

2.5 Commercially available pore pressure transducers

The importance of measuring pore pressure to access the stability of the soil before, during and after construction or to access the stability of slopes has been discussed in Chapter 1. In this Section, commercially available pore pressure sensors are presented.

2.5.1 Conventional pore pressure transducers

The basic principle of operation of all piezometers consists of a porous element that is fitted at the end of the transducer, filtering soil particles and allowing only water pressure to act on the sensing element.

The simplest commercially available pore water pressure piezometer is the standpipe piezometer, also known as the Casagrande piezometer (Figure 2-8a). Figure 2-8b illustrates the installation of this sensor on a borehole (Slope indicator catalogue, 2008). It consists of a filter tip joined to a riser pipe. The filter tip and riser pipe are installed on the borehole and sand is placed into the borehole to surround the filter tip (sand filter zone). Bentonite is then poured in the top of the filter zone for sealing, isolating the pore water at the filter tip. The rest of the space between the borehole and the riser pipe is filled with a bentonite grout that prevents the vertical migration of the water. A vented cap is then attached to the riser pipe at the surface. In this system the pore pressure is monitored though water level indicators. Water level indicators consist of a probe (graduated cable or tape) and a cable reel. During the measurement the probe is lowered down the standpipe and when in contact with the water, a light or sound alert is produced at the cable reel. The pore pressure is then measured by reading the depth of water through the scale of the cable or tape. When the water level produced by the pore pressure produced at the filter tip exceeds the ground level, a Bourdon tube is usually attached to the surface end of the pipe and the readings are performed reading the scale of the Bourdon tube.

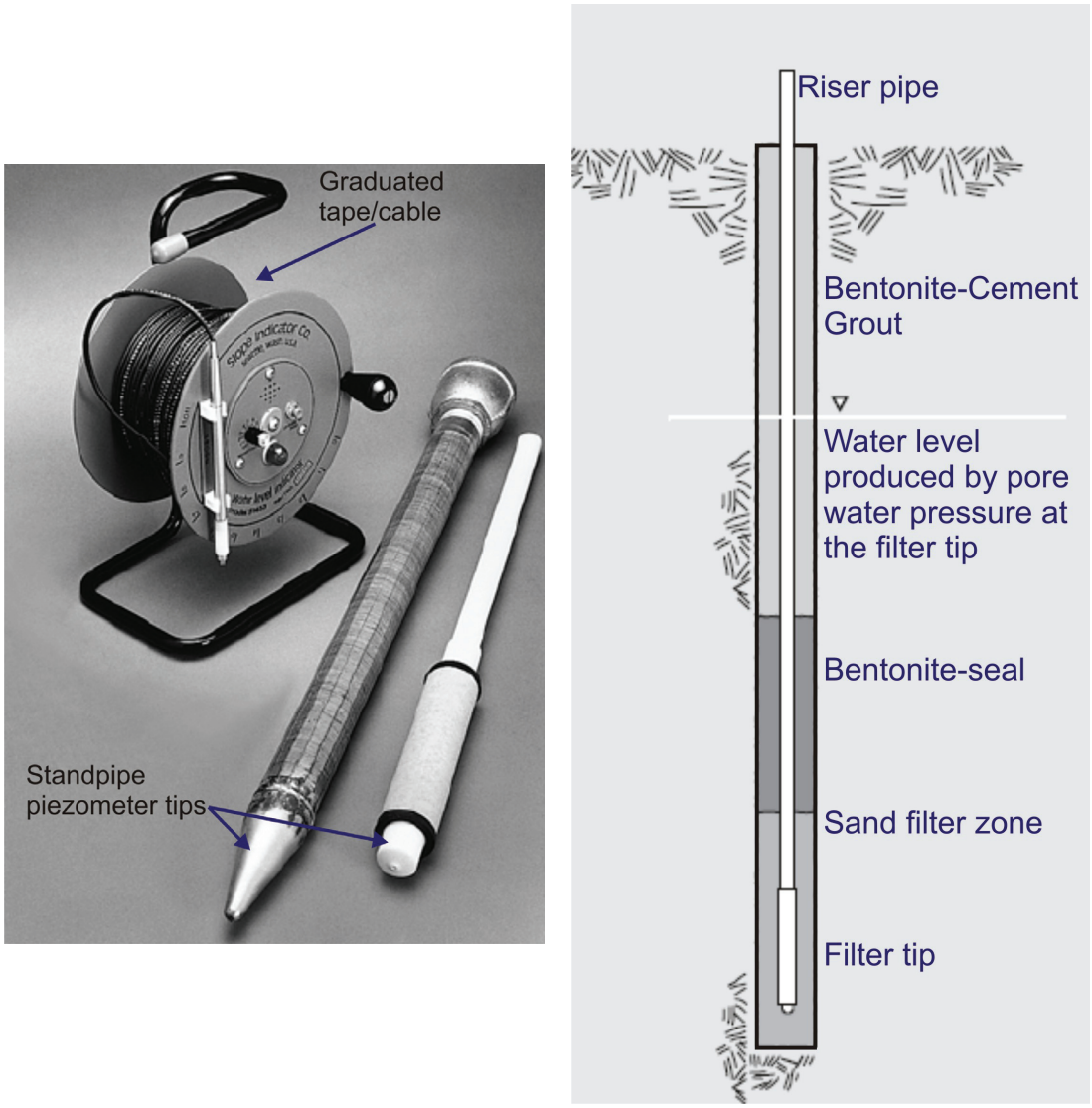

a) b)

Figure 2-8: a) standpipe piezometer; b) diagram of a borehole installation of a standpipe piezometer (Slope indicator catalogue, 2008).

This simple measurement system offers an inexpensive way to read pore water pressure within the soil; however, it is limited by the number of sensors that can be installed in a single borehole and it is not an automatic measurement system, requiring an operator to be present to undertake the measurement. The typical operation range of this piezometer is 20 MPa with a resolution of approximately 0.1 kPa.

Another commonly used and commercially available piezometer is the pneumatic piezometer (Figure 2-9a). Water pressure acts on a flexible diaphragm while gas pressure acts on the opposite side of the diaphragm (Figure 2-9b). Compressed nitrogen gas from the indicator flows through the input tube of the piezometer, increasing the gas pressure on the diaphragm. When the gas pressure is higher than the water pressure the diaphragm moves apart allowing the flow of gas to vent the tube. Once the return flow is detected at the surface, the gas input is turned off and the gas pressure in the piezometer decreases until the water pressure forces the diaphragm to its initial position, equalizing the system. At this point the water and gas pressure are equal and a reading of the water pressure is obtained though the indication of gas pressure on the pressure gauge connected to the gas input tube at the surface. Typical pressure ranges, are 0-1000 kPa or 0 to 3500 kPa with a resolution of 1 kPa (Roctest catalogue, 2008; Slope indicator catalogue, 2008).

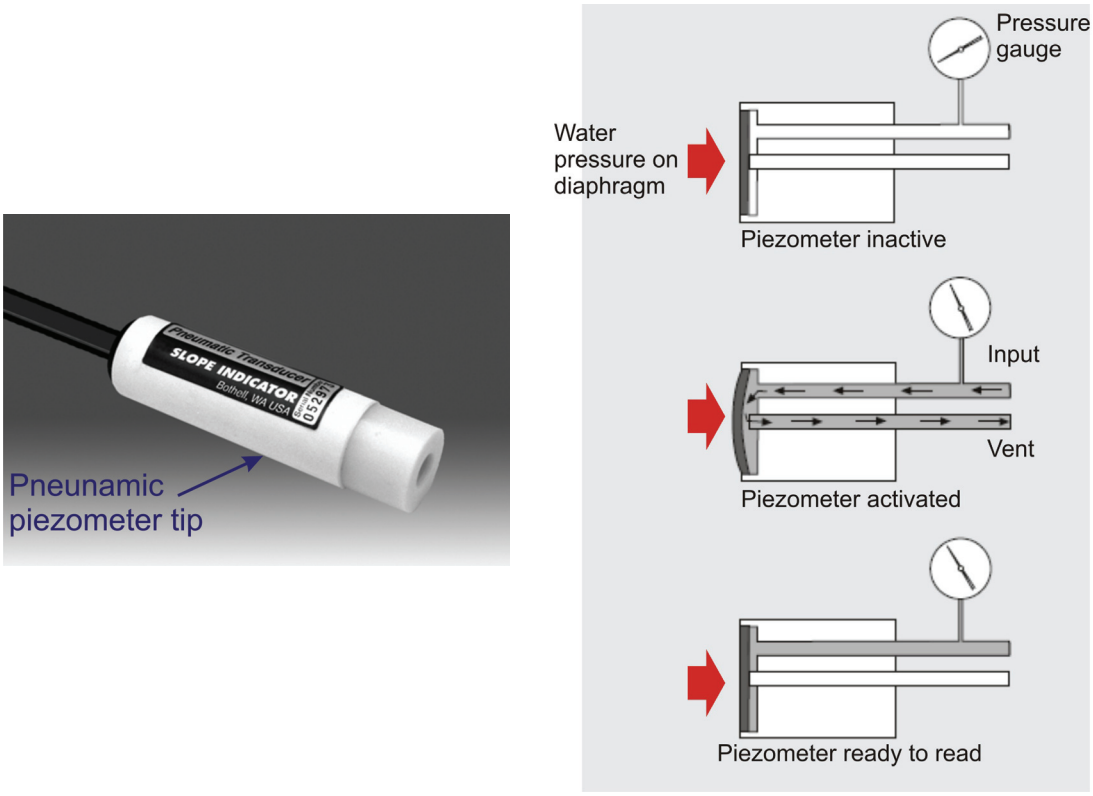

a) b)

Figure 2-9: a) pneumatic piezometer; b) diagram of the working principle of a pneumatic piezometer (Slope indicator catalogue, 2008).

Strain gauge piezometers are the third type of piezometer commonly used. A strain gauge piezometer consists of a sensing probe fitted with a flexible diaphragm where the strain gauges are internally bonded. When water pressure deforms the diaphragm, a signal proportional to the pressure exerted on the diaphragm is transmitted to a data logger. This type of sensor offers accurate continuous reading of pore water pressure over a range of 0 to 137 kPa with resolution 0.027 kPa or 0 to 1723 kPa with resolution 0.3 kPa (Slope indicator catalogue, 2008).

The most common type of piezometer currently used is the vibrating wire piezometer. It consists of a sensing probe fitted with a sensing element that can be either a diaphragm or a bellows with a vibrating wire element attached to the sensing element (Figure 2-10) (Roctest catalogue, 2008; Slope indicator catalogue, 2008). When pressure is applied to the sensing element, its deflection results in a decrease in the wire tension, which results on a change of the resonant frequency induced by an electromagnetic coil. The change of the resonant frequency of the vibrating wire is directly proportional to the pressure applied to the sensing element. The vibrating wire piezometer offers a continuous measurement of pore water pressure with pressure resolution as high as $8x10^{-3}$ kPa over a range of 35 kPa and 1.75 kPa over a range of 7000 kPa.

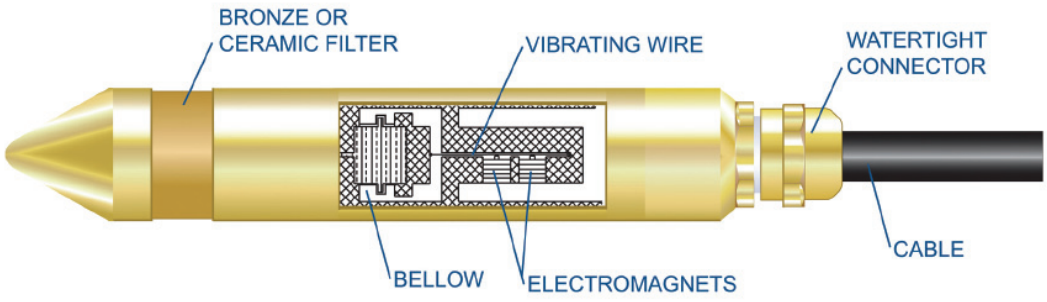

Figure 2-10: Vibrating wire piezometer (Roctest catalogue, 2008).

Table 2-2: Commercially available conventional piezometers

Type of sensor	Manufacturer	Piezometer commercial name/reference model	Measurement range (MPa)	Measurement resolution (kPa)	Reference
Pneumatic	Slope indicator	Pneumatic piezometer	1.2	0.1	Slope indicator catalogue, 2008
Pneumatic	RST Instruments	Pneumatic piezometer	2	1	RST Instruments catalogue, 2008
Strain gauge	Slope indicator	Titanium pressure transducer	0.138 to 1.724	0.02% F.S. 0.03 – 0.3	Slope indicator catalogue, 2008
Vibrating wire	RST Instruments	Vibrating wire piezometer VW2100	0.35 to 100	0.025% F.S. 0.09 – 25	RST Instruments catalogue, 2008
Vibrating wire	Roctest	PW vibrating wire series	0.035 to 7	0.025% F.S. 0.01 – 1.75	Roctest catalogue, 2008
Vibrating wire	Roctest	CL1 absolute pressure transducer	0.3 to 5	0.025% F.S 0.08 – 1.25.	Roctest catalogue, 2008

Typical problems associated with these sensors include electromagnetic interference and low tolerance to vibration and shock, which is more notable on the vibrating wire piezometer. Moreover, multiplexing of sensors is not possible. For these reasons, fibre optic based pore pressure sensors, more precisely fibre Bragg grating based pressure sensors, presented in the following section offer a better option to develop a pore water pressure sensor.

2.5.2 Fibre optic based pore pressure transducers

There are two types of commercially available fibre optic piezometers, one based upon a Fabry-Perot interferometer and one based on an FBG. The Fabry-Perot piezometer is based upon the measurement of the deflection of a diaphragm. The pressure acts on one side of the diaphragm, while the output from an optical fibre illuminates the other side Figure 2-11). Water pressure acting on the diaphragm causes a deflection that changes the length of cavity. The change in length of the Fabry-Perot cavity induces a shift on the reflected fringes obtained for the original cavity resulting in a change of the fibre reflected signal.

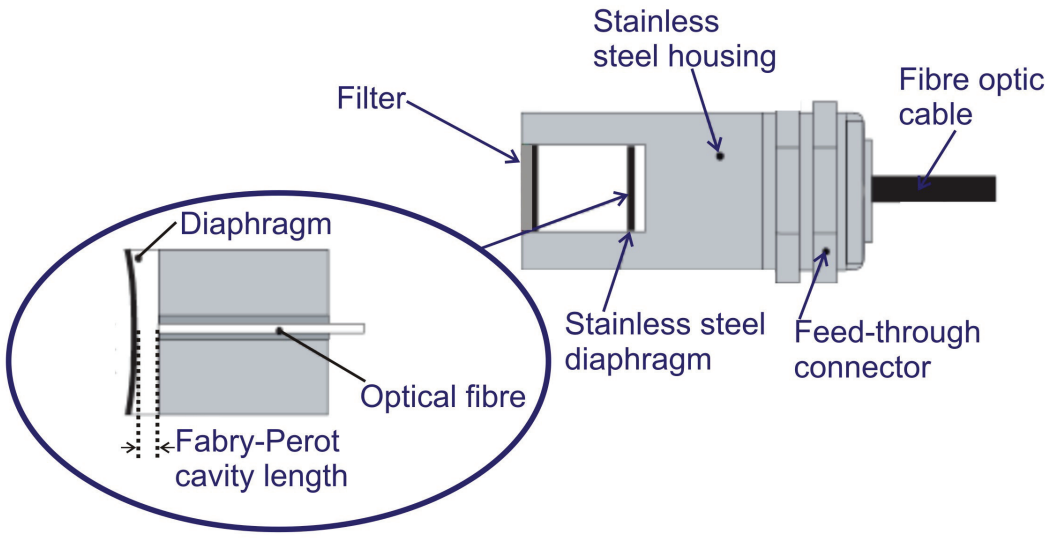

Figure 2-11: Fabry-Perot based piezometer (Roctest catalogue, 2008).

An FBG based piezometer exploits the axial strain sensitivity of the FBG. An FBG is attached under strain to a sensing element that can be either a diaphragm or a bellows. Water pressure acting on the sensing element induces a deflection of the sensing element that reduces the axial strain applied to the FBG and inducing a wavelength shift of the Bragg wavelength proportional to the applied pressure. Figure 2-12 illustrates two commercially available FBG based piezometers and Table 2-3 presents a summary of the specifications of three commercially available fibre optic based piezometers. The resolution values presented for the available FBG based piezometers assume that a 1 pm resolution demodulation system is used to interrogate the sensors. The values presented for the Fabry-Perot interferometer based transducer are the values present on the manufacturer catalogue and no details are provided regarding the way that the sensor is interrogated.

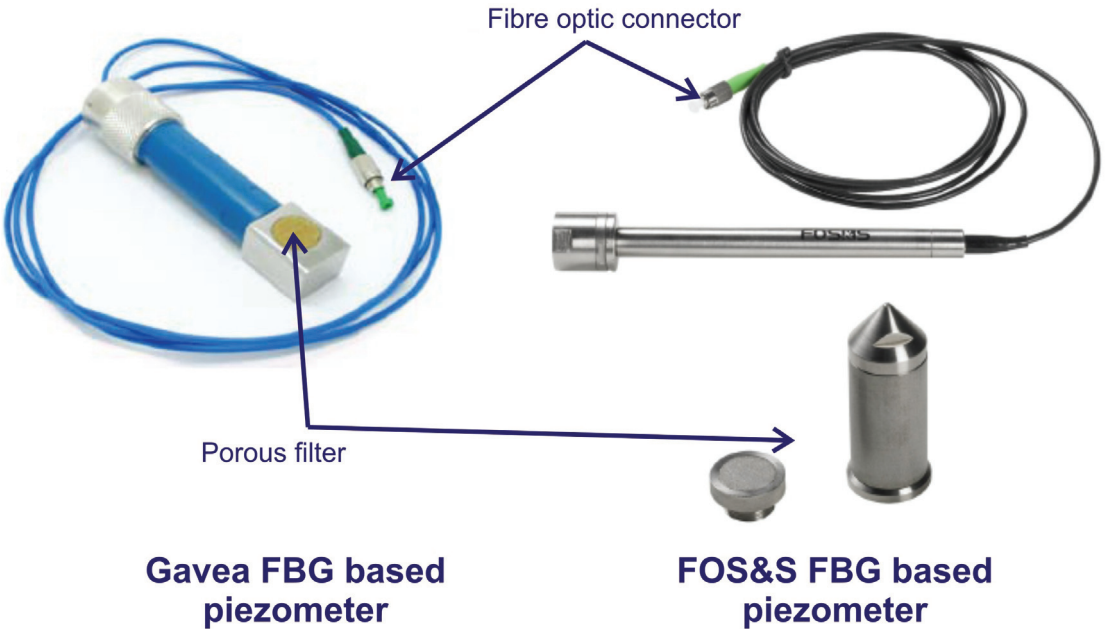

Figure 2-12: FBG based piezometers (Gavea and FOS&S catalogues).

Table 2-3: Commercially available Fibre optic piezometers

Technology employed	Manufacturer reference	Piezometer commercial name reference model	Measurement range (MPa)	Measurement resolution (kPa)
Fabry-Perot interferometer	RocTest (Roctest catalogue, 2008)	FOP	0.2; 0.35; 0.5; 0.75; 1; 1.5; 2; 3; 5; 7	0.025% F.S.
FBG axial strain	FOS&S (FOS&S catalogue, 2008)	PWP	0.1 - 15	0.1% F.S.
FBG axial strain	Gavea sensors (Gavea sensors catalogue, 2008)	GS 6600	0.5	0.3

As mentioned in Chapter 1, the FBG based pore pressure sensor is preferred to the Fabry-Perot interferometer as it offers the opportunity to multiplex many sensors on a single length of fibre, offering dense or extended spatial coverage of the parameters to measure. The FBG based commercially available piezometers makes use of the strain sensitivity of FBGs to transduce pressure. These sensors offer good pressure resolution (~0.1 kPa) over a 100 kPa range. In this study, a new type of pore pressure sensor that transduces pressure into a localised transverse load along a central sub-section of an optical fibre is presented. This technique allows the pressure measurement by tracking the position of a narrow spectral drop-out that is induced in the FBG reflection spectrum offering the possibility to develop a high resolution pressure sensor. Moreover, as the spectral drop-out is confined within the bandwidth of the FBG reflection spectrum and the FBG Bragg envelope stays the original wavelength, this technique allows the multiplexing of more sensors within a specific wavelength range. Compared with the transverse load of an FBG along its length, this loading technique offers the advantage of being sensitive to small loads.

References

Carr, J. J.:1993. Sensors and Circuits: Sensors, Transducers, and Supporting Circuits for Electronic Instrumentation, Measurement, and Control. PTR Prentice hall

Chen, G., Liu, L., Jia, H., Yu, J., Xu, L. and Wang, W.:2003. Simultaneous pressure and temperature measurement using Hi-Bi fiber Bragg gratings. *Optics Communications*. **228** (99-105)

FOS&S catalogue, 2008: Available at: http://www.fos-s.be/products/be-en/181/detail/item/417/navigationcats/230/ (Accessed 7th April 2008)

Gavea sensors catalogue, 2008: Available at: http://www.gaveasensors.com/eng/produtos_sensores_poropressao.html (Accessed 7th April 2008)

Hashemian, H. M., Black, C. L. and Farmer, J. P.:1995, Assessment of Fiber Optic Pressure Sensors, Report number NUREG/CR-6312, Analysis and Measurement Services Corporation, Knoxville.

Hill, D. J. and Cranch, G. A.:1999. Gain in hydrostatic pressure sensitivity of coated fibre Bragg grating. *Electronics Letters*. **35** (1268-1269)

Ho, Y. T., Huang, A. B. and Lee, J. T.:2008. Development of a chirped/differential optical fiber Bragg grating pressure sensor. *Measurement Science and Technology*. **19** (1-6)

Liu, Y., Guo, Z., Zhang, Y., Chiang, K. S. and Dong, X.:2000. Simultaneous pressure and temperature measurement with polymer-coated fibre Bragg grating. *Electronics Letters*. **36** (564-566)

Maier, R. R. J., Barton, J. S., Jones, J. D. C., McCulloch, S. and Burnell, G.:2003. Dual-fibre Bragg grating sensor for barometric pressure measurement. *Measurement Science and Technology*. **14** (2015-2020)

Nellen, Ph. M., Mauron, P., Frank, A., Sennhauser, U., Bohnert, K., Pequignot, P., Bodor, P. and Brandle, H.:2003. Reliability of fiber Bragg grating based sensors for downhole applications. *Sensors and Actuators A*. **103** (364-376)

Roctest catalogue: 2008. Available at:
http://www.roctest.com/index.php?module=CMS&id=72 (Accessed 4th April 2008)

RST Instruments catalogue, 2008: Available at:
http://www.rstinstruments.com/products.html (Accessed 4th April 2008)

Sharifian, S. A.: 2003. Fibre optic pressure transducers for disturbance measurements in transient aerodynamic research facilities (unpublished PhD thesis), University of Southern Queensland, Australia

Sheng, H. J., Fu, M. Y., Chen, T. C., Liu, W. F., Bor, S. S.:2004. A lateral pressure sensor using a fiber Bragg grating. *IEEE Photonics Technology Letters*. **16** (1146-1148)

Slope indicator catalogue: 2008. Available at:
http://www.slopeindicator.com/instruments/piezo-intro.html (Accessed 4th April 2008)

Xu, M. G., Reekie, L., Chow, Y. T and Dakin, J. P.:1993. Optical in-fibre grating high pressure sensor. *Electronics letters*. **29** (398-399)

Xu, M.G., Geiger, H., and Dakin, J. P.:1996. Fibre grating pressure sensor with enhanced sensitivity using a glass-bubble housing. *Electronics Letters*. **32** (128-129).

Yamate, T., Ramos, R. T., Schroeder, R. J., Madhavan, R., Balkunas, S. C. and Udd, E.:2002. Transversely loaded Bragg grating pressure transducer with mechanically enhancing the sensitivity. *OFS 2002: 15th Optical Fiber Sensors Conference Technical Digest* (535-538)

Zhang, W. T., Li, F., Liu, Y. L. and Liu, L. H.:2007. Ultraphin FBG Pressure Sensor With Enhanced responsivity. *IEEE Photonics Technology Letters*. **19** (1553-1555)

Zhang, Y., Feng, D. J., Liu, Z. G., Guo, Z. Y., Dong, X. Y., Chiang, K. S. and Chu, B. C. B.:2001. High-sensitivity pressure sensor using a shielded polymer-coated fiber Bragg grating. *IEEE Photonics Technology Letters* **13** (618-619)

Yu, F. T. S and Yin, S.: 2002. Fiber optic sensors. Marcel Dekker Inc., New York

Yin, S., Ruffin, P. B. and Yu. F. T. S.:2008. Fiber Optic Sensors. 2nd Edition CRC Press (USA)

Chapter 3

Theoretical analysis of fibre Bragg gratings under partial transverse load

3.1 Introduction

The technique chosen to develop the pore pressure sensor was the transverse load of a small central section of an FBG. As mentioned in Section 1.1.1, when an FBG with uniform period is subject to a localised transverse load applied along a short central section of its length, a change of the original FBG refractive index profile occurs over that region and a spectral drop-out appears within the bandwidth of the original FBG spectrum (see Figure 1.6). The spectral drop-out tracks across the FBG spectrum bandwidth in response to increasing load. This technique overcomes the lack of resolution for small loads applied transversely to the entire length of an FBG.

This chapter presents the theoretical study of the effect of the application of a transverse load along a short sub-section of an FBG. In Section 3.2, an explanation of the effect of partial transverse loading of an FBG is presented and in Section 3.3 the theory used to simulate the spectral behaviour of an FBG is outlined. Two techniques were used, the Transfer Matrix Method (TMM) and Rouard's method.

Section 3.4 presents a study of different transverse loading configurations, with the aim of finding the most suitable technique for the development of a pressure sensor. The effect of loading the FBG at different positions along its length, over different lengths and with a fixed ratio of loaded to unloaded lengths, but with different total FBG lengths were studied (Sections 3.4.1, 3.4.2 and 3.4.3). In Section 3.4.4, a study of the effect of applying a load along the entire length of the FBG, apart from a section at its centre, is presented.

A packaging technique that was experimentally investigated (Section 5.2) has also been investigated and is presented in Section 3.5. The packing consisted of embedding the central section of the FBG within an epoxy cube. The deformation of the epoxy cube in response of a transverse load results in the application of an axial strain across the central section of the FBG. The effect of loading the epoxy cube localised at different positions along the FBG and over different lengths was studied and the results are presented in Sections 3.5.1 and 3.5.2. The effect of using different epoxies with different Young's moduli on the transverse load sensitivity of the FBG was also analysed and the results are presented in Section 3.5.3.

3.2 Locally transverse loaded fibre Bragg gratings

As described in Section 1.1.1, when an FBG with uniform period is subject to a localised transverse applied load along a short central section of its length, a spectral drop-out appears within the bandwidth of the original FBG spectrum. The spectral drop-out is result of the refractive index change over the pressed region that changes the optical path between the two sub-gratings that maintain the original period and refractive index but are shorter in length. This creates an FBG Fabry-Perot interferometer with the two sub-gratings acting as mirrors and separated by a cavity (pressed region). As result, destructive interference occurs between the light reflected from the two sub-gratings which induces a spectral drop-out in the FBG reflection spectrum. On the transverse loading of an FBG along the *y* direction, the refractive index change over the loaded region is not equal for the two polarisation axes of the fibre as birefringence is induced into the optical fibre. The variation of the effective refractive index for light polarised along the *x* and *y* directions of the fibre is expressed as (Michaille *et al.*, 2003):

$$\Delta n_x = -\frac{1}{2} n_{eff}^3 \left(P_{11}\varepsilon_x + P_{12}\varepsilon_y \right) \quad \textbf{(3-1)}$$

$$\Delta n_y = -\frac{1}{2} n_{eff}^3 \left(P_{12}\varepsilon_x + P_{11}\varepsilon_y \right) \quad \textbf{(3-2)}$$

where the strain along the *z* direction is assumed to be zero (case of plane strain, $\varepsilon_z = 0$), ε_x and ε_y are the strains along the linear polarisation eigen-directions *x* and *y*, and P_{11} and P_{12} are the elements of strain-optic tensor. The values of the strain can be found from (Wagreich *et al*, 1996)

$$\varepsilon_x = \frac{1+\upsilon}{E}\left[\sigma_x(1-\upsilon) - \upsilon\sigma_y\right] \tag{3-3}$$

$$\varepsilon_y = \frac{1+\upsilon}{E}\left[\sigma_y(1-\upsilon) - \upsilon\sigma_x\right] \tag{3-4}$$

where υ is the Poisson's ratio of the fibre, E is the Young's modulus and σ_x, σ_y are the stress components at the point $M(x, y, z)$ in the FBG in the *x, y* and *z* principal directions respectively. This assumes that the circular cross section of the optical fibre is subject to point loading from two sides. Hertz solutions for stress states in disks under diametrical compression are then applied. Small strains and shape change, point loading and frictionless contact are assumed which are valid for high Young's modulus materials like silica (~71GPa) (Mastro, 2005). The stresses within a disk can be expressed as (Gafsi and El-Sherif, 2000):

$$\sigma_x(x,y) = \frac{-2F}{\pi L}\left\{\frac{x^2(b+y)}{\left[x^2+(b+y)^2\right]^2} + \frac{x^2(b-y)}{\left[x^2+(b-y)^2\right]^2} - \frac{1}{2b}\right\} \tag{3-5}$$

$$\sigma_y(x,y) = \frac{-2F}{\pi L}\left\{\frac{(b+y)^3}{\left[x^2+(b+y)^2\right]^2} + \frac{(b-y)^3}{\left[x^2+(b-y)^2\right]^2} - \frac{1}{2b}\right\} \tag{3-6}$$

with $0 \le |x| \le |b|$ and $0 \le |y| \le |b|$, F is the applied force along the fibre's length L over which the force is applied and *F/L* is a linear distribution of the force. The Hertz solution predicts that the maximum stresses occur at the centre of the disk with tensile stress along the x axis (Mastro, 2005). Solutions of these equations give the normal stresses in the x and y direction for any location (x,y) within the optical fibre cross section. Figure 3-1 and Figure 3-2 present the normal stresses in the optical fibre in the x and y directions when subject to load along the y axis.

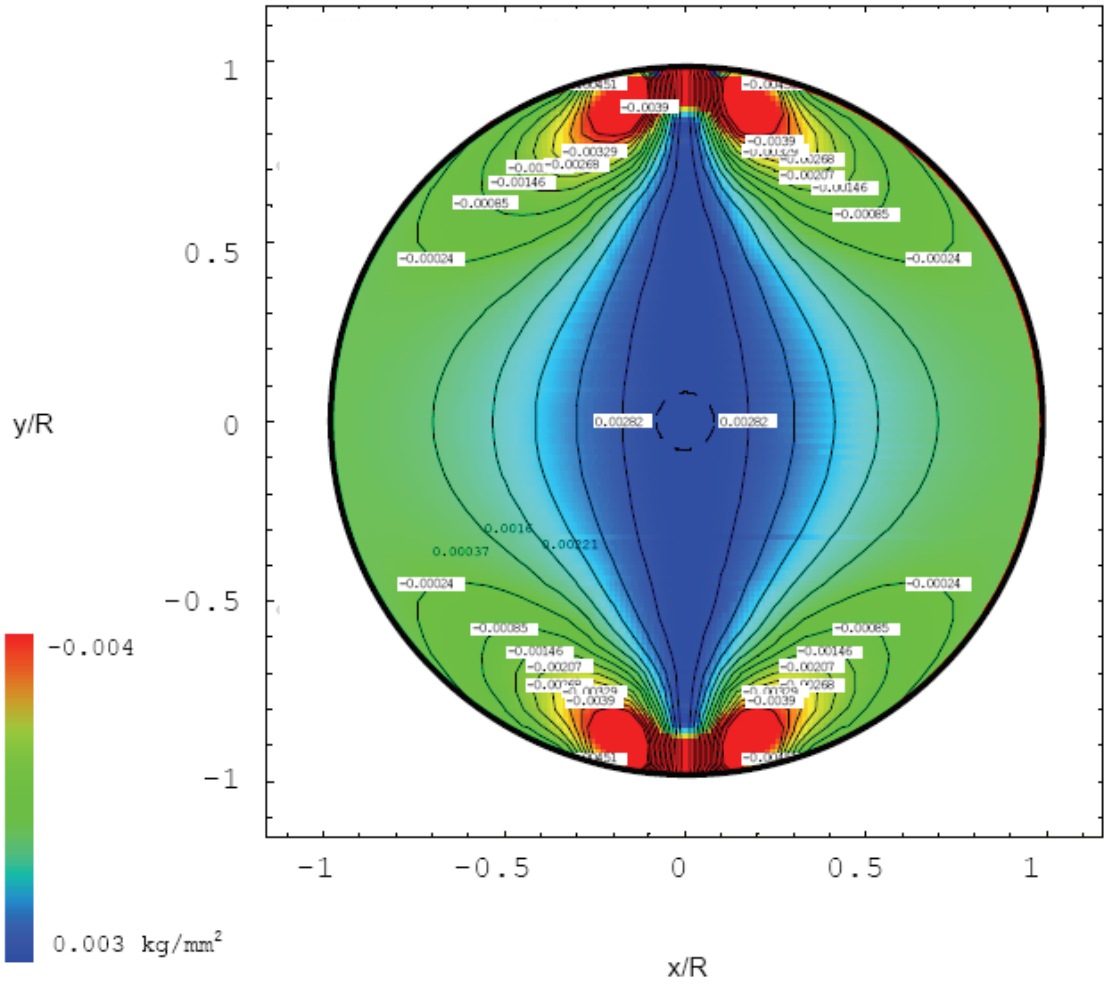

Figure 3-1: Map of the normal stresses on an optical fibre under diametrical load along the y axis, x-direction σ_x (Mastro, 2005).

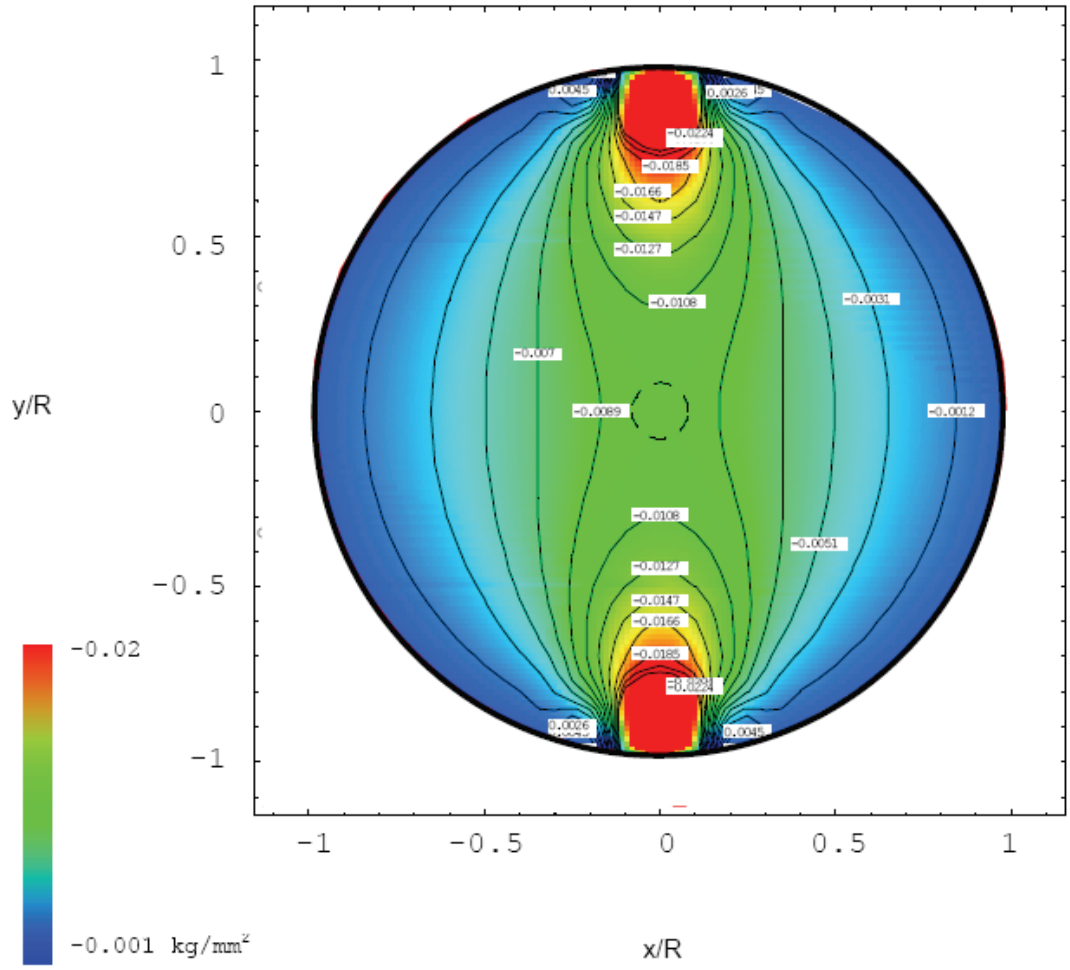

Figure 3-2: Map of the normal stresses on an optical fibre under diametrical load along the y axis, y-direction σ_y (Mastro, 2005).

The change in wavelength $\Delta\lambda$ can be presented as (Gafsi and El-Sherif, 2000):

$$\Delta\lambda_x = -\lambda_x \frac{n_{eff}^2}{2}\left(P_{11}\varepsilon_x + P_{12}\varepsilon_y\right) \tag{3-7}$$

$$\Delta\lambda_y = -\lambda_y \frac{n_{eff}^2}{2}\left(P_{12}\varepsilon_x + P_{11}\varepsilon_y\right) \tag{3-8}$$

3.3 Two mode coupling of fibre Bragg gratings with uniform period

The most common technique used to describe the spectral characteristics of a fibre grating is coupled mode theory, the derivation of which can be found in numerous articles (Yariv, 1973; Kogelnik, 1990). Coupled mode theory uses coupled differential equations to describe the counter propagating fields inside a grating structure, obtained by the modulation of the propagating electric fields of the waveguide. It can be used to describe uniform period gratings, where analytical solutions of the coupled differential equations are easily obtained. To describe more complex grating structures, numerical solutions of the two coupled differential equations are required. Numerical solutions to coupled mode theory can then be readily obtained using matrix methods such as the TMM (Yamada and Sakuda, 1987).

The perturbation of the effective index of refraction n_{eff} of the guided modes of a waveguide is given by:

$$\delta n_{eff}(z) = \overline{\delta n}_{eff}(z)\left\{1 + \upsilon \cos\left[\frac{2\pi}{\Lambda} z + \phi(z)\right]\right\} \quad \textbf{(3-9)}$$

Where υ is the fringe visibility associated with the index change; Λ is the grating period; $\phi(z)$ accounts for grating chirp, and $\overline{\delta n}_{eff}$ is the "dc" refractive index change spatially averaged over the grating period (Erdogan, 1997).

When light travelling in a optical fibre reaches the fibre Bragg grating, a dominant interaction occurs near the wavelength for which reflection occurs from a mode of amplitude $A(z)$ into an identical counter-propagating mode of amplitude $B(z)$. Under these conditions, the coupled mode equations can be simplified to (Erdogan, 1997):

$$\frac{dR}{dz} = i\hat{\sigma}R(z) + ik_{ac}S(z) \quad \textbf{(3-10)}$$

$$\frac{dS}{dz} = -i\hat{\sigma}S(z) - ik_{ac}{}^{*}R(z) \quad \textbf{(3-11)}$$

Where $R(z) = A(z)\exp[i\delta z - \phi/2]$ and $S(z) = B(z)\exp[-i\delta z + \phi/2]$; $R(z)$ is the forward mode and $S(z)$ is the backwards mode that represent the slowly varying mode envelope functions; k_{ac} is the "AC" coupling coefficient also called local grating strength; and $\hat{\sigma}$ is a general "DC" self-coupling coefficient, also called local detuning defined as (Kashyap, 1999):

$$\hat{\sigma} = \Delta\beta + k_{dc} - \frac{1}{2}\frac{d\phi}{dz} \tag{3-12}$$

With $\frac{1}{2}\frac{d\phi}{dz}$ describing a possible chirp of the grating period and ϕ the grating phase. The detuning δ, which is independent of z for all gratings, is represented as:

$$\begin{aligned}\Delta\beta &= \beta - \frac{\pi}{\Lambda} \\ &= \beta - \beta_D \\ &= 2\pi n_{eff}\left(\frac{1}{\lambda} - \frac{1}{\lambda_D}\right)\end{aligned} \tag{3-13}$$

Where $\lambda_D = 2n_{eff}\Lambda$ is the "design wavelength" for Bragg reflectance by a weak grating ($\delta n_{eff} \to 0$) (Erdogan, 1997).

For an FBG written in SM optical fibre the "DC" and "AC" coupling coefficient are defined as (Kashyap, 1999):

$$\begin{aligned}k_{dc} &= \frac{2\pi}{\lambda}\overline{\delta n_{eff}} \\ k_{ac} &= k_{ac}^{*} \\ &= \frac{\pi}{\lambda}\upsilon\overline{\delta n_{eff}}\end{aligned} \tag{3-14}$$

For a grating of uniform period along z, $\overline{\delta n_{eff}}$ is constant and $\frac{d\phi}{dz} = 0$ (which means there is no grating chirp), and thus k_{ac}, k_{dc} and $\hat{\sigma}$ are constants. This simplifies Equations (3-10) and (3-11) into first order ordinary differential equations with constant coefficients. If the appropriate boundary conditions are met, one can arrive at a closed form solution to these equations. Figure 3-3 represents the initial condition and the calculation of the Bragg grating response to an input field.

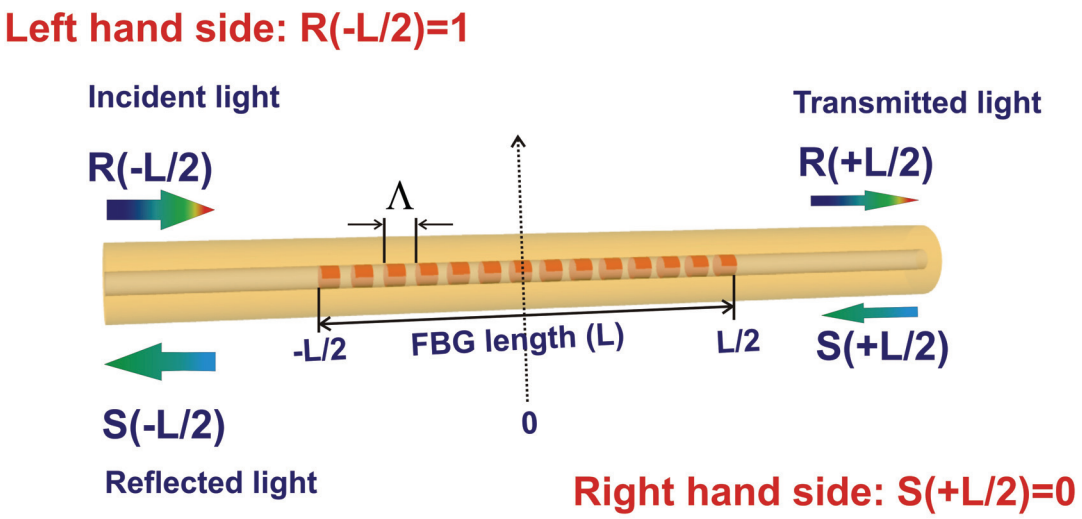

Figure 3-3: Representation of the Initial boundary condition for calculation of the grating response (Zhao, 2001)

Assuming that there is no input signal from the right hand side of the grating $S(+L/2) = 0$, and that a signal incident from the left side exists $R(-L/2) = 1$, then the initial condition of the grating can be written as:

$$\begin{cases} S(-L/2) = ? \\ R(-L/2) = 1 \end{cases} \quad \textbf{(3-15)}$$

$$\begin{cases} R(+L/2) = ? \\ S(+L/2) = 0 \end{cases} \quad \textbf{(3-16)}$$

The reflection and transmission coefficients can then be derived from the initial conditions and the coupled mode equations. The amplitude of the reflection coefficient can be presented as:

$$\rho = \frac{S(-L/2)}{R(-L/2)} \tag{3-17}$$

And the power reflection coefficient "R" (reflectivity) can be described as:

$$R = |\rho^2| \tag{3-18}$$

For a fibre Bragg grating of uniform period and of length L, the reflectivity can be found assuming a forward propagation wave incident from $z = -\infty$, and that no backward propagation wave exists for $z \geq L/2$. The power reflection coefficient can be presented as (Kashyap, 1999):

$$R = \frac{|k_{ac}|^2 \sinh^2 \sqrt{L^2\left(|k_{ac}|^2 - \hat{\sigma}^2\right)}}{|k_{ac}|^2 \cosh^2 \sqrt{L^2\left(|k_{ac}|^2 - \hat{\sigma}^2\right)} - \hat{\sigma}^2} \qquad |k_{ac}| > \hat{\sigma} \tag{3-19}$$

$$R = \frac{|k_{ac}|^2 \sinh^2 \sqrt{L^2\left(|k_{ac}|^2 - \hat{\sigma}^2\right)}}{\hat{\sigma}^2 - |k_{ac}|^2 \cosh^2 \sqrt{L^2\left(|k_{ac}|^2 - \hat{\sigma}^2\right)}} \qquad |k_{ac}| < \hat{\sigma} \tag{3-20}$$

The maximum reflectivity $R_{\max}$ of a Bragg grating can be described as:

$$R_{\max} = \tanh^2(k_{ac}L)| \tag{3-21}$$

and occurs when $\hat{\sigma} = 0$, or at the wavelength (Erdogan, 1997)

$$\lambda_{\max} = \left(1 + \frac{\overline{\delta_{neff}}}{n_{eff}}\right)\lambda_D \tag{3-22}$$

3.3.1 Transfer matrix method

The TMM can be used either to describe fibre Bragg gratings with uniform or non-uniform period which the coupled mode theory is limited to describe uniform period FBGs. In the TMM, a grating of length (L) is divided into N sections, each section with a specific length (δL). A limitation of the TMM is that the number of sections N cannot

be arbitrarily large as several grating periods are required to achieve a complete coupling and is defined as (Prabhugoud, 2004):

$$N < \frac{2n_{eff}L}{\lambda_D} \tag{3-23}$$

moreover, a careful definition of the section length is required in order to obtain an integer number of sections over the FBG length, to avoid extra features in the Bragg spectrum due to the introduction of phase discontinuities within the structure (Chehura, 2002). This modelling technique is a fast and accurate modelling tool which allows the control of the characteristics of FBG over a section. The coupled mode Equations (3-10) and (3-11) are then applied to each grating section with the refractive index change, grating period and coupling coefficient kept constant over that section. Input and output field amplitudes are calculated using a matrix M_i, for the i^{th} section of length δL_i and the output M_i is then used as input of M_{i+1} (next section). This process is repeated N times to obtain the matrices correspondent to each section. At the end of the simulation, a total transfer matrix M is obtained by multiplying all individual matrices, linking together the inputs and outputs of the extremes of the grating.

Assuming that the transfer matrix simulation is started from the end of the grating and propagates backwards, the following boundary conditions are applied: $R_0 = R(L) = 1$ (normalised output) and $S_0 = S(L) = 0$ (no incident field from the output end). At the beginning of the grating structure, the input field are defined as: $R(0) = R_N$ and $S(0) = S_N$. Figure 3-4 presents the index modulation of a single grating section showing two inputs and two outputs.

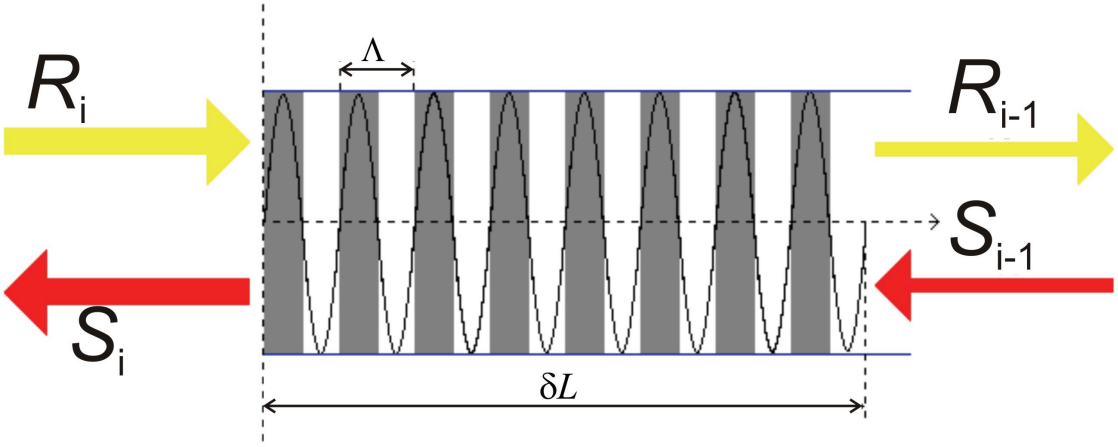

Figure 3-4: Grating section showing 2 inputs and outputs (Chehura, 2002)

The simulation starts assuming that the "DC" and "AC" coupling coefficients, "DC" refractive index change $\overline{\delta n_{eff}}$, and grating chirp ($\frac{1}{2}\frac{d\phi}{dz}$) are constant. The propagation through each section i is described by the matrix M_i as:

$$\begin{bmatrix} R_i \\ S_i \end{bmatrix} = M_i \times \begin{bmatrix} R_{i-1} \\ S_{i-1} \end{bmatrix} \tag{3-24}$$

Depending of the value of α, matrix M_i can take two forms:

$$\alpha_i = \sqrt{|k_{ac}|_i^2 - \hat{\sigma}_i^2} \tag{3-25}$$

When $|k_{ac}|_i > \hat{\sigma}_i$ then α_i is real and M_i is given by:

$$M_i = \begin{bmatrix} \cosh(\alpha_i \delta L) - i\frac{\hat{\sigma}}{\alpha_i}\sinh(\alpha_i \delta L) & -i\frac{|k_{ac}|_i}{\alpha_i}\sinh(\alpha_i \delta L) \\ i\frac{|k_{ac}|_i}{\alpha_i}\sinh(\alpha_i \delta L) & \cosh(\alpha_i \delta L) + i\frac{\hat{\sigma}}{\alpha_i}\sinh(\alpha_i \delta L) \end{bmatrix} \tag{3-26}$$

Where δL is defined as $\delta L = \frac{L}{N}$, the length of a grating section.

When $|k_{ac}|_i < \hat{\sigma}_i$ then α_i is imaginary and M_i is given by:

$$M_i = \begin{bmatrix} \cos(\alpha_i \delta L) - i\frac{\hat{\sigma}_i}{\alpha_i}\sin(\alpha_i \delta L) & -i\frac{|k_{ac}|_i}{\alpha_i}\sin(\alpha_i \delta L) \\ i\frac{|k_{ac}|_i}{\alpha_i}\sin(\alpha_i \delta L) & \cos(\alpha_i \delta L) + i\frac{\hat{\sigma}_i}{\alpha_i}\sin(\alpha_i \delta L) \end{bmatrix} \quad \textbf{(3-27)}$$

The total transfer matrix M is given by Equation (3-28)

$$M = M_N * M_{N-1} ..... M_i ..... M_2 * M_1 \quad \textbf{(3-28)}$$

The output amplitude and phase response can be obtained from:

$$\begin{bmatrix} R_N \\ S_N \end{bmatrix} = M . \begin{bmatrix} R_0 \\ S_0 \end{bmatrix} \quad \textbf{(3-29)}$$

And the boundary conditions are now applied

$$\begin{bmatrix} R_N \\ S_N \end{bmatrix} = \begin{bmatrix} M_{11} M_{12} \\ M_{21} M_{22} \end{bmatrix} . \begin{bmatrix} 1 \\ 0 \end{bmatrix} \quad \textbf{(3-30)}$$

The power reflectivity R of the grating is given by

$$R = \left| \frac{M_{21}}{M_{11}} \right|^2 \quad \textbf{(3-31)}$$

The power transmissivity can be obtained from the relation $T=1-R$.

3.3.2 Rouard's Method

Rouard's method is a recursive technique commonly used in design of thin-film coatings which was modified by Weller-Brophy and Hall for the analysis of diffraction gratings (Weller-Brophy and Hall, 1985). This technique is based on a grating interface characterized by an effective complex reflectivity from a single interface having the same properties. The period of the grating is divided into half length periods that are treated as a layer in a thin-film stack (Othonos and Kalli, 1999). In this method one starts with the layer at the bottom of the stack next to the substrate (Figure 3-5) and proceeds through the stack, replacing each layer considered during each iteration by an interface having the same reflectivity and phase shift. As each layer is treated

independently, the Rouard's method allows a good control of the properties of the FBG such as period and refractive index which the TMM do not.

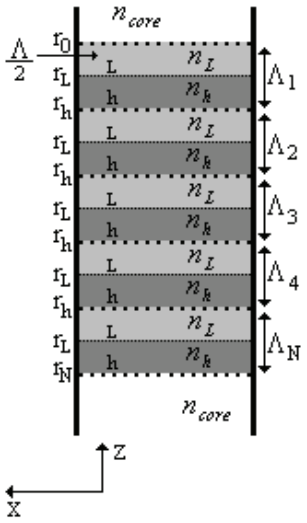

Figure 3-5: Underlying principle of Rouard's method

Rouard's method is outlined, based upon the altered methodology by Chehura *et al*., (2005). Figure 3-5 illustrates the underlying principles of Rouard's method showing all the periods of the FBG. Each period has been subdivided into two equal layers (L and h) of half the size of the original period, each one with low and high refractive index, n_L and n_h respectively.

The reflection coefficient at the interface between the two layers within the same period (L and h) is r_L. The interface between layer h of one period and layer L of the next period has a reflection coefficient of r_h. r_0 and r_N represent the reflection coefficients between the core and the first or final period of the FBG. The Fresnel Equations (3-32) and (3-33), describing the reflections at the interfaces are:

$$r_L = \frac{n_h - n_L}{n_h + n_L} \qquad \textbf{(3-32)}$$

$$r_h = \frac{n_L^* - n_h}{n_L^* + n_h} \qquad \text{* low refractive index of the next FBG period} \qquad \textbf{(3-33)}$$

The phase shift that occurs on traversing the interface between the two layers within the same period is given by Equation (3-34) and the phase shift experienced passing from layer h of one period and layer L of the next period is given by Equation (3-35).

$$\Phi_L = \frac{2\pi . n_L . \frac{\Lambda}{2}}{\lambda} \quad \textbf{(3-34)}$$

$$\Phi_h = \frac{2\pi . n_h . \frac{\Lambda}{2}}{\lambda} \quad \textbf{(3-35)}$$

The effective complex reflectance of the interface between the two layers within the same period is represented by Equation (3-36) and the effective complex reflectance at the interface between layer h of one period and layer L of the next period is given by Equation (3-37).

$$\rho_L = \frac{r_L + \rho_h^* . \exp[-2j\Phi_L]}{1 + r_L . \rho_h^* . \exp[-2j\Phi_L]} \quad \text{* reflectance of the next FBG} \quad \textbf{(3-36)}$$

$$\rho_h = \frac{r_h + \rho_L . \exp[-2j\Phi_L]}{1 + r_h . \rho_L . \exp[-2j\Phi_L]} \quad \textbf{(3-37)}$$

The reflection spectrum is obtained by the $|\rho_N| = \left| \frac{r_L(N) + \rho_h(N).\exp[-2j\Phi_L(N)]}{1 + r_L(N).\rho_h(N).\exp[-2j\Phi_L(N)]} \right|$

3.4 Modelling locally transverse loaded fibre Bragg gratings

The spectral behaviour of an FBG subjected to partial transverse loading can be modelled using the TMM or the Rouard's method. These techniques offer identical and accurate results and the criterion used to select between them was the computation time required. The TMM has the advantage of being faster when compared to the Rouard's method and therefore it was chosen for this simulation.

In the simulations presented next, the refractive index over the pressed region was replaced by the new pressure induced refractive index and remained unchanged for the unperturbed parts. Special care was taken defining the total number of sections in which the FBG is divided as the total number of sections and the number of sections subject to perturbation has to be integer (with the total number of sections M>100).

The unidirectional loading of an optical fibre induces birefringence in the fibre and therefore it is necessary to calculate the reflectivity obtained for each polarisation state R_x and R_y. The total reflectivity when the FBG is addressed by a linear polarisation state with amplitudes components p_x and p_y along the *x* and *y* axes is:

$$R = p_x R_x + p_y R_y \tag{3-38}$$

with $p_x + p_y = 1$.

Different transverse loading configurations were analysed with the aim of finding the most suitable technique to be used in the development of a pressure sensor. The effect of loading the fibre at different positions, over different lengths and over different lengths and with a fixed ratio of loaded to unloaded lengths, but with different total FBG lengths was studied and the results presented in Sections 3.4.1, 3.4.2, 3.4.4 and 3.4.3.

3.4.1 6 mm long FBG transversely loaded along a 1 mm length at different positions along the FBG length

Depending on the position where the FBG is locally transversely loaded, different spectral behaviour occurs. In 2002, Torres and Valente demonstrated that when the FBG is not loaded at its centre, the spectral drop-out is not very deep. In order to verify the spectral behaviour of an FBG when subject to a transverse load across different positions, a simulation of the spectral behaviour of an FBG subject to transverse load along different fibre positions was undertaken.

In order to simulate the reflection spectrum of the FBG used on the experimental work presented in Section 4.3.2, the length of the modelled grating section was 6 mm, the effective refractive index of the fibre n_{eff} used was 1.4465, the Bragg index modulation amplitude δn was $5*10^{-5}$ and the period Λ was calculated as being $5.347*10^{-7}$ m for the designed Bragg wavelength λ_B of 1546.94 nm. The length of fibre under transverse load is 1 mm and the diameters of the fibre cladding and core were 125 and 6.73 μm respectively (Fibercore datasheet). The strain optic tensor coefficients P_{11} and P_{12} are 0.121 and 0.27 respectively, and the Young's modulus of the fibre and Poisson's ratio are 71.7 GPa and 0.17 respectively (Fibercore datasheet). The amount of light present in the two polarisation axes *x* and *y* was assumed to be $p_x = 0.85$ and $p_y = 0.15$. The criteria used to select the number of sections on the TMM was that the number of sections over the perturbed length had to be 100 and the total number of sections integer. For the present simulation a total number of 600 sections for the 6 mm long FBG was chosen and 100 sections were used over the 1 mm FBG perturbed central section.

Figure 3-6 and Figure 3-7 show the theoretically simulated results obtained for the application of a transverse load of 16.7 N along a 1mm length of an FBG of total length 6 mm at different positions along the FBG. It is observed that when the FBG is loaded at the edges of the FBG, no spectral drop-out is formed as no cavity is induced and only a broadening of the Bragg peak is obtained. As the position of the applied load approaches the centre of the FBG (from both left and right sides), the spectral drop-out becomes deeper and more resolvable demonstrating that the centre is the most effective place to apply a transverse load to the FBG. This is due to the correct balancing of the optical power reflected from each sub-grating (equal power) that act as a Fabry-Perot interferometer.

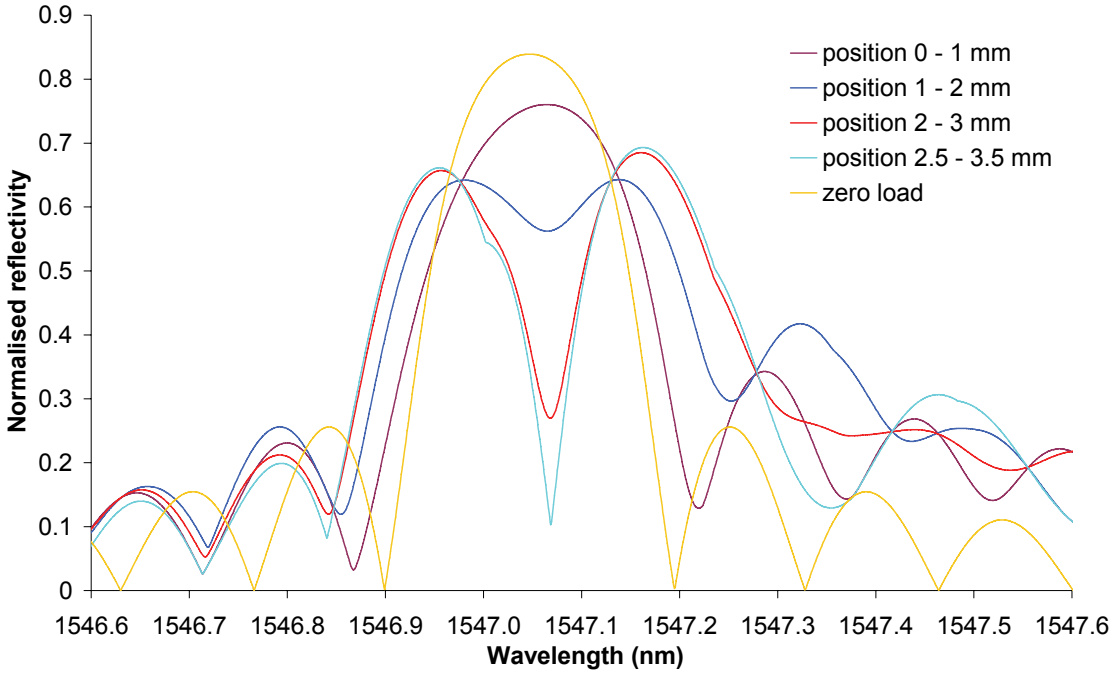

Figure 3-6: Theoretically simulated results obtained for the application of a transverse load of 16.7 N along a 1mm length of an FBG of total length 6 mm at different positions along the FBG (left side).

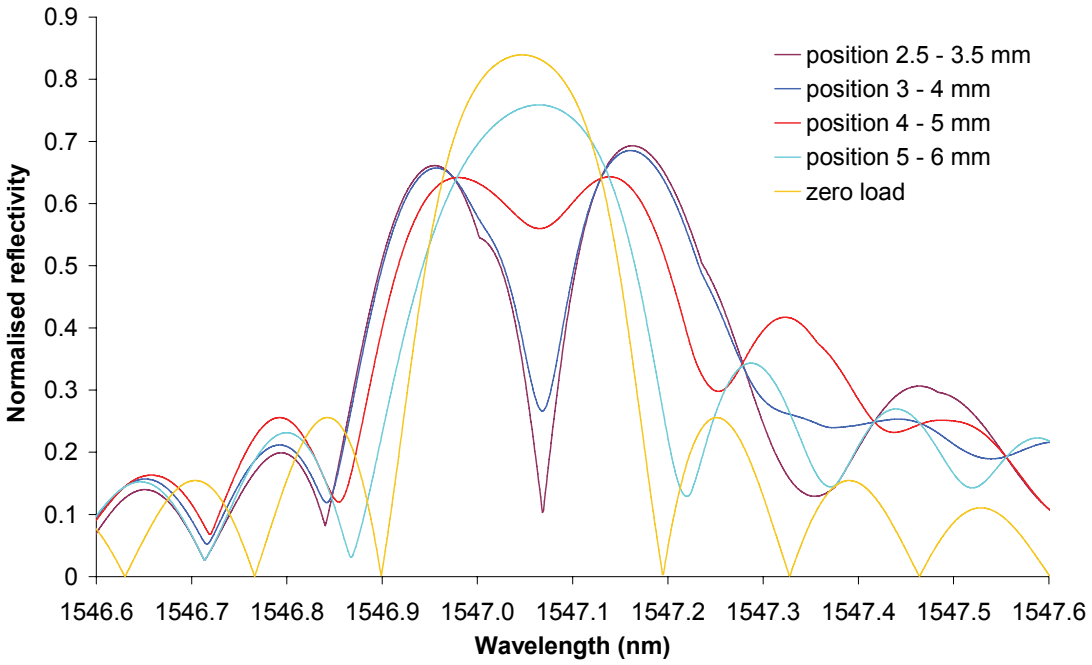

Figure 3-7: Theoretically simulated results obtained for the application of a transverse load of 16.7 N along a 1mm length of an FBG of total length 6 mm at different positions along the FBG (right side).

3.4.2 6 mm long FBG transversely loaded across its centre

A simulation of the effect of transversely loading an FBG over a subsection located at its centre, with different subsection lengths, is presented in this section. The FBG parameters used in the TMM were the same as in Section 3.4.1, apart from the length of the loaded subsection.

The first simulation consisted of applying a transverse load to a 1 mm central section of a 6 mm long FBG. A maximum load of 66.7 N was applied to the central section of the FBG with load increments of 6.7 N. The reflection spectrum response obtained for this loading configuration is presented in Figure 3-8.

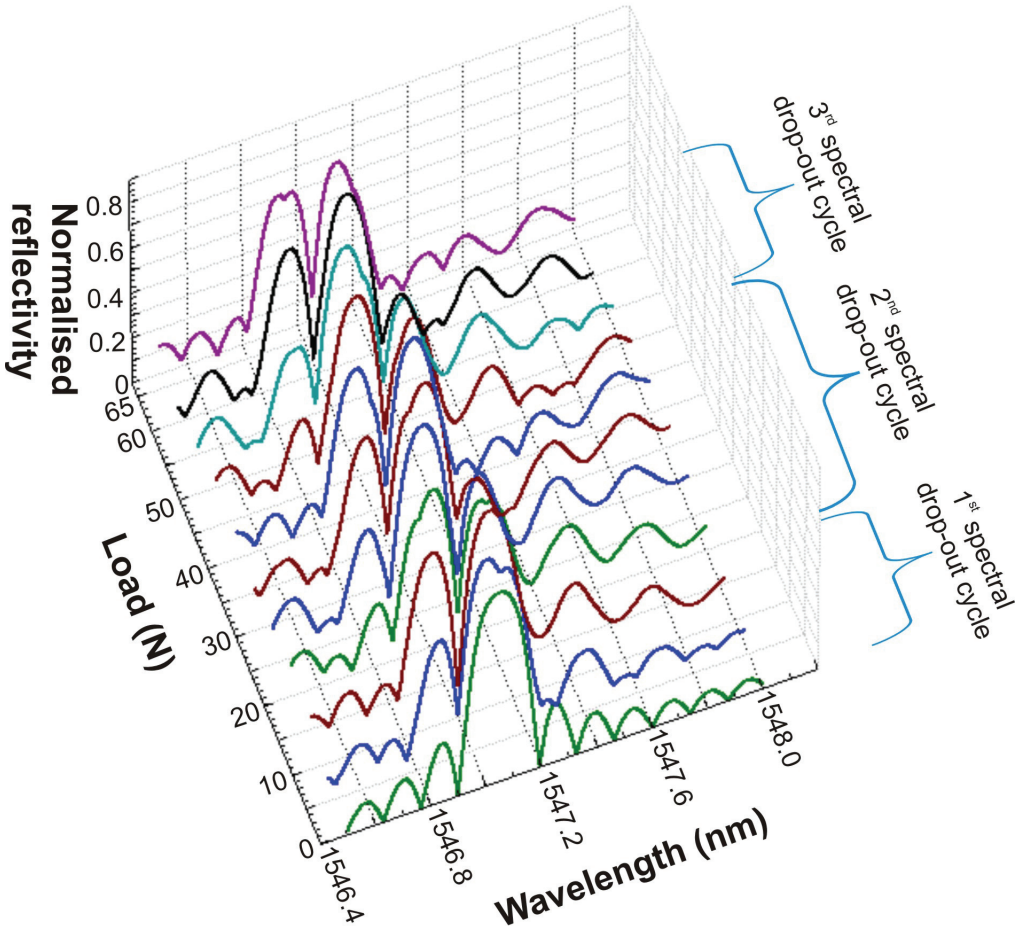

Figure 3-8: Theoretical simulated reflection spectrum of a 6 mm long FBG subject to transverse load over a 1 mm central section. Different colours are used to help visualisation.

In Figure 3-8 it is observed that as the load increased a spectral drop-out started to form on the blue side of the Bragg peak, suffering a red shift with the increase of the load.

When a load of 20 N was applied to the FBG, the spectral drop-out has travelled almost the entire bandwidth of the Bragg peak and a new spectral drop-out started to form on the blue side of the spectrum. At this point, the central wavelength of the Bragg peak equals the original Bragg wavelength of the unperturbed FBG. It is observed that for this loading configuration (16.7 % of the FBG length) the Bragg envelope stays at the same wavelength position (for the two spectral drop-out cycles). According to Torres and Valente (2002), when the perturbed length of an unchirped grating is higher than 10 % of the total length of the FBG, a secondary peak that corresponds to the intra FBG created over the loaded region is created at longer wavelengths. This effect was not observed in this simulation where the loaded section is 16.7 % of the FBG length.

The following simulations considered the application of the same load increments and range to a 3 mm long central section of a 6 mm long FBG. The reflection spectrum obtained for the different applied loads is presented in Figure 3-9.

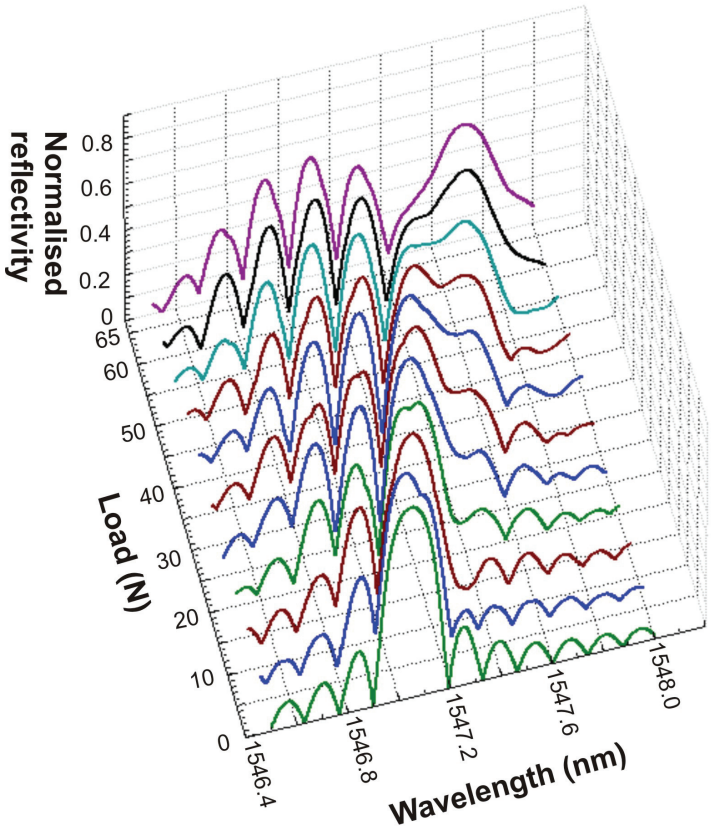

Figure 3-9: Theoretical simulated reflection spectrum of a 6 mm long FBG subject to transverse load over a central 3 mm long section. Different colours are used to help visualisation.

This time as the load increases, the spectral drop-out starts to appear in the blue side of the spectrum and when it is positioned at half the bandwidth of the initial Bragg peak, a new spectral drop-out follows from the blue side of the spectrum. When the first spectral drop-out reaches the red side of the bandwidth of the Bragg peak (33.3 N), a secondary peak separates from the original Bragg peak, moving apart to higher wavelengths as the load is increased. It is noted that, for this load, the amplitude of the main Bragg envelope and the secondary Bragg peak is approximately 61% of the amplitude of the original unperturbed FBG peak. The multiple spectral drop-outs are attributed to the cavity length increase which induces more spectral drop-outs in the reflection spectrum.

Finally, the effect of transversely loading 83.3% of a central section of a 6 mm long FBG was simulated. The reflection spectrum obtained for the same load range and increment applied in the previous simulation is presented in Figure 3-10.

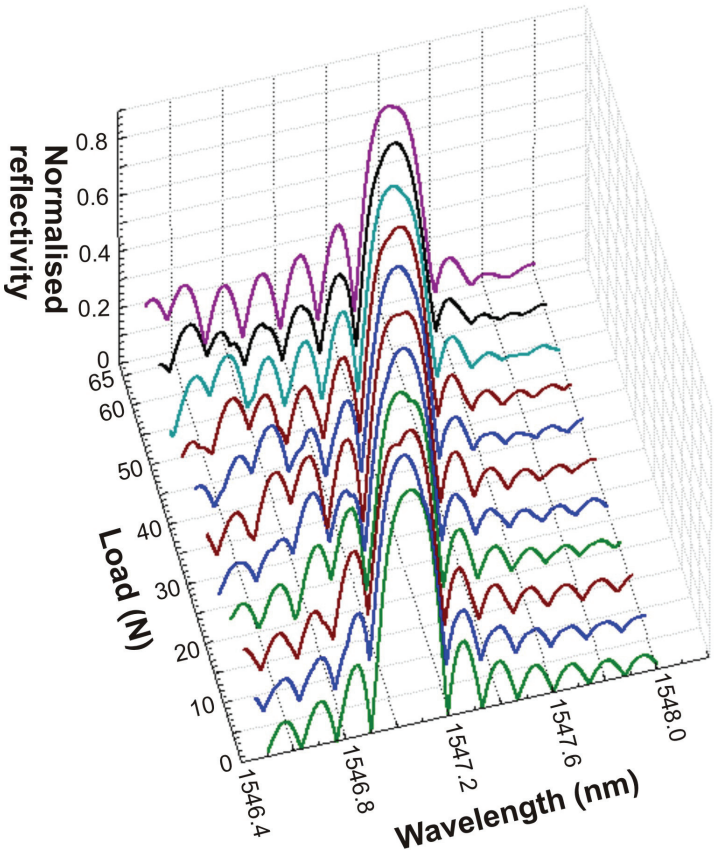

Figure 3-10: Theoretical simulated reflection spectrum of a 6 mm long FBG subject to transverse load over a 5 mm long central section. Different colours are used to help visualisation.

For this loading configuration it was observed that as the load increases, the entire Bragg peak suffers a red shift and that no spectral drop-out is formed within the bandwidth of the FBG peak.

Figure 3-11 shows the simulated reflection spectrum of a 6 mm long FBG subject to a transverse load of 33.3 N at its centre, across different lengths. When this load is applied over a 1 mm section, a spectral drop-out appears in the middle of the original bandwidth of the FBG peak (first spectral drop-out cycle). When the length over which the load is applied increases, the amplitude of the reflected peaks each side of the spectral drop-out decreases and a secondary peak is observed at the blue side of the spectrum. This secondary peak is not visible when the load is applied over a 1 mm length. It becomes visible for loaded lengths > 2 mm, equalising the amplitude of the side peaks of the spectral drop-out for a 3 mm loaded length. For perturbed lengths longer than 3 mm, the spectral drop-out is not well defined and a red shift of the Bragg peak is observed.

The most attractive loading configuration for the development of a pressure sensor is the loading of a central section of an FBG over a length smaller than 20% of the total FBG length. With this loading configuration it is possible, in contrast with all the others, to measure pressure by tracking the position of the spectral drop-out within the bandwidth of the FBG peak without a shift of the Bragg envelope. This offers the possibility to multiplex a higher number of sensors within a specific spectral range. Moreover, it offers the potential to measure other parameters such as temperature by measuring the wavelength shift of the Bragg envelope.

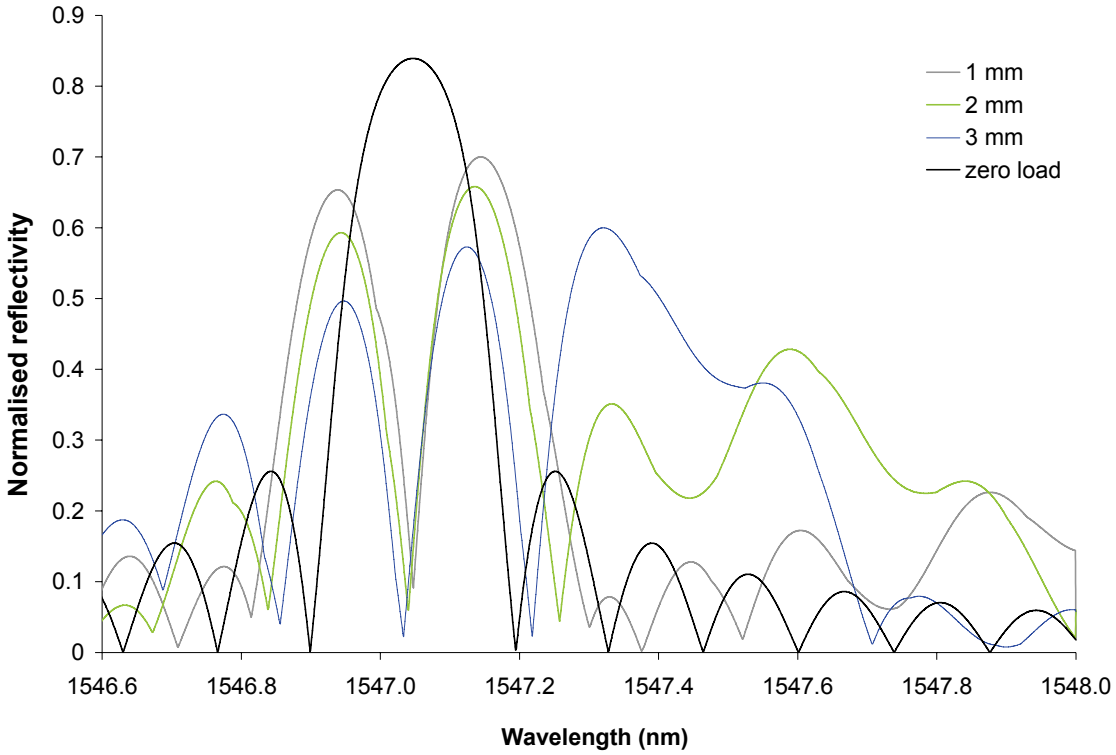

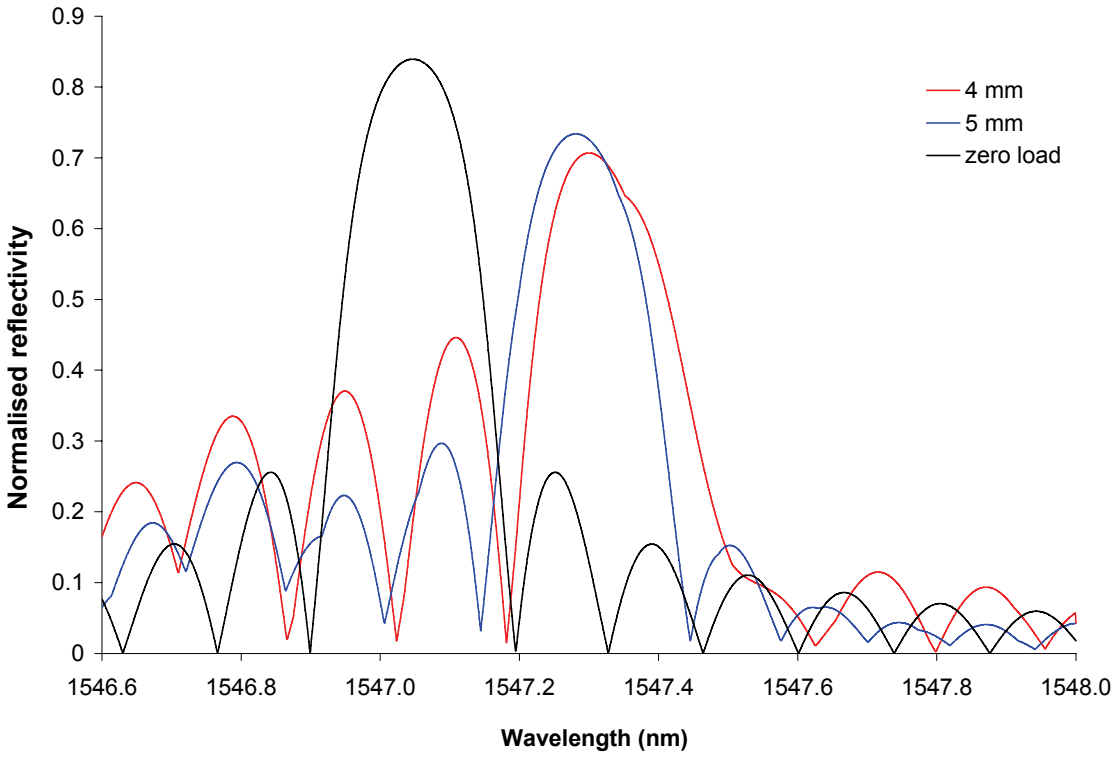

Figure 3-11: Theoretical simulated reflection spectrum of a 6 mm long FBG subject to transverse load of 33.3 N at its centre, across different lengths.

3.4.3 Transverse loading of FBGs of different length when the ratio of loaded to unloaded lengths is constant

In the previous sections it was demonstrated that the most efficient position to transversely load an FBG is at its centre, resulting in a well defined spectral drop-out. It was also observed that by transversely loading less than 20% of the total FBG length, a spectral drop-out that tracked across the bandwidth of the FBG peak without a shift of the Bragg envelope was induced.

To study the effect of the length of the FBG on the sensitivity to transverse load, FBGs with different lengths were subject to a transverse load across 16.67% of their length, with the loaded section located at the centre of the FBG. The percentage of the FBG length subject to perturbation (16.67%) was chosen in order to match the experimental fibre loading and support structure which has a central raised area of 1 mm length. As the first experiments were carried out using a 6 mm long FBG, 1/6 of the total length of the FBG was chosen as reference. The results obtained for the different FBG lengths simulated are presented in Table 3-1. The central wavelength of all FGBs was λ_B = 1546.94 nm and the Bragg index modulation amplitude δn was adjusted to obtain a grating strength of kL=0.61. This wavelength was chosen to match the Bragg wavelength of the FBG experimentally tested in Section 4.3.1. Because the bandwidth of an FBG is dependent on the FBG length and its strength, a grating strength that corresponds to a maximum Bragg reflectivity of approximately 84% was chosen. This reflectivity was chosen to match the strength of the FBG simulated above. The maximum applied load to the FBG was 23.9N which corresponds to a complete cycle of the first spectral drop-out for all the gratings. All the other FBG parameters used in the simulation are the same as in Section 3.4.1.

Table 3-1: FBG parameters used in the simulation of the spectral behaviour of different FBGs with different lengths subject to transverse load across 16.67% of its length and achieved load sensitivity.

FBG length (mm)	Perturbed length (mm)	Bragg index modulation amplitude δn ($x10^{-5}$)	Maximum force per length (N/m)	Force increment (N/m)	Sensitivity (nm/N)	Range (N)
2	0.33	15	71700.00		0.0305	
3	0.50	10	47800.00		0.0203	
4	0.67	7.5	35850.00		0.0153	
5	0.83	6.0	28680.00		0.0122	
6	1.00	5.0	23900.00	3333.33	0.0101	23.9
7	1.17	4.3	20485.71		0.0087	
8	1.33	3.8	17925.00		0.0076	
9	1.50	3.3	15933.33		0.0068	
10	1.67	3.0	14340.00		0.0061	

In Table 3-1 it is observed that for the same load range a higher sensitivity was obtained for the 2 mm long FBG and that the longer the FBG, the lower the sensitivity. Figure 3-12 shows the relationship between the load sensitivity and FBG length.

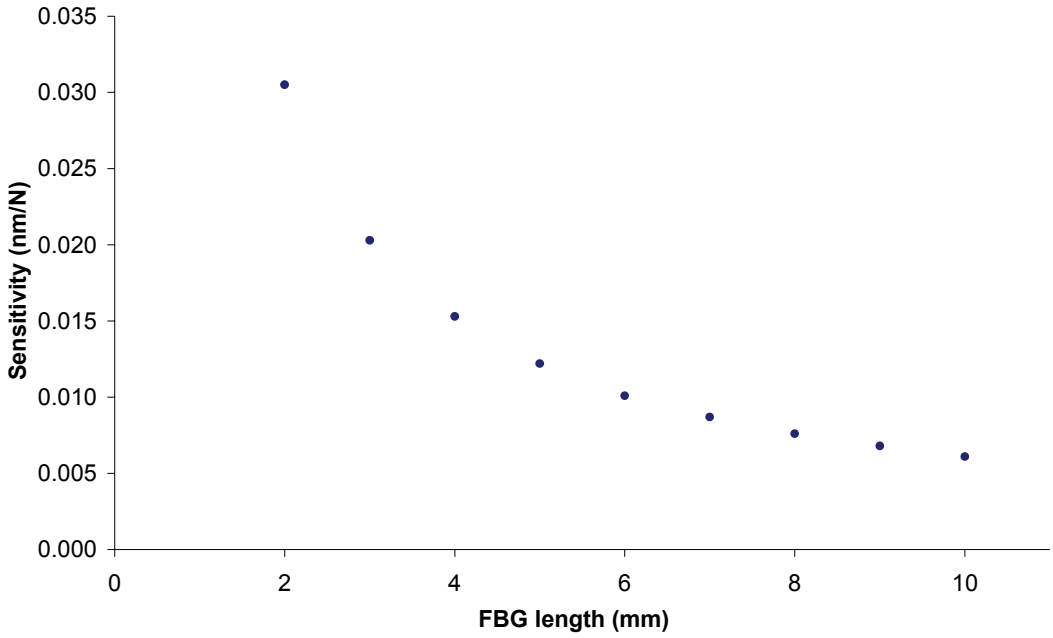

Figure 3-12: Theoretical calculated load sensitivity of different FBGs with different length subject to a transverse load across 16.67% of its length.

The relationship between the load sensitivity and FBG length is not linear as the Bragg peak bandwidth of an FBG decreases non-linearly with the FBG length (Figure 3-13).

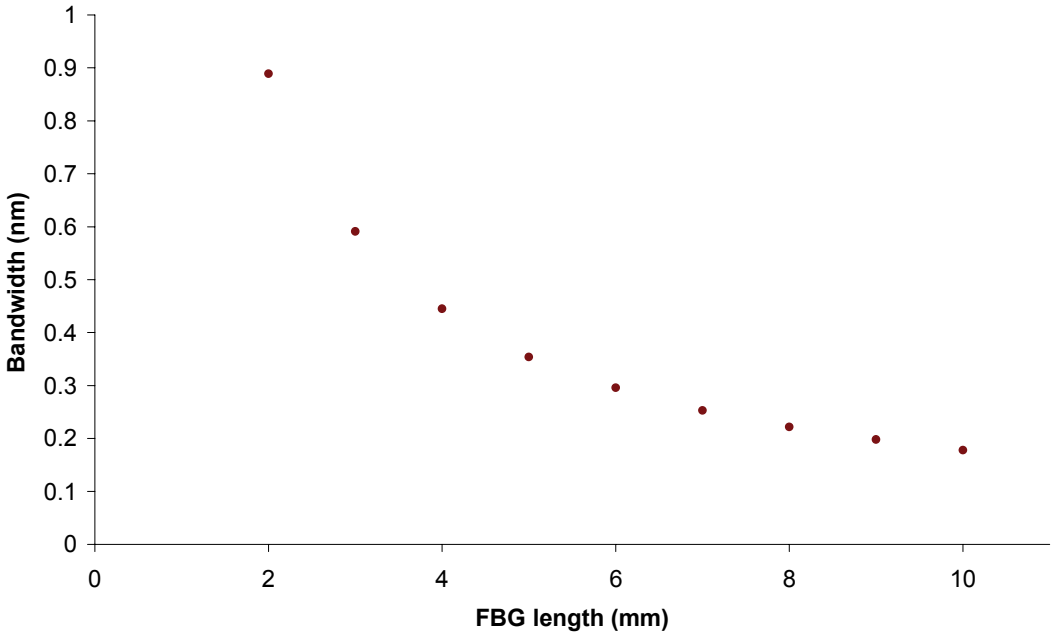

Figure 3-13: Theoretical calculated FBG bandwidth versus FBG length.

3.4.4 6 mm long FBG transversely loaded across its length apart from its centre

In this section, the effect of transverse load on an FBG across its entire length apart from a central section is presented (Figure 3-14). The FBG parameters used in the TMM were the same as in Section 3.4.1 and only the loading configuration on the fibre was changed.

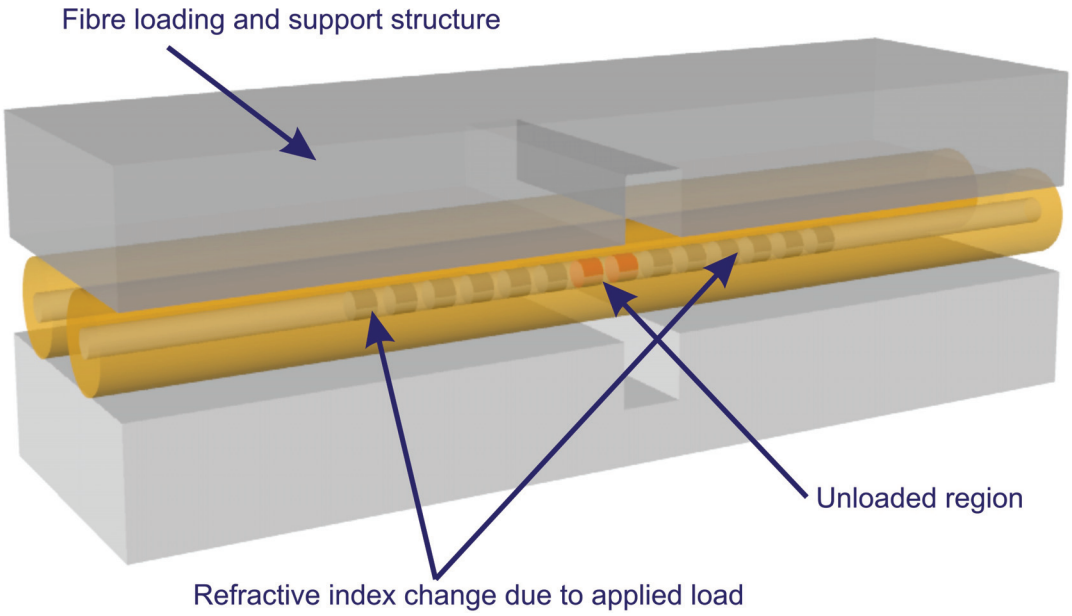

Figure 3-14: Schematic representation of an FBG subject to transverse load all across its length apart from a central section. Different colours represent different effective refractive index changes (in green the original effective refractive index of the FBG and in orange the new local effective refractive index).

Figure 3-15 and Figure 3-16 present the simulated results of the spectral behaviour of a 6 mm long FBG subject to transverse load across its entire length, apart from central sections of length 1 mm and 3 mm respectively.

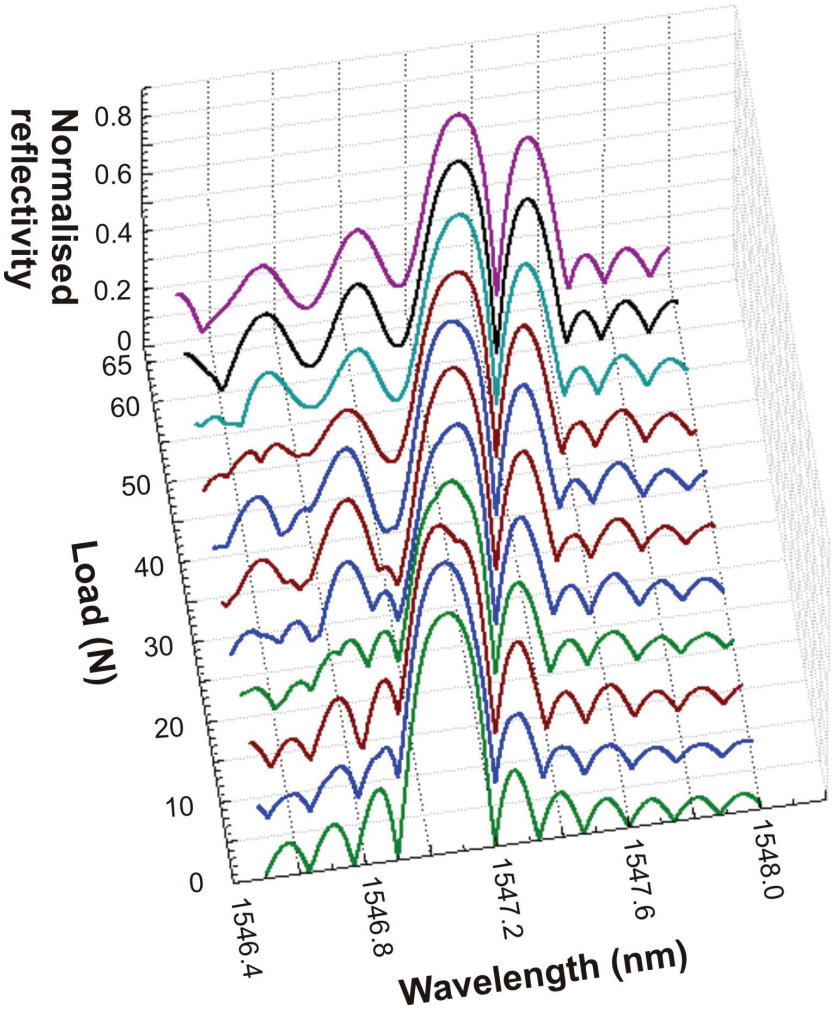

Figure 3-15: Theoretical simulated reflection spectrum of a 6 mm long FBG subject to transverse load across its length apart from a 1 mm central section. Different colours are used to help visualisation.

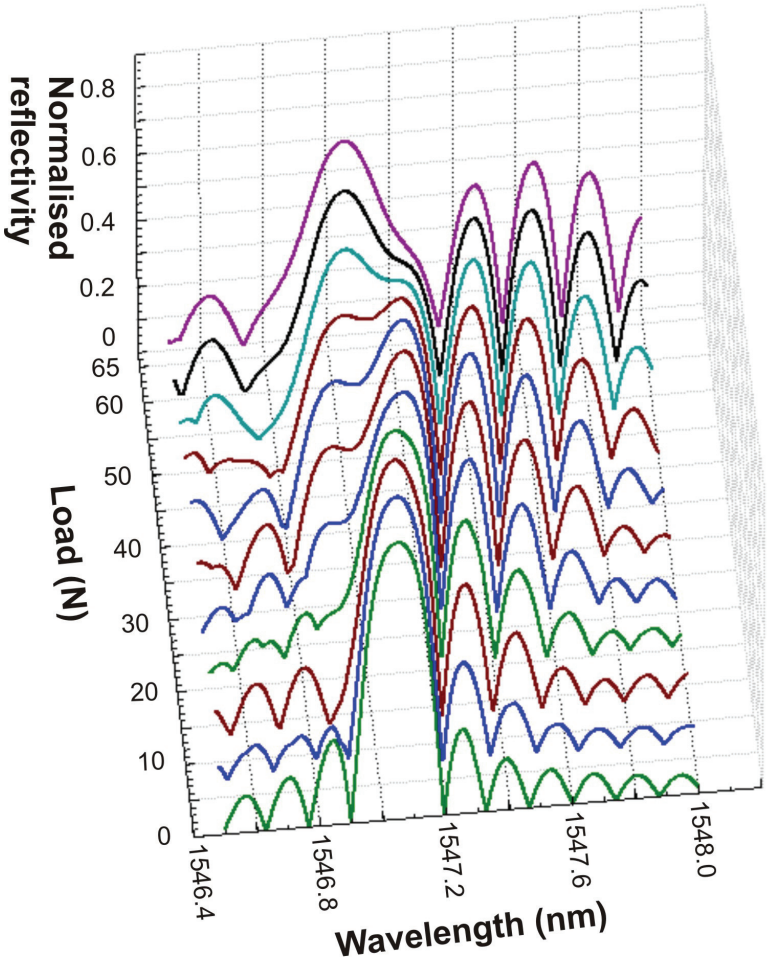

Figure 3-16: Simulated reflection spectrum of a 6 mm long FBG subject to transverse load across its length apart from a 3 mm central section. Different colours are used to help visualisation.

When the entire length of the FBG was loaded apart from a 1 mm central section (Figure 3-15) it is observed that as the load increases, the Bragg envelope suffers a red shift and a spectral drop-out appears from the red side of the FBG bandwidth, moving to the blue side of the peak. In Figure 3-16, when the unperturbed length was 3 mm, the same behaviour occurred but a Bragg peak with a wider bandwidth corresponding to the unperturbed part of the FBG remains at the same central wavelength. The effect of transversely loading an FBG along its entire length apart from a central section was first analysed by Michaille *et al.*, 2003 that observed a similar spectral behaviour as described above. Although this technique induces a spectral drop-out in the reflection spectrum of the FBG, the tracking of the position of the spectral drop-out is not easily achieved due to the wavelength shift of the Bragg envelope and therefore this technique is not desirable for the development of the pore pressure sensor.

3.5 Modelling of transversely loaded fibre Bragg gratings partially embedded in epoxy

In Section 6.2, an experimentally investigated packaging technique that consisted of embedding the central section of the FBG within an epoxy cube is presented. The deformation of the epoxy cube in response to a transverse load results in the application of an axial strain across the central section of the FBG. In this section, the study of the effect of applying an axial strain across a central section of an FBG is presented. Rouard's method was used to simulate the spectral behaviour of the FBG subject to an axial strain across its centre. As in Rouard's method the grating structure is treated in individual layers, each one containing half periods, it is possible to have a good control of the properties of the FBG such as period and refractive index offering a better control of the period change over the stretched FBG length when compared with the TMM.

In the simulation, the FBG period over the stretched region was replaced by the new longitudinal strain induced period change. The period remained unchanged for the unperturbed parts. As shown in Section 1.1.1, the strain applied to an FBG induces a change in both the grating period and the effective refractive index. Superimposing these two effects, the change in grating period due to an effective strain is (Peters *et al.*, 2001):

$$\Lambda(z) = \Lambda_0 \left[1 + \left(1 - \frac{n_{eff}^2}{2} \left(\rho_{12} - \nu \left(\rho_{11} - \rho_{12} \right) \right) \right) \times \varepsilon_z \right] \qquad \textbf{(3-39)}$$

The axial strain induced on the FBG was assumed to equal the strain induced in the z direction of an epoxy resin cube transversely loaded in the *x* direction (Figure 3-17). The force acting on the cube face along the *x* direction induces a strain $\varepsilon_x = -\frac{\sigma_x}{E}$ and a strain in the *y* and *z* directions of $\varepsilon_y = \varepsilon_z = -\frac{\upsilon \sigma_x}{E}$ where υ is Poisson's ratio of the epoxy, *E* is Young's modulus of the epoxy and σ_x is the stress in the *x* direction equal to $\sigma_x = \frac{F_x}{A_x}$ (Benham *et al.*, 1996). This is an approximate solution as the inclusion of the optical fibre in the epoxy cube will result in a smaller strain along the *z* direction. A

more accurate and quantitative modelling of the axial strain induced in the FBG due to the deformation of the epoxy cube would require a finite element analysis which has not been undertaken as part of this work. As a qualitative analysis, it was assumed in this work that the strain induced in the cube is totally transferred to the optical fibre.

As the Young's modulus of the epoxy cube to be modelled is very small compared with one of the optical fibre (more than 2 orders of magnitude) and the thickness of the cube is high (more than 0.5 mm) no birefringence was assumed to be induced in the optical fibre. This was experimentally proved in Section 5.3.4, when transversely loading a 6 mm long FBG written in PM optical fibre.

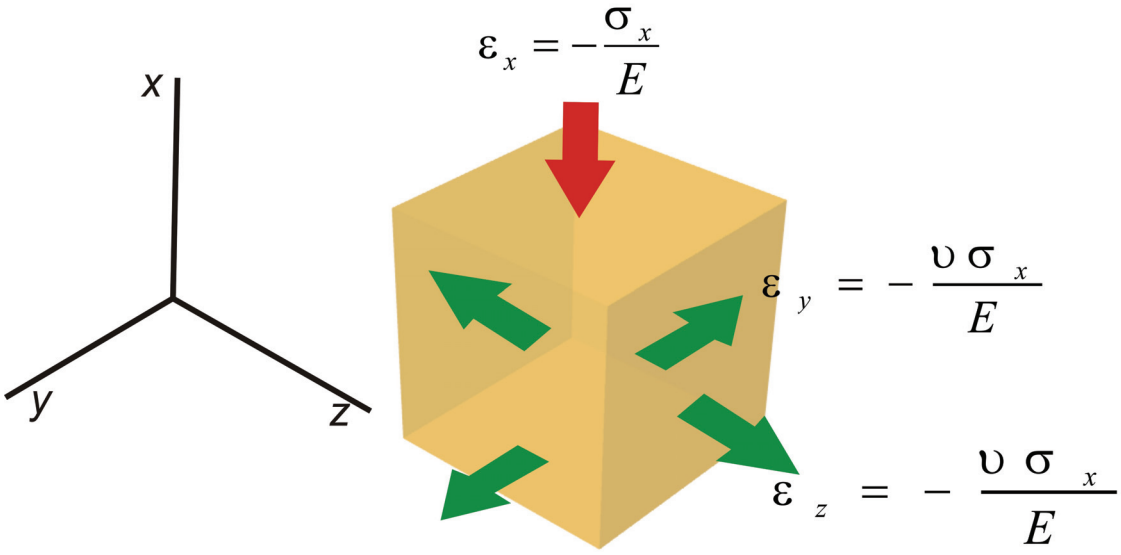

Figure 3-17: Schematic representation of a cube subject to uniaxial stress and the corresponding strains.

Different embedding configurations were analysed with the aim of finding the most suitable technique to be used in the development of a pressure sensor. The effect of loading the epoxy cube localised in different positions along the FBG and over different lengths was studied and the results are presented in Sections 3.5.1 and 3.5.2. Furthermore, a study of the effect of using different epoxy Young's modulus on the FBG load sensitivity is presented in Section 3.5.3.

3.5.1 Transverse load of a 6 mm long fibre Bragg grating embedded in 2 mm of epoxy localised across different positions along the fibre

In order to investigate the spectral behaviour of the embedded FBG when subject to a transverse load at different positions along its length, the spectral behaviour of a 6 mm long FBG subject to transverse load along a 2 mm epoxy cube localised at different fibre positions was simulated.

The length of the modelled grating section was 6 mm, the effective refractive index of the fibre n_{eff} used was 1.4465, the Bragg index modulation amplitude δn was $5\text{x}10^{-5}$ and the period Λ was calculated to be $5.42\text{x}10^{-7}$ m for the designed Bragg wavelength λ_B of 1566.673 nm. The length of fibre subject to axial strain is 2 mm and the diameter of the fibre cladding and core used was 125 and 6.73 μm, respectively. The strain optic tensor coefficients P_{11} and P_{12} are 0.121 and 0.27 respectively, and the Young's modulus of the fibre and Poisson ratio were considered to be 71.7 GPa and 0.17 respectively. The mechanical properties of an Epotek OG-134 epoxy used in the experimental work presented in Section 6.3.2 were used in this simulation. Acording to the manufacturer these are: Young's modulus 689 MPa and Poisson's ratio 0.4.

Figure 3-18 and Figure 3-19 show the theoretically simulated results obtained for the application of a transverse load of 1.415 N along a 2 mm epoxy cube localised at different positions of along a 6 mm long FBG. It is observed that when the FBG is strained on the sides due to the transverse loading of the epoxy cube, no spectral drop-out is formed and only a broadening of the Bragg peak was obtained. As the position of the epoxy cube approaches the centre of the FBG, from both left and right sides, the spectral drop-out becomes deeper and more resolvable. The axial stretching of an FBG along different positions show that the most effective location to apply the perturbation is at the centre of the FBG.

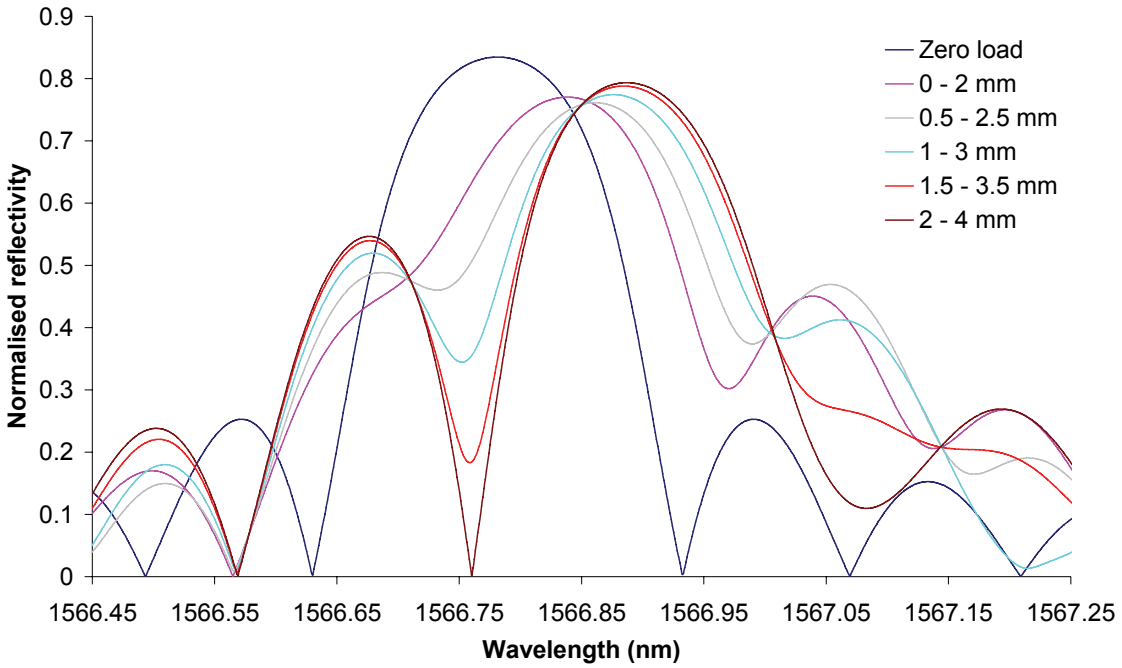

Figure 3-18: Theoretical simulated reflection spectrum of a 6 mm long FBG subject to a transverse load of 1.415 N along a 2 mm epoxy cube localised at different positions of the FBG (left side).

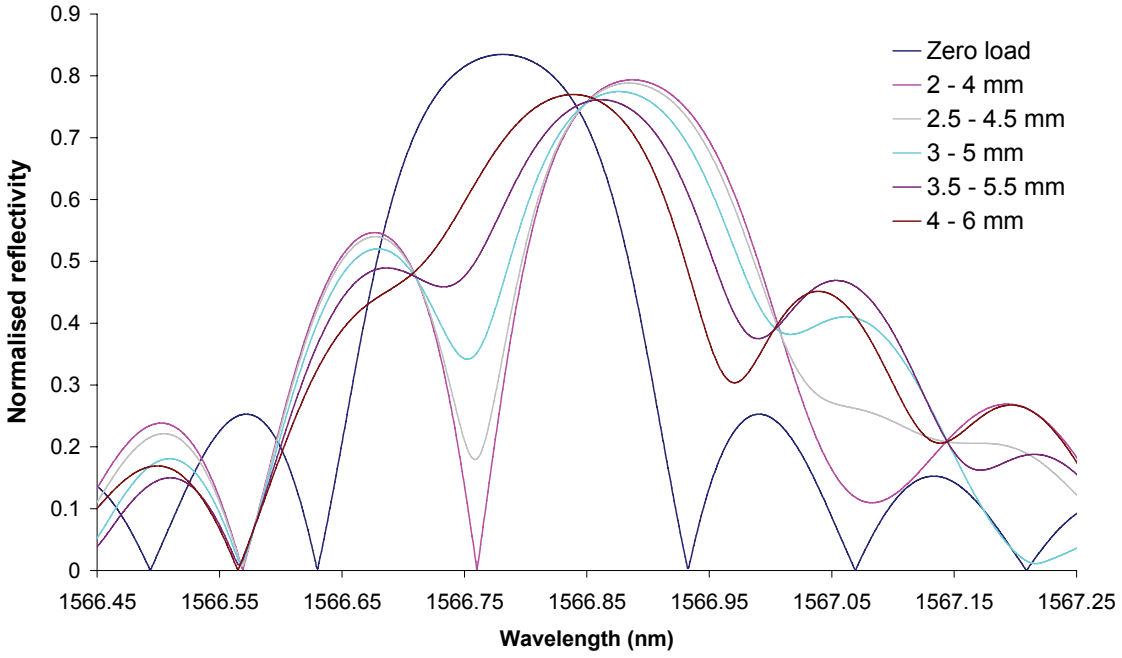

Figure 3-19: Theoretical simulated reflection spectrum of a 6 mm long FBG subject to a transverse load of 1.415 N along a 2 mm epoxy cube localised at different positions of the FBG (right side).

3.5.2 Transverse loading of a 6 mm long fibre Bragg grating embedded over different lengths with different size epoxy cubes

The simulation of the effect of transversely loading an epoxy resin cube that embeds the FBG at its centre over different lengths is presented. The FBG parameters used in Rouard's method were the same as in Section 3.5.1 apart from the length of fibre subject to axial strain. The first simulation consisted of applying a transverse load to a 1 mm epoxy cube localised at a central section of a 6 mm long FBG. A maximum load of 3.3 N was applied to the epoxy cube which induces a strain of 1910 με over the embedded central section of the FBG. The reflection spectrum response obtained is presented in Figure 3-20.

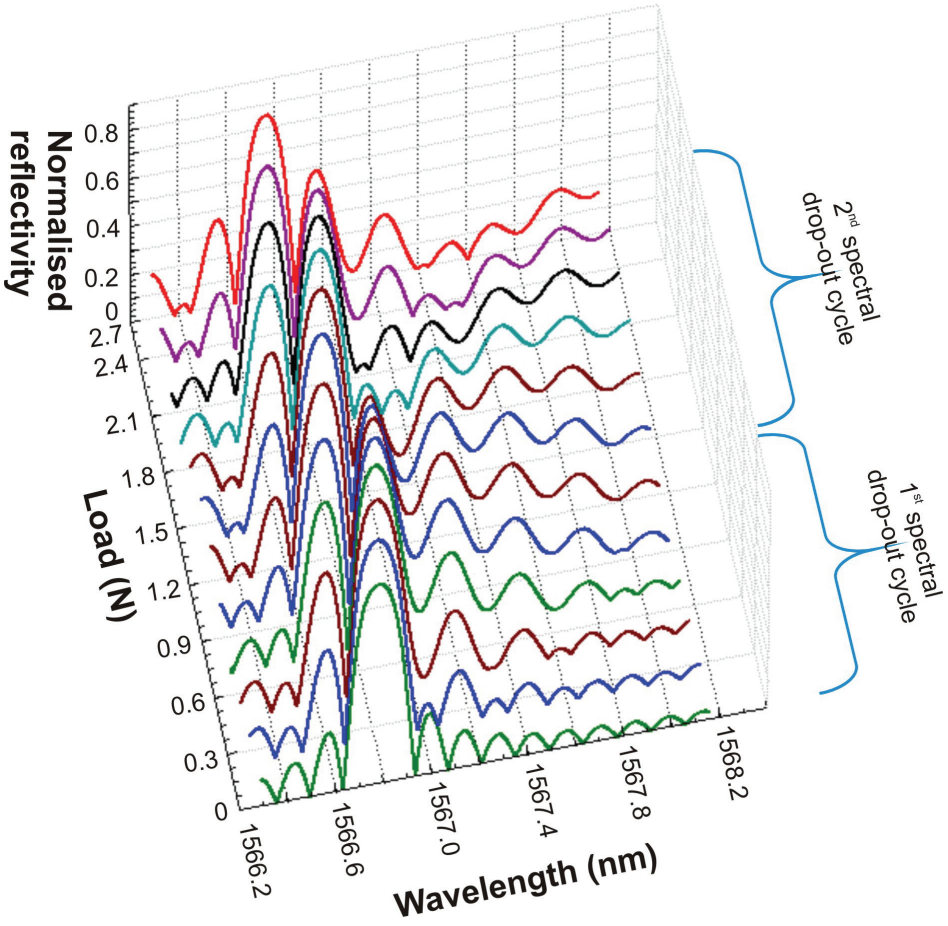

Figure 3-20: Theoretical reflection spectrum from a 6 mm long FBG embedded within a 1mm epoxy cube along its centre, with the applied transverse load. Different colours are used to help visualisation.

From Figure 3-20 it is observed that as the load increased, a spectral drop-out formed on the blue side of the Bragg peak, suffering a red shift with the increasing load. When a load of 1.17 N was applied to the epoxy cube, the spectral drop-out has travelled almost the entire bandwidth of the Bragg peak and a new spectral drop-out started to form on the blue side of the spectrum. At this point, the central wavelength of the Bragg peak equals the original Bragg wavelength of the unperturbed FBG. It was observed that for the stretching of a 1 mm central section of an FBG (16.7 % of the FBG length) the Bragg envelope stays at the same wavelength position (for the two spectral drop-out cycles) and that no secondary peak is observed at higher wavelengths after the first spectral drop-out cycle.

The next simulations consisted of applying a transverse load to a 2 mm and 5 mm epoxy cube localised at the central section of a 6 mm long FBG. A maximum load of 4.95 N and 5.89 N was applied to the 2 mm and 5 mm epoxy cubes, respectively, which induces a strain of 718 με and 94.9 με respectively. The reflection spectrum responses obtained are presented in Figure 3-21 and Figure 3-22.

In Figure 3-21, it was observed the same behaviour as for the loading of a 1 mm cube apart from the secondary peak that separates from the main Bragg peak and suffers a red shift as the fibre is further stretched. It was also noted that higher loads are required to obtain a complete cycle of the spectral drop-out (2.4 N in contrast with 1.2 N for the 1 mm cube). This is due to the increase of cube volume that inherently requires a higher load to suffer the same deformation. In Figure 3-22 it is observed that as the load increases, the entire Bragg peak suffers a red shift and that no spectral drop-out is formed within the bandwidth of the FBG peak. This follows the same behaviour as the transverse load of 5 mm section of a 6 mm long FBG presented in Section 3.4.2.

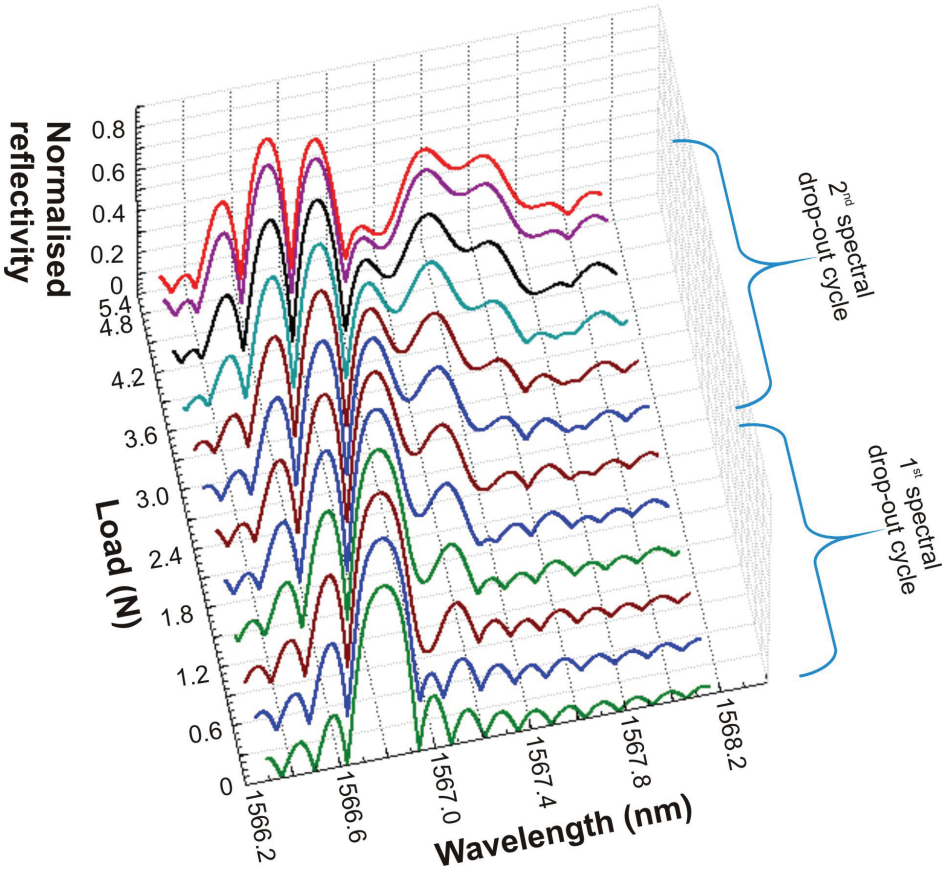

Figure 3-21: Theoretical reflection spectrum from a 6 mm long FBG embedded with epoxy along 2 mm of its centre, with the applied transverse load. Different colours are used to help visualisation.

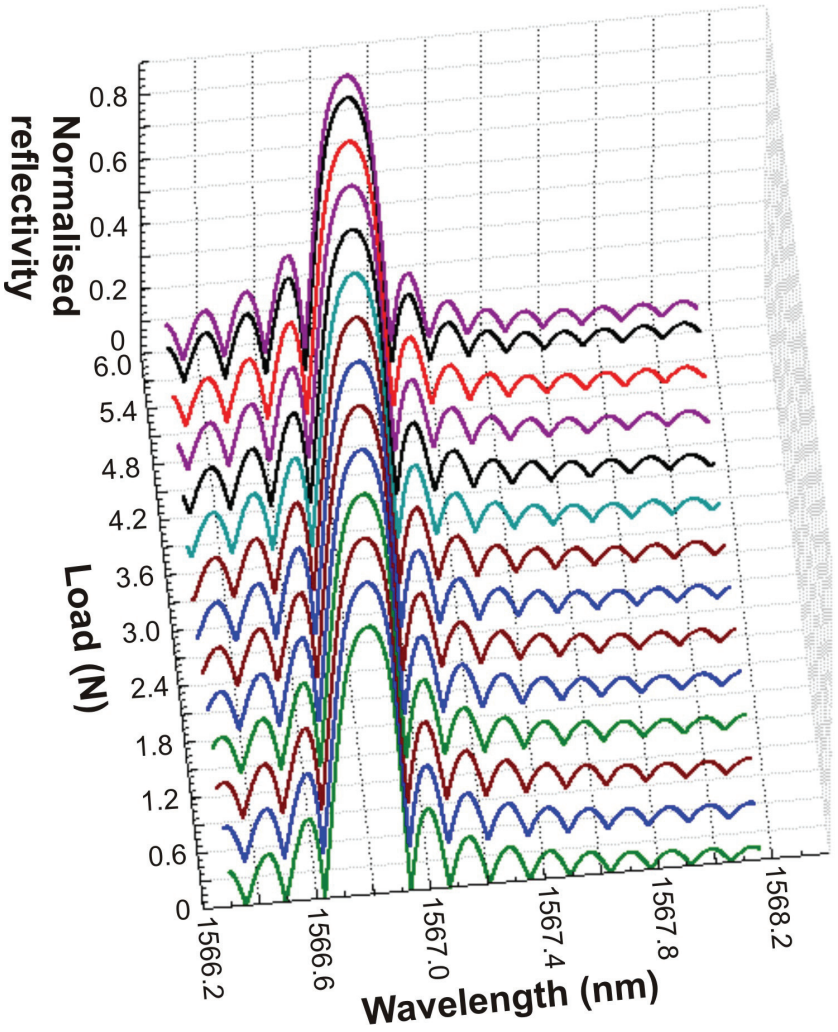

Figure 3-22: Theoretical simulated reflection spectrum of a 6 mm long FBG embedded with epoxy along 5 mm of its centre, with the applied transverse load. Different colours are used to help visualisation.

3.5.3 Transverse loading of a 6 mm long fibre Bragg grating embedded around its centre in a 2 mm epoxy cube with different Young's modulus

The simulation of the effect different values of epoxy Young's modulus on the transverse sensitivity of a 2 mm epoxy cube embedding a 6 mm long FBG around its centre is presented. The epoxy Young's modulus values used in the simulation ranged from 400 to 1000 MPa and the total load applied to the epoxy cube was 3.3 N. The FBG parameters used in Rouard's method were the same as presented in Section 3.5.1. Figure 3-23 presents the load sensitivity of the spectral drop-out over the first spectral

drop-out cycle for the different epoxy Young's modulus values used. It was observed that for lower values of the epoxy Young's modulus, the higher the transverse load sensitivity (Figure 3-23).

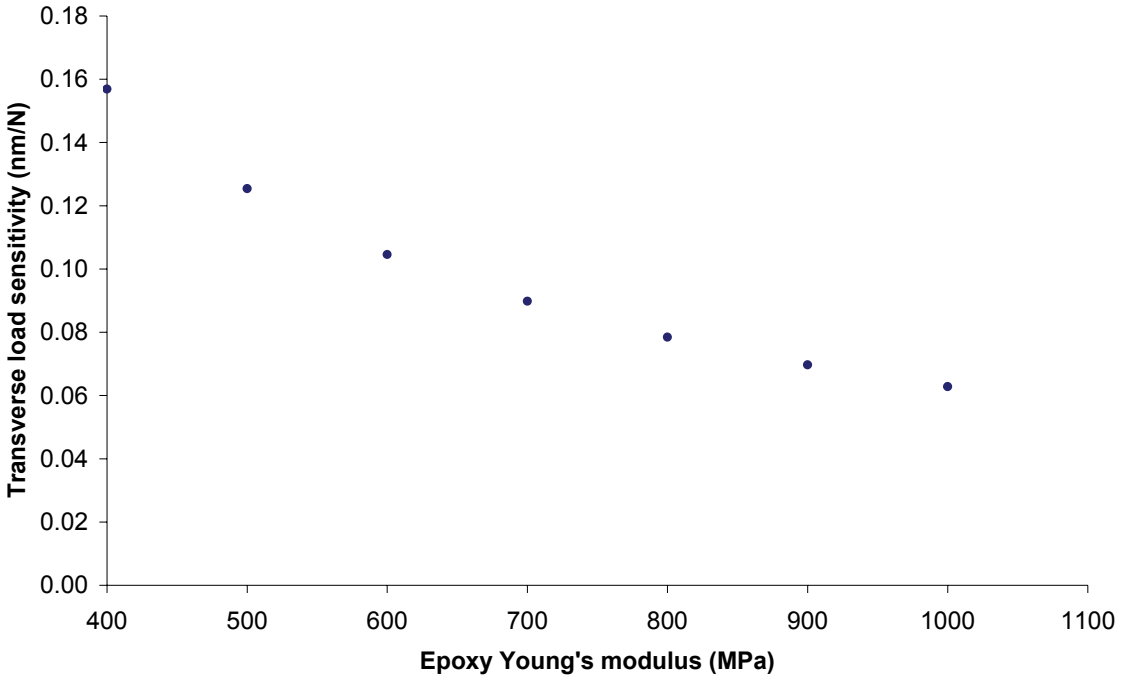

Figure 3-23: Theoretical calculated dependence of the transverse load sensitivity of a 6 mm long FBG embedded in a 2 mm epoxy cube with the epoxy Young's modulus.

3.6 Summary

In Section 3.4.1 it was shown that when a fixed transverse load was applied along a 1 mm section across different positions of the FBG a well defined spectral drop-out was obtained when the load was located at the centre of the FBG. When the load was applied at other positions the spectral drop-out was not very deep and resolvable. This shows that the most effective place to transversely load the FBG is at its centre.

Following the results from Section 3.4.1, a study of the effect of applying a transverse load at the centre of the FBG along different lengths was undertaken in Section 3.4.2. The results obtained shown that when the load is applied to 16.7% of the FBG length a spectral drop-out tracks across the bandwidth of the FBG in response to applied load. When the spectral drop-out reached the red side of the FBG bandwidth a new spectral drop-out started to appear from the blue side of the spectrum a new cycle started. It was

noticed that for the different spectral drop-out cycles the Bragg envelope remained at the same wavelength. When the load was applied over 50 % of the FBG length it was observed that a spectral drop-out was also created but when the first spectral drop-out was positioned at half the bandwidth of the FBG a new spectral drop-out had started already to form from the blue side of the spectrum. It was also observed that after the first spectral drop-out cycle a secondary peak separated from the main Bragg peak and that it suffered a red shift as the load was further increased. A load applied over 83.3% of the FBG length showed that no spectral drop out is formed within the bandwidth of the FBG reflection spectrum and that a red shift of the Bragg envelope is obtained. This study shows that the transverse load of less than 16.7% of the length of the FBG is desirable as it is possible to measure the applied load by tracking the position of the spectral drop-out while the Bragg envelope stay at the same wavelength position and no secondary peaks are observed. This offers the possibility to allocate a higher number of sensors over a specific spectrum range.

Section 3.4.3 showed the effect of applying a transverse load across (<20 %) at the centre of different FBG lengths. The sensitivity increases with the decrease of FBG length. That is due to the fact that a π phase shift of the spectral drop-out on a short FBG corresponds to a higher wavelength shift of the spectral drop-out because the bandwidth of a short FBG is higher than the one of a long FBG. Therefore it was concluded that an FBG with small length is desirable for the development of the pressure sensor.

In Section 3.4.4 the effect of apply a load across the entire length of the FBG apart from a central section showed that a spectral drop out is formed within the bandwidth of the reflection FBG spectrum and that it tracks to the blue side of the spectrum while the Bragg envelope suffers a red shift. Similar to the load of a long length of an FBG this technique is not desirable to the development of a pressure sensor.

A study of the effect of applying an axial strain to a small section of an FBG was carried to investigate if a spectral drop-out was formed within the bandwidth of the FBG. To transfer a load applied perpendicular to the fibre into an axial strain, the FBG is embedded in an epoxy cube with Young's modulus lower than the one from the fibre. When a transverse load is applied to the epoxy cube its deformation along the longitudinal direction of the fibre induces an axial strain over the embedded fibre length. Rouard's method was used to simulate the spectral behaviour of the reflection spectrum of the FBG subject to localised axial strain.

In Section 3.5.1 the effect of applying an axial strain at different positions along the FBG length and the results obtained showed that a deep and well resolvable spectral drop-out is formed within the bandwidth of the FBG when the strain is applied at the centre of the FBG. When the position of the epoxy cube moves away from the centre the spectral drop-out is not deep and not visible when the cube is localised at the extremes of the FBG. This shown that the most effective place to apply an axial strain to the FBG is at its centre and that localised axial stretching of an FBG follows the same behaviour observed for the localised transverse load of an FBG. The effect of the applying the localised axial stretching at the centre of the FBG over different lengths (Section 3.5.2) showed the same spectral behaviour as the transverse load of a central section presented of an FBG in Section 3.4.2. It was concluded that as in the transverse load of a central section of an FBG the axial stretching of (<20 %) of a central section of an FBG is more suitable for the development of a pressure sensor.

The transverse load and stretching of a central section of an FBG show good potential for the development of a pressure sensor based on the local perturbation of a short section of an FBG (<20%) of its length.

References

Benham, P. P., Crawford, R. J. and Armstrong, C. G.:1996. Mechanics of Engineering Materials. 2nd Ediction, Longman (London)

Chehura, E., James, S. W., and Tatam, R. P.:2005. Rouard's method as a modelling tool for the sensing characteristics of complex fibre Fabry-Perot interferometers formed between chirped fibre Bragg Gratings. *Proceedings of SPIE* **5855** (338-341)

Chehura, E.:2002. In-Line Fibre-Optic Laser Doppler Velocimeter using Bragg Grating Interferometric Filters as Frequency to Intensity Transducers (unpublished PhD thesis), Cranfield University, Cranfield

Erdogan, T.:1997. Fiber Grating Spectra. *IEEE Journal of Lightwave Technology*. 15(8), p. 1279

Gafsi, R. and El-Sherif, M. A.:2000. Analysis of induced-birefringence effects on fiber Bragg gratings. *Optical Fiber Technology*. **6** (299-323)

Kashyap, R.:1999. Fiber Bragg Gratings. Academic Press (London)

Kogelnik, H.:1990. *Theory of optical waveguides in Guided-Wave Optoelectronics*. T. Tamir, New York Cited in: Erdogan, T.:1997. Fiber Grating Spectra. *IEEE Journal of Lightwave Technology*. 15(8), p. 1279

Mastro, S. A.:2005. Optomechanical Behavior of Embedded Fiber Bragg Grating Strain Sensor (Unpublished PhD thesis), Drexel University, Philadelphia

Michaille, L., Mccall, M. W., Lai, Y. C., and Williams, J. A. R.:2003. Analysis of single and multiple, non-permanent, tunable, birefringent spectral holes in a fibre-Bragg grating stop-band produced via uniaxial pressure. *Optics Communications*. **222** (1-8)

Prabhugoud, M. and Peters, K.:2004. Modified Transfer Matrix Formulation for Bragg Grating Strain Sensors. *Journal of Lightwave Technology*. **22**(10) (2302-2309)

Othonos, A. and Kalli, K.:1999. Fiber Bragg Gratings: Fundaments and Applications in Telecommunications and Sensing. Artech House

Peters, K., Studer, M., Botsis, J., Locco, A., Limberger, H. and Salathe, R.:2001. Embedded Optical Fiber Bragg Grating Sensor in a Nonuniform Strain Field: Measurements and Simulations. *Experimental Mechanics*. **41** (19-28)

Torres, P. and Valente, L. C. G.:2002. Spectral response of locally pressed fiber Bragg grating. *Optics Communications*. **208** (285-291)

Wagreich, R. B., Atia, W. A., Singh, H. and Sirkis, J. S.:1996 Effects of diametric load on fibre Bragg gratings fabricated in low birefringent fibre. *Ellectronics letters*. **32** (1223-1224)

Weller-Brophy, L. A. and Hall, D. G.:1985. Analysis of waveguide gratings: application of Rouard's method. Journal of the Optical Society of America A. **2** (863-871)

Yariv, A.:1973. Coupled-mode theory for guided-wave optics. *IEEE Journal of Quantum Electronics*, (9), p. 919-933. Cited in: Erdogan, T.:1997. Fiber Grating Spectra. *IEEE Journal of Lightwave Technology*. **15**(8), p. 1279

Zhao J.:2001. An Object-oriented Simulation Program for Fibre Bragg Gratings (unpublished MSc thesis), Rand Afrikaans University, Johannesburg

Yamada, M and Sakuda, K.:1987. Analysis of almost-periodic distributed feedback slab waveguide via a fundamental matrix approach. *Applied Optics* **26** (3474-3478)

Chapter 4

Experimental analysis of fibre Bragg gratings under partial transverse load

4.1 Introduction

As described and simulated in Chapter 3, when an FBG is subject to a transverse load along a central sub-section, the resulting refractive index increase in the loaded region leads to a local change of the Bragg wavelength. The net effect is that an optical cavity is created between the two unloaded sections of the original FBG, creating a spectral drop-out within the Bragg spectrum that tracks across the spectrum in response to changes in the applied load. To study this effect a transverse loading fixture and fibre loading and support structures were designed to allow a transverse load to be applied along the central sub-section of an FBG. In this chapter an experimental study of the effect of transversely loading an FBG along a sub-section located at its centre is presented.

In Section 4.2, the instrumentation used in this study is presented. In Section 4.3 the spectral characteristics of partially transverse loaded FBGs recorded in SM fibre are experimentally investigated. Two different loading techniques are reported; the loading of a sub-section located at the centre of the FBG (Section 4.3.1), and the loading of a sub-section that is half of the length of the FBG (Section 4.3.3). A technique that allows the independent and simultaneous measurement of temperature and pressure is presented in Section 4.3.2. Section 4.4.1 shows the effect of partial transverse loading of FBGs written in Polarisation Maintaining (PM) optical fibre.

4.2 Instrumentation design

In order to measure the wavelength shift of the FBG spectral drop-out caused by a change in load, it is necessary to implement an interrogation system that continuously interrogates the FBG reflection spectrum (Wippich and Dessau, 2003). The chosen interrogation system should provide reproducible measurement of the wavelength shift in the form of an electrical signal with high sensitivity to Bragg wavelength shifts and with a large measurement range (Santos and Ferreira, 2002).

The FBG interrogation systems chosen for the present work uses a tunable laser as the optical source. Separate systems were used for the FBGs fabricated in SM fibre and for the FBGs written in PM fibre which are shown in Figure 4-1 and Figure 4-2, respectively. The SM FBG interrogation system consists of the tunable external cavity laser, an SM fibre directional coupler, a loading fixture, a photo-detector and a data acquisition card. For the PM FBG interrogation system the same tunable laser, acquisition card, loading fixture and two photo-detectors were used and a PM fibre coupler and polarisation fibre splitter were employed.

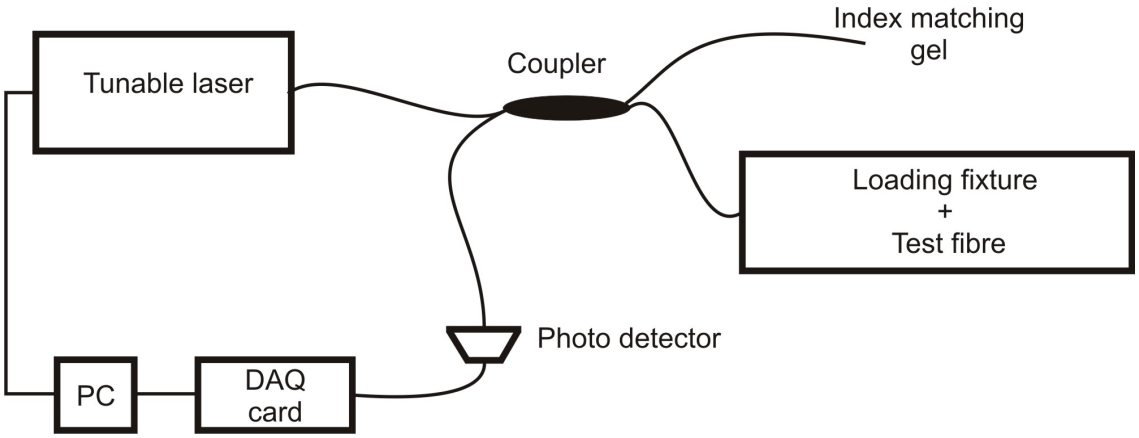

Figure 4-1: Schematic diagram of the SM FBG interrogation system

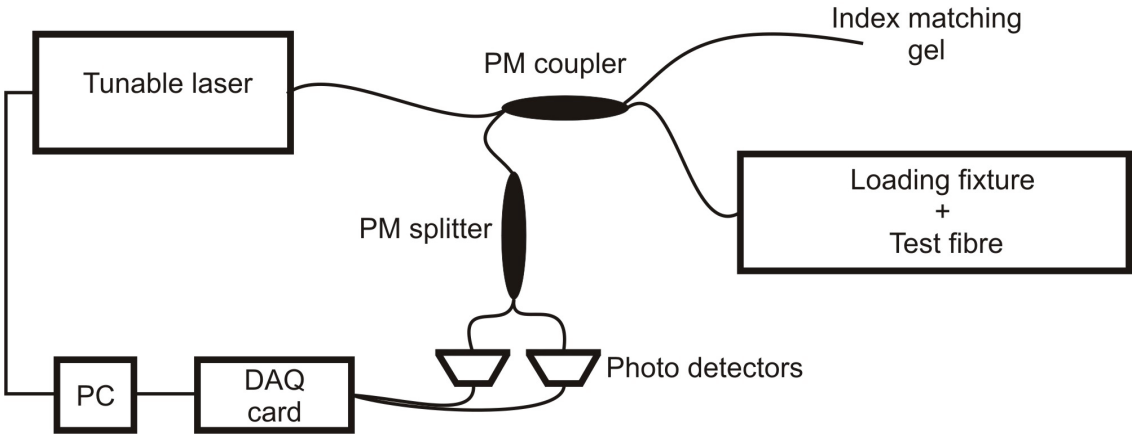

Figure 4-2: Schematic diagram of the PM FBG interrogation system

4.2.1 Optical fibre transverse loading fixture

The loading fixture (Figure 4-3) was designed to minimise fibre twist, keeping the load applied always over the same fibre direction and has previously been used to characterise the transverse load sensitivity of FBGs written in PM fibre (Ye *et al.*, 2002). The loading fixture consists of a polished glass plate glued to the bottom surface of the loading fixture and a parallel glass plate that vertically moves along two guiding columns. Load was applied at the top plate by placing calibrated weights on a cantilever arm system. As the load applied to the plate depends of the position of the weights on the cantilever arm, it was possible to increase or decrease the applied load range and load increments.

A Fibre Loading and Support Structure (FLSS) was designed to apply a localised load onto a sub-section of an FBG (Figure 4-3). This FLSS consists of two machined stainless steel blocks, each with three raised contacts. The central contact was used to apply the localised load into the FBG and the other two were used for balancing. The FBG was placed between the two FLSSs and a dummy fibre was placed parallel to the first fibre to balance the system. The centre of the FBG was then positioned perpendicularly to the central FLSS contact. In this configuration, the load applied to the FLSS was distributed along six contact points with the fibres.

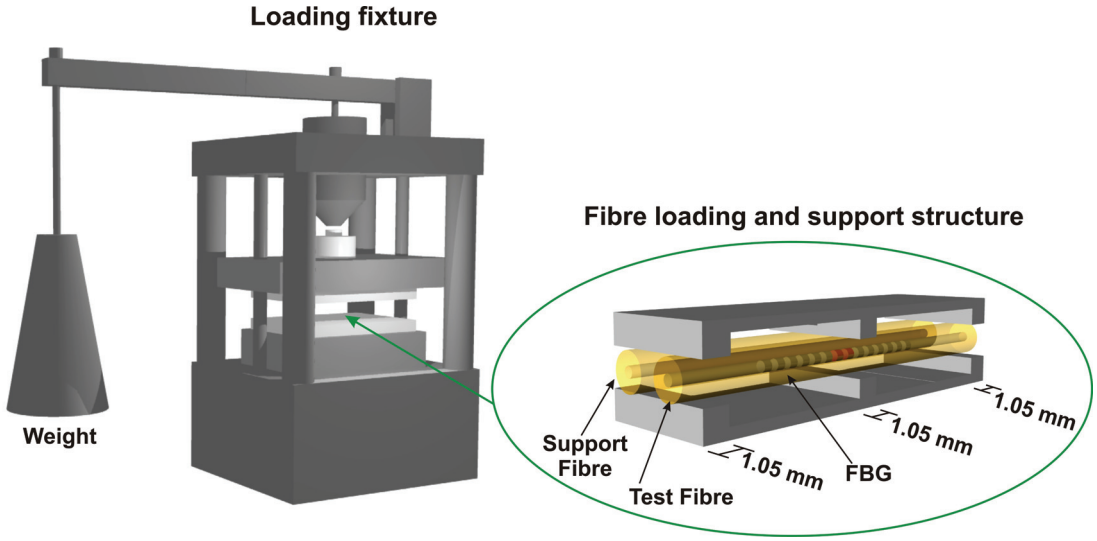

Figure 4-3: Diagram of the loading fixture and fibre loading and support structure used to apply a transverse load to the central section of the FBG.

4.2.2 Tunable external cavity laser source

Tunable External Cavity Lasers (TECL) typically use a diffraction grating as the wavelength-selective element in the external resonator (Liu and Zhang, 2007). The tunable external cavity laser employed in this work was a TUNICS-Plus CL that uses a modified Littman-Metcalf configuration where the first-order reflection from the diffraction grating is incident on a dihedral reflector. The dihedral reflector directs the optical feedback back into the laser diode via a second reflection from the diffraction grating. The tuning of the external-cavity diode laser is accomplished by varying the angle of the dihedral reflector, allowing the feedback of a different spectral component into the laser diode.

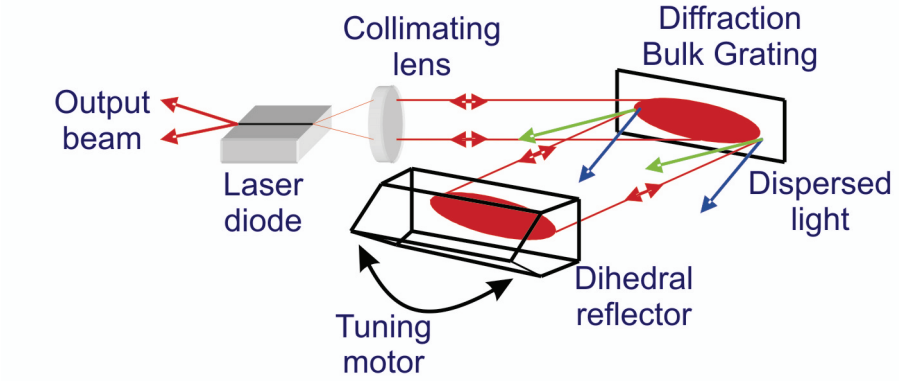

Figure 4-4: Diagram of the Littman-Metcalf configuration used in the external cavity TECL Tunics-Plus CL (Shing, 2004).

The tunable external cavity laser used provides a smooth, mode-hop free scan over a spectral range of up to 150 nm, with a tuning speed of 100 nm/s and resolution of up to 1 pm. Alternatively, the tunable laser can also be step scanned with step sizes of up to 1 pm and time intervals of 0.1 to 25 seconds per step. The source permits high resolution spectral analysis over a range of 1500 nm to 1640 nm and provides a maximum power output of 20 mW. The wavelength jitter is < 3 pm and its linewidth is better than 150kHz.

4.3 Fibre Bragg gratings recorded in single mode optical fibre

The experimental arrangement used is presented in Figure 4-1. The wavelength range of interest was step scanned with a resolution of 3 pm and a 0.1s time interval per step using the tuneable external cavity laser (TUNICS-Plus CL) coupled with the 3dB SM fibre coupler. The test fibre containing the FBG was attached to one output arm of the SM fibre coupler while the end of the other output port was immersed in a refractive index matching gel to prevent unwanted reflections. The reflected signal from the FBG was detected by a high speed low noise wide band amplified Indium gallium arsenide (InGaAs) PIN photodiode PDA-400-EC from Thorlabs. A 16 bit resolution, 250 kS/s DAQ card NI-6221 was used to acquire the signal to the computer. The FBG was placed between the two FLSSs and its centre positioned perpendicular to the central contact point. A support fibre was placed parallel to the test fibre. The FBG was located by coupling the output from a He-Ne laser (632.8 nm) into the fibre, and observing the scattering from the FBG (Maier et al., 2002). The FBGs used in this study were

fabricated in-house by Dr. Edmon Chehura using an injection seeded frequency-quadrupled Nd:YAG laser operating at a wavelength of 266 nm with a two beam interferometer technique (Figure 4-5).

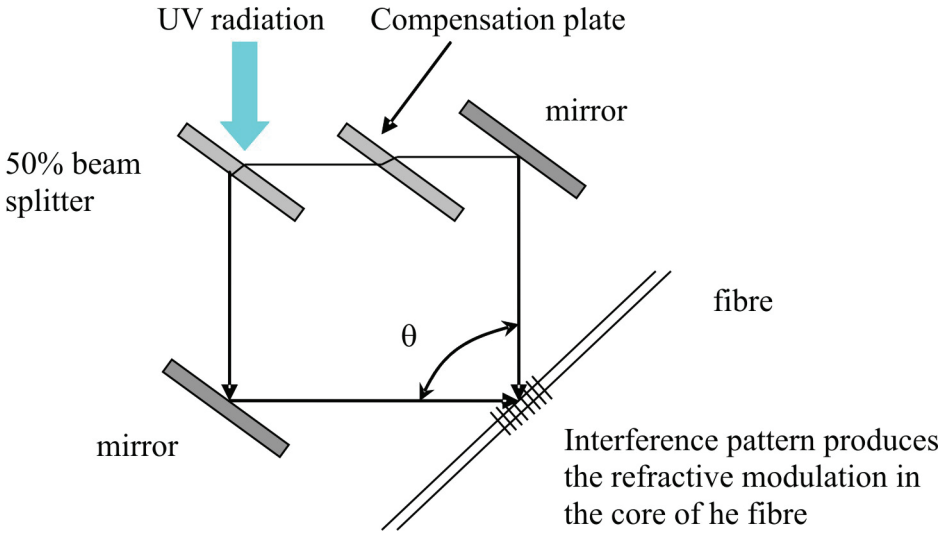

Figure 4-5: Two beam transverse interferometer (Shing, 2004).

4.3.1 Transverse load of a central sub-section of a fibre Bragg grating

In this experiment, a 6 mm long FBG with centre wavelength 1547 nm was written in SM optical fibre (Fibercore PS1250) and was subject to transverse load at a constant room temperature of 21ºC using the FLSS presented in Figure 4-6. Different weights were placed on the cantilever arm until a force of 140 N produced a measurable change on the FBG reflection spectrum.

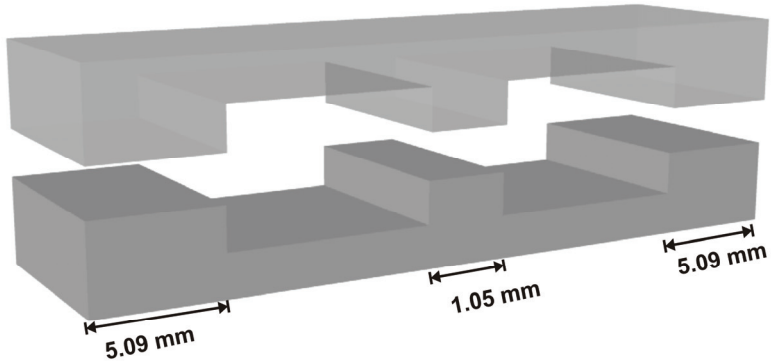

Figure 4-6: Fibre loading and support structure with two 5 mm and one 1 mm contact points.

Figure 4-7 shows the response of the spectrum of the FBG to the applied load. It was observed that, as the load applied to the FBG was increased, a spectral drop-out appeared at the blue side of the spectrum, tracking across the bandwidth of the Bragg spectrum, towards the red end of the spectrum. When the spectral drop-out reached the red end of the Bragg spectrum, further increase in the load applied to the FBG (293 N) led to the formation of a new spectral drop-out at the blue end of the spectrum, and a new cycle was initiated. The experimental results are consistent with the theoretical prediction detailed in Section 3.2.

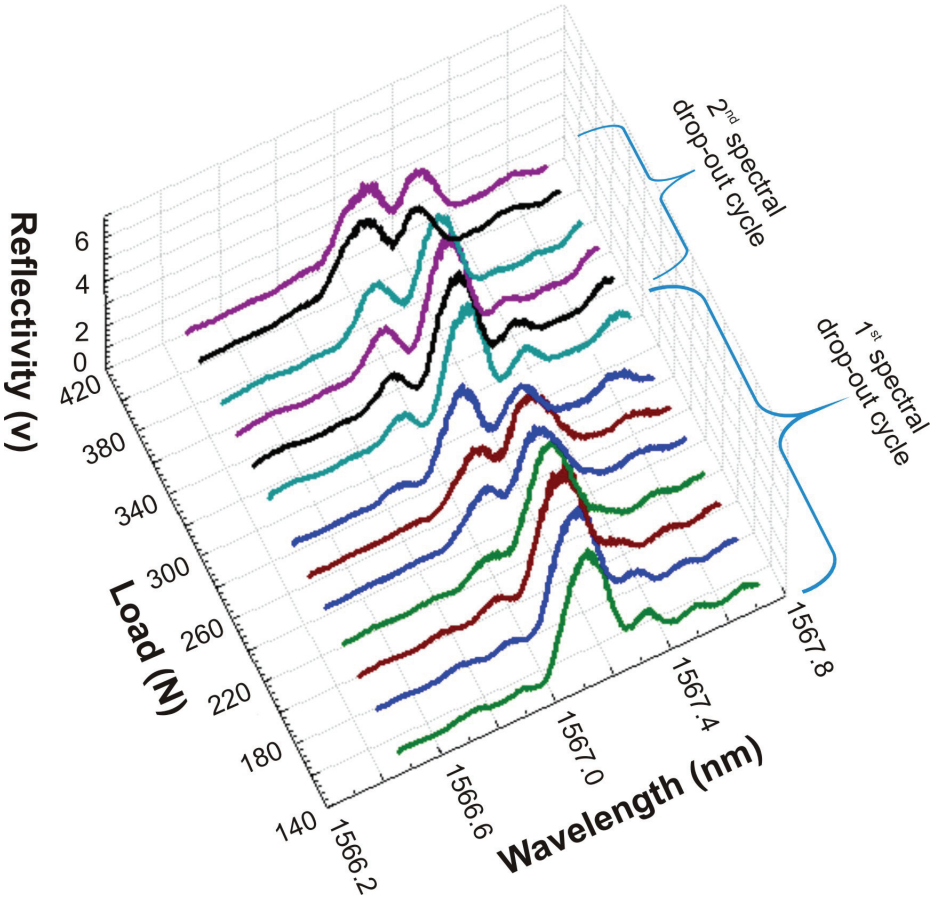

Figure 4-7: Experimentally determined evolution of the reflection spectrum from a 6 mm long SM FBG subject to a local transverse load applied along a 1.05mm length, located at its centre with the 5.09 mm support contacts FLSS. Different colours are used to help visualisation.

Figure 4-8 shows the dependence of the central wavelength of the spectral drop-out on the applied load for two spectral drop-out cycles. The central wavelength of the spectral drop-out was found by finding the zero of a second order polynomial function fitted to the spectrum acquired data correspondent to the location of the spectral drop-out. The wavelength response of the spectral drop-out to the applied load exhibits good linearity for both cycles. The sensitivity achieved in terms of wavelength shift per applied force was $1.69\pm0.1\text{x}10^{-3}$ nm/N and $1.99\pm0.12\text{x}10^{-3}$ nm/N for the first and second spectral drop-out cycles respectively.

Assuming that the applied load has been uniformly distributed over the 21.17x18.97 mm^2 area of the FLSS and that the entire load was transmitted to the fibre, the corresponding pressure sensitivity was 0.68±0.04 nm/MPa and 0.79±0.05 nm/MPa for the first and second spectral drop-out cycles respectively.

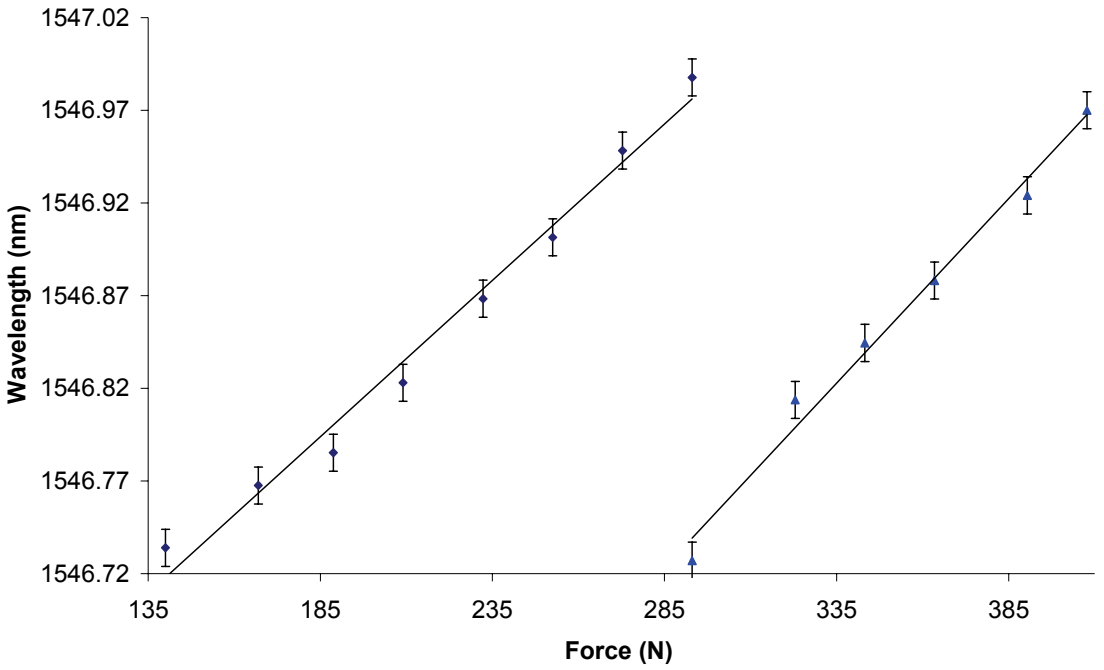

Figure 4-8: Dependence of the central wavelength of the spectral drop-out on the applied load of a 6 mm long SM FBG subject to a local transverse load applied along a 1.05mm length, located at its centre with the 5.09 mm support contacts FLSS.

The load necessary to cause a measurable change in the Bragg spectrum was 140 N which limits the minimum measurable load. This happens because only 4.45% of the load applied to the FLSS was transmitted to the centre of the FBG. The remaining

95.55% of the load was distributed over the two supports of the FLSS. To overcome this limitation, a new FLSS presented in Figure 4-9 was designed. This new FLSS consists of three 1.05 mm raised contacts. As the length of the support contacts was reduced from 5.09 mm to 1.05mm the load transmitted to the FBG increased from 4.45% to 16.67% of the total applied load. A 6 mm long FBG with centre wavelength 1547 nm was written in SM optical fibre (Fibercore PS1250) and was placed on the new FLSS which was subject to the procedure described above.

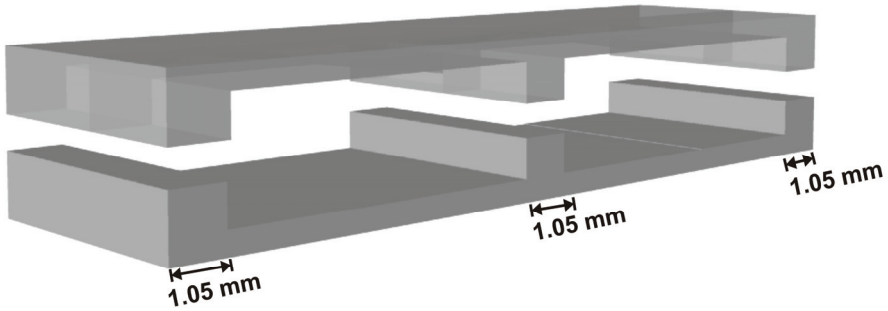

Figure 4-9: Fibre loading and support structure with three 1.05 mm contact points.

The load necessary to produce a measurable change on the FBG spectrum was 36.91 N exhibiting a reduction of the minimum detected load. It was shown on the previous experiment that the load applied to the FLSS was being distributed mainly into the two support raised areas. Figure 4-10 shows the response of the spectrum of the FBG to the applied load. Similarly to the previous experiment, it was observed that as the load applied to the FBG was increased, a spectral drop-out appeared at the blue side of the spectrum, tracking across the bandwidth of the Bragg spectrum, with the cycle repeating when the load exceeded 203.7 N.

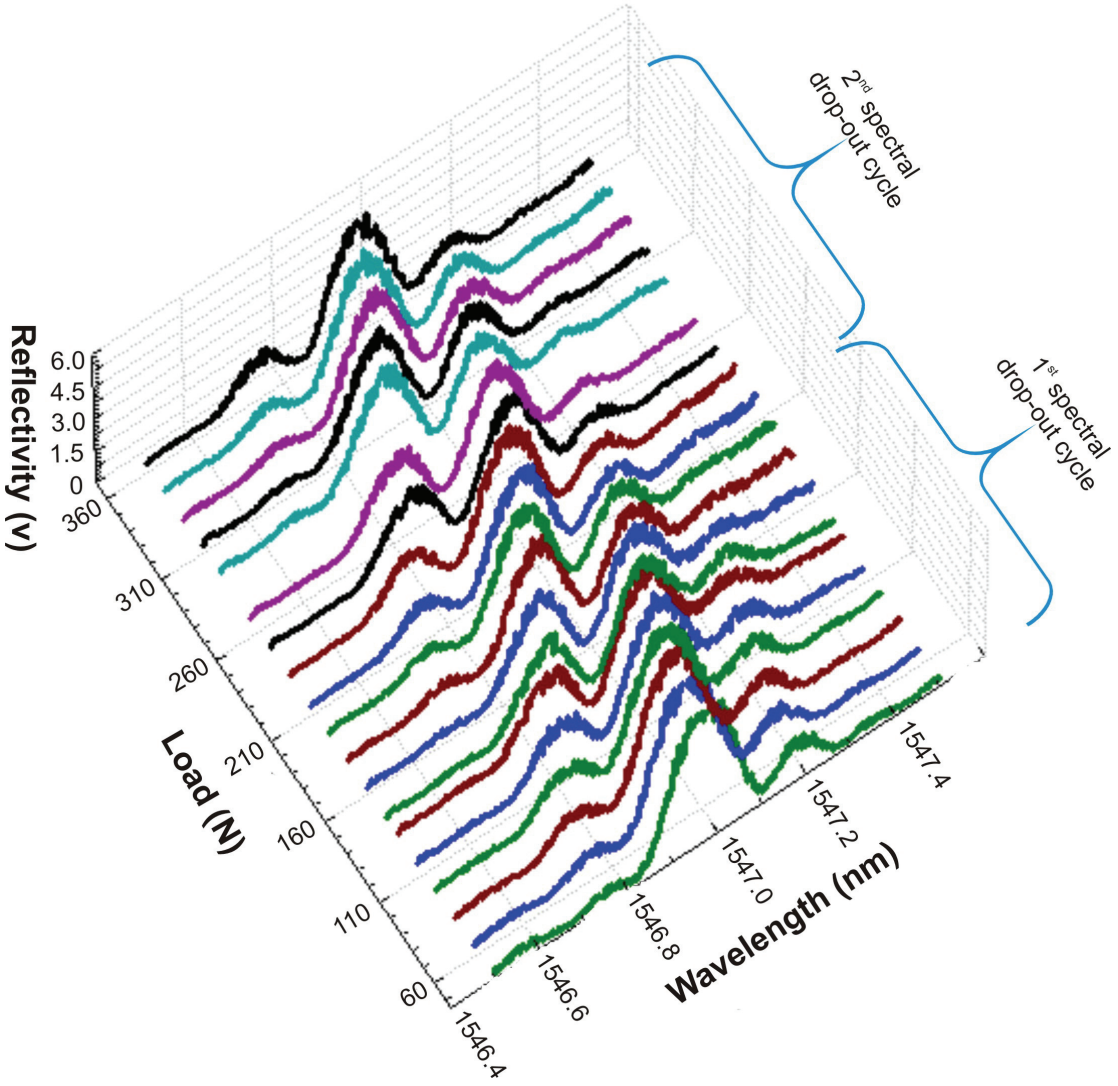

Figure 4-10: Experimentally determined evolution of the reflection spectrum from a 6 mm long SM FBG subject to a local transverse load applied along a 1.05mm length, located at its centre with the 1.05 mm support contacts FLSS. Different colours are used to help visualisation.

The dependence of the central wavelength of the spectral drop-out on the applied load for two spectral drop-out cycles is illustrated in Figure 4-11. The wavelength response of the spectral drop-out to the applied load exhibited good linearity for both cycles. The sensitivity achieved in terms of wavelength shift per applied force was $1.92\pm0.05\text{x}10^{-3}$ nm/N and $1.83\pm0.07\text{x}10^{-3}$ nm/N for the first and second spectral drop-out cycles, respectively. Pressure sensitivities of 0.77±0.02 nm/MPa and 0.74±0.03 nm/MPa for the first and second spectral drop-out cycles, respectively, were achieved for a load distributed over the 21.17x18.97 mm^2 area of the FLSS.

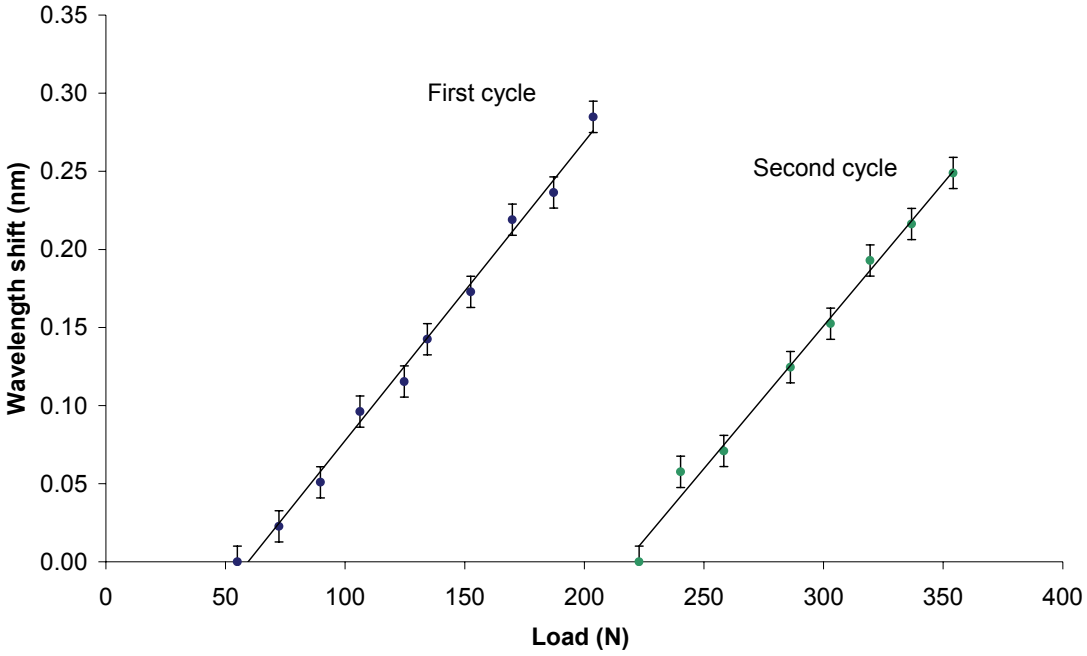

Figure 4-11: Dependence of the central wavelength of the spectral drop-out on the applied load for two spectral hole cycles of a 6 mm long SM FBG subject to a local transverse load applied along a 1.05mm length, located at its centre with the 1.05 mm support contacts FLSS.

A theoretical simulation of the spectral behaviour of a 6 mm FBG with central wavelength 1547.05 nm subject to transverse load along a 1 mm section of its centre was undertaken using the TMM presented in Section 3.4. The load applied to the FBG was assumed to be 16.67% of the load applied to the FLSS as half of the load applied to the FLSS is sustained by the support fibre while the other half is distributed over 3 equal length contacts. Figure 4-12 presents the theoretical and experimental dependence, for two spectral drop-out cycles, of the central wavelength of the spectral drop-out on the load applied to the system that consists of the test and support fibre.

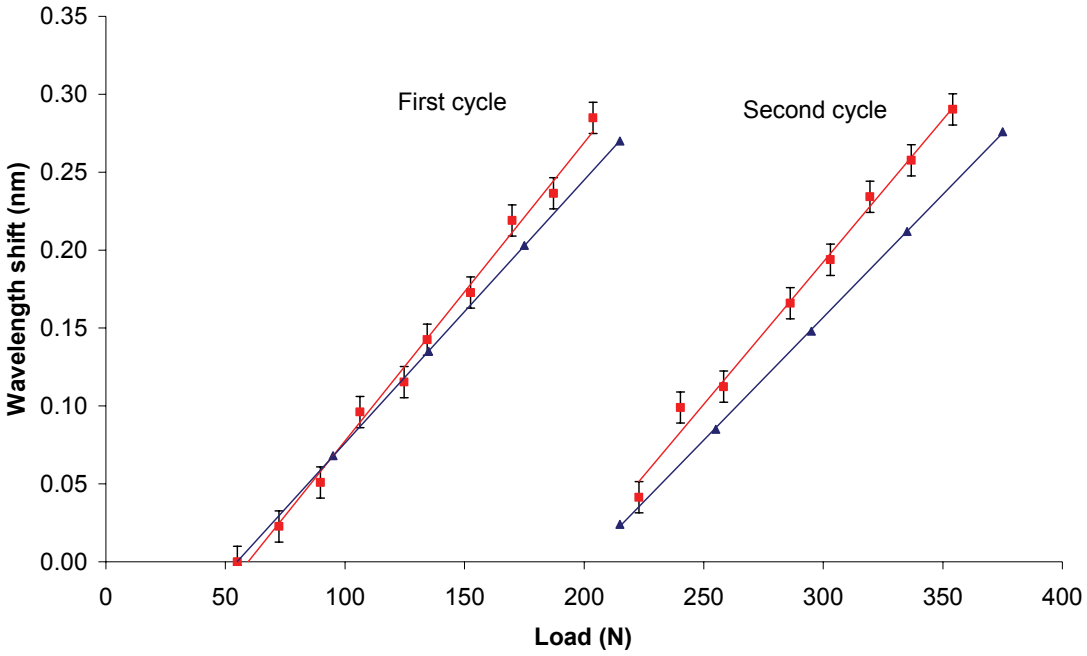

Figure 4-12: Theoretical and experimental dependence of the central wavelength of the spectral drop-out on the applied load for two spectral drop-out cycles of a 6 mm long SM FBG subject to a local transverse load applied along a 1.05mm length, located at its centre with the 1.05 mm support contacts FLSS. Blue (▲): Theoretical; Red (■): Experimental.

The theoretical and experimental dependence of the central wavelength of the spectral drop-out shown similar behaviour. The difference may be caused by the fibre Young's modulus value used in the simulation. The theoretical calculated sensitivity of the FBG to load was 1.7×10^{-3} nm/N and 1.6×10^{-3} nm/N for the first and second spectral drop-out cycles, respectively. These values are similar to the ones obtained experimentally of $1.92 \pm 0.05 \times 10^{-3}$ nm/N and $1.83 \pm 0.07 \times 10^{-3}$ nm/N.

An alternative method for demodulating this sensor at constant temperature is to monitor changes in the form of the Bragg spectrum. When a load is applied to the FBG, the Bragg spectrum appears to have two peaks located either side of the spectral drop-out (Figure 4-13). With the variation of the applied load, the relative intensities of these peaks change according to the position of the spectral drop-out within the Bragg peak. Equation (4-1) represents the normalised difference in intensity (NI)

$$NI = \frac{I_A - I_B}{I_A + I_B} \qquad \textbf{(4-1)}$$

Where I_A is the intensity of the peak A and I_B the intensity of peak B. Peaks A and B are identified in Figure 4-9.

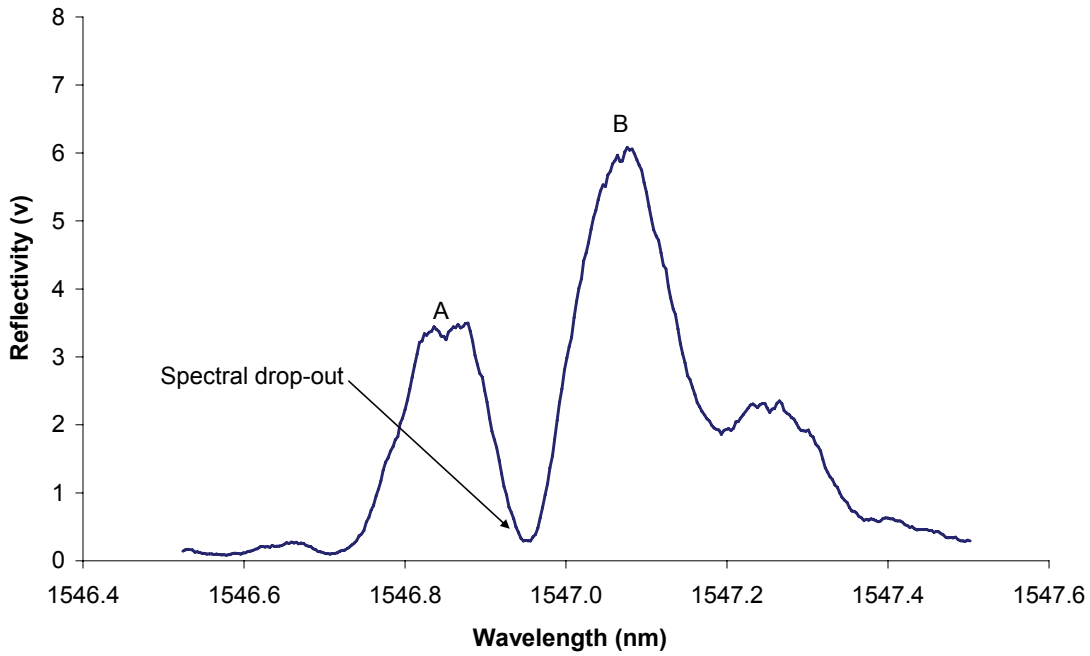

Figure 4-13: Illustration of the two peaks that lie either side of the spectral drop-out.

The results of the analysis are presented in Figure 4-14. This parameter demonstrates a linear response over the same measurement range for the two cycles. The corresponding pressure sensitivities for the two spectral drop-out cycles were 3.30±0.08 MPa^{-1} and 3.06±0.16 MPa^{-1}, respectively.

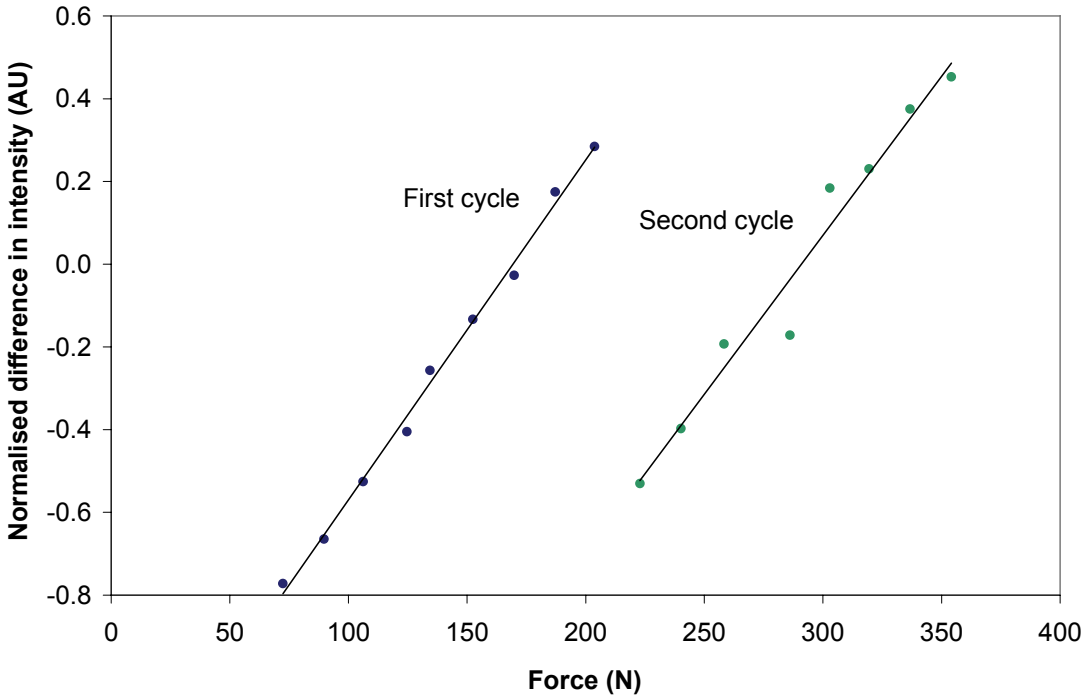

Figure 4-14: Dependence of the normalised difference in reflectivity of the two peaks that bound the spectral drop-out on the applied load of a 6 mm long SM FBG subject to a local transverse load applied along a 1.05mm length, located at its centre with the 1.05 mm support contacts FLSS.

4.3.2 Temperature-pressure cross sensitivity of a fibre Bragg grating transversely loaded along a central sub-section

The sensitivity of the Bragg wavelength to temperature and the means for separating the thermal and strain responses has been researched extensively (Frazão *et al.*, 2005). Using this concept of transversely loading the central sub-section of the FBG, it is possible to discriminate between the effects of pressure and temperature. The absolute wavelength of the spectral drop-out is influenced by both temperature and pressure. To a first order approximation, the spectral envelope of the Bragg reflection is sensitive to temperature and insensitive to the pressure applied using the configuration described here. Thus the measurement of the wavelength of the spectral drop-out relative to another feature of the Bragg spectrum is predominantly sensitive to pressure.

The absolute and relative wavelength response of the spectral drop-out to pressure and temperature were characterised. In order to achieve this, the wavelength separation

between the spectral drop-out and the left peak on its side (peak A Figure 4-13) was measured. The absolute wavelength response of the spectral drop-out to load at constant temperature was not characterised in this experiment and was assumed to be equal to the one presented in Section 4.3.1.

To characterise the thermal response of this system, the loading fixture containing a 6 mm FBG written in SM optical fibre was placed inside an oven and the temperature was varied over a 50 ºC range at a fixed applied pressure of 216 kPa. Two thermocouples were used to monitor the temperature of the fibre and of the FLSS. Figure 4-15 shows the response of the spectrum of the SM FBG to temperature when subject to a constant pressure along a central sub-section of the FBG.

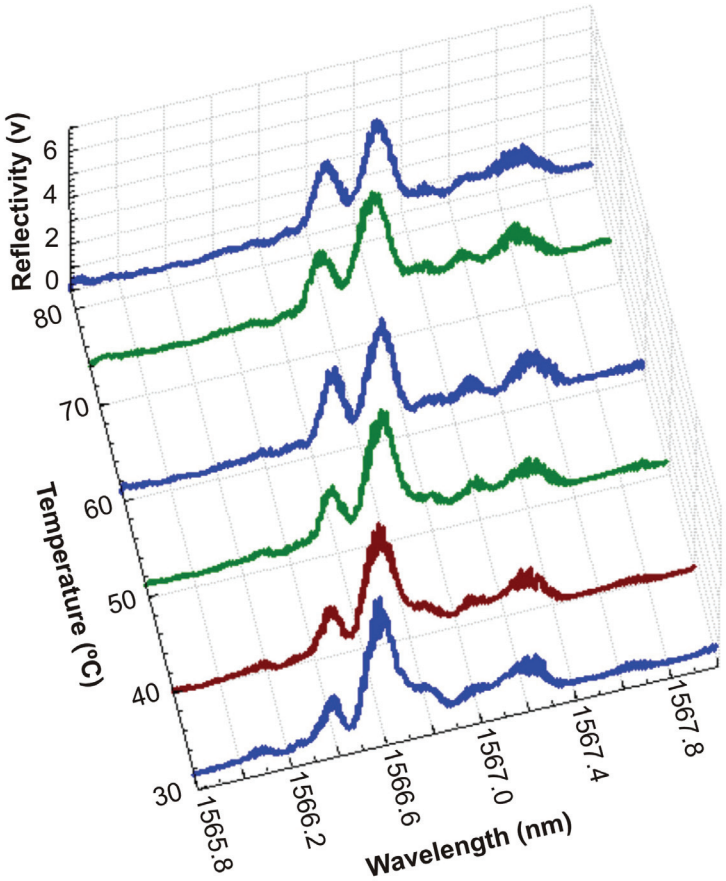

Figure 4-15: Experimentally determined evolution of the reflection spectrum from a 6 mm long SM FBG subject to a constant pressure of 216 kPa along a 1.05mm length, located at its centre with the 1.05 mm support contacts FLSS with temperature. Different colours are used to help visualisation.

With a temperature increase, the spectral envelope of the Bragg reflection spectrum shifts to higher wavelengths. This can be observed in Figure 4-16, which shows the dependence of the absolute wavelength shift of the spectral drop-out upon the temperature for a constant pressure of 216 kPa. The temperature sensitivity of the FBG was 10.1±0.35 pm/ºC measuring the absolute wavelength shift of the spectral drop-out. Figure 4-17 plots the dependence of the wavelength separation between the spectral drop-out and the lower wavelength spectral peak that borders the spectral drop-out as a function of temperature.

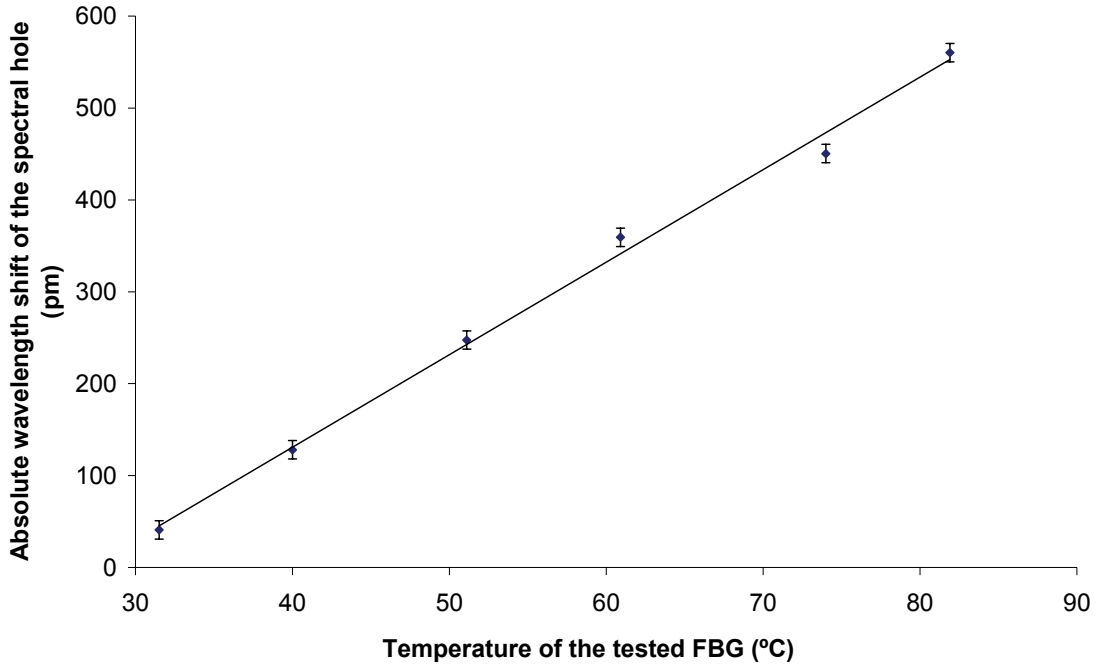

Figure 4-16: Dependence of the absolute wavelength shift of the spectral drop-out of a 6 mm long SM FBG subject to a constant pressure of 216 kPa applied along a 1.05mm length, located at its centre with the 1.05 mm support contacts FLSS as a function of temperature.

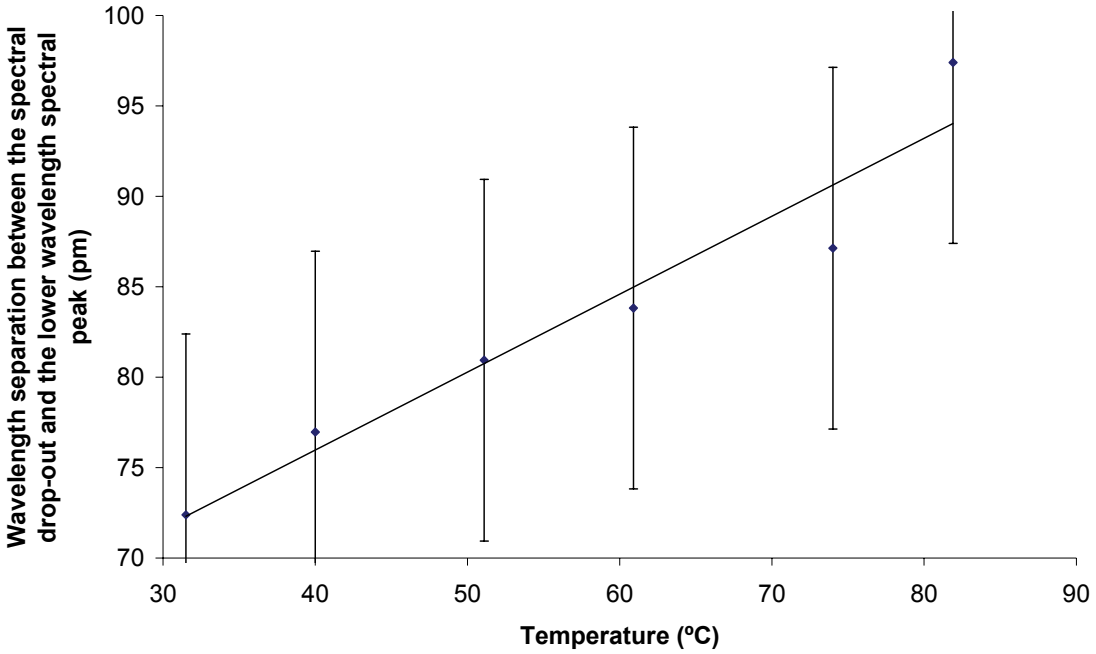

Figure 4-17: Temperature dependence of the wavelength separation between the spectral drop-out and the lower wavelength spectral peak that borders the spectral drop-out for a constant pressure of 216 kPa.

The temperature sensitivity of the FBG, measuring the relative wavelength shift of the spectral drop-out was 0.4±0.06 pm/ºC. Figure 4-17 shows that the position of the spectral drop-out within the envelope exhibits a small dependence on temperature. This may be caused by the difference between the temperatures of the loaded section of the fibre, which is in contact with the metallic FLSS, and the unloaded section of the fibre. Another possible cause is due to the thermal expansion of the FLSS. The fibre containing the FBG is anchored at three locations, and thus the unloaded sections of the FBG may experience a thermally induced axial strain, which changes the phase relationship between the two sections of the FBG.

The pressure dependence of the wavelength separation between the spectral drop-out and the lower wavelength spectral peak that borders the spectral drop-out is presented in Figure 4-18. The pressure sensitivity of the FBG measuring the relative wavelength shift of the spectral drop-out was 160±14.5 pm/MPa.

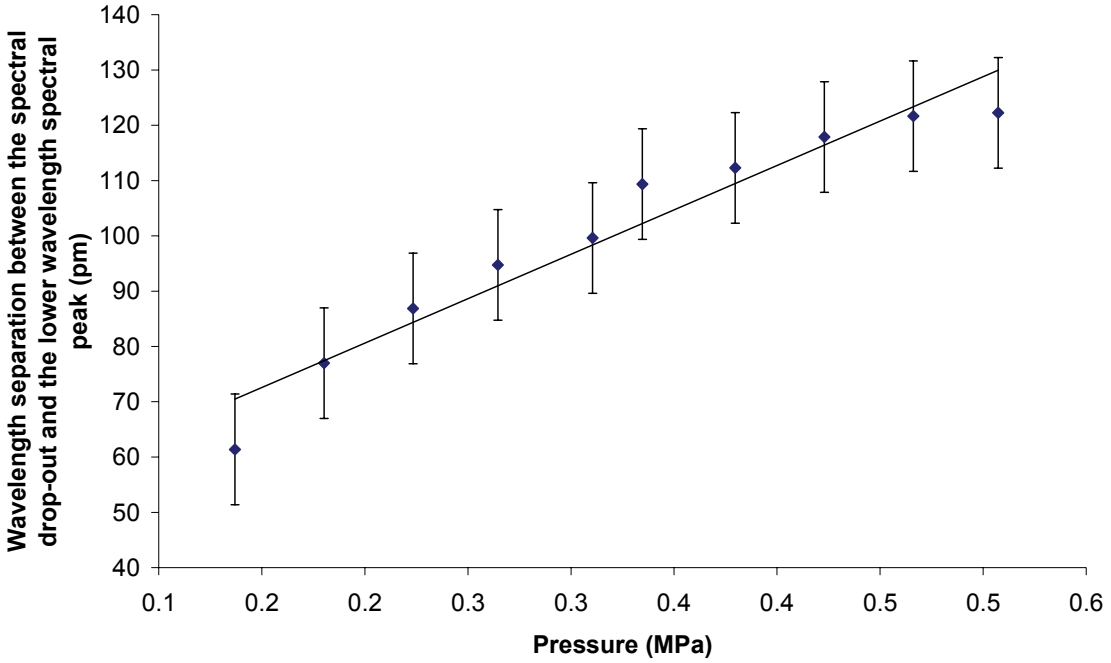

Figure 4-18: Pressure dependence of the wavelength separation between the spectral drop-out and the lower wavelength spectral peak that borders the spectral hole, measured at a constant temperature of 21ºC.

Using Equation (4-2) it is possible to separate the pressure and temperature responses of the device.

$$\begin{bmatrix} \Delta\lambda_{abso} \\ \Delta\lambda_{rel} \end{bmatrix} = \begin{bmatrix} K_{abs,P} & K_{abs,T} \\ K_{rel,P} & K_{rel,T} \end{bmatrix} \begin{bmatrix} P \\ T \end{bmatrix} \qquad \textbf{(4-2)}$$

Where $\Delta\lambda_{abs}$ and $\Delta\lambda_{rel}$ are the absolute wavelength shift of the spectral drop-out and the relative wavelength shift of the spectral drop-out. From the results presented in Figure 4-11, Figure 4-16, Figure 4-17 and Figure 4-18 we can obtain the sensitivity coefficients calculated for the absolute and relative measurements: $K_{abs},P = 769.0 \pm 21.2$ pm/MPa, $K_{abs},T = 10.1 \pm 0.35$ pm/ºC, $K_{rel},P = 160.0 \pm 14.5$ pm/MPa and $K_{rel},T = 0.4 \pm 0.06$ pm/ºC.

The temperature-pressure discrimination performance of the sensor system is presented in Table 4-1. Two types of error are presented considering (i) only wavelength measurement precision errors that are maximum accumulated errors, (ii) only matrix component errors that are maximum accumulated errors arising from the uncertainties

in the matrix element values. The error formulations used are described by Jin *et al.* (1997). Errors obtained by taking the modulus of individual terms in the error-formulae are referred to as maximum or cumulative errors as they provide the worst possible error scenario. The wavelength measurement precision used was 1 pm and the temperature and pressure measurement were assumed to vary over a range of 50 ºC and 300 kPa. The matrix inversion conditioning number (Jin *et al.*, 1997), was calculated to be 471.6 based on maximum errors in the measurement system. The calculated pressure error of ±58 kPa is significant due to relatively large errors in matrix pressure coefficients.

Table 4-1: Error analysis

	ΔT (ºC)	ΔP (kPa)
λ measurement induced errors	0.7	8
Matrix calculation induced errors	6	58

4.3.3 Fibre Bragg grating transversely loaded along half of its length

In this experiment, a 2 mm FBG with centre wavelength 1561 nm was subject to transverse load along half of its length (1 mm) as illustrated in (Figure 4-19). Load was applied to the FBG until a force of 8.92 N caused a measurable change on the FBG reflection spectrum. The maximum applied load was 111.55 N.

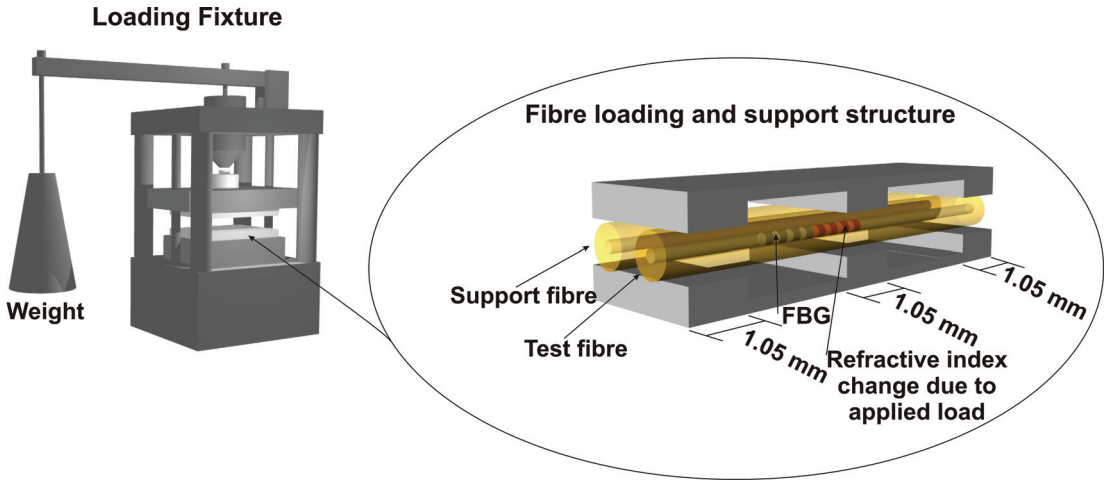

Figure 4-19: Diagram of the loading fixture and a FLSS used to apply a transverse load along half of the FBG length.

As the load increases, the spectral width of the Bragg peak broadens until two peaks can be resolved (Figure 4-20). When the load is further increased, the new Bragg peak is red-shifted and the Bragg peak that corresponds to the unloaded section of the FBG suffers a significantly smaller wavelength change. The limitation with this loading configuration is that for small loads the second Bragg peak is not resolvable and it was therefore not possible to measure the load being applied. The dependence of the wavelength separation of the central wavelength of the two peaks with the applied load is shown in Figure 4-21. A sensitivity of $2.34\pm0.04\text{x}10^{-2}$ nm/N over a measurement range of [24.77 – 111.5] N was obtained.

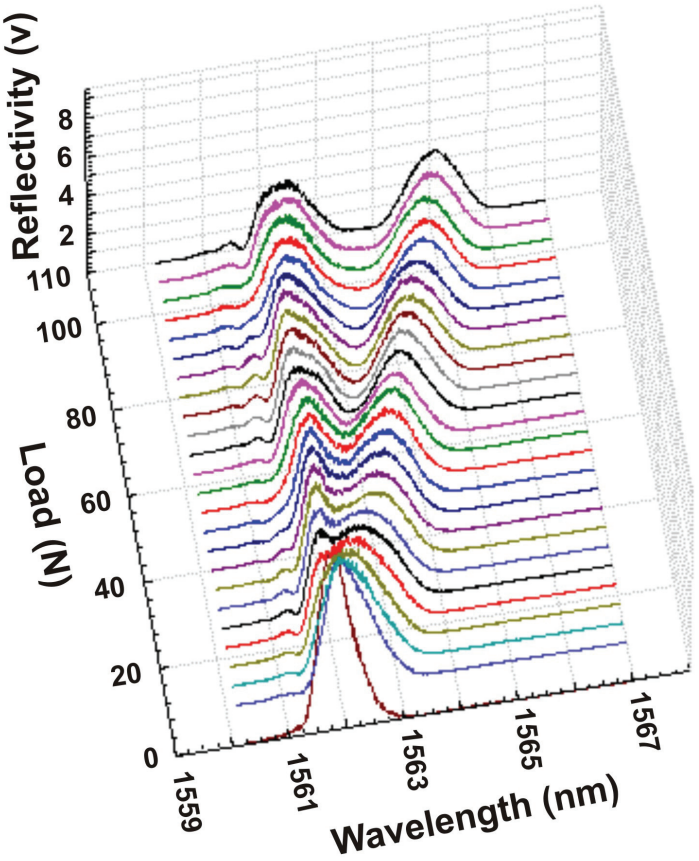

Figure 4-20: Response of the spectrum of a 2 mm long FBG to the transverse load applied to half of the FBG length. Different colours are used to help visualisation.

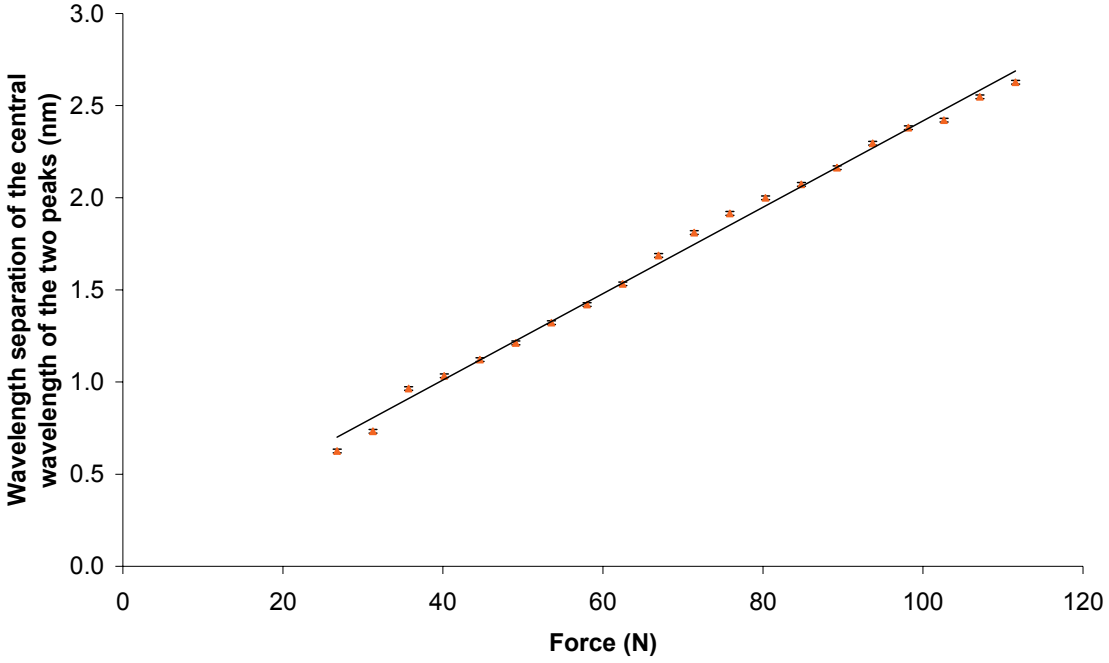

Figure 4-21: Dependence of the wavelength separation of the central wavelength of the two peaks of a 2 mm long FBG to the transverse load applied to half of the FBG length.

An alternative approach involves measuring the wavelength of the Bragg spectrum that corresponds to a specified reflectivity normalised to the reflectivity of the central wavelength of the quiescent Bragg spectrum. This is illustrated in Figure 4-22, where all wavelengths in the Bragg spectrum with a normalised reflectivity smaller than 10% are plotted.

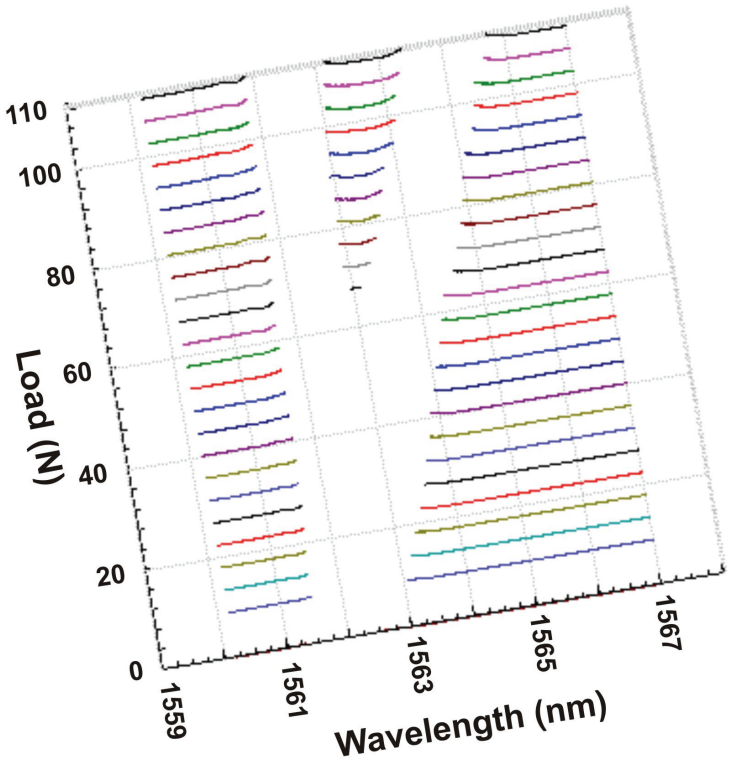

Figure 4-22: A plot showing all wavelengths having a reflectivity <10% (normalised to the reflectivity of the central wavelength of the quiescent Bragg spectrum). Different colours are used to help visualisation.

For small loads it is possible to track the wavelength separation between the blue edge of the Bragg peak corresponding to the unloaded section of the FBG and red edge of the Bragg peak that is shifting with the applied load (Figure 4-22). The dependence of the wavelength separation of the blue and red edges of the peaks for a normalised reflectivity smaller than 10% upon the applied load, is illustrated in Figure 4-23, showing good linearity.

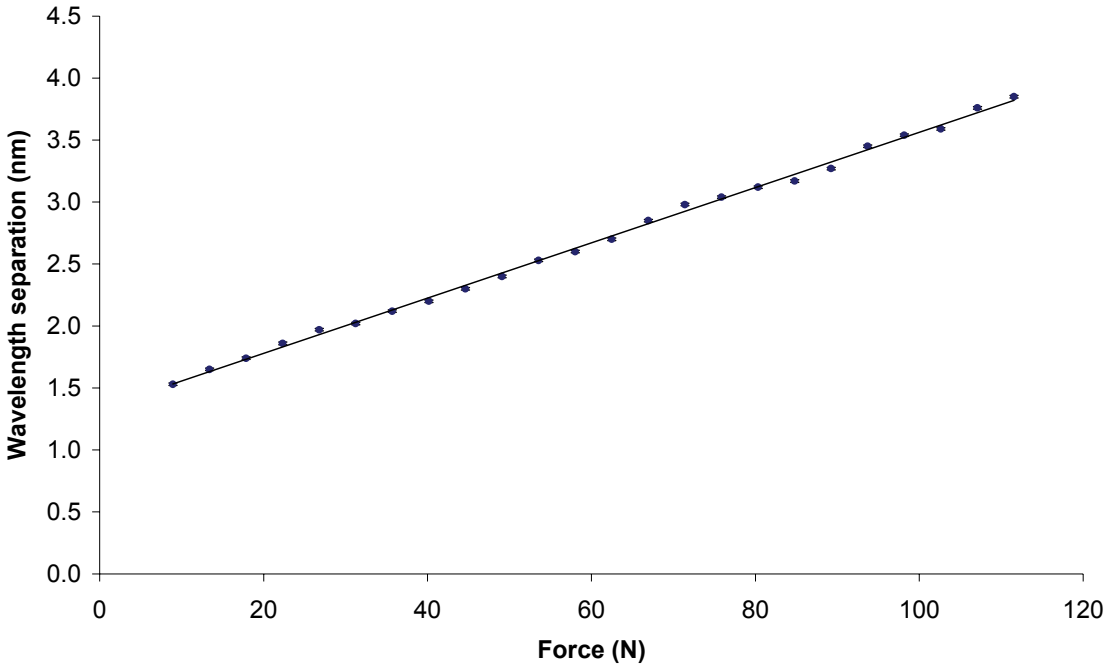

Figure 4-23: Dependence of the wavelength separation of the blue and red edges of the peaks for a reflectivity < 10%, normalised to the reflectivity of the central wavelength of the quiescent Bragg spectrum of a 2 mm long FBG to the transverse load applied to half of the FBG length.

With this technique, the measurement range was improved to [8.92 – 111.5] N with a sensitivity of $2.23\pm0.02\text{x}10^{-2}$ nm/N, allowing an improvement in the minimum detectable load. The pressure sensitivity achieved with this technique was 8.96±0.08 nm/MPa.

4.4 Fibre Bragg gratings recorded in polarisation maintaining optical fibre

The experimental arrangement used for this experiment is presented in Figure 4-2. The wavelength range of interest was step scanned with a resolution of 3 pm and a 0.1s time interval per step by using the tuneable external cavity laser (TUNICS-Plus CL) coupled to a PM fibre coupler.

The PM fibre used in this study was a Fibercore bow-tie fibre HB-1500. The cladding diameter of the fibre was 125 μm, the numerical aperture 0.17, the cut-off wavelength 1258 nm, the beat length 1.3 mm at 633 nm and the core ellipticity 1.0–1.4, as specified by the manufacturer. The FBGs were written in-house into the PM fibre by Dr. Edmon

Chehura using an injection seeded frequency-quadrupled Nd:YAG laser operating at a wavelength of 266 nm using a two beam interferometer technique (Figure 4-5) with the fibre fast axis aligned perpendicular to the laser beam.

A 3mm FBG with centre wavelength 1565.7 nm was written in PM bow-tie optical fibre (Fibercore HB1500) and attached to one output arm of the PM fibre coupler, while the end of the other output port was immersed in an index matching gel to prevent unwanted reflections. The FBG was then placed in the FLSS presented in Figure 4-6 and the optical fibre slow axis aligned perpendicularly to the FLSS though the rotation of the fibre. A support fibre was placed parallel to the test fibre to balance the loading system. The FBG reflected light from the two orthogonal linear polarisation components was recorded separately by two photo-detectors. The room temperature was kept constant at 21 ºC during the duration of the experiment.

4.4.1 Experimental results

Figure 4-24a and Figure 4-24b show the response of the slow and fast axes, respectively, of the FBG spectrum to the applied load. The slow axis FBG reflection spectrum (Figure 4-24a) showed that, as the load applied to the FBG was increased, a spectral drop-out appeared at the blue side of the spectrum (89.8 N), tracking across the FBG spectrum. When the spectral drop-out reached the red end of the Bragg spectrum, further increase in the load applied to the FBG (204 N) led to the formation of a new spectral drop-out and a new cycle initiated. For the fast axis of the FBG reflection spectrum (Figure 4-24b) it was observed that no spectral drop-out appeared during the first cycle. When the second cycle was about to start, a spectral drop-out started to appearing in the reflection spectrum of the fast axis. The spectral drop-out appeared on the fast axis possibly due to a small rotation of the fibre and consequent transfer of part of the load to the fast axis.

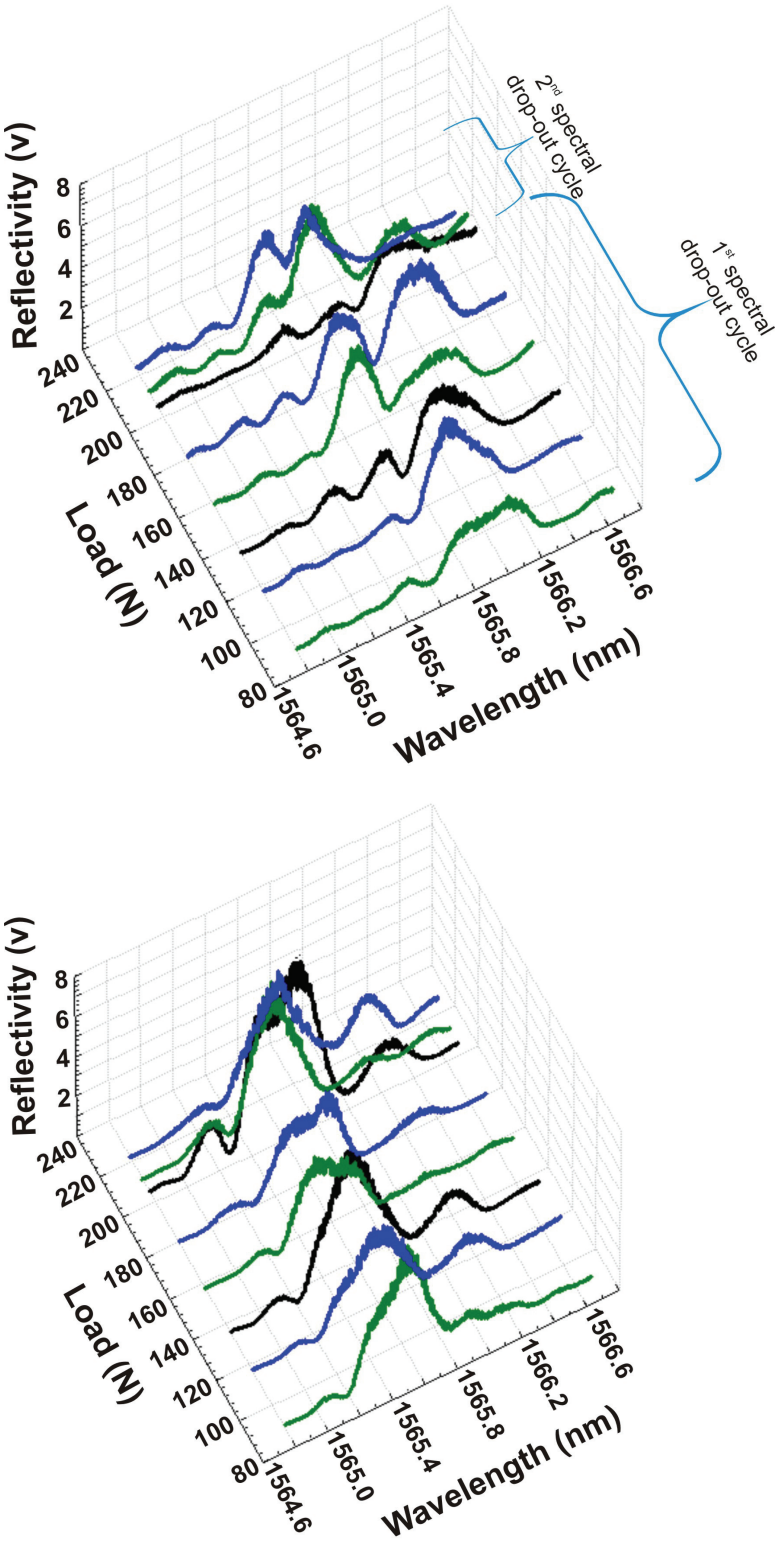

Figure 4-24: Experimentally determined evolution of the (a) slow axis and (b) fast axis reflection spectrum of a 3 mm long FBG written in PM bow-tie fibre subject to a local transverse load applied along a 1.05mm length, located at its centre with the 5.09 mm support contacts FLSS. Different colours are used to help visualisation.

The dependence of the central wavelength of the spectral drop-out on the applied load for first cycle is illustrated in Figure 4-25. The wavelength response of the spectral drop-out to the applied load exhibits good linearity. The sensitivity achieved in terms of wavelength shift per applied force was $3.4\pm0.2\text{x}10^{-3}$ nm/N for the first cycle. A pressure sensitivity of 1.38±0.08 nm/MPa for the first cycle was achieved for a load distributed over the 21.17x18.97 mm^2 area of the FLSS.

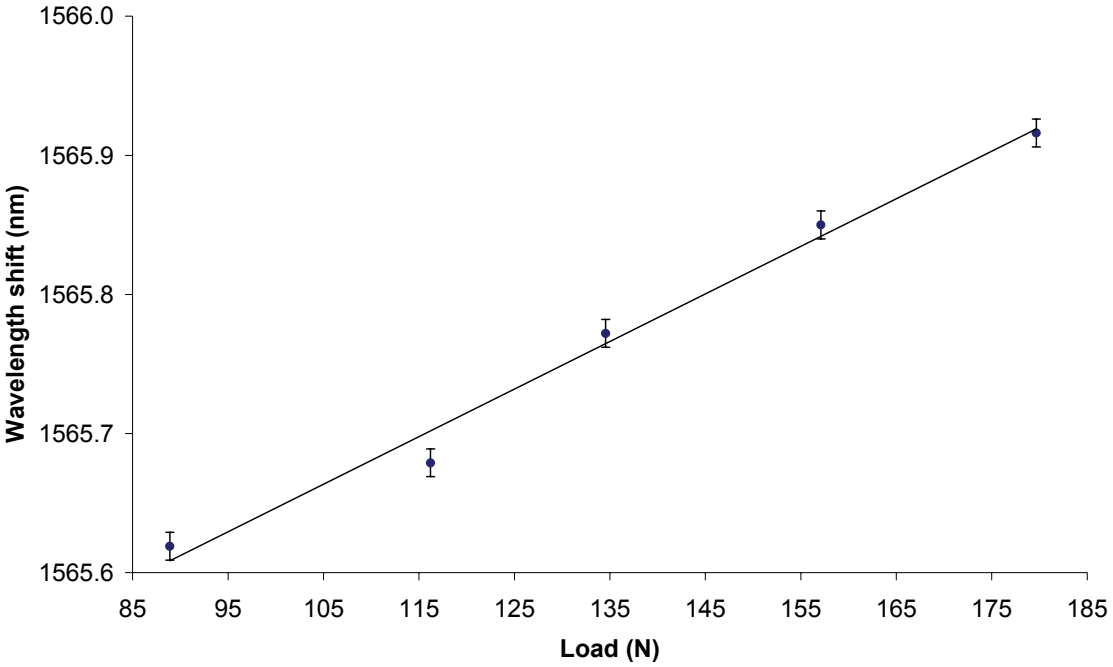

Figure 4-25: Dependence of the central wavelength of the spectral drop-out of a 3 mm long FBG written in PM bow-tie fibre subject to a local transverse load applied along a 1.05mm length, located at its centre with the 5.09 mm support contacts FLSS on the applied load (slow axis).

4.5 Summary

The experimental results achieved for the transversely loaded FBG recorded in SM optical fibre are consistent with the theoretical simulation presented in Section 3.2. A spectral drop-out was created within the bandwidth of the Bragg spectrum by transversely loading a short subsection at the centre of the FBG. The wavelength shift of the spectral drop-out in response to the applied load showed good linearity. Initial results showed that the load applied to the FBG was mainly distributed over the two

5.09 mm support contacts of the FLSS. Using a three 1.05 mm contact FLSS, the minimum detected load decreased from 140 N to 36.91 N.

Two signal processing schemes were developed for the study of FBGs subject to a transverse load along a short central section of the FBG. One based upon measuring the normalised difference in reflectivity of the two peaks that bound the spectral drop-out. The other was based on measuring the dependence of the wavelength separation between the spectral drop-out and the lower wavelength spectral peak that borders the spectral hole. This signal processing scheme offered the opportunity to independently measure pressure and temperature using a single FBG.

An FBG subject to a transverse load along half of its length was investigated and a new interrogation technique developed. This technique offered the opportunity to accurately measure changes in the Bragg spectrum of a transversely loaded low birefringence SM FBG for small loads.

The experimental results achieved for the transversely loaded FBG recorded in PM bow-tie optical fibre shown that loading the fibre along the fibre slow axis the spectral drop-out appeared on the FBG spectrum correspondent to that axis. When the second spectral drop-out appeared, a spectral drop-out appeared in the fast axis FBG spectrum. The spectral drop-out appeared on the fast axis possibly due to a small rotation of the fibre and consequent transfer of part of the load to the fast axis.

Table 4-2 presents a summary of the minimum detected load and load sensitivities obtained in the different experiments undertaken. The experimental results obtained with the 2 mm SM FBG loaded along half of its length exhibited the smallest value of detected load (8.92 N) and the highest value was obtained with the 6 mm SM FBG loaded in its centre with the 5.09 mm contact supports FLSS. The highest sensitivity to load was obtained with the 2 mm SM FBG loaded along half of its length ($3.4\pm0.2\text{x}10^{-3}$ nm/N) and the lowest with the 6 mm SM FBGs ($1.83\pm0.07\text{x}10^{-3}$ nm/N).

Table 4-2: Summary of the minimum detected load and load sensitivities obtained for the different experiments.

	Minimum detected load (N)	Sensitivity (nm/N)
6 mm SM FBG loaded in its centre with the 5.09x1.05x5.09 mm FLSS	140	1st spectral drop-out: $1.69\pm0.1\times10^{-3}$ 2nd spectral drop-out: $1.99\pm0.12\times10^{-3}$
6 mm SM FBG loaded in its centre with the 1.05x1.05x1.05 mm FLSS	36.91	1st spectral drop-out: $1.92\pm0.05\times10^{-3}$ 2nd spectral drop-out: $1.83\pm0.07\times10^{-3}$
3 mm PM FBG loaded in its centre with the 5.09x1.05x5.09 mm FLSS	89.8	1st spectral drop-out: 3.4×10^{-3}
2 mm SM FBG loaded along half of its length	8.92	$2.23\pm0.02\times10^{-2}$

The major limitation of the direct transverse load of an FBG is the inherent fragility of the optical fibre to transverse load. In all the experiments, the tested FBG broke with the applied load. Increased robustness is desirable for the development of a pressure sensor that is continuously subject to changes in pressure. Methods for protecting the optical fibre were investigated and are presented in Chapter 5.

References

Frazão, O., Ferreira, L. A., Araújo, F. M., Santos, J. L.: 2005. Applications of fiber optic grating technology to multi-parameter measurement. Fib*er and Integrated Optics* **24** (227-244)

Jin, W., Michie, W. C., Thursby, G., Konstantaki, M. and Culshaw, B.:1997. Simultaneous measurement of strain and temperature: error analysis. *Opt. Eng.* **36**(2) (598-609)

Liu, A. Q. and Zhang, X. M.:2007. A review of MEMS external-cavity tunable lasers. *Journal of Micromenchanics and Microengineering*. **17** (R1-R13)

Maier, R. J., Barton, J. and Jones, J. DC.:2002. Fibre Bragg grating location by a side scatter technique based on cladding mode coupling. *Optical Fiber Sensors Conference Technical Digest*. (99-102).

Santos, J. L and Ferreira, L. A.: 2002. Fibre Bragg Grating Interrogation Techniques *In*: Huigera, J. M. L. (ed.) *Handbook of optical fibre sensing technology*. Great Britain, Wiley: 379-403

Shing, C. S.:2004. An investigation of chirped fibre Bragg gratings Fabry-Perot for sensing applications. PhD thesis, Cranfield University, Cranfield

Wippich, M. and Dessau, K.L.:2003. Tunable Lasers and Fiber-Bragg-Gratings Sensors. *The Industrial Physicist* 24-27. USA: American Institute of Physics

Ye, C-C., Staines, S. E., James, S. W. and Tatam, R. P.:2002. A polarisation maintaining fibre Bragg grating interrogation system for multi-axis strain sensing. *Measurement Science and Technology*. **13** (1446-1449)

Chapter 5

Pressure sensitivity enhancing techniques for fibre Bragg gratings subject to transverse load

5.1 Introduction

In this chapter, techniques for enhancing the pressure sensitivity of FBGs subject to transverse loads are presented. Previously reported sensitivity enhancing techniques are reviewed and the technique chosen for this study is presented in Section 5.2. This involves embedding a subsection of the FBG within an epoxy resin block. Section 5.3.1 presents the technique used to embed the FBG within the epoxy block and Section 5.3.2 presents the experimental results when the sensor was subject to transverse load. In Section 0 a study of the effect of axially compressing the epoxy block along the direction of the fibre was undertaken. A study of transverse loading an embedded subsection of an FBG written in PM fibre was undertaken and the experimental results obtained are presented in Section 5.3.4.

In the techniques discussed thus far, the spectral drop out is not present in the Bragg spectrum unless there is a transverse load applied to a subsection of the FBG. In Section 5.4, methods for generating a spectral drop-out within the Bragg spectrum for zero load are investigated and the response of the structure to transverse load characterised. The first consisted of pre-loading an FBG embedded in 2 mm of composite material around its centre, with the experimental results presented in section 5.4.1. The second experiment was based on embedding a pre-strained FBG in 2 mm of epoxy around its centre with the experimental results presented in section 5.4.2.

5.2 Transverse load sensitivity enhancing techniques of fibre Bragg gratings

As discussed in chapter 1, the sensitivity of bare optical fibre to transverse load is low. Transducing the transverse load into an axial strain, it is possible to enhance the transverse load sensitivity, as the sensitivity of an FBG to axial strain is considerably larger than that to transverse strain. A method for enhancing the transverse load sensitivity of an FBG, which also provides protection of the optical fibre from mechanical damage, is to embed the FBG in a polymer coating (Zhang *et al.*, 2001; Sheng *et al.*, 2004; Liu *et al.*, 2000; Suresh and Tjin, 2005; Hao *et al.*, 2003). In these previously reported experiments, the FBG was completely embedded in a polymer coating and transverse load (or pressure) was then applied to the polymer. As the polymer deformed with the applied load, it transferred the applied transverse load into an axial strain that changed the period along the entire length of the FBG, leading to a wavelength shift of the Bragg peak. This transfer of transverse load into axial strain increases the measured transverse load sensitivity. Hao *et al.* (2003) reported the embedding of an FBG in a carbon fibre reinforced laminated composite material with the carbon fibres orientated 90° relative to the axis of the optical fibre, which caused splitting of the Bragg peak in the FBG reflection spectrum. This was due to the reinforced fibres compressive forces that acted on the FBG inducing birefringence, resulting in the two reflected wavelength peaks visible in the reflection spectrum.

In the study reported in this Chapter, epoxy coating and carbon fibre reinforced laminated composite coating techniques were used in combination with the loading technique presented in Section 4. In the epoxy coating technique, the central section of an FBG was embedded within a block of epoxy (Figure 5-1). When a transverse load is applied to the epoxy, the latter deforms and transfers the load to the optical fibre in the form of an axial strain that changes the period of the FBG over the epoxy-embedded region. This introduces a phase shift between the two resulting identical gratings that lie either side of the loaded section creating a spectral drop-out within the bandwidth of the FBG as simulated in Section 3.5.

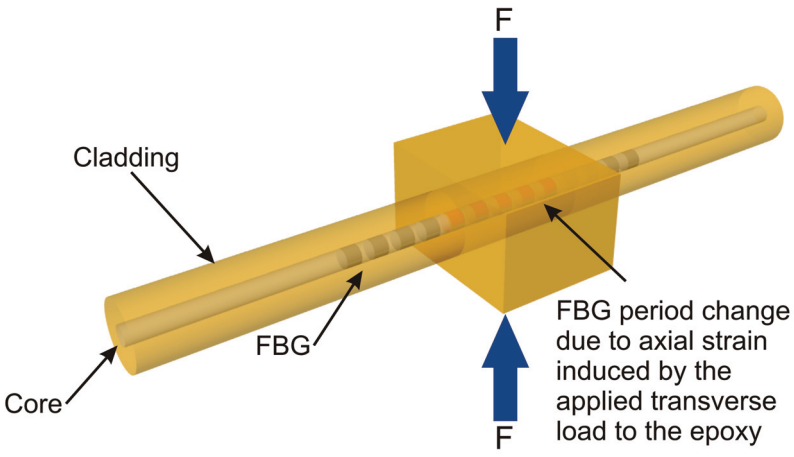

Figure 5-1: Schematic of an FBG embedded within epoxy material. F: force.

In the carbon fibre reinforced laminated composite embedding technique, the central section of the FBG was embedded between layers of composite material with the carbon fibres orientated at 90° relative to the axis of the optical fibre containing the FBG (Figure 5-2). When a transverse load is exerted on the composite material, the carbon reinforcing fibres apply compressive forces to the embedded section of the FBG, inducing birefringence over that region. This creates a phase shift between the two resulting gratings and induces a spectral drop-out in its reflection spectrum.

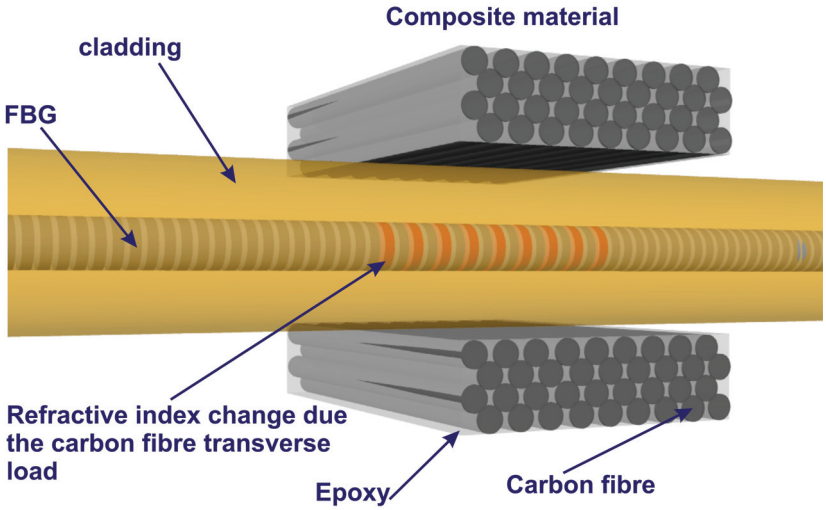

Figure 5-2: Schematic of the central section of an FBG embedded in a fibre reinforced composite material.

5.3 Epoxy partially embedded fibre Bragg gratings

The experimental arrangement used to interrogate the FBGs written in SM optical fibre was presented in chapter 4, Figure 4-1. In these experiments, the test fibre containing the epoxy cube block around its centre and a dummy support fibre containing two identical resin blocks (used for balancing) were placed parallel to each other on the loading fixture bottom glass plate, with the epoxy blocks forming a triangle as illustrated in Figure 5-3.

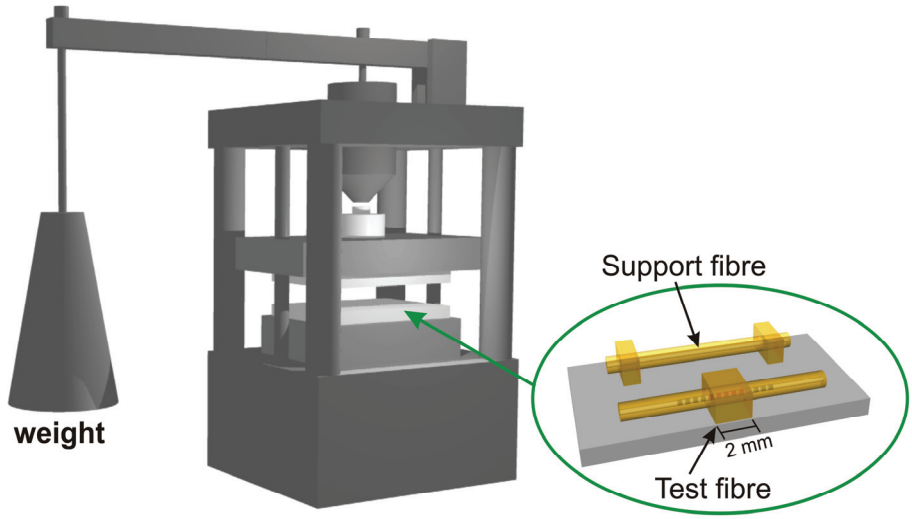

Figure 5-3: Loading fixture and test fibre embedded an epoxy block.

5.3.1 Fibre Bragg grating epoxy embedding technique

The epoxy used in this study was EpoTek OG134. This is a flexible, UV cured epoxy with low index of refraction that can operate between -50 to 150 °C. Prior to curing it has a refractive index of 1.4163 measured at 589 nm. The Young's modulus of the epoxy after curing is, according to the manufacturer, approximately 689 MPa with a Poisson's ratio of 0.4. A flexible epoxy was chosen allowing the transfer of transverse load into the axial axis of the fibre. In order to embed the fibre within an epoxy cube, a poly(tetrafluoroethylene) (PTFE) mould shown in Figure 5-4 was designed and manufactured. PTFE is a synthetic fluoropolymer which finds numerous industrial applications mainly due to its non-adhesion and non-reactive properties. The non-adhesion property was the main reason for its selection as a mould because after curing the epoxy resin, it is necessary to be able to remove the epoxy cube easily.

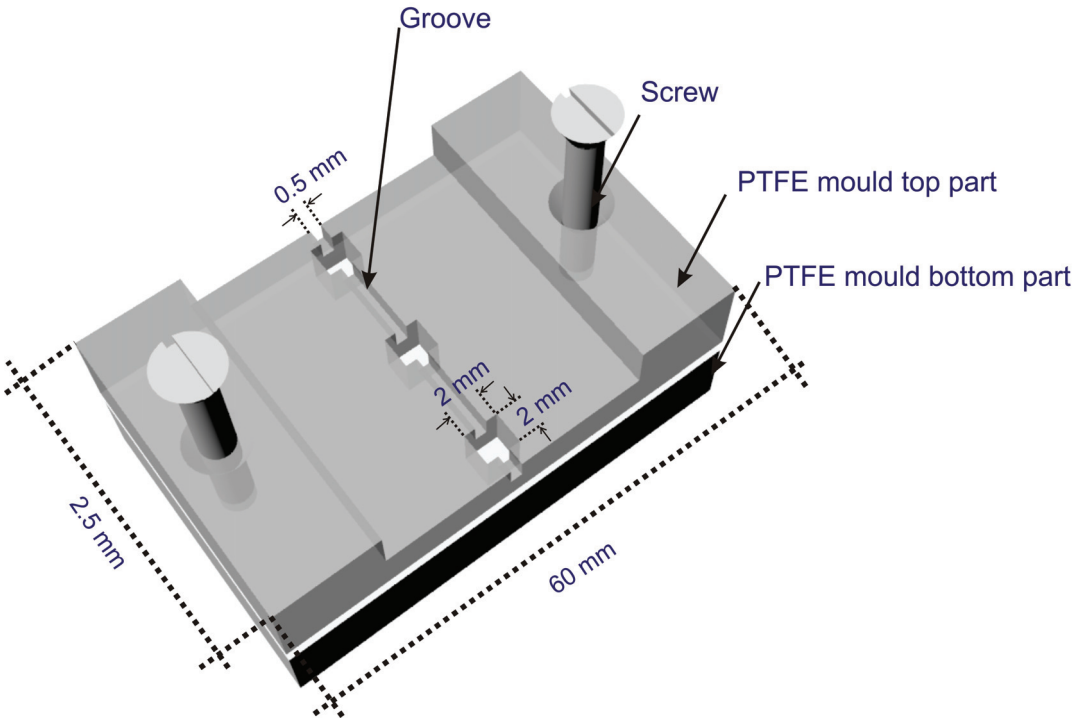

Figure 5-4: Schematic of the Poly(tetrafluoroethylene) (PTFE) epoxy mould.

The physical location of the FBG on the fibre was determined by coupling the output from a He-Ne laser (632.8 nm) into the fibre, and observing the scattering from the FBG (Maier *et al.*, 2002). The edges of the FBG were marked with a permanent marker. To embed the central part of the FBG in the epoxy the fibre was placed in the mould groove with its centre positioned within the 2 mm height, of the 2mm height, 4 mm length and 3 mm depth cuboid hole.

As the epoxy used has very low viscosity (100 cPs at 23ºC), the parts of the FBG placed in the groove were protected by placing a rubber seal embedded in silicon grease into the grooves. The epoxy was then poured into the cubic hole and cured over a period of 1.5 hours using a 4 W, 365 nm UV lamp source. Figure 5-5 shows a photograph of the curing experimental setup. Once the curing process has finished, the light was switched off. After waiting for 30 minutes for it to cool down, the top of the epoxy cube was polished flat and was then removed from the mould.

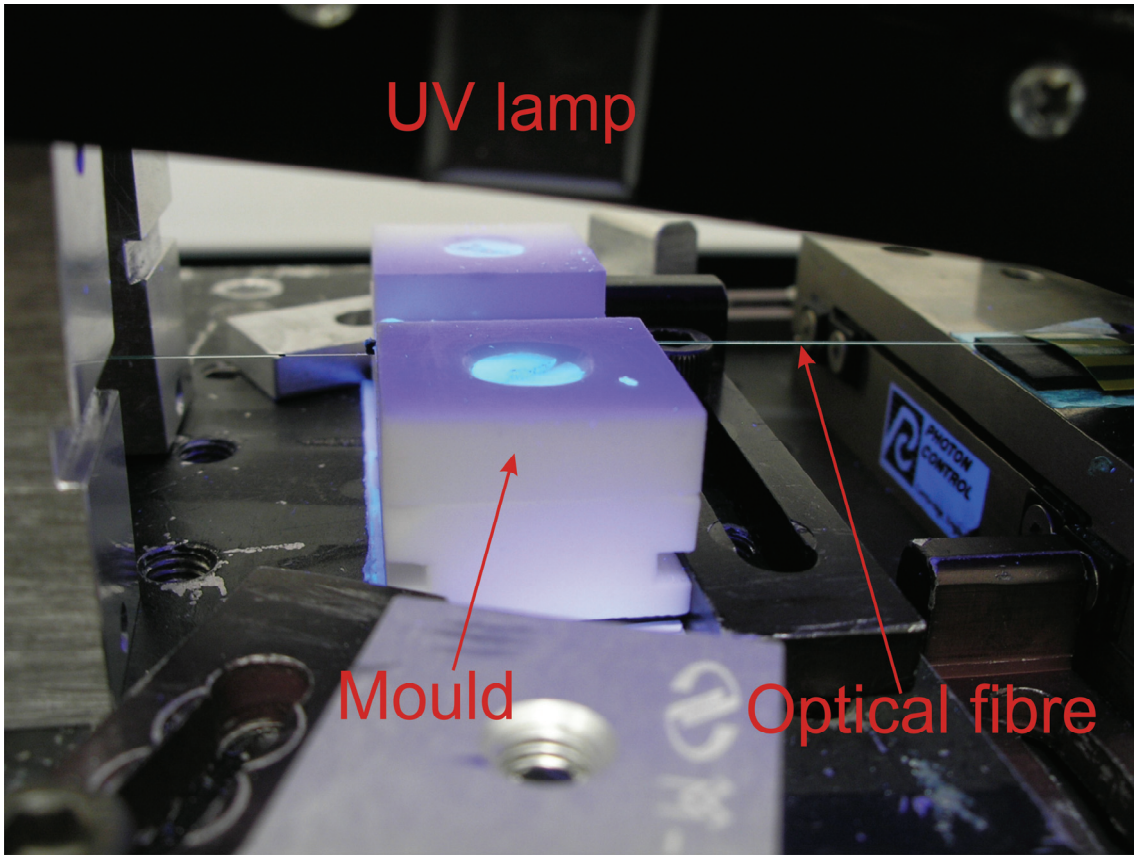

Figure 5-5: Photograph of the epoxy block curing experimental setup.

5.3.2 Transverse load of a single mode fibre Bragg grating embedded in 2 mm of epoxy

The transverse load response of an FBG of length 6 mm and centre wavelength 1566.7 nm with its central section embedded in an epoxy cuboid was analysed. The FBG was written in photosensitive SM optical fibre (Fibercore PS1250). In this experiment the FBG was embedded in a 2 mm width by 4 mm length by 3 mm depth cuboid (Figure 5-6) as described in Section 5.2. A dummy support fibre containing two identical resin blocks was also fabricated. These were placed in the loading fixture as described in Section 5.3 and were subject to a gradual increase in transverse load by placing calibrated weights onto the loading fixture cantilever arm, up to a maximum load of 89 N. The experimental results are presented in Figure 5-7. As the load increased, the spectral drop-out appeared and tracked across the bandwidth of the Bragg spectrum with a new spectral drop-out cycle repeated for a load of 44.6 N. No peak splitting or birefringence related effects were observed.

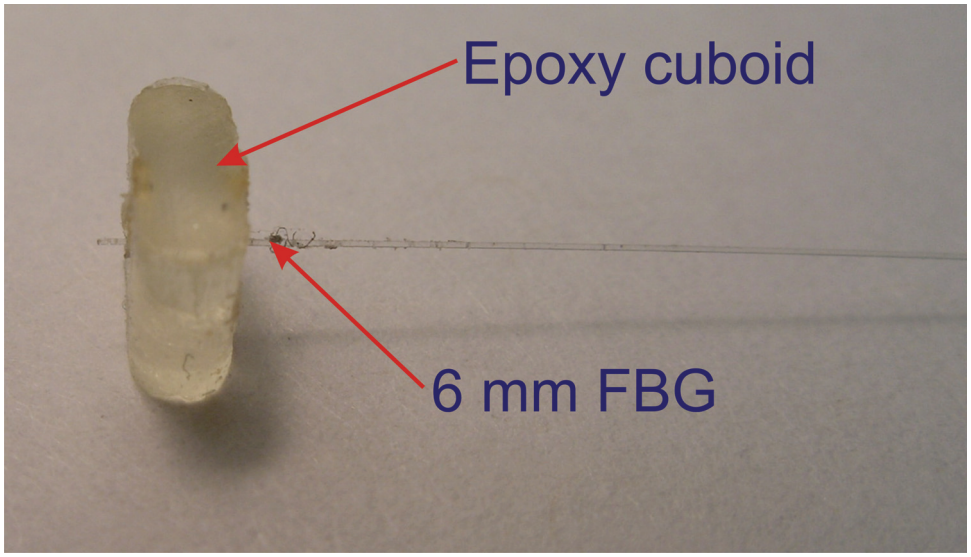

Figure 5-6: Photograph of a 6mm FBG embedded in a 2 mm width by 4 mm length by 3 mm depth epoxy cuboid.

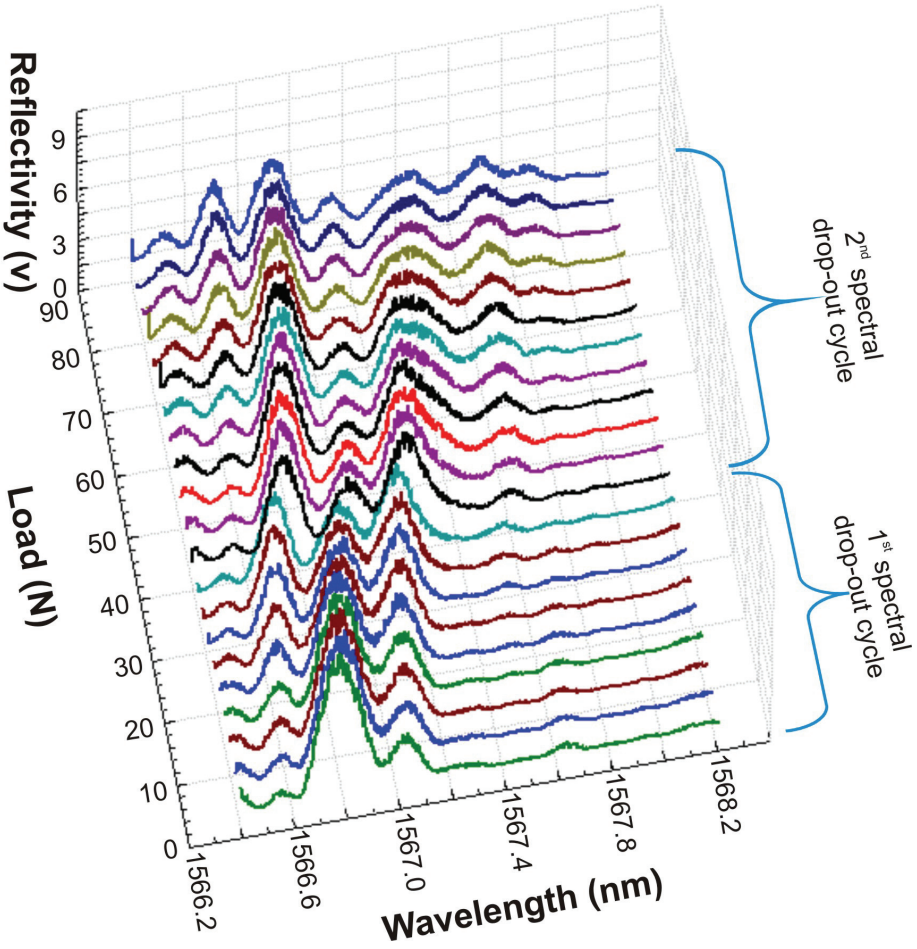

Figure 5-7: Experimentally determined evolution of the reflection spectrum from a 6 mm long SM FBG embedded with epoxy along 2 mm of its centre, with the applied transverse load.

The dependence of the central wavelength of the spectral drop-out on the applied load for two spectral drop-out cycles is illustrated in Figure 5-8. The wavelength response of the spectral drop-out to the applied load exhibited good linearity for both cycles. The sensitivity achieved in terms of wavelength shift per applied force was $5.74\pm0.08\text{x}10^{-3}$ nm/N and $3.87\pm0.04\text{x}10^{-3}$ nm/N for the first and second spectral drop-out cycles respectively. The different sensitivities obtained for each spectral drop-out cycle are attributed to the non-symmetric deformation of the epoxy cuboid that starts bending for the load correspondent to the beginning of the second spectral drop-out cycle (Figure 5-9).

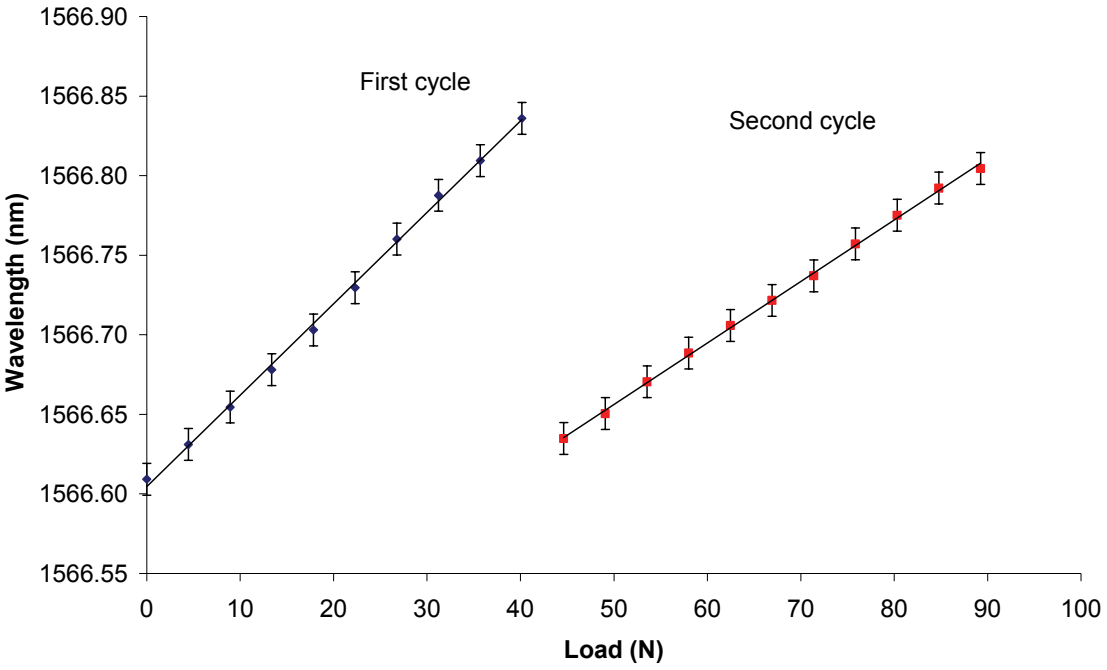

Figure 5-8: Dependence of the central wavelength of the spectral drop-out of a 6 mm long SM FBG embedded with epoxy along 2 mm of its centre on the applied transverse load.

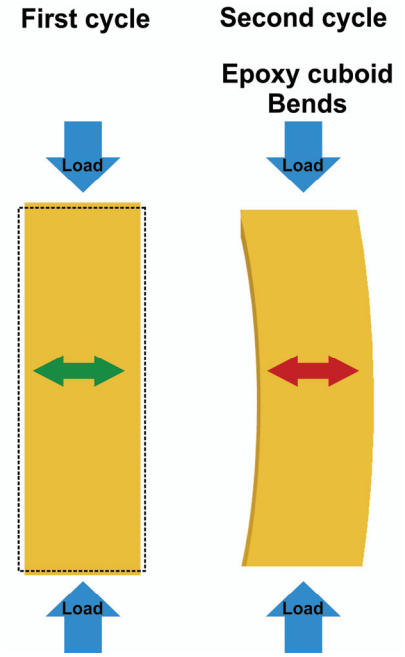

Figure 5-9: Schematic representation of the epoxy cuboid deformation with the applied load.

5.3.3 Axial compression load of a fibre Bragg grating embedded in 2 mm of epoxy

To study the effect of the application of an axial compression load to the central epoxy embedded section of an FBG, a 6 mm length FBG with centre wavelength 1556.5 nm was fabricated in photosensitive SM optical fibre (Fibercore PS1250) and embedded around its centre with a 2 mm epoxy cube.

In order to apply an axial load to the epoxy cube, the fibre loading and support structure presented in Figure 5-10 was developed. The fibre loading and support structure consists of two machined stainless steel blocks, each containing a 0.5 mm diameter hole. The test fibre was passed through the hole, allowing the epoxy cube to rest against the stainless steel block. To ensure that the top block that sandwiches the epoxy cube was balanced, a dummy support fibre containing two identical resin blocks was placed parallel to the test fibre, forming a triangle as illustrated in Figure 5-10.

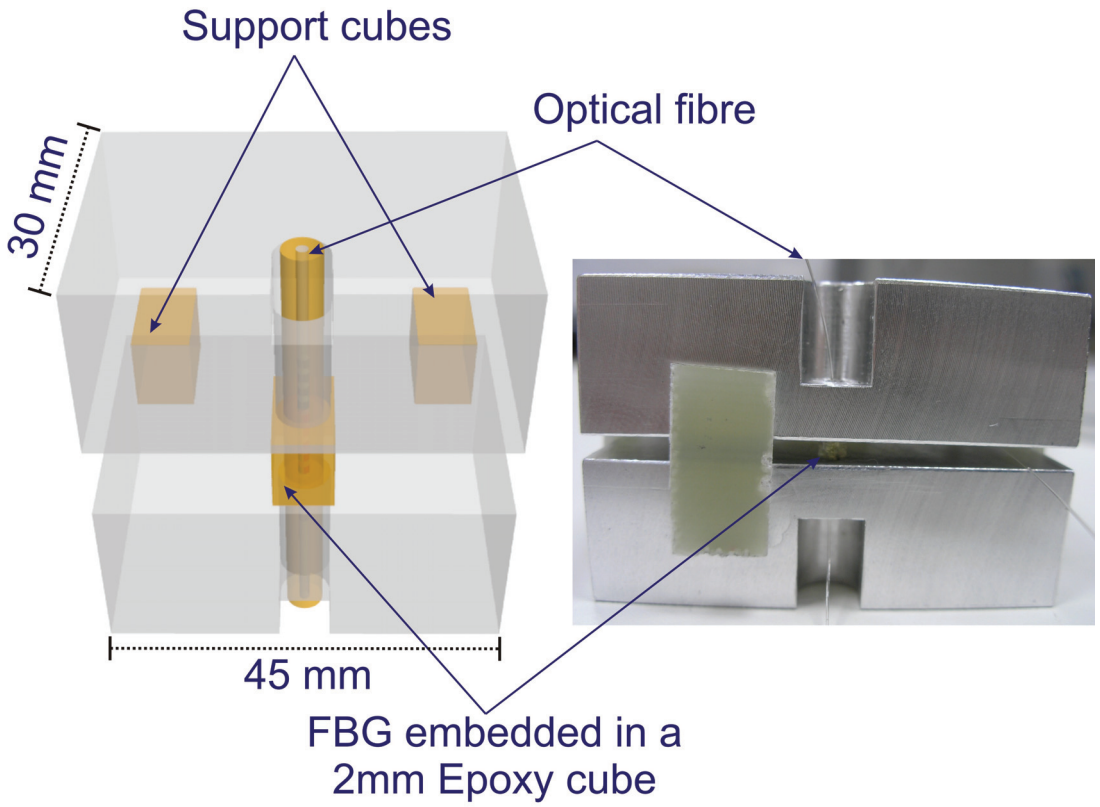

Figure 5-10: Axial compression fibre loading and support structure: a) schematic representation; b) photograph.

The fibre loading and support structure was placed on the loading fixture presented in Figure 5-3. In this experiment the weights were placed on the top of the loading fixture piston rather than on the cantilever arm because the weight of the cantilever arm itself was sufficient to induce changes in the reflection spectrum of the FBG. Figure 5-11 presents the experimental results obtained for a maximum load of 15 N.

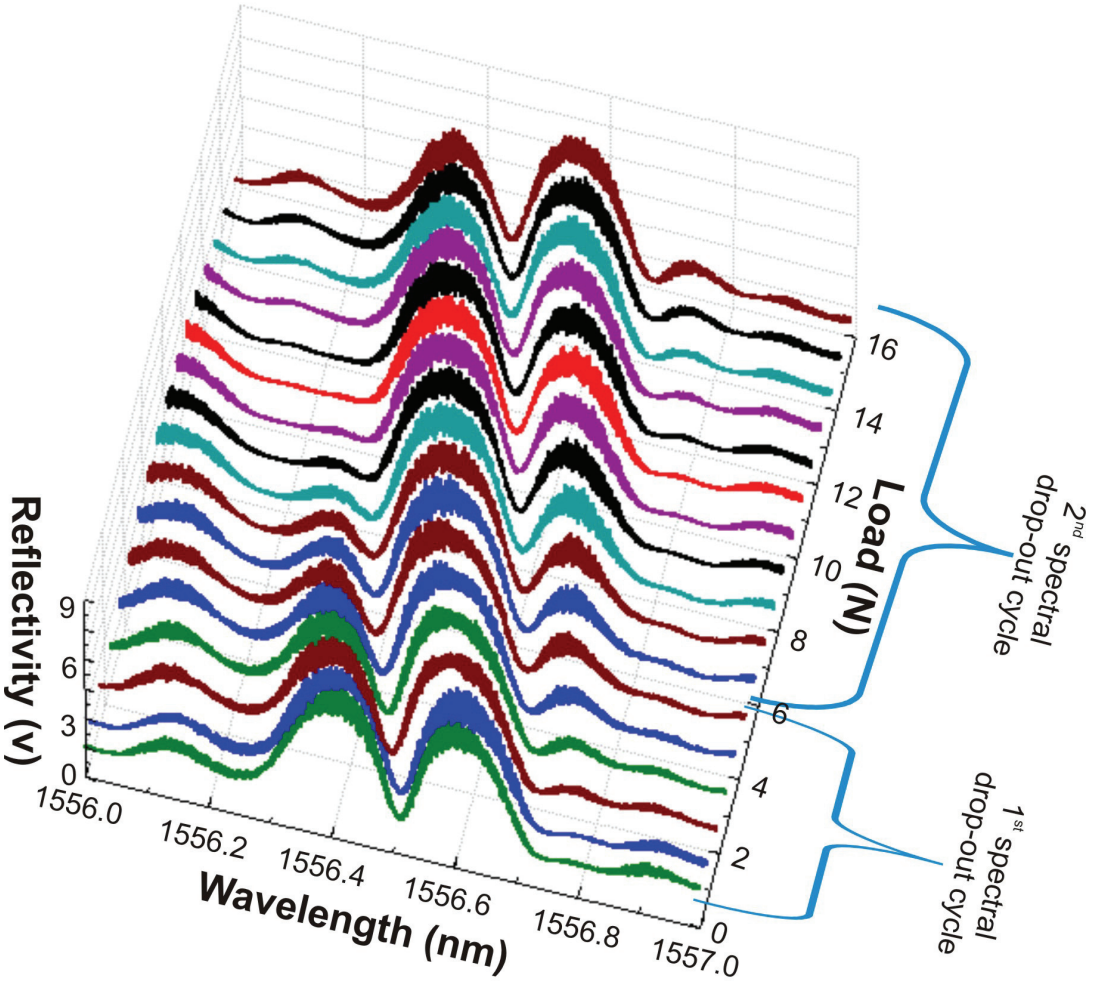

Figure 5-11: Experimentally determined evolution of the reflection spectrum from a 6 mm long SM FBG embedded with epoxy along 2 mm of its centre, with the applied axial compression load.

In Figure 5-11 it can be seen that the weight of the loading fixture and support structure induced a change in the reflection spectrum of the FBG, positioning the spectral drop-out almost in the centre of the FBG bandwidth. With increasing load, the spectral drop-out suffered a blue shift, moving across the bandwidth of the FBG to lower wavelengths. When it reached the blue end of the FBG a new cycle was initiated.

In contrast with the transverse load of the epoxy cube, the axial compression induces a decrease of the FBG period over the loaded region, which results in the observed blue-shift of the spectral drop-out. Figure 5-12 presents the dependence of the central wavelength of the spectral drop-out on the applied load for the two spectral drop-out cycles. The wavelength response of the spectral drop-out to the applied load exhibits

good linearity for both cycles. With this technique, the sensitivity achieved in terms of wavelength shift per applied force was -2.45±0.07x10^{-2} nm/N and -1.87±0.02x10^{-2}nm/N for the first and second spectral drop-out cycles respectively. An increase of sensitivity by a factor of 4.3 and 4.8 was obtained comparing with the results obtained for the first and second spectral drop-out cycles of the cuboid transverse load. The reason for this increase is that, when a load is applied to the epoxy cube, the strain along the axis where the load is being applied is higher than across the other two axes. As presented in Section 3.5 the strain induced in a cube subject to a unidirectional load along the x axis is $\varepsilon_x = -\frac{\sigma_x}{E}$ whilst for the other directions y and z is $\varepsilon_y = \varepsilon_z = -\frac{\upsilon\sigma_x}{E}$, where υ is the Poisson ratio of the material.

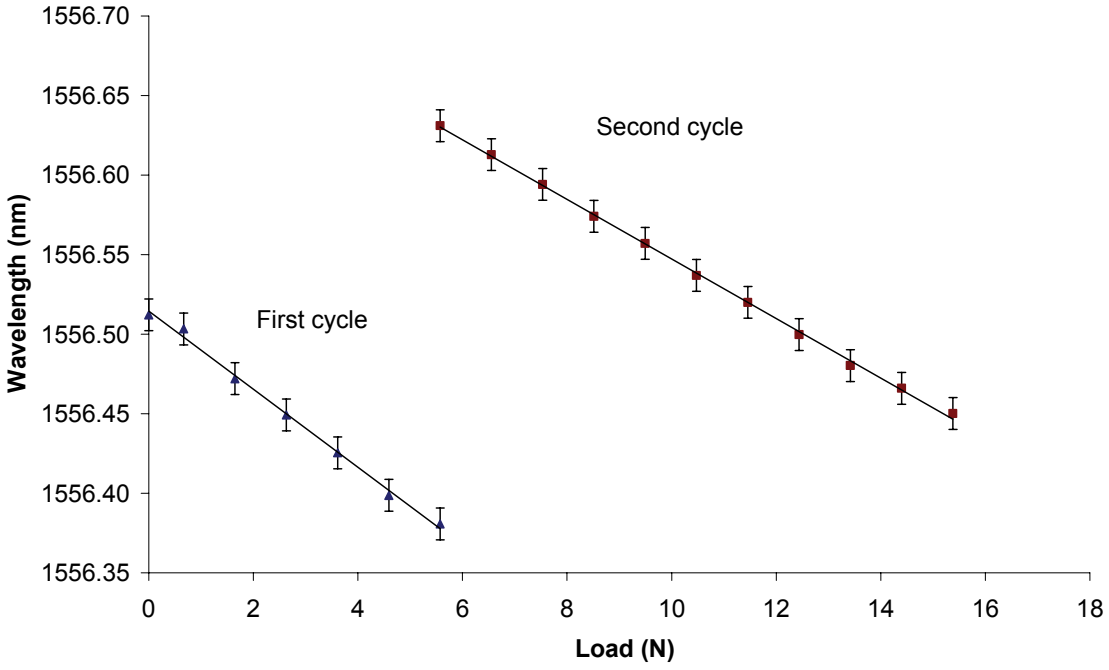

Figure 5-12: Dependence of the central wavelength of the spectral drop-out of a 6 mm long SM FBG embedded with epoxy along 2 mm of its centre on the applied axial compression load.

5.3.4 Transverse load of a fibre Bragg grating written in HiBi fibre and embedded in 2 mm of epoxy

In section 4.4 it was shown that when a transverse load is applied directly to a sub-section of an FBG written in HiBi fibre, parallel to one of the eigenaxes, the spectral drop-out appears only in the reflected light polarised along that eigenaxis. This suggests that this technique modifies the birefringence of the fibre, which is not desirable when multiplexing with sensors that depend on birefringence. However, using the technique described in Section 5.2, no birefringence was induced into the optical fibre as the transverse load applied to the epoxy cube was transduced into an axial strain acting on the optical fibre. To verify this, the experiment presented in Section 4.4.1 was repeated using this new technique.

The experimental arrangement is presented in chapter 4, Figure 4-2. An FBG of length 6 mm and centre wavelength 1553 nm was written in PM bow-tie optical fibre (Fibercore HB1500) in-house by Dr. Edmon Chehura. The cladding diameter of the fibre was 125 μm, the numerical aperture 0.17, the cut-off wavelength 1258 nm, the beat length 1.3 mm at 633 nm and the core ellipticity 1.0–1.4, as specified by the manufacturer. The fibre was hydrogen loaded before the writing process to increase its photosensitivity. Figure 5-13 shows the reflection spectrum from the slow and fast axes of the 6 mm long FBG written in PM Bow-tie fibre.

The central section of the FBG written in the test fibre was embedded in a 2 mm epoxy cube with the slow axis of the fibre aligned vertically using the procedure explained in Section 5.3.1. The test fibre containing the epoxy cube block and a support dummy fibre containing two identical blocks were placed parallel to each other in the loading fixture (Figure 5-3). The fibre slow axis was aligned with the loading direction. The epoxy cube block was subject to transverse load placing calibrated weights on the loading fixture cantilever arm, to a maximum load of 178 N.

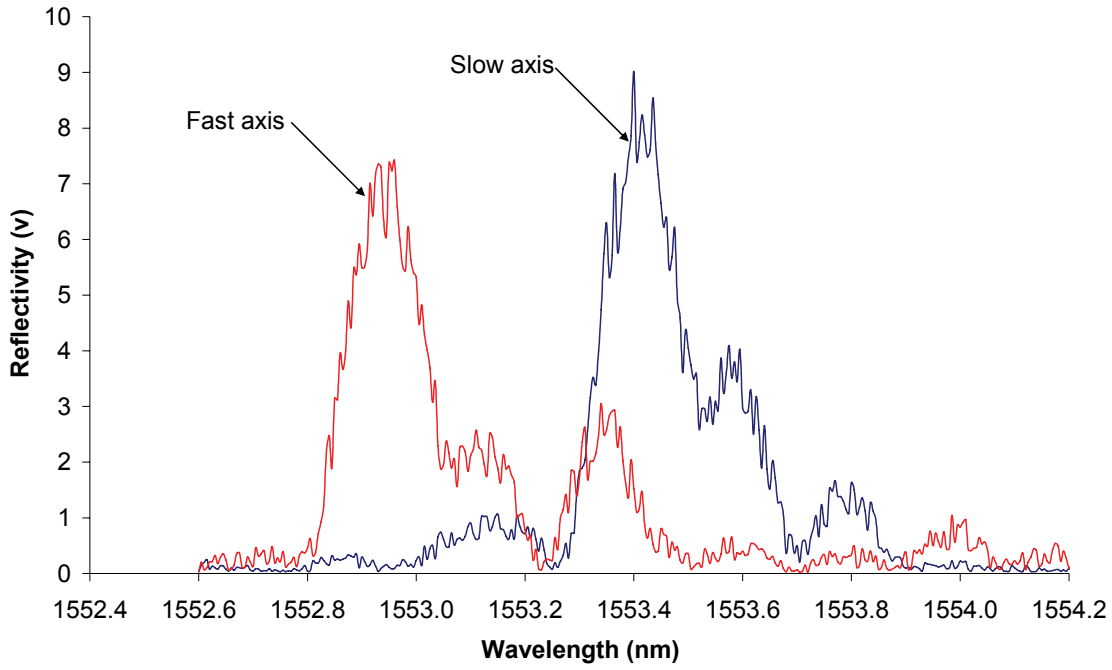

Figure 5-13: Reflection spectrum of the fast and slow axes of a 6 mm long FBG written in PM Bow-tie fibre.

Figure 5-14a and Figure 5-14b present the experimental results obtained for both eigenaxis, the fast and slow respectively. It was observed on both eigenaxes that as the applied load increases, the spectral drop-out starts to form, moving across the bandwidth of the Bragg reflection spectrum. When it reaches the red end of the spectrum, a new spectral drop-out forms and a new cycle starts. In contrast with the results presented in Section 4.4, the spectral drop-out appears in both eigenaxes, demonstrating that this technique does not induce birefringence into the optical fibre. Figure 5-15a and Figure 5-15b show the dependence of the central wavelength of the spectral drop-out on the applied load for both the fast and slow eigenaxis, respectively.

The measurement sensitivity of $2.78\pm0.03\text{x}10^{-3}$ nm/N was achieved when monitoring the first spectral drop-out cycle over the slow axis and $2.05\pm0.06\text{x}10^{-3}$ nm/N for the second cycle. For the fast axis, a sensitivity of $2.69\pm0.02\text{x}10^{-3}$ nm/N was obtained for the first spectral drop-out cycle and $2.1\pm0.06\text{x}10^{-3}$ nm/N for the second cycle. The fact that similar sensitivities were obtained for the different axes shows that the applied transverse load was predominantly transduced into an axial strain acting on the optical fibre.

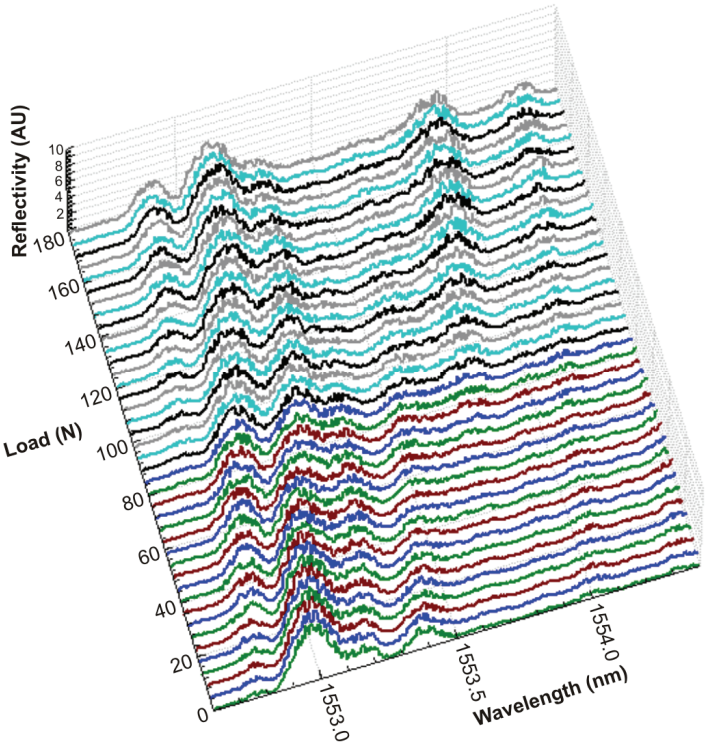

a)

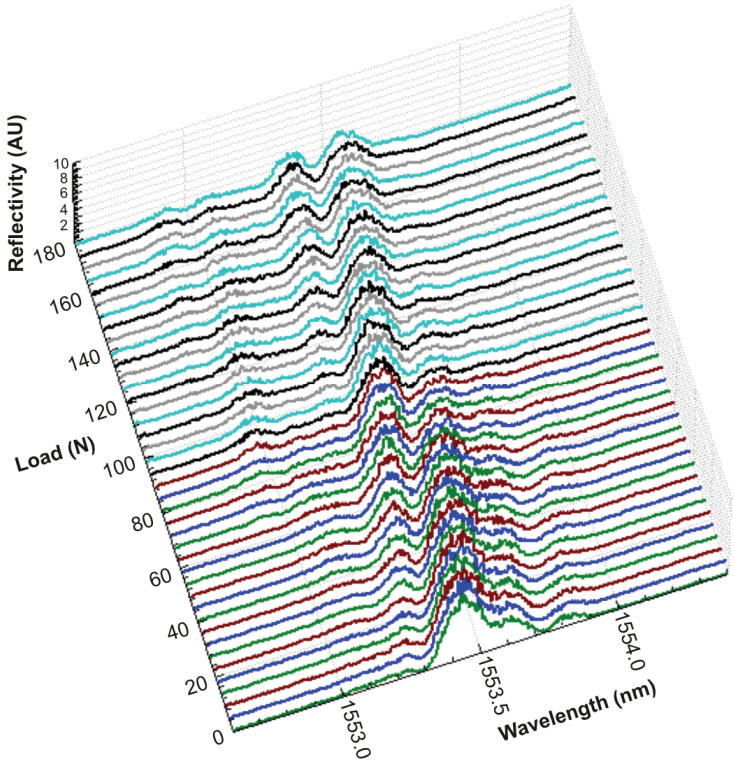

b)

Figure 5-14: Experimentally determined evolution of the reflection spectrum from the a) fast axis and b) slow axis of a 6mm long bow-tie HiBi FBG, embedded in epoxy along a length of 2 mm at its centre, with the applied load.

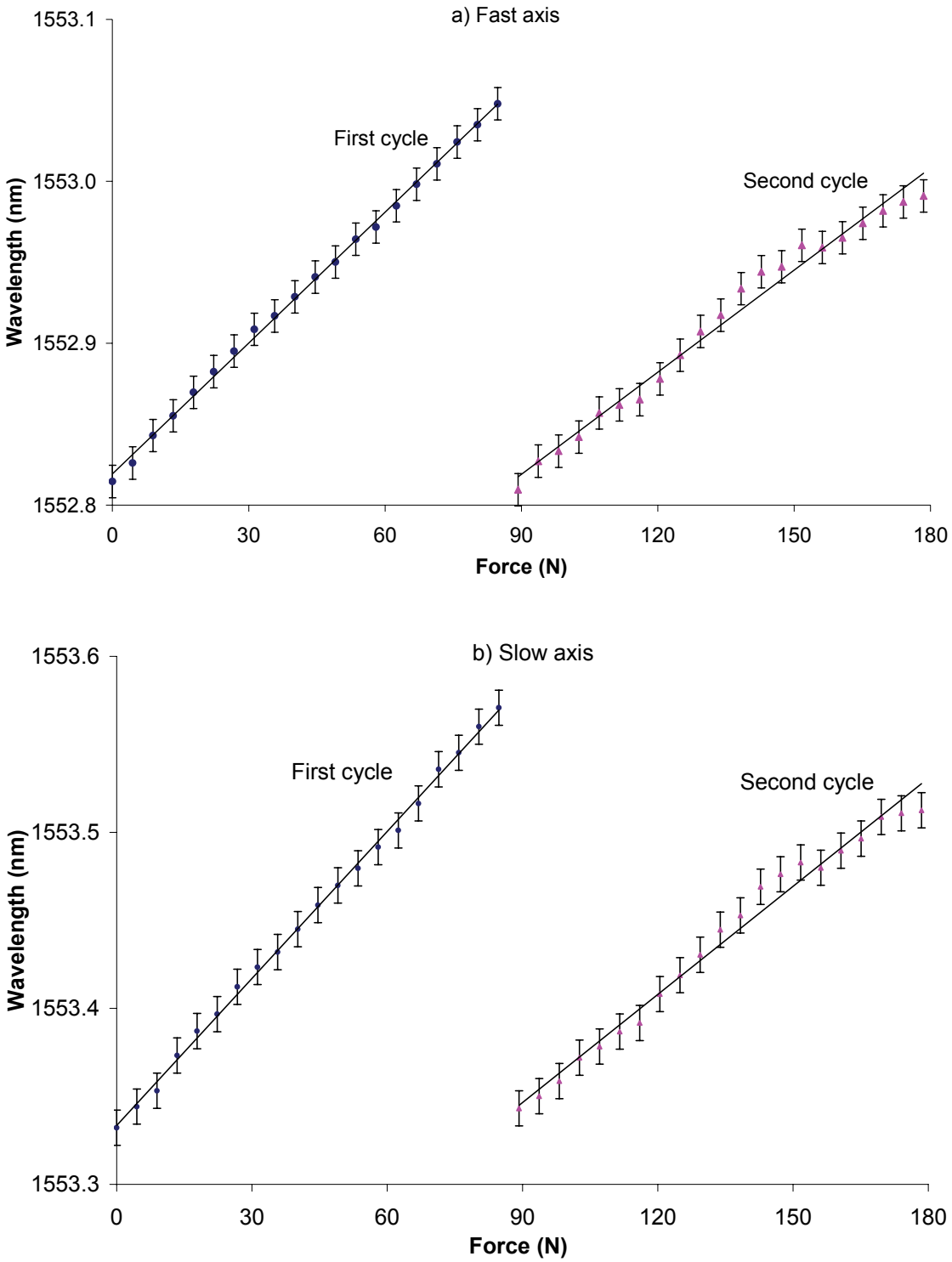

Figure 5-15: Dependence of the central wavelength of the spectral drop-out of a 6mm long bow-tie HiBi FBG, embedded in epoxy along a length of 2 mm at its centre on the applied load a) fast axis; b) slow axis.

5.4 Partially pre-loaded fibre Bragg gratings

The goal of these experiments was to test if it is possible to form a spectral drop-out formed within the bandwidth of the FBG for a zero applied load. This technique is beneficial for the development of a sensor that measures dynamic pressure as an easier tracking of the spectral drop-out is obtained for small loads. Another potential future application of this technique is the development of a fibre optic tuneable filter.

5.4.1 Pre-loaded fibre Bragg grating embedded in 2 mm of fibre reinforced composite material

To obtain a spectral drop-out within the FBG reflection spectrum, an FBG of length 6 mm and centre wavelength 1571.5 nm was fabricated in photosensitive SM optical fibre (Fibercore PS1250) and its centre embedded within two carbon fibre reinforced composites. The carbon fibre reinforced used in this experiment was a HexPly-8552 toughened epoxy with a unidirectional matrix of carbon fibres used in the aerospace industry. A 2 mm long central section of the FBG was placed on the top of two layers of carbon fibre reinforced composite material and oriented perpendicularly to the composite carbon fibres, as illustrated in Figure 5-2. Two other layers were placed on the top of the test fibre. A dummy optical fibre with two identical pieces of the above described block of composite material, separated 2 cm from each other, were afterwards placed parallel to the test fibre. The metal plate containing the specimens was placed inside an oven and another metal plate was placed on the top of the specimens. To ensure that a spectral drop-out was induced in the reflection spectrum before the curing process, different weights were placed on the top of the metal plate until the spectral drop-out appeared in the middle of the FBG bandwidth reflection spectrum. The curing process was then initiated increasing the oven temperature up to 200 ºC and maintaining this temperature constant for 2 hours.

During the curing process, the central length of the FBG covered by the composite material increased from 2 mm to 3 mm. Figure 5-16 presents a photograph of the embedded FBG after curing and the support dummy fibre. Figure 5-17 illustrates the FBG reflection spectrum before the curing process subject to a transverse load and after the curing process without transverse load.

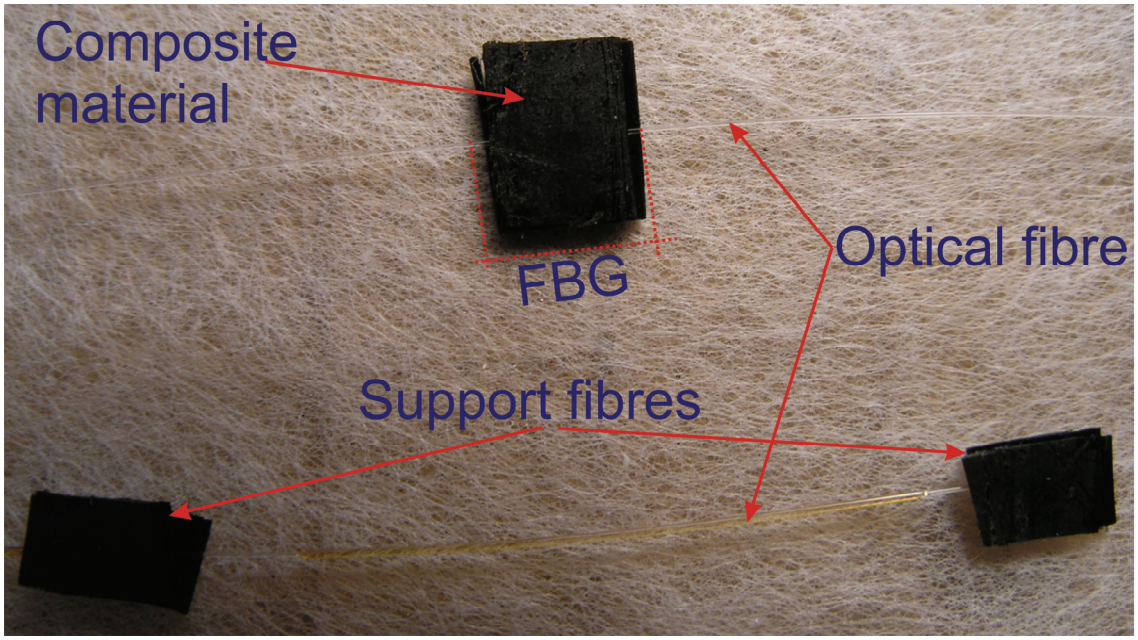

Figure 5-16: Photograth of the 6 mm FBG embedded between two layers of carbon reinforced composite material and support fibre.

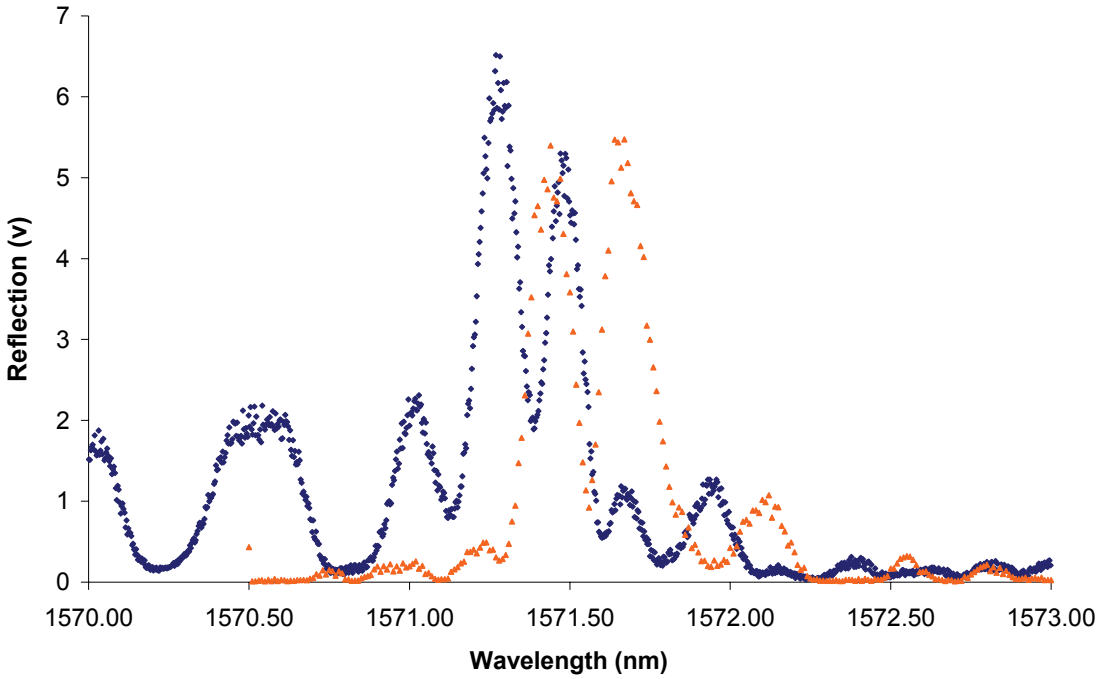

Figure 5-17: Reflection spectrum of a 6 mm SM FBG pre-loaded with a weight on top of the composite material that covered 2 mm of its centre (Orange (▲): before curing process and a weight on top; Blue (◆): after the curing process and without weight on top).

It was observed that after the curing process and removing the pre-load, the spectral drop-out previously induced by the load applied to the composite material remained in the FBG reflection spectrum (Figure 5-17). It was also noticed that the position of the spectral drop-out within the bandwidth of the FBG reflection spectrum passed the centre and a second spectral drop-out started forming on the blue end side. That is due to increased contact area of the composite material with the FBG. In Figure 5-17 a 0.5 nm blue shift of the Bragg envelope is observed due to shrinkage of the composite after curing which affected the period of the FBG over the embedded area.

To characterise the response of the composite embedded FBG to transverse load, the test fibre and the support dummy fibre were placed parallel to each other on the loading fixture, with the composite blocks forming a triangle. Different weights were added to the loading fixture cantilever arm up to a maximum load of 111.6 N. The experimental results obtained are presented in Figure 5-18. The first and the second induced spectral drop-out tracked across the bandwidth of the Bragg spectrum as the load increased. When the first spectral drop-out reached the red end, a new cycle was repeated. The numbers shown in Figure 5-18 represent the different spectral drop-outs obtained with an increasing load. The dependence of the central wavelength of the different spectral drop-outs on the applied load is presented in Table 5-1.

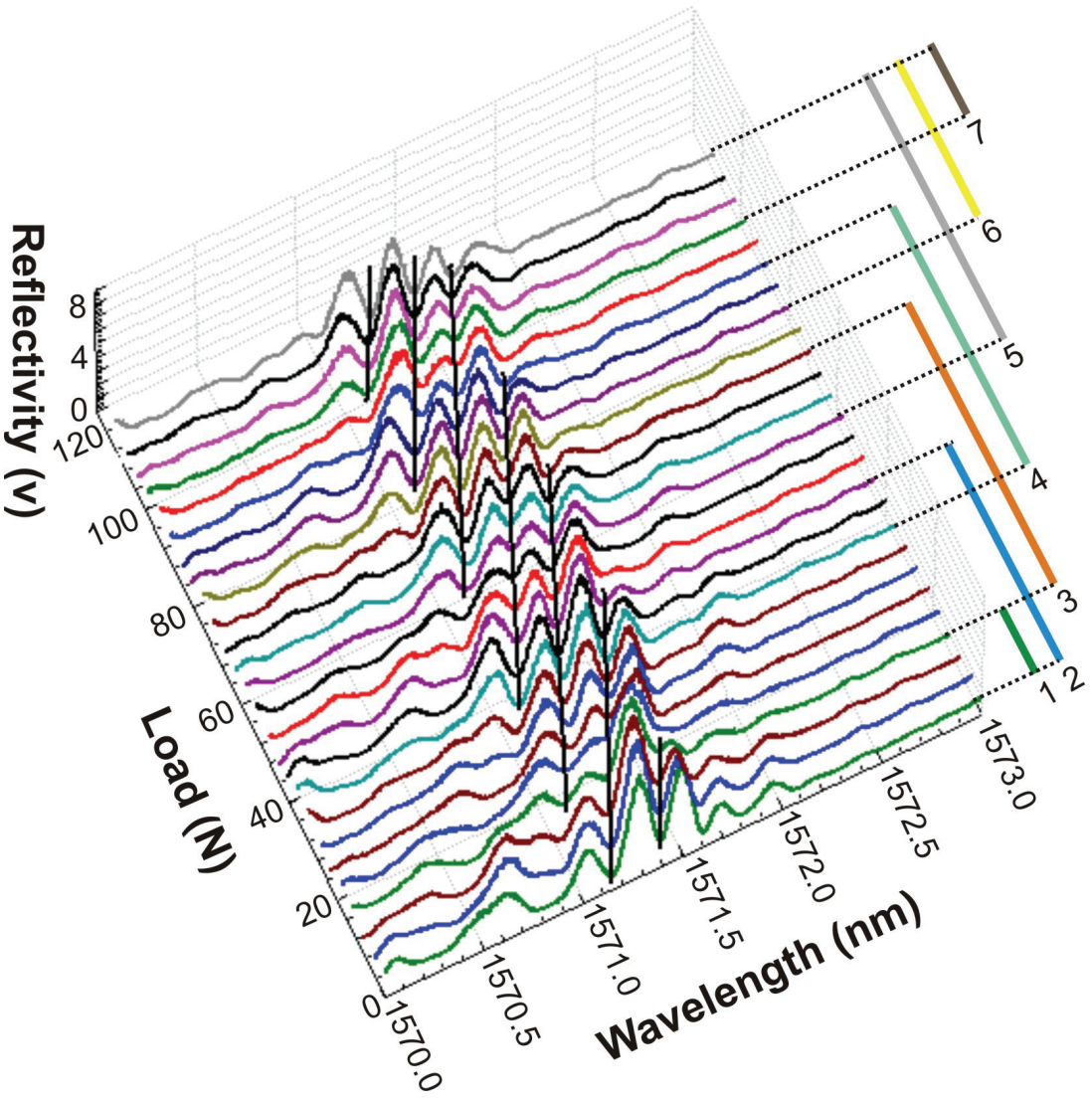

Figure 5-18: Experimentally determined evolution of the reflection spectrum from a 6 mm long SM FBG embedded with composite material that covered 2 mm of its centre, with the applied transverse load.

Table 5-1: Dependence of the central wavelength of the different spectral drop-outs on the applied load

Spectral drop-out	Sensitivity (x10^{-2} nm/N)
1	1.28±0.13
2	1.17±0.03
3	1.02±0.02
4	1.04±0.02
5	1.06±0.01

The wavelength response of the spectral drop-outs to the applied load exhibited good linearity for all the spectral drop-out cycles. The sensitivity coefficients obtained for the first and second spectral drop-out were slightly higher than those obtained for the third, fourth and fifth spectral drop-outs, which is a result of the saturation of the composite material.

5.4.2 Pre-strained fibre Bragg grating embedded in 2 mm of epoxy

In this experiment an FBG was pre-strained before a central section of its length was embedded in an epoxy block. This experiment aimed at verifying if after the curing process and after releasing the pre-strain a spectral drop-out would be induced in the FBG reflection spectrum due to the strain over the embedded region. Different FBGs of length 6 mm and centre wavelength around 1555 nm were fabricated in photosensitive SM optical fibre (Fibercore PS1250). The fibres were pre-strained and their central section embedded in a 2 mm width by 2 mm length by 2 mm depth epoxy block (Figure 5-19).

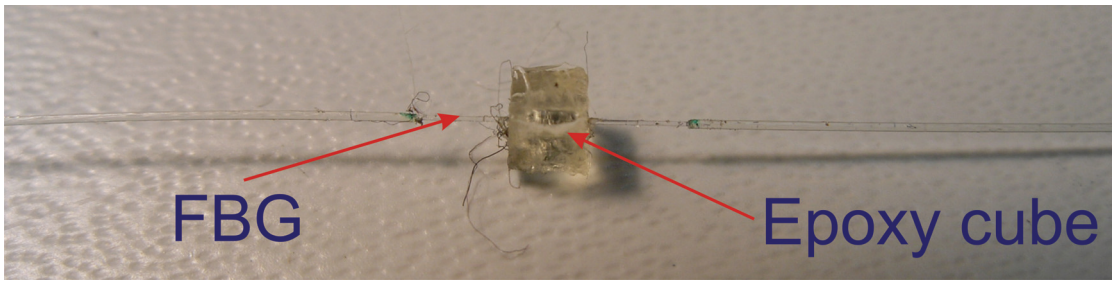

Figure 5-19: Photograph of a SM FBG embedded in a 2 mm width by 2 mm length by 2 mm depth epoxy resin cube.

Different pre-strain values were applied to the different FBGs but no spectral drop-outs were observed within the FBG bandwidth and the spectrum before and after the curing process was identical. The reason is that the Young modulus of the epoxy (689 MPa) is very small compared to the Young modulus of the fibre (~71 GPa). Therefore, for small strains, the epoxy block cannot hold the applied strain. The maximum strain applied to the FBG was 4400 με, which corresponds to a 4 nm wavelength shift of the Bragg envelope. When the curing process was finished and the strain released, a change on the FBG spectrum was observed (Figure 5-20). A small change on the reflection spectrum occurred with a spectral drop-out appearing on the red side of the spectrum. The reason

for this behaviour is that the epoxy did hold part of the strain but not uniformly, which created a chirped period in the central part of the FBG.

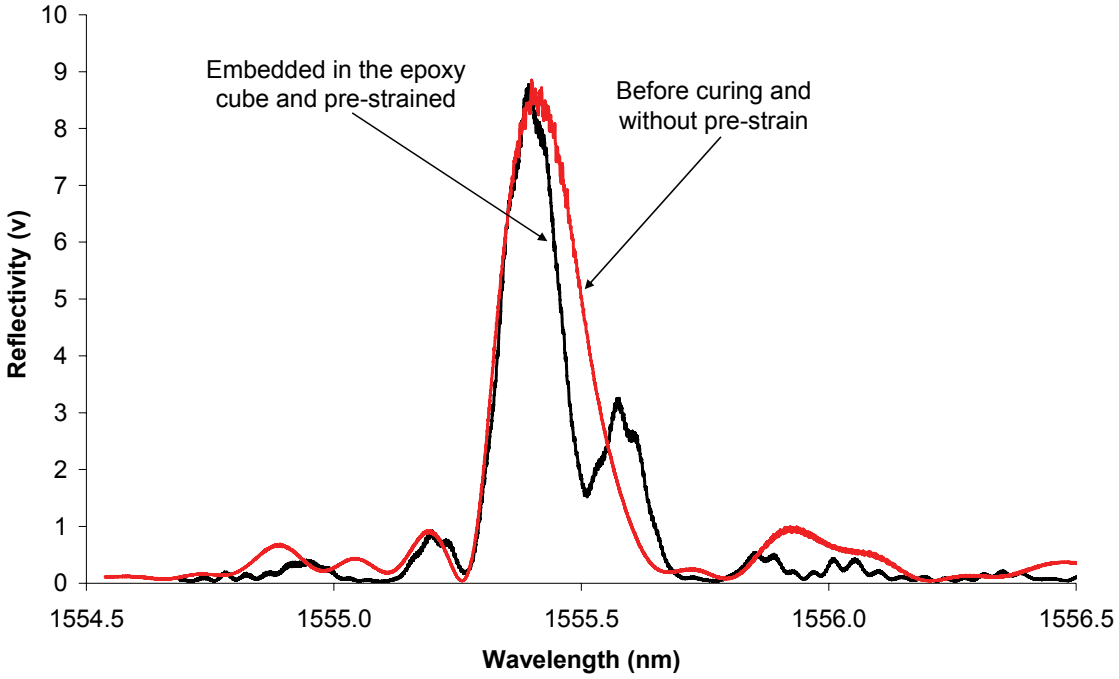

Figure 5-20: Reflection spectrum of a 6 mm FBG embedded with epoxy along 2 mm of its centre (before the curing process and without pre-strain and after curing with pre-strain applied over the embedded region).

5.5 Summary

A new loading technique was developed and consisted of transducing the transverse load applied to an epoxy cube embedded around a central section of an FBG to an axial strain. Transducing the transverse load applied to the epoxy cube into an axial strain over the central section of the FBG induced a spectral drop-out within the bandwidth of the FBG reflection spectrum. This is due to increase of the FBG period over the embedded region. Compared with the results obtained for direct transverse load of an FBG presented in Section 4.3.2, this technique increases the transverse load measurement sensitivity in terms of wavelength shift per applied force by a factor of 3. Moreover, the partial embedding of the FBG is an effective protection of the FBG to mechanical damage.

When a transverse load was applied to the epoxy cube in which the central section of an FBG written in HiBi fibre was embedded, (Section 5.3.4) a spectral drop-out was obtained in the two eigenaxes. This shows that this technique does not induce birefringence in the optical fibre, which is desirable when multiplexing sensors that depend on birefringence

The axial compression load of the epoxy cube, compressed along the same direction as the axis of the optical fibre, created a spectral drop-out within the bandwidth of the FBG reflection spectrum. With this loading configuration, the spectral drop-out tracked to lower wavelengths, and not higher wavelengths, due to a decrease of the FBG period over the embedded region. The measurement sensitivity obtained with this loading configuration in terms of wavelength shift per applied force improved by a factor of three. This technique offers another way of transduce the pressure to the FBG.

Two experiments were undertaken with the aim to produce a preloaded FBG with a spectral drop-out pre-formed within the bandwidth of the FBG. On the first, a carbon fibre reinforced composite was placed in the centre of the FBG and pre-loaded with a weight during the curing process. This technique produced good results with a spectral drop-out induced in the bandwidth of the FBG reflection spectrum for zero load. The second experiment consisted of pre-strain the FBG before embedding its centre in an epoxy cube. After the curing process, no spectral drop-out was obtained within the FBG bandwidth as the epoxy did not hold the pre-strain applied into the FBG and only a slight change on the FBG reflection spectrum was obtained when a pre-strain of 4400 με was applied. This change on the FBG reflection spectrum was due to a chirp effect caused in the central section of the FBG, which results on partial hold of the applied pre-strain.

References

Hao, J. Z., Tay, C. M., Liaw, C. Y., Lu, C. and Tjin, S. C.:2003. A Novel FBG pressure sensor with low temperature sensitivity. IEEE LEOS Annual meeting conference proceedings. **1**: 21-22.

Liu, Y., Guo, Z., Zhang, Y., Chiang, K. S. and Dong, X.:2000. Simultaneous pressure and temperature measurement with polymer-coated fibre Bragg grating. *Electronics Letters*. **36**: 564-566.

Maier, R. J., Barton, J. and Jones, J. DC.:2002. Fibre Bragg grating location by a side scatter technique based on cladding mode coupling. *Optical Fiber Sensors Conference Technical Digest*. (99-102).

Sheng, H. J., Fu, M. Y., Chen, T. C., Liu, W. F. and Bor, S. S.:2004. A lateral pressure sensor using a fiber Bragg grating. *IEEE Photonics Technology Letters*. **16**: 1146-1148.

Suresh, R. and Tjin, S. C.:2005. Effects of dimensional and material parameters and cross-coupling on FBG based shear force sensor. *Sensors and Actuators A*. **120**: 26-36.

Zhang, Y., Feng, D., Liu, Z., Guo, Z. Y., Dong, X., Chiang, K. S. and Chu, B. C. B.:2001. High-sensitivity pressure sensor using a shielded polymer-coated fiber Bragg grating. *IEEE Photonics Technology Letters*. **13**: 618-619.

Chapter 6

Pore pressure transducer design and calibration

6.1 Introduction

In this chapter, the design, construction and calibration of a fibre optic pore water pressure transducer is presented. Section 6.2 describes the sensor and Section 6.3.1 presents the results of an initial performance evaluation of the pressure sensor housing, pressurised with air.

The long term stability and repeatability of measurements made with the pressure sensor were assessed. The experimental arrangement used to calibrate the water pressure sensor is presented in Section 6.4.1 and the experimental results in Section 6.4.2.

6.2 Pore pressure transducer design

The FBG sensing principle exploited to develop the pore water pressure transducer was the transverse loading of the central, epoxy-embedded section of an FBG, discussed in chapter 5. This technique was selected because it provides protection of the FBG against mechanical damage and presents a high sensitivity to the applied load. In order to measure the pore water pressure within the soil independently from any other pressure that the soil particles may exert, a novel sensor housing was designed. The sensor housing transduces the water pressure into a transverse load applied on the epoxy cube surrounding the central section of the FBG. Figure 6-1 presents a schematic of the developed pore pressure sensor housing.

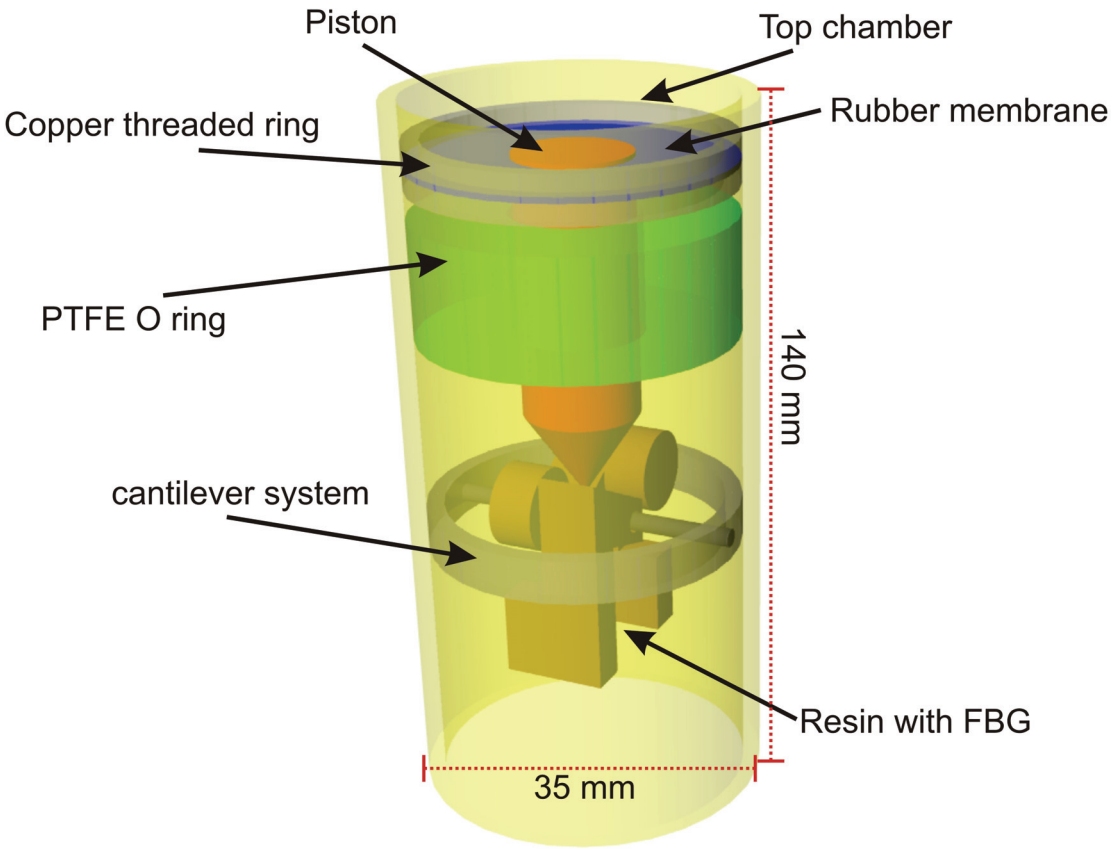

Figure 6-1: Schematic diagram of the developed pore pressure sensor housing.

The pore water pressure transducer housing consists of a 120 mm long stainless steel tube of 35 mm and 31 mm external and internal diameter, respectively. It is internally divided into two compartments, the top compartment being the pressure chamber and the bottom compartment being the sensing chamber. The sensing chamber includes the FBG and the system for transducing the pressure into a transverse load applied to the expoy-embedded section. The pressure chamber was isolated from the sensing chamber using a rubber membrane that is attached to a piston and clamped between two copper threaded rings. Figure 6-2a shows a photograph of the pressure chamber of the pore pressure sensor.

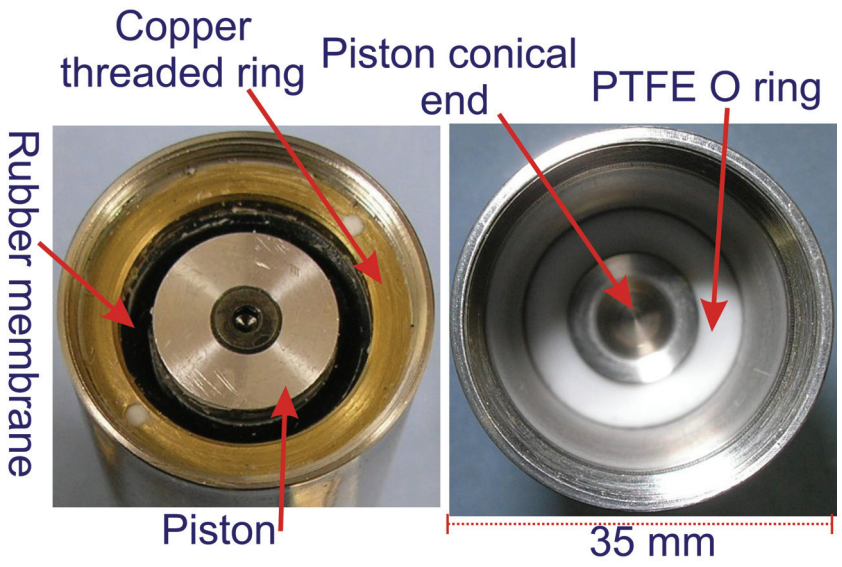

a) b)

Figure 6-2: Photograph of: a) Top compartment (pressure chamber) of the pore pressure sensor housing; b) Bottom compartment (sensing chamber) of the pore pressure sensor housing.

To vertically guide the piston inside the sensor housing without tilt, a PTFE O ring was used (Figure 6-2b). PTFE was chosen for manufacturing the O ring due to its low friction properties, providing a smooth and low friction movement of the piston.

In order to allow an amplification or reduction of the load transmitted through the piston due to the water pressure, the cantilever system presented in Figure 6-3 was developed. The cantilever system consists of two parallel stainless steel arms centrally connected by a pivot and with bearings attached at the top end. When the conical end of the piston applies a vertical load to the bearings, the bottom end of the cantilever system sandwiches the epoxy block positioned between them. The amplification or reduction of the load can be obtained by changing the position of the pivot. For these experiments, the cantilever arm was designed in order not to amplify the load applied to the bearings. This was achieved by equalising the distances from the top and bottom loading points relative to the pivot.

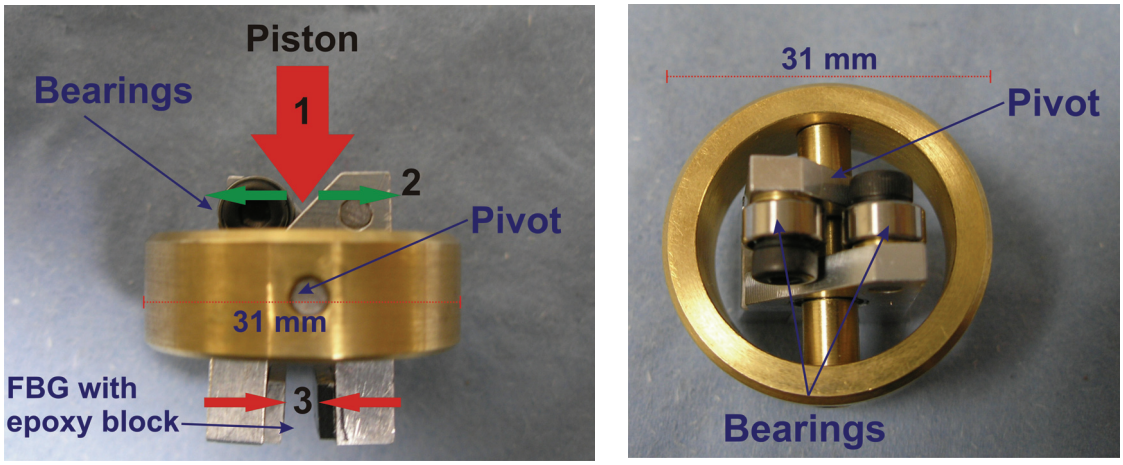

a) b)

Figure 6-3: Photograph of the cantilever system: a) lateral view; b) top view.

To ensure that the water existent in the soil passes the to the pressure chamber and that the soil particles are filtered, a cap containing a sintered stainless steel filter (Figure 6-4) was used. A 50 µm pore size aperture sintered stainless steel filter is the conventional filter used in pore water pressure transducers to measure positive pressures (Hanna, 1985). For measuring negative pressures, a 1 µm pore size aperture filter is normally used. As the sensor developed here will be used to measure positive pressure changes, a 50 µm pore size aperture sintered stainless steel filter was chosen. The cap containing a sintered stainless steel filter was screwed onto the top sensor housing pressure chamber to filter the soil particles.

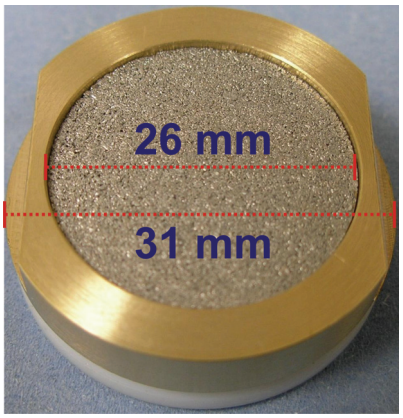

Figure 6-4: Photograph of the cap containing a sintered stainless steel filter with 50 µm pore size aperture.

To isolate the sensing chamber of the pore pressure sensor housing from the surrounding environment and to guide the optical fibre out, a bronze cap welded to a 7 mm diameter stainless steel tube was attached to the sensor housing (Figure 6-5). For field measurements, the stainless steel tube may be replaced, for instance, by a ruggedised fibre optic patch cable. Figure 6-6 shows a photograph of the assembled pore pressure sensor and Figure 6-7 shows the sensor housing components.

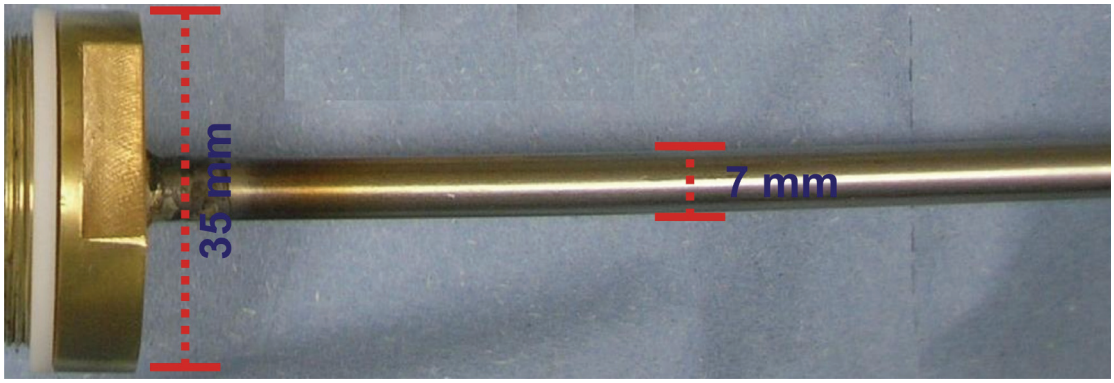

Figure 6-5: Isolating cap and fibre guide tube.

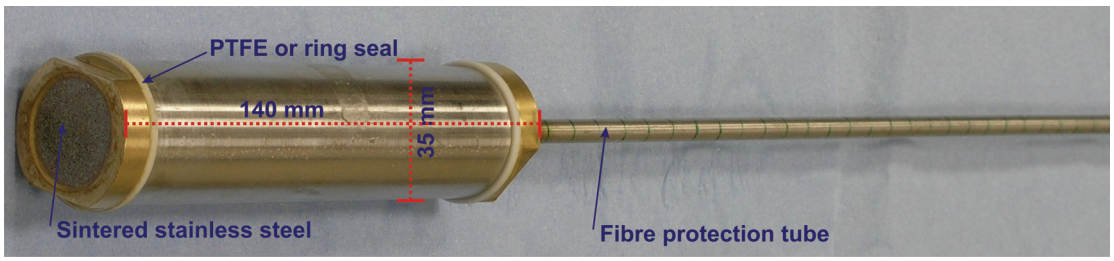

Figure 6-6: Photograph of the assembled pore pressure transducer.

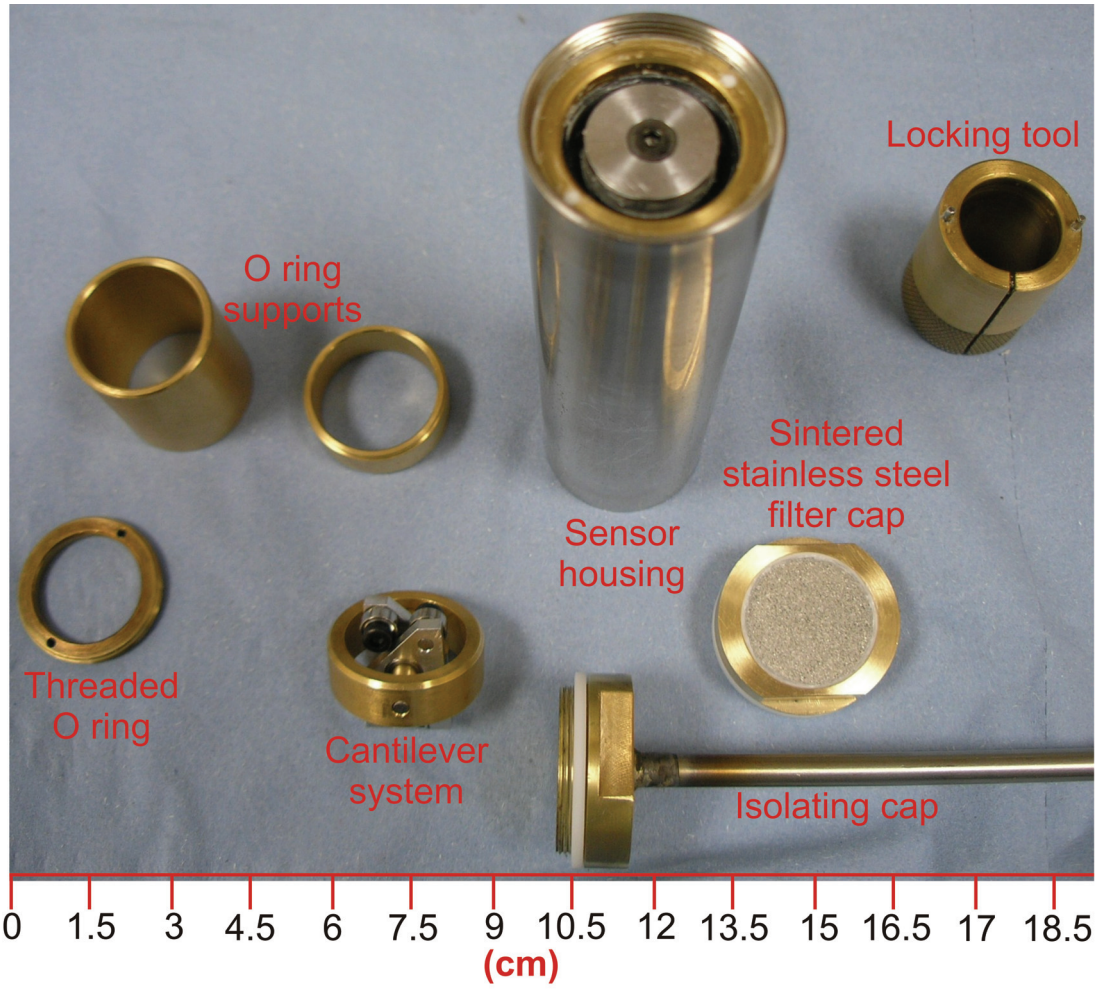

Figure 6-7: Photograph of the pore pressure transducer housing components.

6.3 Pressure sensor housing characterisation

After the pore water pressure transducer was constructed and assembled, its performance was evaluated. The sensor described and presented in section 6.2 can be used to measure pore water pressure within the soil and for numerous other applications, such as the measurement of air pressure. A pre-calibration exercise was carried out by pumping air into the pressure chamber in order to test the pressure sensor and to ensure that the sensor housing did not leak. In this experiment the cap containing the sintered stainless steel filter was replaced by a cap containing a pressure pipe plug (Figure 6-8).

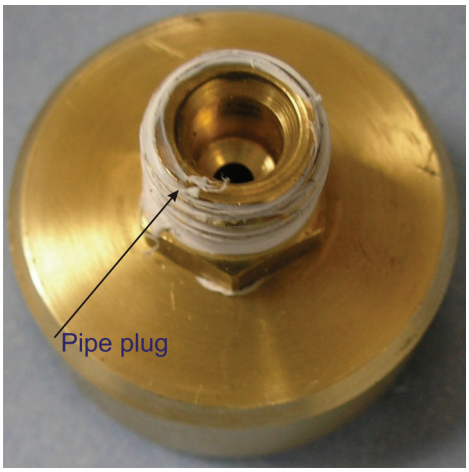

Figure 6-8: Photograph of the cap with pressure pipe plug.

In order to pressurise the pressure sensor, an air pump and precision pressure calibrated transducer, Druck DPI-602, was used. The Druck DPI-602 allows the fine tunning of the applied pressure, offering a pressure resolution of 1 kPa over a range 2060 kPa. The experimental arrangement used to interrogate the sensor is presented in Section 4.2, Figure 4-1.

6.3.1 Experimental results

An FBG of length 6 mm and centre wavelength 1566.7 nm was embed over in a 2 mm width by 4 mm length by 3 mm depth cuboid and placed in the cantilever system described in Figure 6-3. The pressure sensor housing was then connected to the air pump and precision pressure calibrated transducer. Pressure increments of 5 kPa were applied from 0 kPa – 100 kPa and afterwards increments of 10 kPa from 100 kPa – 300 kPa. The air pressure was subsequently decreased to investigate the hysteresis of the sensor. The experimental results are shown in Figure 6-9.

For the studied measurement range only one spectral drop-out was observed within the bandwidth of the FBG reflection spectrum and its wavelength response to the applied load exhibits good linearity as observed in Figure 6-10.

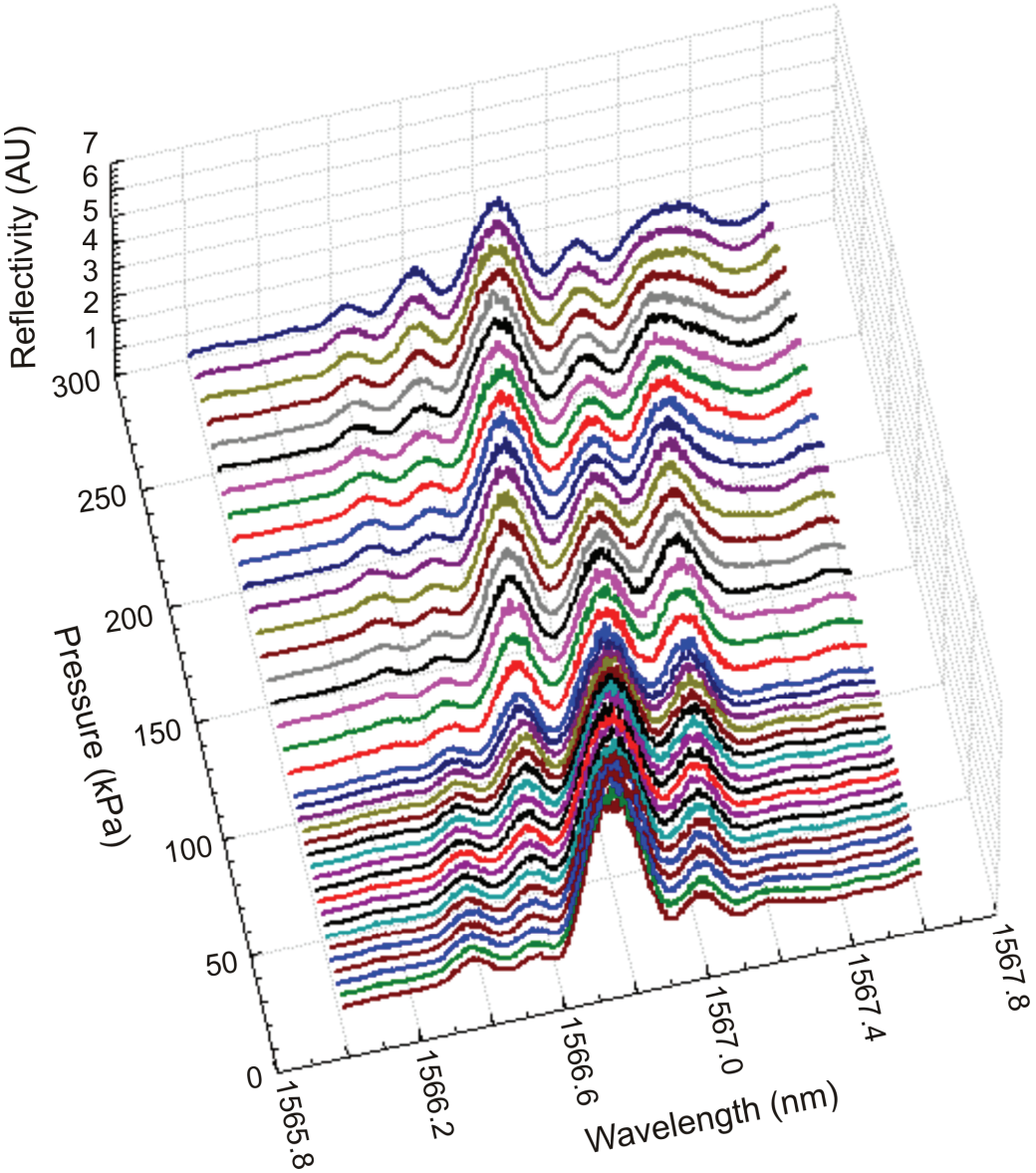

Figure 6-9: Experimentally determined evolution of the reflection spectrum of a 6 mm long SM FBG which had is central 2mm long section embedded within a 2 mm width by 4 mm length by 3 mm depth epoxy cuboid, in response to the pressure applied to the sensor housing (increase) via the calibrated transducer Druck DPI-602.

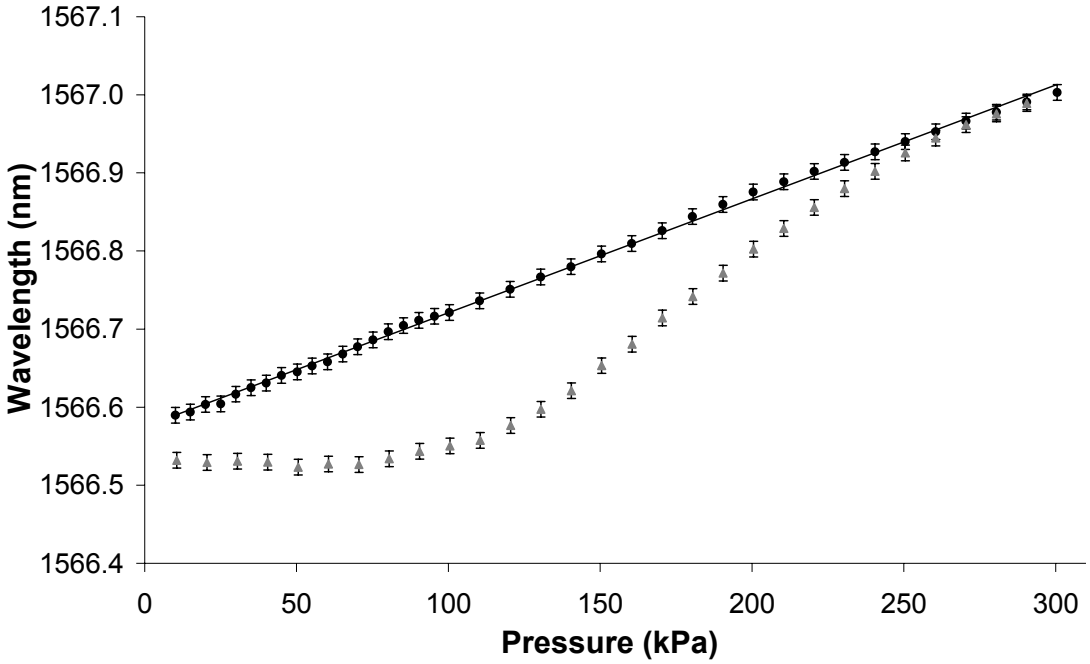

Figure 6-10: Dependence of the central wavelength of the spectral drop-out of a 6 mm long SM FBG which had is central 2mm long section embedded within a 2 mm width by 4 mm length by 3 mm depth epoxy cuboid on the applied pressure. Black (●): increasing pressure; Grey (▲): decreasing pressure

The pressure sensitivity obtained in terms of wavelength shift of the spectral drop-out per applied pressure was 1.5±0.008 pm/kPa. This corresponds to a pressure resolution of 0.67kPa when using an interrogation system with 1 pm resolution.

When the pressure was decreased, the sensor exhibited non-linear behaviour. This is attributed to the cuboid (rectangular prism) geometry of the epoxy. When the load is applied to this cuboid, it initially deforms uniformly until it starts bending (Figure 5-9). During the pressure decrease, as the applied load is decreased, the stress in the epoxy cuboid is different resulting on a different strain applied to the FBG which leads to the non-linear recovering behaviour of the spectral drop-out.

In order to overcome this issue, a new PTFE mould with a 2 mm width by 2 mm length by 2 mm depth cubic hole was produced. A 6 mm long FBG was then positioned in the mould and embedded around its centre with epoxy using the procedure described in section 5.3.1. The new test FBG was placed in the cantilever system and the procedure described above was repeated. Figure 6-11 shows the experimentally determined

evolution of the reflection spectrum of the FBG in response to the pressure. Figure 6-12 shows the dependence of the central wavelength of the spectral drop-out on the applied pressure.

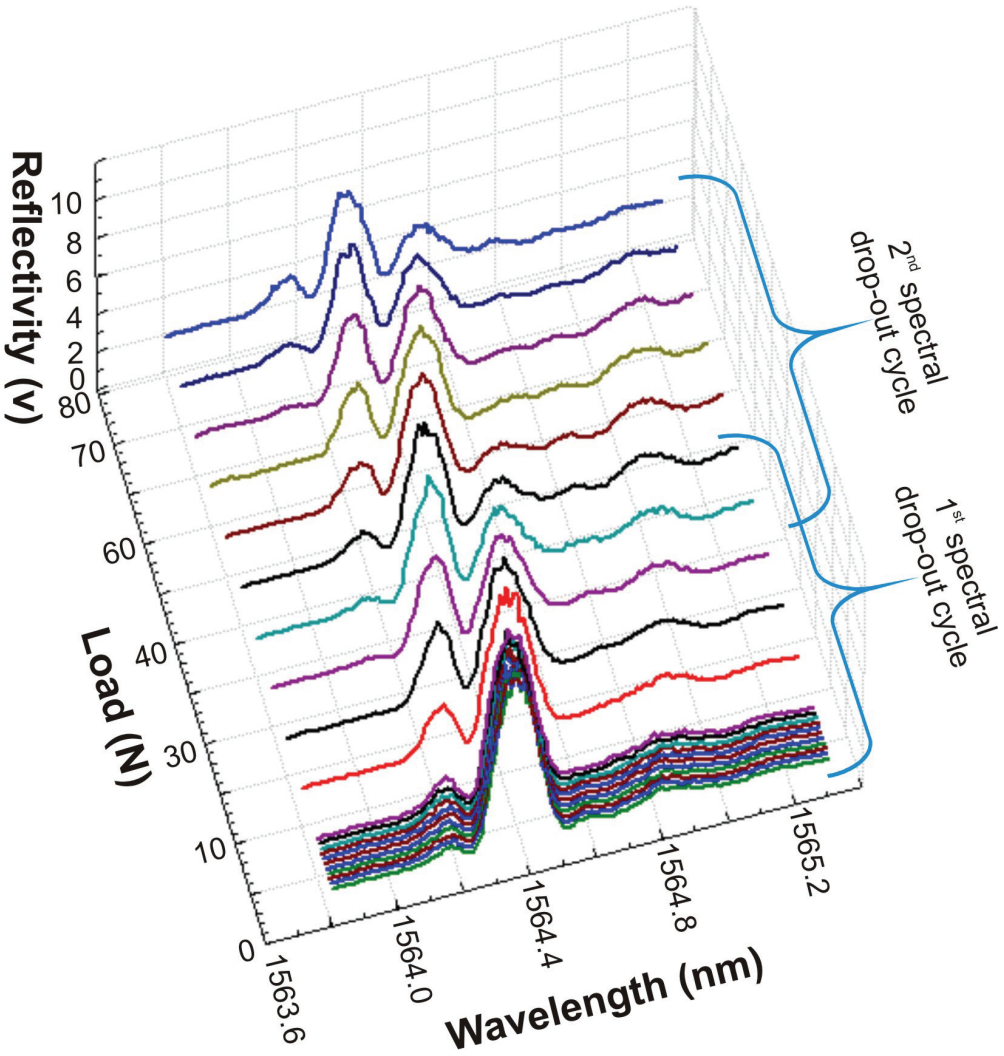

Figure 6-11: Experimentally determined evolution of the reflection spectrum from a 6 mm long SM FBG embedded with epoxy along 2 mm of its centre (cube block) in response to the air pressure applied to the sensor housing (increase) via the pressure transducer Druck DPI-602.

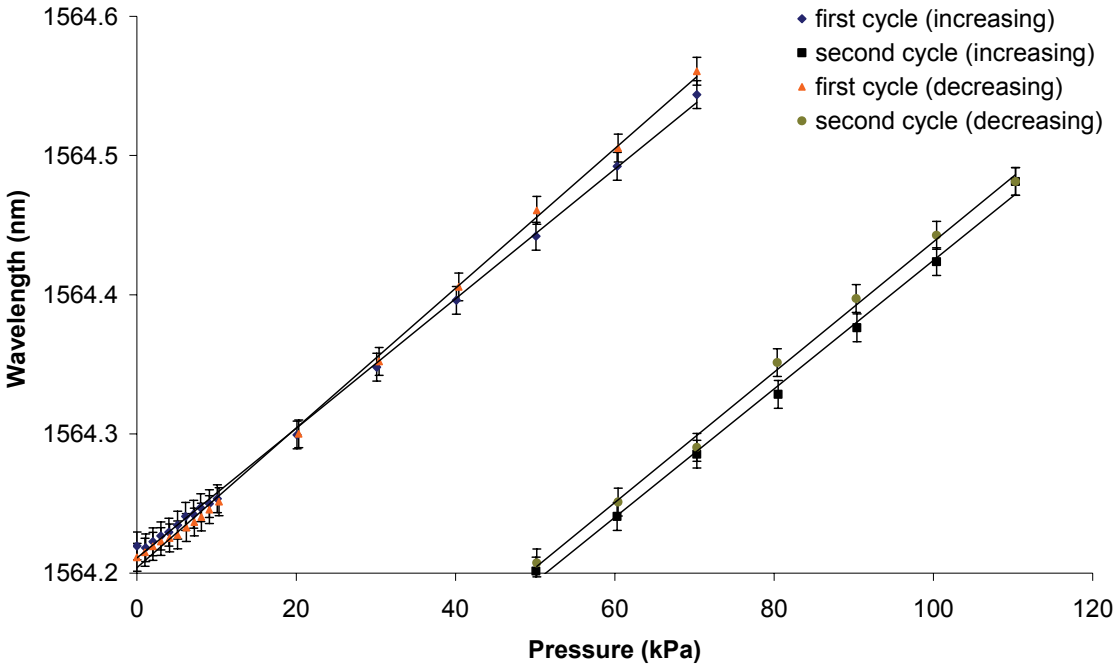

Figure 6-12: Dependence of the central wavelength of the spectral drop-out of a 6 mm long SM FBG embedded with epoxy along 2 mm of its centre (cube block), on the applied pressure.

In Figure 6-12, an hysteresis effect is observed. When the pressure decreases, the central wavelength of the spectral drop-out does not recover to the previous wavelength correspondent to that pressure presenting an higher wavelength value. The measurement range was 110 kPa and two spectral drop-outs were obtained during this range. The reason for the increased sensitivity and thus decreased measurement range is the geometry of the embedded epoxy that is now an equal sided 2 mm cube. The stress exerted on the cuboid due to a load of 10 N is $\sigma_x = \frac{F}{A} = \frac{10}{2\times10^{-3}\times4\times10^{-3}}$ equal to $1.25\text{x}10^6$ N/m^2 whist for a 2 mm equal length cube is $2.5\text{x}10^6$ N/m^2. The higher stress value on the epoxy cube leads to an higher strain over the axial direction where the fibre is located.

The pressure sensitivity obtained in terms of wavelength shift of the spectral drop-out per applied pressure was 4.66±0.04 pm/kPa and 4.61±0.12 pm/kPa for the first and second spectral drop-outs respectively for increasing pressure and 5.02±0.05 pm/kPa and 4.7±0.11 pm/kPa respectively for the first and second spectral drop-outs for decreasing pressure. This corresponds to a pressure measurement resolution of 0.21 kPa

and 0.22 kPa when monitoring the first and second spectral drop-out during the pressure increase and of 0.2 kPa and 0.21 kPa during the decrease in pressure.

6.4 Pore pressure transducer calibration

In field applications, the pore water pressure within the soil changes due to the change of water head and other soil physical factors. After the initial characterisation of the pressure sensor housing, an evaluation and calibration of the pressure sensor was undertaken using water as the pressurised liquid.

Using a 6 mm FBG embedded in a 2 mm equal length cube a pressure measurement range of 100 kPa was obtained (Section 6.3.1). This corresponds to a change of water level of 10 metres. To simulate the change in water level in laboratory conditions, a 900 mm long calibration water pipe with 80 mm of diameter (Figure 6-13) was used.

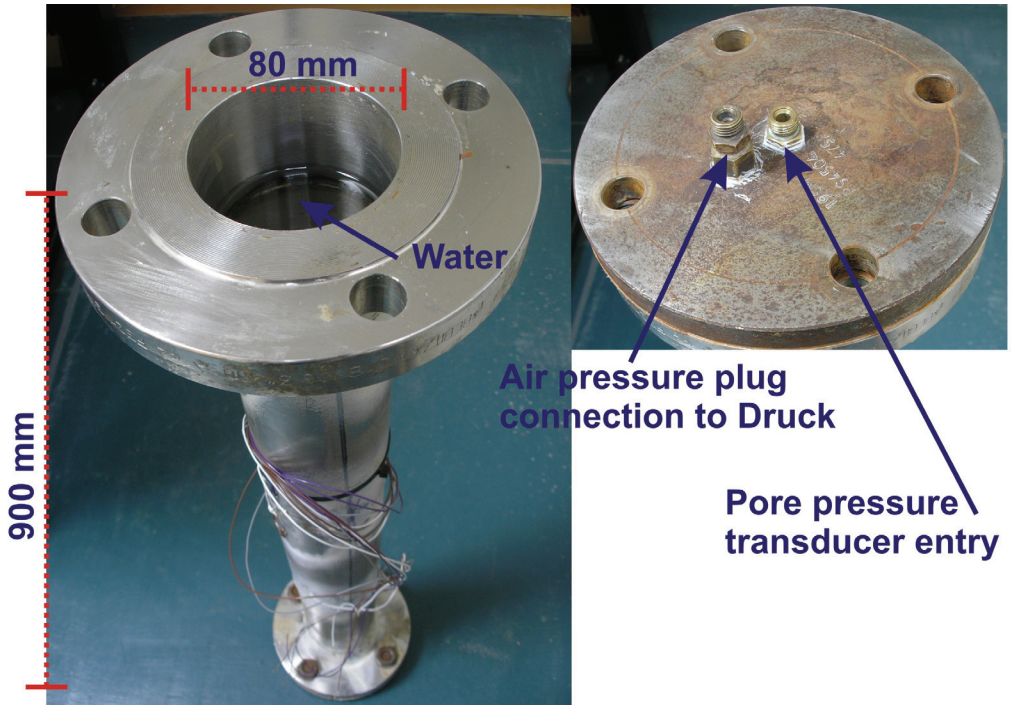

Figure 6-13: Photograph of the calibration water pipe.

The water column pipe was filled with water to a level 50 mm below the top of the column. The pressure transducer (Figure 6-6a) was submerged in the water and the column sealed with the top cap of the water pipe (Figure 6-6b). The pressure transducer was placed at a depth of 830 mm from the water surface. Water was pressurised with

the Druck DPI-602, which was connected to the air entry of the column cap. When the air was pumped into the water pipe, the air present in the pipe was pressurised applying pressure to the water surface and changing the water pressure.

6.4.1 Experimental arrangement

The tunable laser source TUNICS-Plus CL used in the interrogation system presented in Section 4.2 can be used in *step scan* mode or *sweep scan* mode. When used in *step scan* mode, a high scan resolution of up to 1 pm can be obtained, but the scan frequency is as low as 3.4×10^{-5} Hz to scan over a 100 nm range. When used in *sweep scan* mode, a scan resolution better than 1 pm and higher scan frequency of 0.38 Hz can be achieved for a scan over a 100 nm range. For the calibration of the pore water pressure sensor and for future use under field conditions, a high scan frequency is desirable and therefore the laser was used in *sweep scan* mode.

The laser *sweep scan* mode is enabled on the front panel of laser source. After entering the lower and higher wavelength limits and the time interval between each scan, the laser scans over the selected range with a speed of 100 nm/s. The Tunics plus changes the wavelength by varying the angle of the dihedral reflector (see Figure 4.3). This angle change is obtained by the movement of a motor that is connected to the dihedral reflector. When the laser executes a sweep scan, it scans from the lower wavelength limit to the higher wavelength limit and then pauses for an interval of time selected by the user. After the pause, it then scans backwards from the higher wavelength limit to a wavelength below the lower wavelength limit, and then returns to the lower wavelength limit. This acts to eliminate the backlash of the tuning micrometer screw.

The laser model used in this work does not have a trigger output to allow the start of the data acquisition when the laser is scanning. The only available output is a signal that monitors the movement of the motor that changes the dihedral reflector. This motor movement signal was used to allow the start and stop triggering of the data acquisition. Figure 6-14 shows the output signal obtained from the motor trigger.

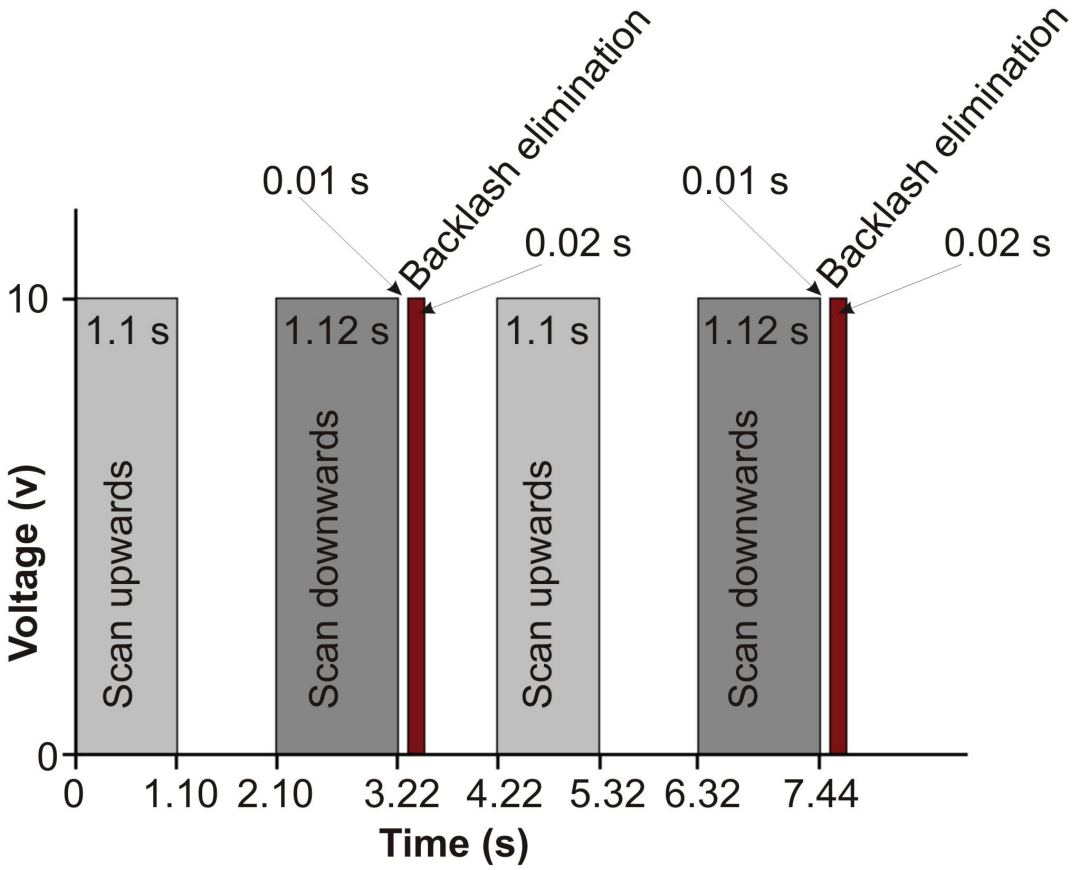

Figure 6-14: Dihedral reflector motor movement output signal.

Three peaks were observed in the trigger signal. The first and second peaks correspond to the upwards and downwards scanning, and the shorter third pulse relates to the movement used to eliminate the backlash of the tuning screw. When monitoring the pulse width of the different peaks, it was observed that the pulse width of the upwards and downwards scan was not constant. This is due to the acceleration and deceleration of the motor. In this work, only the reflection spectrum that corresponds to the upwards scan was acquired. This was achieved by starting the Labview data acquisition program before enabling the sweep scan, so that, on the rising edge of the first trigger signal, data acquisition at a rate of 250k samples per second would start. In order to acquire only during the upward scan of the laser, a counting of the peaks was taken using a counter function in LabView. Ignoring the second and third peaks (downwards and backslash peaks) and acquiring the following one it was possible to lock to the peak correspondent to the upward scan.

As the laser scan speed is 100 nm/s, the duration of one scan should be 1 second. However, the measured value of the trigger peak pulse width was 1.1 seconds. The 0.1 seconds difference is due to the acceleration and deceleration on the first and last 10 nm of the scanning range. Due to this non speed linearity it was not possible to get a linear conversion of the time scale output of the acquired data into a wavelength scale. To overcome this, a temperature stabilised reference FBG with a central wavelength 20 nm higher than the lower wavelength of the scanning limit was used. When the reference FBG peak is detected, the sample acquired for that time corresponds to the central wavelength of the FBG. Moreover, because from that wavelength onwards the scanning speed is constant (100 nm/s), it was then possible to determine the wavelength value of each acquired sample.

6.4.2 Experimental results

The pore pressure transducer, presented in Section 6.2, was calibrated using the water column presented in Figure 6-13. The sensing FBG of length 6 mm and centre wavelength 1564.36 nm was placed in the cantilever system of the pressure transducer. The FBG was embedded over in a 2 mm equal sizes epoxy cube. The experimental setup shown in Figure 4-1 was used to interrogate the transducer, with the laser source running in *sweep scan* mode.

The water column was pressurised using the air pump and precision pressure calibrated transducer over a range of 0 kPa – 100 kPa with 10 kPa increments. The pressure was then decreased to verify if the sensor presented a linear behaviour. Figure 6-15 presents the experimentally determined evolution of the reflection spectrum of the FBG in response to the increase of water pressure. Figure 6-16 shows the dependence of the central wavelength of the spectral drop-out on the applied pressure (pressure increase and decrease).

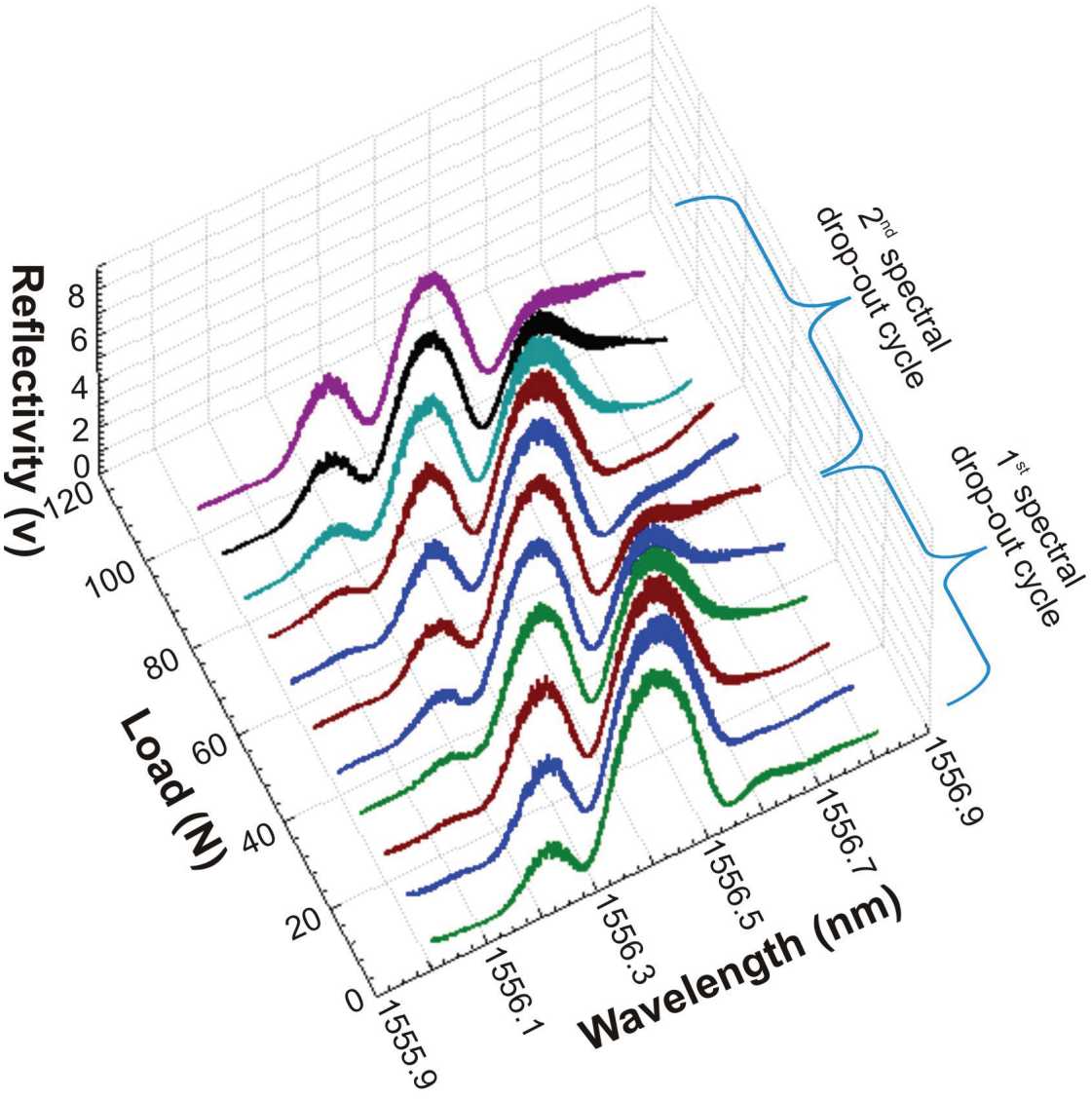

Figure 6-15: Experimentally determined evolution of the reflection spectrum from a 6 mm long SM FBG embedded with epoxy along 2 mm of its centre in response to the applied water pressure (increase).

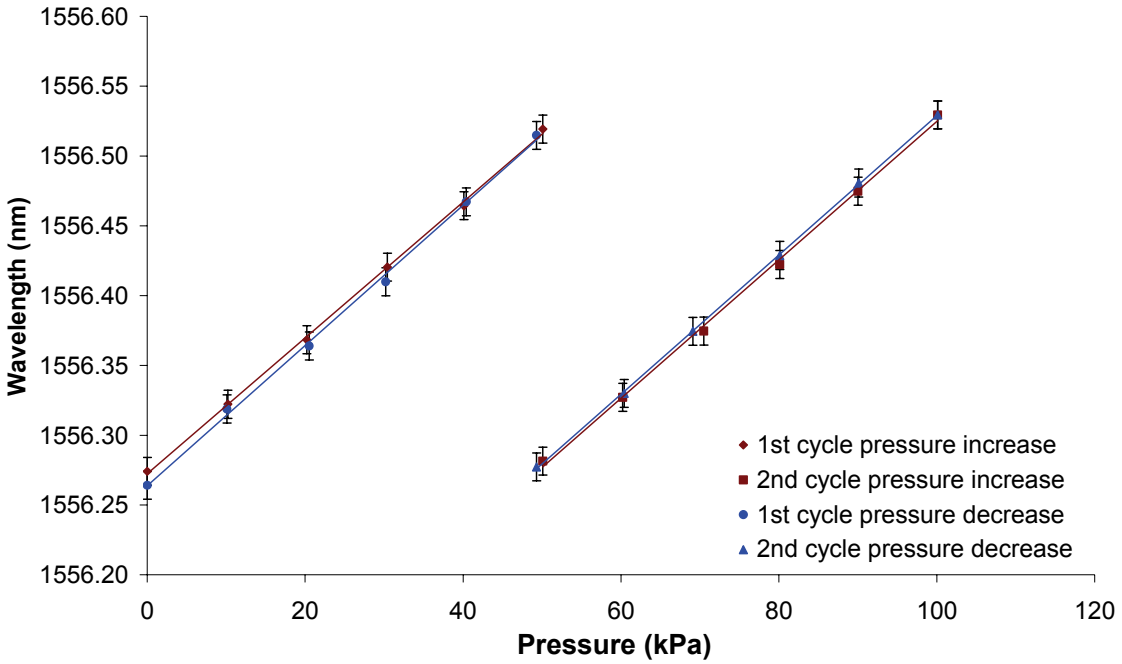

Figure 6-16: Dependence of the central wavelength of the spectral drop-out of a 6 mm long SM FBG embedded with epoxy along 2 mm of its centre on the applied water pressure.

As the pressure that acts on the water surface of the water column pipe increased, the water pressure increased and a spectral drop-out started to appear in the reflection spectrum of the FBG. Two spectral drop-out cycles were observed for a pressure measurement range of 100 kPa. The response of the central wavelength of the spectral drop-out to the increase and decrease of pressure demonstrated good linearity. The pressure sensitivity obtained was 4.86±0.06 pm/kPa and 4.96±0.09 pm/kPa for the first and second spectral drop-outs respectively for increasing pressure and 5.02±0.09 pm/kPa and 4.99±0.05 pm/kPa for the first and second spectral drop-out for decreasing pressure. This corresponds to an average 0.20 kPa pressure measurement resolution obtained when using a 1 pm resolution interrogation system. This sensing resolution corresponds to the measurement of 20 mm change in water level.

To test the long term stability of the pressure transducer, a constant pressure of 27 kPa was applied to the water column pipe over a period of 24 hours and the reflection spectrum of the FBG recorded at different times (Figure 6-17). Figure 6-18 shows the variation of the central wavelength of the spectral drop-out over the 24 hour period

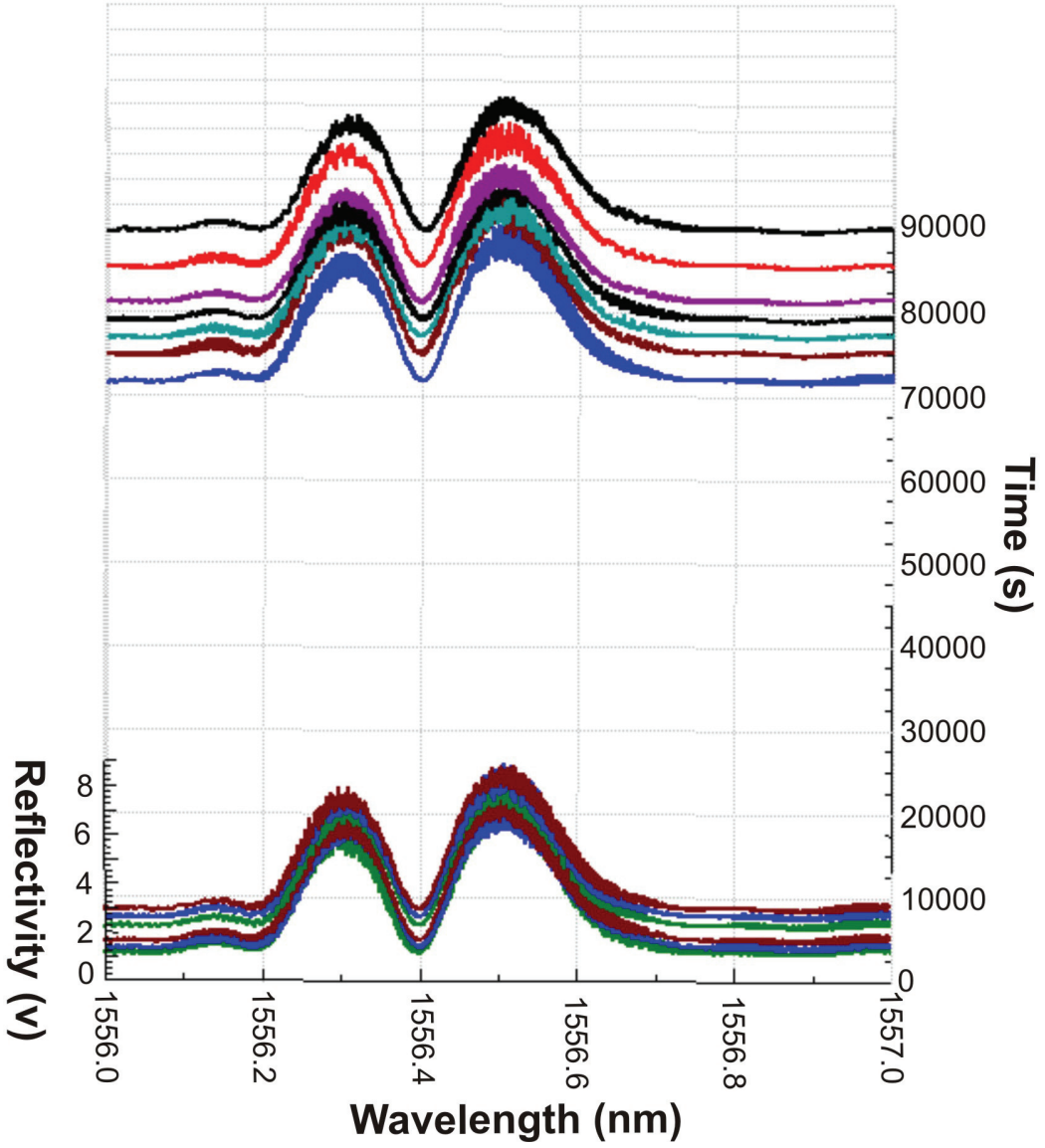

Figure 6-17: Experimentally determined evolution of the reflection spectrum of a 6 mm long SM FBG embedded with epoxy along 2 mm of its centre over 24 hours for a constant applied water pressure of 27 kPa.

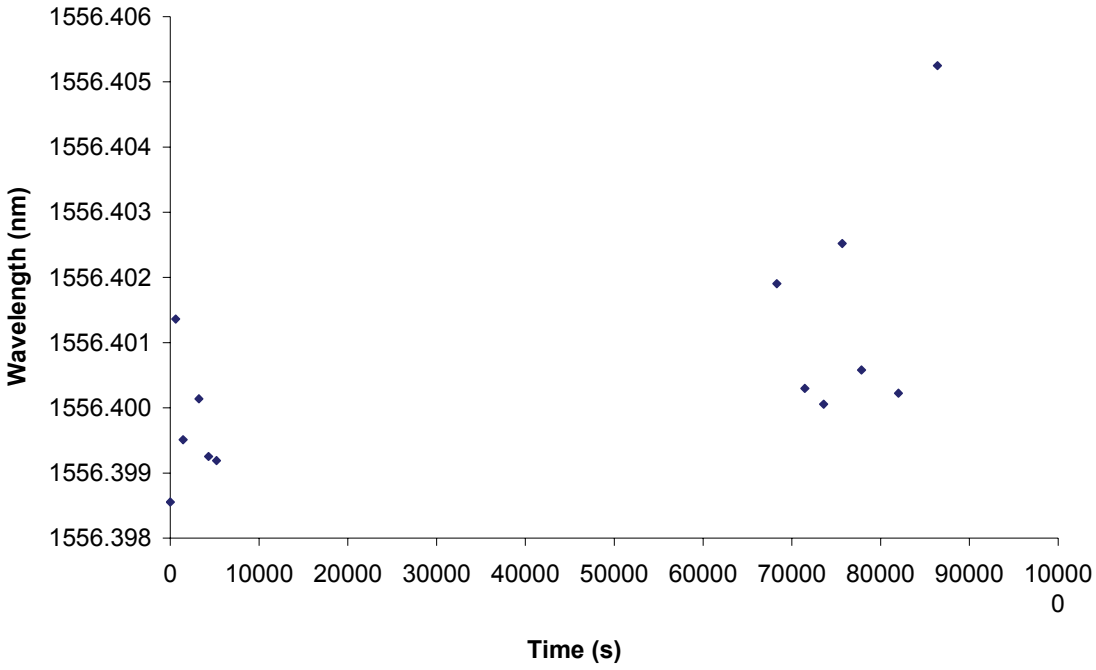

Figure 6-18: Dependence of the central wavelength of the spectral drop-out of a 6 mm long SM FBG embedded with epoxy along 2 mm of its centre over time for a constant applied pressure of 27 kPa.

In Figure 6-18 it can be seen that the central wavelength of the spectral drop-out was kept almost constant over the 24 hours period presenting an average value of 1556.401 nm with a standard deviation of 2 pm which is within the tunable laser accuracy of 10 pm. Hence, the developed transducer exhibits good long term stability.

The repeatability of a sensor is one of its most important performance parameters. To test the repeatability of the pore pressure transducer, the water column pipe was pressurised and depressurised six times over a range of [0 – 100] kPa with 10 kPa increments. Figure 6-19 shows the experimentally determined dependence of the central wavelength of the spectral drop-out on the applied pressure (pressure increase and decrease) for the consecutive measurements.

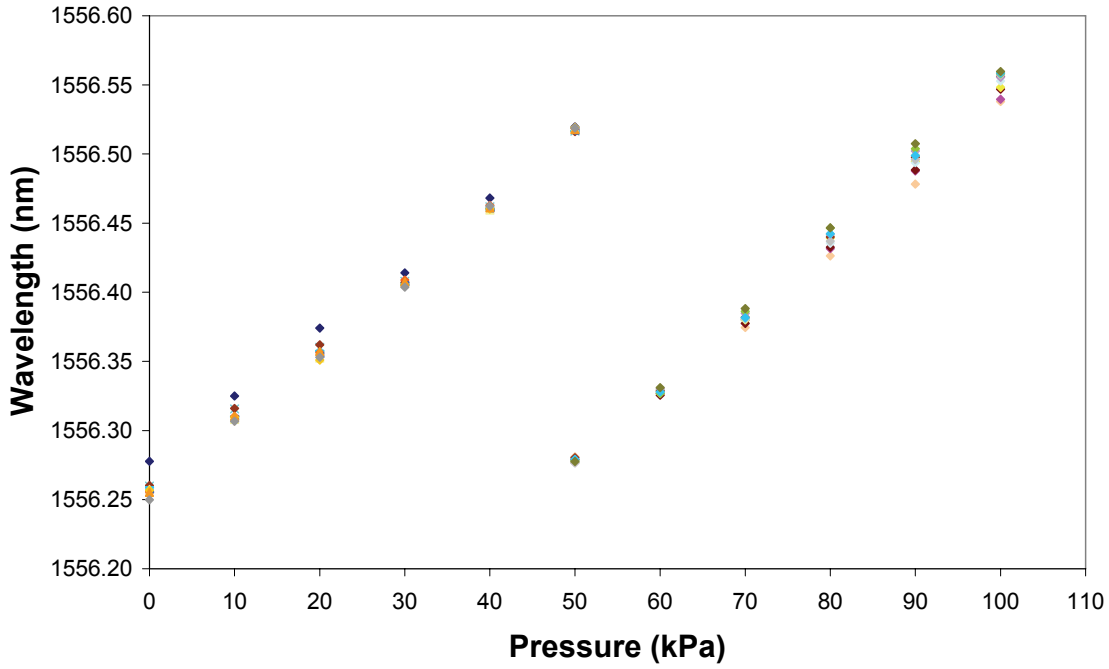

Figure 6-19: Experimentally determined dependence of the central wavelength of the spectral drop-out on the applied water pressure (pressure increase and decrease) for six consecutive measurements.

The first measurement cycle, the sensor demonstrated a similar behaviour to the one observed in Figure 6-16. In this first cycle, the response of the central wavelength of the spectral drop-out exhibits some hysteresis as previously observed during the pre-calibration with air (Figure 6-12). On the second and consecutive measurement cycles, the hysteresis effect was reduced with the response of the spectral drop-out to the applied pressure presenting identical response during the pressure increase and decrease.

The different measurement cycles exhibited some variability as can be observed in Table 6-1, which shows the standard deviation of the response of the spectral drop-out to the applied pressure for all the measurement cycles. Ignoring the first measurement cycle, the response of the spectral drop-out to the applied pressure exhibits a more repeatable behaviour. The highest variability was observed for the extremes of the pressure range (0 and 100 kPa) whilst for a pressure of 50 kPa, a lower standard deviation of 1.5 pm was obtained. The limited repeatability of the pressure sensor is

attributed to the plastic deformation of the rubber membrane. This can be improved by using a thin metallic membrane.

Table 6-1: Standard deviation of the response of the spectral drop-out to the applied pressure for all the six cycles and for the last five measurement cycles.

Pressure (kPa)		Standard deviation (nm)	
		6 cycles	5 cycles
First spectral drop-out	0	0.0068	0.0028
	10	0.0052	0.0027
	20	0.0062	0.0032
	30	0.0027	0.0015
	40	0.0024	0.0013
	50	0.0015	0.0015
Second spectral drop-out	50	0.0014	0.0011
	60	0.0016	0.0017
	70	0.0037	0.0032
	80	0.0061	0.0045
	90	0.0080	0.0055
	100	0.0074	0.0043

6.5 Summary

A pressure sensor that allows the measurement of pore water pressure within soil was developed and characterised. Initial characterisation of the sensor housing using air as the pressurised fluid showed that embedding the central section of the FBG within a cuboid epoxy block did not produce a linear behaviour when subject to consecutive increase and decrease of pressure. To overcome this issue a new PTFE mould was developed and used to embed the central section of the FBG in a 2 mm epoxy cube. This configuration resulted in a linear behaviour to both increasing and to decreasing pressure.

The calibration, long term stability and repeatability analysis of the pressure sensor to the measurement of water pressure were undertaken using a water column designed to simulate a change in water level. The experimental results obtained from the repeatability analysis indicated that, on the first measuring cycle (increase and decrease of pressure), the sensor exhibited hysteresis as previously observed during the pre-calibration with air. Ignoring the first measurement cycle, it was observed that the repeatability of the response of the spectral drop-out to the applied pressure between different measurement cycles exhibits a reasonable repeatable behaviour with the highest variability observed for the extremes of the pressure range used (0 and 100 kPa). For 50 kPa, a lower standard deviation was obtained. The non repeatability of the pressure sensor is attributed to the plastic deformation of the rubber membrane and to the non-repeatable transducing of the load in the cantilever system. The pressure resolution of the developed sensor using a 1 pm resolution interrogation system was 0.20 kPa when monitoring the first and second spectral drop-out during the pressure increase and decrease. This sensing resolution corresponds to the measurement of 20 mm of water level. Regarding the long term stability, the results obtained showed that the sensor provides a stable reading for a fixed applied pressure, with a standard deviation of 2 pm which corresponds to a pressure of 0.4 kPa.

References

Hanna, T. H.:1985 Field Instrumentation in Geotechnical Engineering Trans Tech Publications Germany

Chapter 7

Conclusions and recommendations for future work

7.1 Conclusions

A novel pore pressure sensor was developed in this research study. It is based in transducer water pressure into a transverse load applied over a sub-section of an FBG. A theoretical simulation of the reflection spectrum of an FBG when subject to a transverse load along a sub section of the FBG was undertaken using the transfer matrix method. The effect of the location where the load is applied over the FBG, the length over which it is applied, and the influence of the FBG length on the spectral response of the FBG were analysed and the simulated results were presented in Section 3.4. It was concluded that:

1) The best location to transversely load the FBG was at its centre, resulting in a deep and well resolvable spectral drop-out within the FBG reflection spectrum.

2) A transverse load applied across less than 50% of the FBG length induces a spectral drop-out within the bandwidth of the FBG reflection spectrum. This feature tracks across the bandwidth of the FBG in response to the applied load while the Bragg envelope stays fixed at the original wavelength. When more than 50% of the FBG length was loaded the Bragg envelope suffered a red shift. This red shift of the Bragg envelope is not desirable as it makes it difficult to track the spectral drop-out.

3) The transverse loading of a fixed ratio of loaded to unloaded lengths, but with different total FBG lengths showed that the shorter the FBG the higher the sensitivity to transverse load.

The effect of transversely load a central sub-section of an FBG following the optimised simulated results was experimentally tested. A 6 mm long FBG was transversely loaded using a fibre loading and support structure designed to apply a transverse load onto a 1.05 mm long sub-section of the FBG. The experimental results obtained are qualitatively and quantitatively in agreement with the simulated results. Moreover, this technique allows the independent measurement of pressure and temperature using one single FBG (Section 4.3.2).

The transverse load of the FBG over a small section exhibited good potential for the development of a pore pressure sensor. The main limitation of this technique was the inherent fragility of the fibre to a load applied transversally. Moreover, birefringence is introduced in the optical fibre, which may be a disadvantage when multiplexing this sensor with sensors that are birefringence dependent. To overcome this issue, a method for enhancing the sensitivity of the FBG to transverse load and protect the fibre from mechanical damage was studied.

A novel packaging technique was investigated and is presented in Section 3.5. The packing consisted of embedding the central section of the FBG within an epoxy cube. The deformation of the epoxy cube in response to a transverse load results in the application of an axial strain across the central section of the FBG. The effect of loading the epoxy cube localised at different positions along the FBG and over different lengths was simulated using Rouard's method, being concluded that:

1) The best location to axially strain the FBG is at its centre. Similarly to the transverse load of the FBG, this creates a well defined and deep spectral drop-out within the bandwidth of the FBG reflection spectrum.

2) The effect of straining the FBG at its centre over different lengths was analysed. When 20% of the FBG length was strained, a spectral drop-out appeared within the bandwidth of the FBG reflection spectrum tracking across its bandwidth in response to the applied load while the Bragg envelope stayed at the original wavelength. If more that 50% of the FBG length was strained, the Bragg envelope suffered a red shift.

Based on the theoretically simulated results, an experimental study of the effect of embedding an FBG in an epoxy block around a central sub-section of its length applying a transverse load to the block was analysed. Experimentally, a 2 mm central sub-section of 6 mm FBGs were embedded in blocks of OG-134 UV cured epoxy. The FBG reflection spectrum obtained when a block was subject to a transverse load followed the simulated behaviour. Comparing with the direct load method, the sensitivity increased by a factor of 3. Moreover, this technique produced efficient protection of the optical fibre against mechanical damage. The transverse load of an epoxy block that embedded a 2 mm long central section of a 6 mm FBG written in HiBi fibre shown that the spectral drop-out appeared in the reflection spectrum of both eigenaxes. This effect showed that contrary to the direct transverse load, the transverse load of the epoxy block does not induce birefringence in the optical fibre.

A novel pore pressure sensor that transduces pressure into a transverse load applied to the epoxy cube was developed. A cantilever system that allows for the amplification or de-amplification of the load transmitted through the sensing element was designed and tested. Two types of epoxy blocks were used, a cuboid and cube. Preliminary calibrations of the sensor housing using air were undertaken. The continuous change of pressure applied to the cuboid shown a non linear behaviour with decreasing load. Such effect was not observed using an equal length cube.

A pressure resolution of 0.2 kPa over a measurement range of 100 kPa was obtained when the pressure sensor transducer was calibrated in a pipe with water. The pressure resolution achieved satisfies the established resolution requirements for monitoring pore pressure in soils. The measurement range of 100 kPa is considered suitable and further enhancement is possible.

7.2 Additional considerations and recommendations for future work

7.2.1 Pore pressure transducer

In Section 6.4.2 it was shown that the sensor developed exhibited a hysteresis effect which is attributed mainly to the rubber membrane used to sense pressure. For future optimisation of the sensor the use of a thin metallic plate to eliminate/reduce the hysteresis effect should be investigated.

An improvement of the developed pore pressure transducer to measure negative pore water pressure is suggested. Negative pore water pressure can be defined as the condition where soil water is held largely under a state of tension within the soil by capillary forces resulting on a pressure smaller than atmospheric pressure. The measurement of negative pore water pressure could be achieved by inducing a pre-load on the piston by means of a spring such that for "zero pressure" the spectral drop-out would be positioned within the reflection Bragg spectrum. Negative pore water pressure acting on the diaphragm would then pull the piston releasing the pre-applied load and inducing the shift of the spectral drop-out to its original position. Figure 7-1 shows a schematic representation of this device.

An analysis of the capability of this sensor to discriminate between the effects of pressure and temperature using a single optical fibre would be beneficial. Similarly to the transverse load of a central section of an FBG, the wavelength shift of the spectral drop-out within the bandwidth of the FBG is mainly sensitive to pressure, whilst temperature affects the position of the Bragg envelope. With the configuration used in this work, there could be a thermal gradient across the embedded FBG in the epoxy block. This thermal gradient can be decreased if the FBG is centrally embedded in an epoxy block and a thin coating of the epoxy is placed over the sides of the FBG (Figure 7-2).

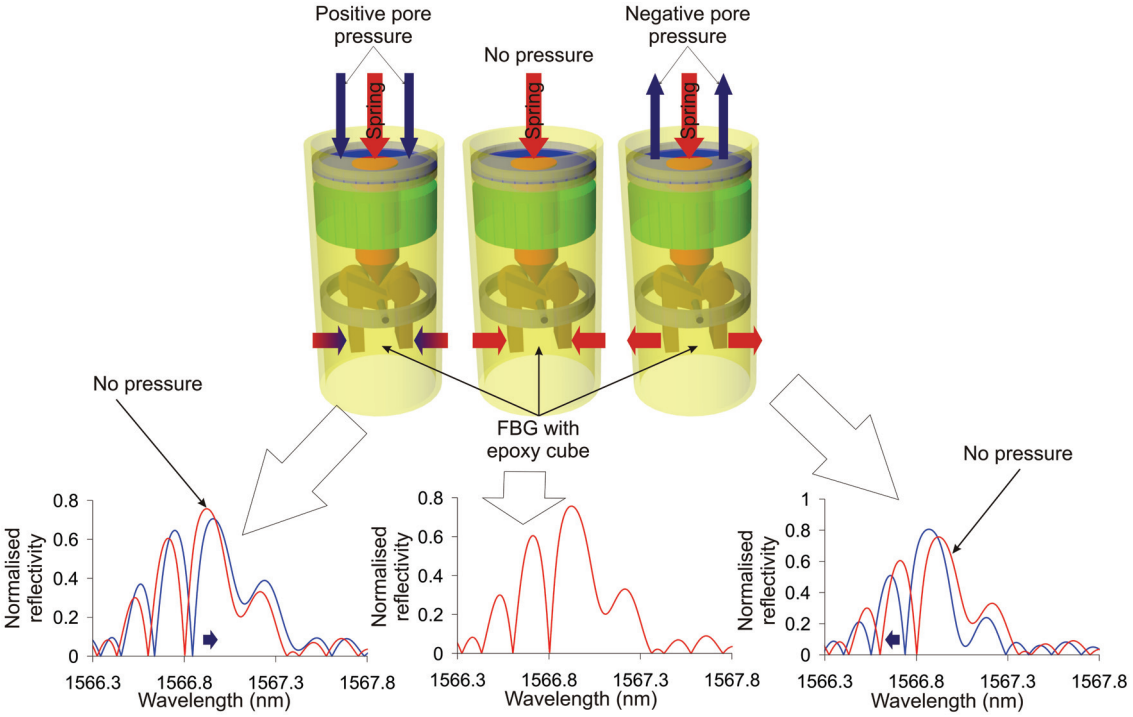

Figure 7-1: Schematic diagram a negative pore pressure sensor and the FBG reflection spectrum that could be obtained depending of the pressure (positive or negative) acting on the membrane.

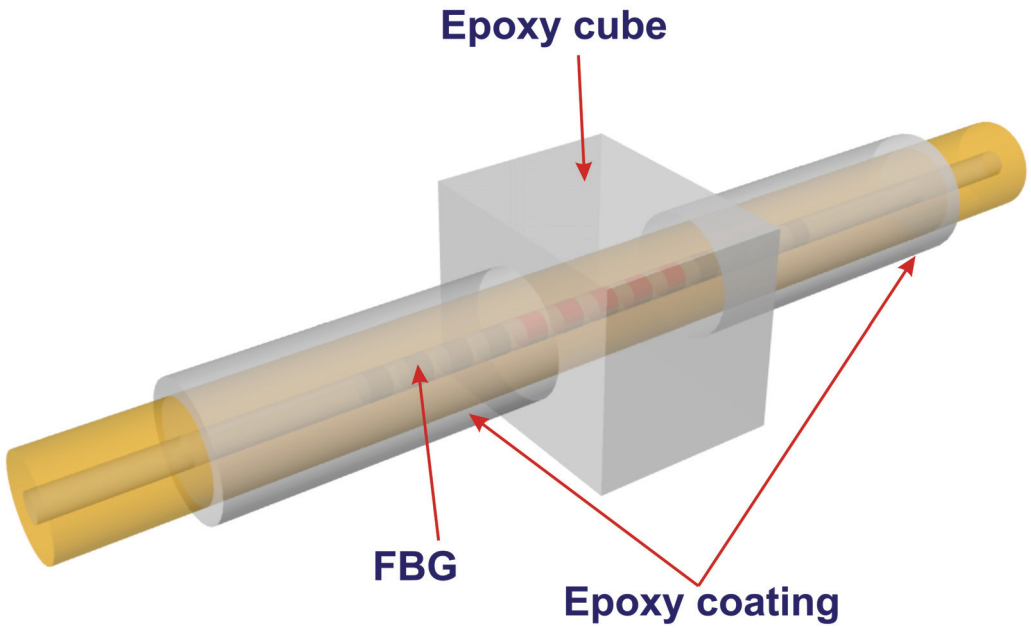

Figure 7-2: Schematic diagram of an FBG embedded around its centre with an epoxy cube and with a thin epoxy coating over the sides.

7.2.2 Transverse load of partially embedded chirped FBGs

The transverse loading of an epoxy cube that embeds a central section of a chirped FBG is suggested as further work. In 2003, Torres *et al.* simulated the effect of applying a transverse load to a 4 cm long linear chirped FBG at different positions. They observed that a spectral drop-out was induced in the reflection spectrum. When the same load was applied over different positions of the FBG the position of the spectral drop-out was dependent on the location of the load. As the bandwidth of a chirped FBG is high compared to an un-chirped FBG this technique may offer the potential to improve not only the pressure sensitivity but also the pressure measurement range.

7.2.3 Micromachining of an FBG along a central sub-section

If an FBG is micromachined all around a central sub-section of its length, a spectral drop-out is induced in the FBG reflection spectrum due to the local refractive index change over the FBG central section that changes the optical path between the two resulting sub-gratings (Iadicicco *et al.*, 2007). Moreover as the fibre diameter is reduced, the axial strain sensitivity over that region increases. To improve the sensor sensitivity, the FBG could be micromachined over a central sub section of its length. Embedding of the micromachined region in an epoxy cube could offer protection of the fibre and allow efficient transfer of the transverse load into axial strain. Figure 7-3 presents a schematic diagram of such structure. Two main techniques could be used to micromachine an optical fibre: chemical etching using Hydrofluoric acid (Cusano *et al.*, 2005; Pereira *et al.*, 2004 and Kamikawachi *et al.*, 2008) and femtosecond laser micromachining (Alemohammad *et al.*, 2008). Femtosecond laser micromachining is preferable to chemical etching as it is maskless, flexible, fast and less hazardous.

Another potential use of this micromachined FBG could be to sense pressure through deformation of a thin-plate. The micromachined section of an FBG could be glued to the centre of a thin-plate (Figure 7-4). When the thin-plate deforms in response to the applied load resultant from the applied pressure, an axial stretching of the micromachined region would induce a wavelength shift of the spectral drop-out.

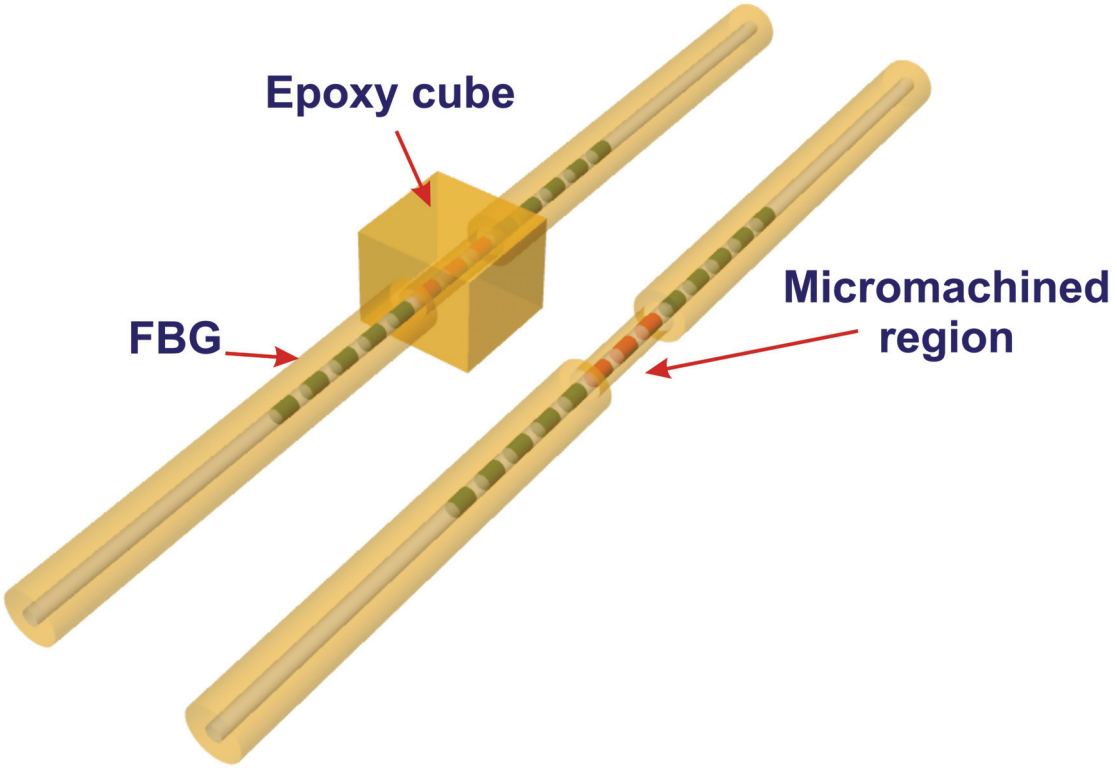

Figure 7-3: Schematic diagram of an FBG micromachined around its centre and embedded in an epoxy cube.

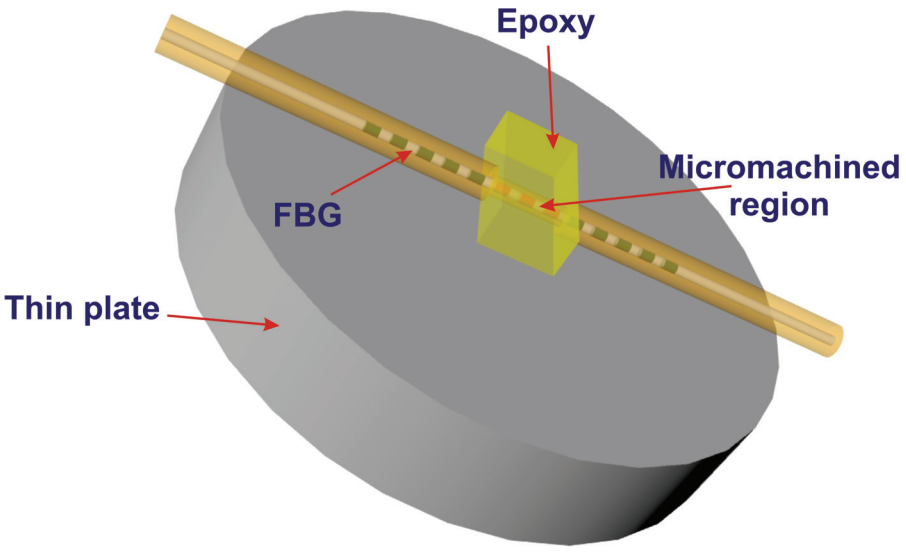

Figure 7-4: Schematic diagram of an FBG which micromachined region is glued to a thin metallic plate.

7.2.4 Pi-phase shift FBG embedded in resin

In section 5.4.2 an approach to obtain a spectral drop-out within the reflection spectrum of an FBG was presented. This attempted to pre-strain the central section of an FBG embedded in an epoxy block. It was observed that the epoxy block could not maintain the pre-applied strain due to the smaller Young's modulus of the epoxy compared to the fibre. An alternative solution would be to fabricate a π-phase shift FBG that contains a spectral drop-out in the middle of the FBG bandwidth and embed the central section in an epoxy cube. When the transverse load is applied to the epoxy, the spectral drop-out would suffer a red shift with the increasing load. Figure 7-5 presents the reflection spectrum of a 6 mm long π-phase shift FBG with central wavelength 1551.4 nm obtained by Edmon Chehura, Cranfield University.

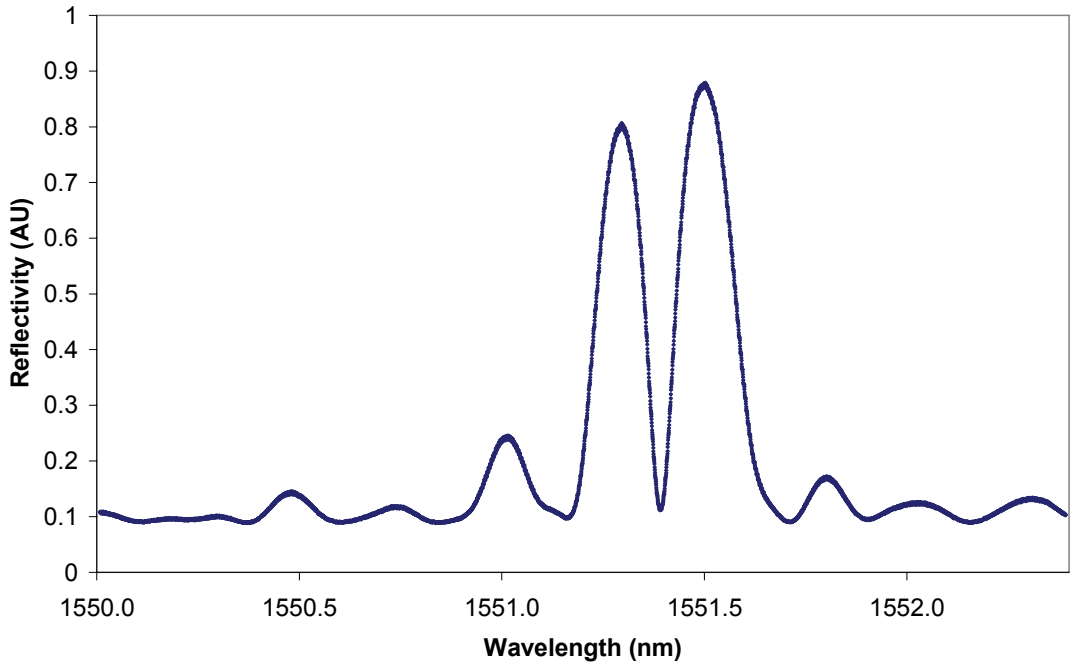

Figure 7-5: Experimentally obtained reflection spectrum of a 6 mm long π-phase shift FBG with central wavelength 1551.4 nm obtained by Edmon Chehura, Cranfield University.

7.3 Summary

This research study contributed with new insights in the employment of locally transverse load FBGs to develop pressure sensors. A novel pore pressure sensor capable of measuring pore water pressure within the soil was developed using a novel packaging technique that consisted of embedding the central section of an FBG within an epoxy cube. The developed sensor transduces pressure applied to a membrane into a transverse load applied through a cantilever system that allows the amplification or de-amplification of the load. Future improvement of the developed sensor may allow the measurement of both positive and negative pore water pressure. The micromachining of the optical fibre along the central section where the FBG is located will offer the possibility to develop a pressure sensor with higher sensitivity allowing the manufacturing of a more compact sensor. The future study of the effect of transverse load a chirped FBG will offer the potential of improving the measurement range due to the higher bandwidth of its reflection spectrum compared to a uniform FBG.

References

Alemohammad, H., Toyserkani, E. and Pinkerton, A. J.:2008 Femtosecond laser micromachining of fibre Bragg gratings for simultaneous measurement of temperature and concentration of liquids

Cusano, A., Iadicicco, A., Campopiano, S., Giordano, M. and Cutolo, A.:2005. Thinned and micro-structured fibre Bragg gratings: towards new all-fibre high-sensitivity chemical sensors. *Journal of Optics A*: Pure and applied optics. **7** (734-741)

Iadicicco, A., Campopiano, S., Paladino, D., Cutolo, A. and Cusano, A.:2007. Micro-structured fiber Bragg gratings: optimization of the fabrication process. *Optics Express* **23** (15011-15021)

Kamikawachi, R., Abe, I., Paterno, A., Kalinowski, H., Muller, M., Pinto, J. and Fabris, J.:2008 Determination of thermo-optic coefficient in liquids with fiber Bragg grating refractometer. *Optics Communications*. **281** (621–628)

Pereira, D., Frazão, O. and Santos, J.:2004 Fiber Bragg grating sensing system for simultaneous measurement of salinity and temperature. *Optical Engineering* **43** (288–304)

List of publications

Correia R., Chehura, E., James, S. W. and Tatam, R. P.: 2007. A pressure sensor based upon the transverse loading of a sub-section of an optical fibre Bragg grating. *Measurement Science and Technology*. **18** (3103-3110).

Correia R., Li J., James, S. W. and Tatam R. P.: 2007. Fibre optic pressure sensor for geotechnical applications, *in 2nd International Workshop on Opto-electronic Sensor-based Monitoring in Geo-engineering Technical Digest*.

Correia R., Chehura E., James S. W. and Tatam R.: 2007. Transversely loaded fibre Bragg grating for pressure measurements, *Proc. SPIE Int. Soc. Opt. Eng. 6619, 66191A*.

Correia, R., Chehura, E., James, S. W. and Tatam, R. P.:2007. Innovations in fibre optic technology for pressure sensing applications. *SET for Britain presentations at the House of Common*. London.

Correia R., Chehura E., Li J., James, S. W. and Tatam R. P.: 2007. Pressure sensors based upon the transverse loading of fibre Bragg gratings. *Presented at the IoP meeting on In-Fibre Gratings and Special Fibres, Coventry, October 2007*.

Correia R., Chehura E., James S. W. and Tatam R. P.: *2006*. Locally pressed Fibre Bragg Grating Pressure Sensor. *in 18th International Optical Fiber Sensors Conference Technical Digest (Optical Society of America, Washington, DC) TuE32*.

Correia R., Chehura E., James S. W. and Tatam R.: 2006. Experimental and theoretical study of locally transverse loaded fibre Bragg gratings for pressure sensing applications, *in Photon06 Conference Technical Digest*.

Appendix A1

Programming code of the transfer matrix method Matlab simulation program of fibre Bragg gratings under partial transverse load

```
clear all
format long
tic

sr=600; %Number of Sections
points=1500; %Spectrum resolution
dneffmax=0.5e-4; % peak value of the dc effective index of refraction change
neff=1.4465;
lambdaBx=1546.94e-9; %Designed Bragg wavelength x
lambdaBy=1546.94e-9; %Designed Bragg wavelength y
periodstart=(lambdaBx./(2.*neff)); %period
lambdamin=1546.5e-9; %Spectrum lower wavelength
lambdamax=1548e-9; %Spectrum higher wavelength
L=6e-3; % FBG length
lambda=linspace(lambdamin,lambdamax,points);
lambda=repmat(lambda,sr,1);
period=periodstart*ones(sr,points);

%phase shift

%location of phase shift
lps=0*L;
lps=floor(sr*(lps+L/2)/L)./2;
ps=4*pi/8;
ko=2.*pi./lambda;

dn=dneffmax*ones(sr,points);
dz=L/sr;
v=0.17;
p11=0.121; %strain optic tensor coefficients
p12=0.27; %strain optic tensor coefficients
LF=1*10^-3; %length of fibre subject to perturbation

initialpos=250; %Initial section over which the perturbation is applied
finalpos=350; %Last section over which the perturbation is applied

kapadc=4*pi*dn./lambda; %DC coupling coefficient
kapaac=kapadc./2; %AC coupling coefficient
```

```
deltax=kapadc+2.*pi.*neff.*(1./lambda-1./lambdaBx);
deltay=kapadc+2.*pi.*neff.*(1./lambda-1./lambdaBy);
alphax=sqrt(kapaac.^2-deltax.^2);
alphay=sqrt(kapaac.^2-deltay.^2);

T11x=cosh(alphax.*dz)-i*(deltax./alphax).*sinh(alphax.*dz);
T22x=cosh(alphay.*dz)+i*(deltay./alphay).*sinh(alphay.*dz);
T12x=-i*(kapaac./alphax).*sinh(alphax.*dz);
T21x=i*(kapaac./alphay).*sinh(alphay.*dz);

T11y=T11x;
T22y=T22x;
T12y=T12x;
T21y=T21x;
x=[];

% aviobj = avifile('Fbgmatrix_thesis_direct_load_amended.avi','fps',1.5,'quality',100);
% set(gcf,'NextPlot','replace','Visible','off');

for fc=0:40:400 % Applied force range and increment

fcm=fc/6;     %N/m
E=71705475836.8; %Optical fibre Young's modulus

%change of wavelength due to applied load
if fc==0
   lambdaBfx=lambdaBx;
   lambdaBfy=lambdaBy;
else
lambdaBfx=lambdaBx+(lambdaBx.*(-1*(neff.^2*(1+v))/(2*E))*((1-
v)*(p11*((fcm/(LF))*(5034.192159))+p12*((fcm/(LF))*(-15338.15406)))-
v*((fcm/(LF))*(5034.192159)+(fcm/(LF))*(-15338.15406))))
lambdaBfy=lambdaBy+(lambdaBy.*(-1*(neff.^2*(1+v))/(2*E))*((1-
v)*(p11*((fcm/(LF))*(-15338.15406))+p12*((fcm/(LF))*(5034.192159)))-
v*((fcm/(LF))*(5034.192159)+(fcm/(LF))*(-15338.15406))))
end

ko2=2*pi./(lambda);
kapadc2=4*pi*dn./(lambda);
kapaac2=kapadc2./2;

delta2x=kapadc2+2.*pi.*neff.*(1./lambda-1./lambdaBfx);
delta2y=kapadc2+2.*pi.*neff.*(1./lambda-1./lambdaBfy);
alpha2x=sqrt(kapaac2.^2-delta2x.^2);
alpha2y=sqrt(kapaac2.^2-delta2y.^2);

T112x=cosh(alpha2x.*dz)-i*(delta2x./alpha2x).*sinh(alpha2x.*dz);
T112y=cosh(alpha2y.*dz)-i*(delta2y./alpha2y).*sinh(alpha2y.*dz);
```

```
T222x=cosh(alpha2x.*dz)+i*(delta2x./alpha2x).*sinh(alpha2x.*dz);
T222y=cosh(alpha2y.*dz)+i*(delta2y./alpha2y).*sinh(alpha2y.*dz);
T122x=-i*(kapaac2./alpha2x).*sinh(alpha2x.*dz);
T122y=-i*(kapaac2./alpha2y).*sinh(alpha2y.*dz);
T212x=i*(kapaac2./alpha2x).*sinh(alpha2x.*dz);
T212y=i*(kapaac2./alpha2y).*sinh(alpha2y.*dz);

for q=1:points
  MATx=[1 0;0 1];
  MATy=[1 0;0 1];
  for p=sr:-1:1
     if ((p>=initialpos)&(p<=finalpos));
      Tx(1,[1,2],p,q)=[T112x(p,q) T122x(p,q)];
      Ty(1,[1,2],p,q)=[T112y(p,q) T122y(p,q)];
      Tx(2,[1,2],p,q)=[T212x(p,q) T222x(p,q)];
      Ty(2,[1,2],p,q)=[T212y(p,q) T222y(p,q)];
      else
      Tx(1,[1,2],p,q)=[T11x(p,q) T12x(p,q)];
      Ty(1,[1,2],p,q)=[T11y(p,q) T12y(p,q)];
      Tx(2,[1,2],p,q)=[T21x(p,q) T22x(p,q)];
      Ty(2,[1,2],p,q)=[T21y(p,q) T22y(p,q)];
      end
         phi=0;
    MATx([1 2],[1 2])=MATx([1 2],[1 2])*Tx([1 2],[1 2],p,q)*[exp(-i*phi/2) 0;0
exp(i*phi/2)];
    MATy([1 2],[1 2])=MATy([1 2],[1 2])*Ty([1 2],[1 2],p,q)*[exp(-i*phi/2) 0;0
exp(i*phi/2)];
  end
  Rx(q)=abs(MATx(2)/MATx(1));
  Ry(q)=abs(MATy(2)/MATy(1));
  R(q)=0.85.*Rx(q)+0.15.*Ry(q);
end
   if fc==0
      x=[lambda(1,:)'.*10^9 R'];
   end
   if fc>0
      x=[x R'];
   end
%    plot(lambda, R)
%    xlabel('Wavelength')
%    ylabel('Reflectivity')
%
%    frame = getframe(gcf);
%    aviobj = addframe(aviobj,frame);
end
x=x';
fid =
fopen('Fbgmatrix(lambdaB)_direct_6mm_FBG_centre_1mm_higher_loads.xls','w');
```

```
fprintf(fid,'%6.13f\t %f\t %f\t %f\t %f\t %f\t %f\t %f\t %f\t %f\t %f\t %f\n',x);
fclose(fid)
% aviobj = close(aviobj);
toc
warndlg('End','!! Warning !!')
```

Appendix A2

Programming code of the Rouard's method Matlab simulation program of epoxy embedded fibre Bragg gratings under partial transverse load

```
clear all
clc
format long
tic;

disp('calculating Bragg grating spectrum!!!!!!!')

neff=1.4465;
dneffmax=1.6e-4; %peak value of the dc effective index of refraction change
lambda=1566.673e-9; %Designed Bragg wavelength
lambdamin=1566.286e-9; %Spectrum lower wavelength
lambdamax=1568.156e-9; %Spectrum higher wavelength
L=6e-3; % FBG length
period=(lambda./(2.*neff)) %period
nperiods=L/period; %number of periods

a = round(2*nperiods)/2;
whole = floor(a);
part = a-whole;

if part > 0 % to ensure that the number of half periods is even
   nhalfperiods=round(2*nperiods)+1;
else
   nhalfperiods=round(2*nperiods);
end
strainmatrix=[];
L=(nhalfperiods/2)*period % ajusted length of the grating
finall=[];
LF=2e-3; %length of fibre subject to perturbation
fhalfperiods=round((LF)*nhalfperiods/L); %number of half periods under the applied
force
a = fhalfperiods/2;
whole = floor(a);
part = a-whole;
```

```
if part > 0 % to ensure that the number of half periods under the applied force is even
   fhalfperiods=fhalfperiods+1;
else
   fhalfperiods=fhalfperiods;
end

LF=L*fhalfperiods/nhalfperiods %length of the applied force adjusted

a = round((nhalfperiods/2)-(fhalfperiods/2))/2;
whole = floor(a);
part = a-whole;

if part > 0 % to ensure that is even
   Llimit=(nhalfperiods/2)-(fhalfperiods/2)+1 %first halfperiod under the force
   Hlimit=(nhalfperiods/2)+(fhalfperiods/2)+1 %last halfperiod under the force
else
   Llimit=(nhalfperiods/2)-(fhalfperiods/2) %first halfperiod under the force
   Hlimit=(nhalfperiods/2)+(fhalfperiods/2) %last halfperiod under the force
end

v=0.17; %Fibre Poissons ratio
p11=0.121; %strain optic tensor coefficients
p12=0.27; %strain optic tensor coefficients

nl=neff; %Low refractive index
nh=neff+dneffmax; %high refractive index
r=[(nl-neff)/(nl+neff)]; %interface reflection
rodd=(nh-nl)/(nh+nl); %interface reflection
reven=(nl-nh)/(nl+nh); %interface reflection
mnlnh=[];

for n=1:2:nhalfperiods
   mnlnh=[mnlnh; nl; nh];
end
mnlnh = mnlnh(1:nhalfperiods,1);

for i=1:2:nhalfperiods+1
   r=[r; rodd; reven];
end

r=r(1:nhalfperiods,1);

%force
for fc=0:0.4713:11.7825 % Applied force range and increment


   fcm=fc/2;     %N/m
   Efibre=71705475836.8; %Optical fibre Young's modulus
```

```
    Eresin=689480000; %Epoxy Young's modulus
    vresin=0.4; %Epoxy Poissons ratio
    strain=vresin*((fcm/(LF*LF))/Eresin); %strain to be applied to the fibre due to
defoormation of the epoxy
 strainmatrix=[strainmatrix strain];

    if fc==0
        periodf=period;
        neff2=0;
    else

periodf=period*(1+(1-(neff^2/2)*(p12-v*(p11-p12)))*strain); %new strain induced
period
neff2=0;

     end

    nlf=nl+neff2;
    nhf=nh+neff2;
    roddf=(nhf-nlf)/(nhf+nlf);
    revenf=(nlf-nhf)/(nlf+nhf);

    for n=Llimit:2:Hlimit-2
        mnlnh(n:n+1,1)=[nlf;nhf];
    end

    for i=Llimit+1:2:Hlimit+1-2
        r(i,1)=revenf;
        r(i+1,1)=roddf;
    end

    r(nhalfperiods+1,1)=(neff-nh)/(neff+nh);
    final=[];

    for lambdai=lambdamin:0.001e-9:lambdamax
        ro=(r(2,1)+r(1,1)*exp(-2i*(2*pi*nl*(period/2)/lambdai)))/(1+r(1,1)*r(2,1)*exp(-
2i*(2*pi*nl*(period/2)/lambdai)));
        n=1;

        for j=2:2:Llimit-2
            ro=(r(j+1,1)+ro*exp(-
2i*(2*pi*mnlnh(j,1)*(period/2)/lambdai)))/(1+r(j+1,1)*ro*exp(-
2i*(2*pi*mnlnh(j,1)*(period/2)/lambdai)));
            ro=(r(j+2,1)+ro*exp(-
2i*(2*pi*mnlnh(j+1,1)*(period/2)/lambdai)))/(1+r(j+2,1)*ro*exp(-
2i*(2*pi*mnlnh(j+1,1)*(period/2)/lambdai)));
            n=n+2;
        end
```

```
        for j=Llimit:2:Hlimit-2
            ro=(r(j+1,1)+ro*exp(-
2i*(2*pi*mnlnh(j,1)*(periodf/2)/lambdai)))/(1+r(j+1,1)*ro*exp(-
2i*(2*pi*mnlnh(j,1)*(periodf/2)/lambdai)));
            ro=(r(j+2,1)+ro*exp(-
2i*(2*pi*mnlnh(j+1,1)*(periodf/2)/lambdai)))/(1+r(j+2,1)*ro*exp(-
2i*(2*pi*mnlnh(j+1,1)*(periodf/2)/lambdai)));
            n=n+2;
        end

        for j=Hlimit:2:nhalfperiods-1
            ro=(r(j+1,1)+ro*exp(-
2i*(2*pi*mnlnh(j,1)*(period/2)/lambdai)))/(1+r(j+1,1)*ro*exp(-
2i*(2*pi*mnlnh(j,1)*(period/2)/lambdai)));
            ro=(r(j+2,1)+ro*exp(-
2i*(2*pi*mnlnh(j+1,1)*(period/2)/lambdai)))/(1+r(j+2,1)*ro*exp(-
2i*(2*pi*mnlnh(j+1,1)*(period/2)/lambdai)));
            n=n+2;
        end
            ro=(r(nhalfperiods,1)+ro*exp(-
2i*(2*pi*nh*(period/2)/lambdai)))/(1+r(nhalfperiods,1)*ro*exp(-
2i*(2*pi*nh*(period/2)/lambdai)));

        final=[final; lambdai abs(ro) imag(ro)/real(ro)];
    end
%     plot(final(:,1)',final(:,2)')
%     xlabel('Wavelength')
%     ylabel('Reflectivity')
%     title(fcm)
    if fcm==0
       finall=[(1*10^9*final(:,1))];
    end
    finall=[finall final(:,2)];
end


fid = fopen('ROUARDS_METHOD_CUBE_amended.xls','w');
% fprintf(fid,'%6.13f\t %f\t %f\t %f\t %f\t %f\t %f\t %f\t %f\t %f\t %f\t %f\n',finall');
fprintf(fid,'%6.13f\t %f\t %f\t %f\t %f\t %f\t %f\t %f\t %f\t %f\t %f\t %f\t %f\t %f\t
%f\t %f\t %f\t %f\t %f\t %f\t %f\t %f\t %f\t %f\t %f\t %f\t %f\t %f\n',finall');
fclose(fid)

fid = fopen('ROUARDS_METHOD_CUBE_amended_strain.xls','w');
fprintf(fid,'%f\t %f\t %f\t %f\t %f\t %f\t %f\t %f\t %f\t %f\t %f\t %f\t %f\t %f\t %f\t
%f\t %f\t %f\t %f\t %f\t %f\t %f\t %f\t %f\t %f\t %f\t %f\t %f\n',strainmatrix);
fclose(fid)
```

```
aviobj = avifile('ROUARDS_METHOD_CUBE_amended.avi','fps',1.5,'quality',100);
set(gcf,'NextPlot','replace','Visible','off');

    frame = getframe(gcf);
    aviobj = addframe(aviobj,frame);
    plot(finall(:,1),finall(:,2))
    xlabel('Wavelength')
    ylabel('Reflectivity')
```